Investigation of microstructural evolution and recrystallisation mechanisms in 316L and 316Nb austenitic stainless steels during early stages of industrial open-die forging

---

Arthur PAQUETTE

Supervisors : Salaheddin RAHIMI, Laurent LANGLOIS,
Tatyana KONKOVA

Industrial sponsors : Christian DUMONT, Sébastien NOUVEAU

A thesis submitted in fulfilment of the requirements for the degree of
Doctor of Philosophy (PhD)

University of
Strathclyde
Glasgow

AUBERT&DUVAL

Design, Manufacturing and Engineering Management

2025

AFRC
ADVANCED FORMING RESEARCH CENTRE
UNIVERSITY OF STRATHCLYDE

LCFC
Conception Fabrication Commande

DECLARATION OF AUTHENTICITY AND AUTHOR'S RIGHTS

This thesis is the result of the author's original research. It has been composed by the author and has not been previously submitted for examination which has led to the award of a degree.

Signed:

Date: 15/05/2025

PREVIOUSLY PUBLISHED MATERIAL

Parts of this thesis have appeared in the following peer reviewed publications:

- Paquette A., Rahimi S., Violatos I., Langlois L., Dumont C., Blaizot J., Rosochowska M., Bigot R. (2021). On the evolution of microstructure and mechanical properties of type 316 austenitic stainless steel during ingot to billet conversion process. Paper presented at ESAFORM 2021. 24th International Conference on Material Forming, Liège, Belgium. DOI: https://dx.doi.org/10.25518/esaform21.929
- Paquette A., Langlois L., Violatos I., Rahimi S., Dumont C., Bigot R., Determination of recrystallisation phenomenon in type 316 stainless steel VIM-VAR ingots during cogging operations, Materials Research Proceedings, Vol. 28, pp 621-628, 2023. DOI: https://doi.org/10.21741/9781644902479-67

ABSTRACT

The ingot-to-billet conversion process is a critical thermomechanical stage in the manufacturing of high-value engineering components, where the refinement of coarse, columnar as-cast microstructures into fine, equiaxed grains ensures optimal mechanical properties and structural integrity. This PhD research focuses on the deformation and recrystallisation behaviour of 316L and 316Nb austenitic stainless steel grades during the ingot-to-billet conversion process. While existing studies largely focus on either laboratory-scale experiments or industrial-scale observations, this work bridges the gap between both scales by employing intermediate-scale experiments that balance industrial representativeness while ensuring experimental control. Compared to laboratory-scale studies, intermediate-scale experiments involve larger samples containing a significantly higher number of grains. As a result, they offer a statistically more representative depiction of the deformation and recrystallisation behaviour of as-cast materials under industrial-scale processing conditions.

An experimental campaign involving small-scale hot upsetting tests and large-scale forging trials (i.e., cogging and upsetting) was designed to investigate material behaviour in the early stages of the ingot-to-billet conversion process. The experimental work was supported by finite element (FE) simulations incorporating anisotropic material models and an innovative quantitative characterisation methodology developed to capture microstructural evolution over large surface areas, enabling the effective tracking of recrystallisation progress at large length scales and allowing for meaningful analysis of microstructural changes in partially recrystallised as-cast material. The results demonstrated the significant influence of crystallographic texture on anisotropic deformation behaviour of the as-cast material, and the role of the coarse as-cast grain size on its heterogeneous deformation and recrystallisation during forging. The presence of Niobium in the 316Nb grade was shown to result in a finer initial grain structure and promoted the retention of secondary phases after homogenisation. Through an increased number of nucleation sites and reduced grain boundary mobility, both characteristics promoted enhanced recrystallisation in 316Nb compared to the 316L grade.

This research highlights the complementary roles of laboratory and intermediate-scale studies in the design and optimisation of ingot-to-billet manufacturing routes. It also demonstrates the value of larger scale experimental and characterisation approaches in understanding material and process interactions for efficient and quality-driven ingot-to-billet conversion processes, with direct relevance to industrial sectors including energy, aerospace, and transportation.

RÉSUMÉ

Le processus de conversion de lingots en billette est une étape critique de transformation thermomécanique dans la fabrication de composants d'ingénierie à haute valeur ajoutée, où l'affinement des microstructures grossières et colonnaires en grains fins et équiaxes garantit les propriétés mécaniques et l'intégrité structurelle des composants. Cette thèse de doctorat se concentre sur le comportement en déformation et l'évolution microstructurale des aciers inoxydables austénitiques 316L et 316Nb au cours du processus de conversion du lingot en billette. Alors que les études existantes se concentrent principalement sur des expériences à l'échelle du laboratoire ou sur des observations à l'échelle industrielle, ce travail comble le fossé entre ces deux échelles. Il met en œuvre des expériences à plusieurs échelles intermédiaires, qui équilibrent la représentativité industrielle tout en garantissant le contrôle expérimental.

Une campagne expérimentale comprenant des essais de refoulement à chaud à petite échelle et des essais de forgeage à grande échelle par étirage et refoulement a été conçue pour étudier le comportement des matériaux aux cours des premières étapes du processus de conversion de lingots en billettes. Les travaux expérimentaux ont été étayés par des simulations par éléments finis intégrant des modèles de matériaux anisotropes. Une méthodologie innovante de caractérisation quantitative a été mise au point pour étudier l'évolution de la microstructure au sein d'échantillons de grandes dimensions. Les résultats de cette étude ont démontré l'influence significative de la texture cristallographique sur le comportement de déformation anisotrope du matériau brut de coulé, ainsi que le rôle de la taille grossière des grains après solidification du matériau sur sa déformation et recristallisation hétérogènes pendant le forgeage. Il a été démontré que la présence de Niobium dans la nuance 316Nb entraînait une structure de grain initiale plus fine et favorisait la rétention des phases secondaires après homogénéisation comparé à l'acier 316L. Grâce à un nombre accru de sites de germination et à une mobilité réduite des joints de grains, ces deux caractéristiques ont favorisé une meilleure recristallisation pour la nuance 316Nb, par rapport au 316L.

Cette thèse met en évidence les rôles complémentaires des études en laboratoire et à échelle intermédiaires pour la conception et l'optimisation des gammes de conversion de lingots en billettes. Elle démontre également l'intérêt des approches expérimentales et de caractérisation effectuées à plus grande échelle pour une meilleure compréhension des interactions entre le matériau et les procédés de transformation au cours de la conversion de lingots en billettes. Cela bénéficie au développement de procédés de fabrication efficients et permettant de répondre à des standards qualité exigeants, avec une applicabilité directe pour les secteurs industriels tels que l'énergie, l'aérospatiale et les transports.

ACKNOWLEDGEMENTS

Firstly, I would like to express my deepest gratitude to my supervisors, Dr. Salaheddin Rahimi and Dr. Laurent Langlois, for their invaluable motivation, support and guidance throughout this long journey. Their encouragement and patience during my PhD have been truly appreciated. I would also like to extend special thanks to Dr. Ioannis Violatos and Dr. Tatyana Konkova for their supervision and advice during this project.

I am grateful to Aubert & Duval, especially Christian Dumont for offering his expertise and supplying the ingot materials critical to my project, and Sebastien Nouveau for his technical and emotional support over the years. Our many valuable discussions, often extending beyond the scope of this thesis, have been immensely enriching for my personal development. Thanks to Marine Ross for undertaking his continuation at the Advanced Forming Research Centre (AFRC). This project could not have been accomplished without the help and advice of Jérôme Blaizot and Jean-Baptiste Maillet. I am equally thankful to Emile Delaunay for his significant contribution during his internships at the AFRC, and for the memorable trip we shared to the Isle of Skye.

I would also like to thank the interns who assisted me during my thesis work, Clément Friche and Malak Bousmaha.

My sincere thanks also goes to Dr. Dorothy Evans for her kind support and helping with the administrative side of this PhD. Thanks to all of the AFRC staff who gave guidance and access to the laboratory and research facilities. This work would not have been possible without the precious help, advice, and support from the staff of the Laboratoire de Conception, Fabrication et Commande (LCFC).

Also, I have a special thanks for Corentin, Jean-François, Clément and Damien for making my stay in Metz unforgettable. My submarine will proudly stand in my office to remind me these good times.

Thank you to my fellow PhD students at the AFRC – Matthew Ferguson, Angus Coyne and Beatrice Crocco – for your support and camaraderie; you made my stay in Glasgow much more enjoyable. A special mention to Sean Peters, who helped me escape from that chaotic house with dogs and chickens wandering through the living room – your flat made all the difference.

I would like to thank my dear friends, for their support, encouragements and patience: les Boquets, Scud, Toss, Korky, Patate, LuLu, Steph', Seb', Sigaux, and all the other! Boncubi, I am proud of your limitless and relevant support; even though not all your advice were followed, I finally made it!

Most of all, I am deeply grateful to my family for their love and encouragement, which pushed me to carry this project across the finish line. To you, Floriane, thank you for your love and your unwavering confidence in me; let us now enjoy together this beautiful life "just right here".

TABLE OF CONTENTS

Chapter 1 : INTRODUCTION

1.1 BACKGROUND AND MOTIVATION

The production of high-value, high-integrity engineering components demands complex and carefully controlled thermomechanical processing routes. These sequential operations are essential for developing tailored microstructures and mechanical properties that ensure the final component performs reliably under service conditions (see Figure 1.1). Among these operations, the ingot-to-billet conversion process plays a pivotal role in transforming the as-cast microstructure—typically characterised by coarse, columnar dendritic grains and strong crystallographic texture—into a more homogeneous, fine-grained, and equiaxed microstructure suitable for downstream processing.

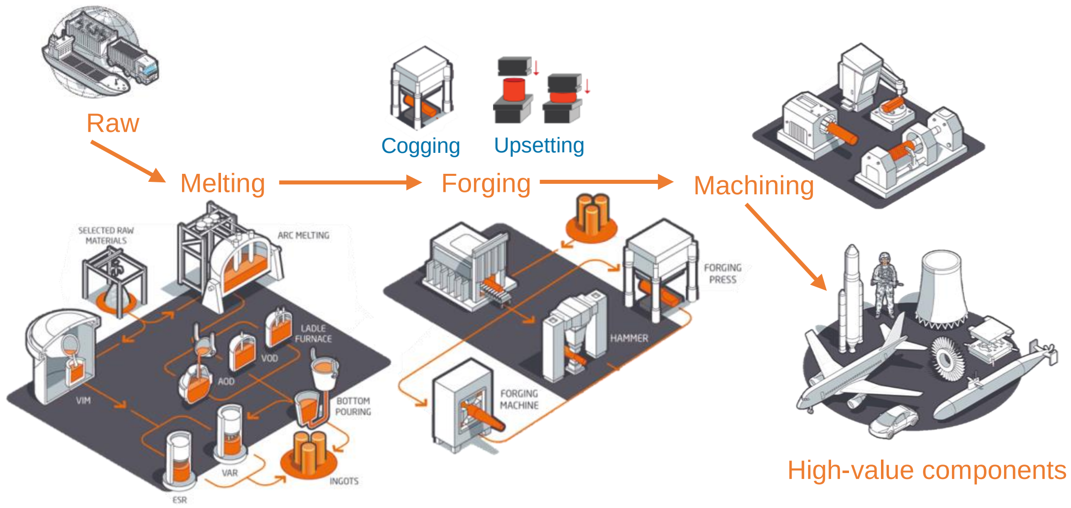

Figure 1.1 : Schematic representation of a typical industrial manufacturing sequence for high-value engineering components. (Images sourced from Aubert & Duval website).

This primary conversion process is indispensable in the manufacturing route of many critical engineering components, especially in safety- and performance-sensitive sectors such as aerospace, energy, defence, and transportation. The ingot-to-billet conversion step is often the only feasible method to produce billets with the requisite internal soundness and microstructural quality. These billets then serve as feedstock for further thermomechanical operations such as open- or closed-die forging, heat treatments, and machining.

The ingot-to-billet conversion process involves subjecting as-cast ingots to high-temperature deformation through combinations of upsetting and incremental cogging operations using open-die forging techniques. As a function of chemical composition and processing parameters—namely strain, strain rate, and temperature—dynamic and post-dynamic recrystallisation mechanisms are activated, leading to substantial microstructural refinement (see Figure 1.2).

Given the demanding requirements for structural integrity, corrosion resistance, and microstructural homogeneity in such components, a deep understanding of the physical mechanisms governing microstructure evolution during this conversion step is essential.

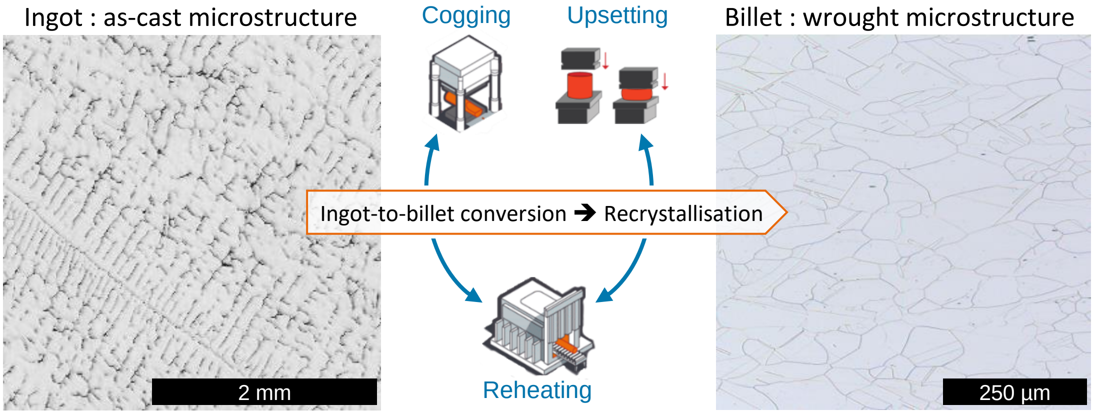

Figure 1.2 : Schematic depiction of the microstructural transformation occurring during ingot-to-billet conversion—from coarse columnar grains to fine equiaxed grains.

Despite significant advances in understanding microstructural evolution in metallic systems, most existing studies fall into two categories: laboratory-scale experiments or industrial-scale observations. Laboratory-scale investigations offer high control over processing conditions and enable in-depth microstructural characterisation. However, they often lack industrial representativeness, especially regarding deformation heterogeneities and heat transfer phenomena. In contrast, industrial-scale studies provide realistic conditions but suffer from limitations such as high operational costs, complex deformation histories, and limited instrumentation for in-process monitoring and data acquisition.

To bridge this gap, recent developments in intermediate- to industrial-scale research facilities, such as the FutureForge platform at the Advanced Forming Research Centre (AFRC) shown in Figure 1.3, provide a unique opportunity to conduct controlled, realistic forging experiments under conditions closely resembling industrial practice.

This PhD thesis aims to investigate the microstructural evolution and recrystallisation behaviour of 316L and 316Nb austenitic stainless steels during the early stages of the ingot-to-billet conversion process, using intermediate- to industrial-scale open-die forging. The objective is to generate fundamental insights that inform the optimisation of forging parameters and support the development of cost-effective and quality-driven manufacturing routes.

316L and 316Nb austenitic stainless steels were selected for this study due to their excellent formability, thermal stability, resistance to cracking, and cost-effectiveness, as well as their limited susceptibility to detrimental precipitation. These attributes make them ideal candidate materials for investigating the fundamental mechanisms of recrystallisation and microstructural transformation during high-temperature processing.

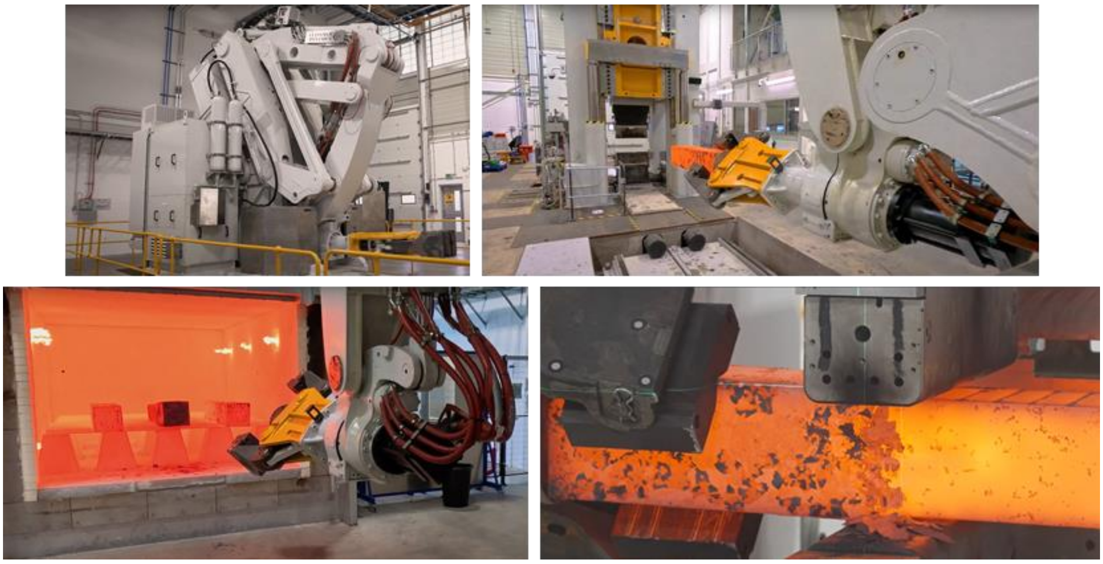

Figure 1.3 : The FutureForge research platform at the Advanced Forming Research Centre (AFRC). This facility includes a 2000-tonnes hydraulic press with open-die, closed-die, and isothermal forging capabilities, coupled with dual industrial scale Gas and Electric furnaces and a robotic manipulator arm. Adapted from (AFRC FutureForge, 2024).

1.2 THESIS OUTLINE

This thesis is structured as follows:

Chapter 2 introduces the fundamental principles underpinning microstructure evolution and recrystallisation in austenitic stainless steels. It also reviews relevant literature on the ingot-to-billet conversion process, with a focus on as-cast material behaviour and austenitic alloys.

Chapter 3 describes the materials used in this study, along with the experimental methods, thermomechanical processing approaches, finite element (FE) simulations, and microstructural characterisation techniques developed to investigate the ingot-to-billet conversion process.

Chapter 4 and 5 present the core findings of the thesis. These chapters include experimental results, numerical simulations, and quantitative microstructural analyses across the different processing scales.

Chapter 6 provides a critical discussion of the results, contextualising them within the broader scientific literature and extracting key implications for industrial forging processes.

Chapter 7 summarises the principal conclusions of the thesis, highlighting the most significant scientific and practical contributions.

Chapter 8 outlines potential avenues for future research, including methodological improvements and broader applications of the findings within the field of advanced thermomechanical processing.

Chapter 2: LITERATURE REVIEW

CONTENT

2.1 INTRODUCTION

This chapter provides an overview of relevant previous research on microstructure evolution during ingot-to-billet conversion processes. To begin with, common industrial processes involved in casting and ingot-to-billet conversion processes are introduced. The specifics of as-cast material microstructures and their deformation behaviours are covered, and compared to that of wrought materials (i.e., material with fine and equiaxed grains produced by the end of forging). Microstructure evolution mechanisms throughout hot working are then reviewed, including details of Nb-containing grades of austenitic stainless steels. The methods commonly reported for both the investigation of the as-cast microstructures evolution during hot forging, and the development of manufacturing routes for the ingot-to-billet conversion process are finally summarised. Citations and examples introduced in this literature review were chosen to provide examples in the scope of as-cast and austenitic stainless steels type of materials where possible. Note that values for grade composition are provided in weight %.

2.2 AUSTENITIC STAINLESS STEELS

Stainless steels are Fe-based alloys containing at least 10.5 % Chromium (Cr), less than 1.2% Carbon (C), and numerous additional alloying elements. They are renowned for their corrosion resistance and mechanical properties. These alloys derive their name from their remarkable ability to resist staining (i.e., corrosion) thanks to a significant proportion of Cr, which forms a passive oxide layer on the material surface, providing a protective barrier against corrosive environments.

Annual world-wide production of stainless steels almost continuously increased since 1950, and reached ≈ 51×10^6 tonnes in 2020 (International Stainless Steel Forum, 2021).

Stainless steels are classified into several families with specific composition and microstructure characteristics, each of which is tailored to specific applications and environments. The main families of stainless steels include austenitic, ferritic, martensitic, duplex (i.e., a balanced composition of austenitic and ferritic phases), and precipitation-hardening stainless steels. The standard AISI (American Iron and Steel Institute) designation scheme for stainless steels uses a numerical system to classify the different families and grades of stainless steels, based on their composition and characteristics. As examples, the AISI 200 and 300 series stand for the austenitic stainless steels family, including the AISI 316 grade. With additional information on the grade properties, Figure 2.1 summarises the compositional relationship between the main families of stainless steels based on the AISI classification system. Despite that the AISI designation scheme is widely used in research and industry, other standards and classification systems were developed by organisations such as the ISO (International Organisation for Standardisation), and ASTM (American Society for Testing and Materials).

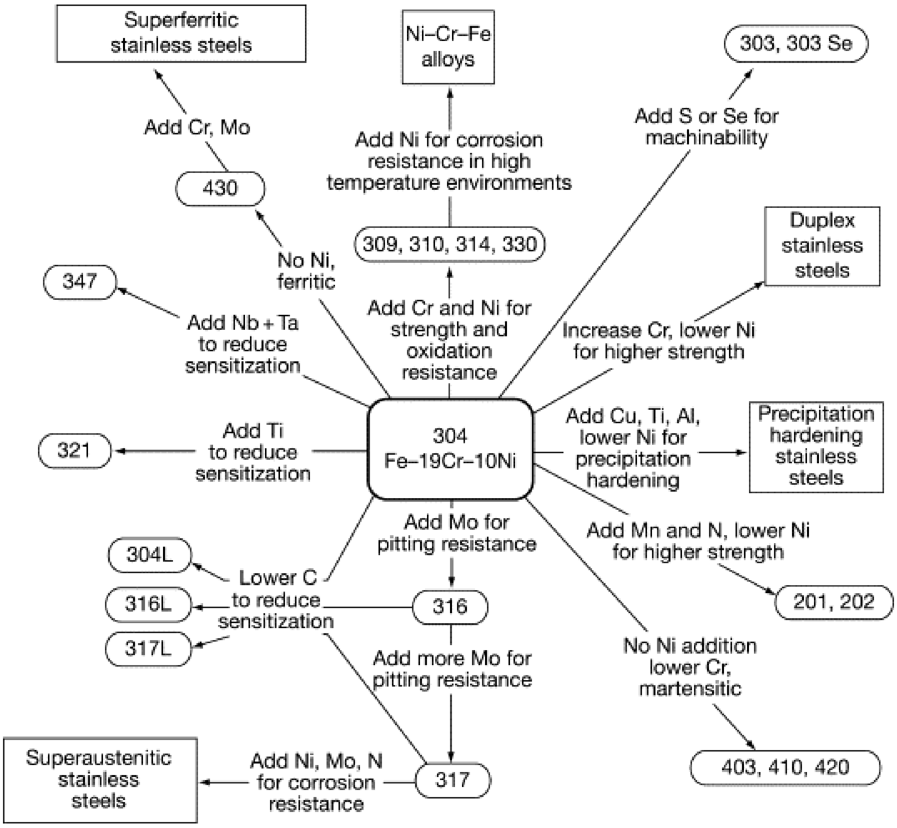

Figure 2.1 : Compositional relationship between different families of stainless steels according to the AISI classification system, (Sedriks, 1996).

Among all types of stainless steels, austenitic stainless steels contain a significant amount of Cr and Ni alloying elements, and are renewed for their high corrosion resistance, excellent formability, and good mechanical properties. The balance between these different properties can be adjusted by varying the composition of the alloy. Typical alloying elements and corresponding composition ranges of austenitic stainless steels are summarised in Table 2.1, with the effects of different alloying elements on the overall properties highlighted in Figure 2.1. Cr depletion of austenite near the grain boundaries caused by the formation of $Cr_{23}C_6$ carbides at grain boundaries can lead to detrimental intergranular corrosion of austenitic stainless steels. This can be impeded by reducing the amount of C, either from decreasing the C content from the grade composition, or by introducing Nb in the grade composition. Thanks to its strong affinity for C, Nb allows to replace precipitation of $Cr_{23}C_6$ carbides at grain boundaries by NbC carbides intragranularly, and therefore reduce the susceptibility of the material to sensitisation and therefore subsequent intergranular corrosion. Nb containing grades are thus termed as "stabilised". Nb also act as a grain refiner and has advantageous effects on the material creep resistance and mechanical properties due to the strengthening effect of the solute Nb atoms and NbC carbides. Grades with low-carbon composition (i.e., below 0.04%), and those containing over 8 times the amount of C in Nb have their AISI designation extended with "L" (e.g., 316L) and "Nb" (e.g., 316Nb), respectively. Similarly, the "H" letter in the AISI designation of 316H grade stands for a higher C content, up to 0.1%, compared to the normal 316 grade. The higher carbon content enhances its strength at elevated temperatures, making it suitable for high-temperature applications such as petrochemical processing, heat exchangers, and boilers. Also, the "N" letter of the 316LN designation stands for nitrogen enrichment, which can improve physical, chemical and mechanical properties, especially at high temperature.

Table 2.1 : Typical composition ranges for austenitic stainless steels (wt %), (Lippold and Kotecki, 2005).

Cr	Ni	Mn	Si	C	Mo	N	T, Nb
16 - 25	8 – 20	1 – 2	0.5 – 3	0.02 – 0.08	0 – 2	0 – 0.15	0 – 0.2

As the name indicates, austenitic stainless steels are mainly composed of austenite (γ) and have a face-centred cubic (FCC) crystal structure, in which the atoms are typically located at the vertices and centres of the face of the unit cell (see Figure 2.2 a)). Table 2.2 summarises the different phases and precipitates which can be found in austenitic stainless steels. As can be seen from Figures 2.3 and 2.4, those phases may exist depending on the grade composition and temperature exposure of the material.

δ-ferrite phase can also be found within the γ austenite matrix in austenitic stainless steels. It is formed either during solidification of the alloy or through further solid-state phase transformations, and has deleterious effects on corrosion resistance and mechanical properties (Xu et al., 2019). δ-ferrite phase has a body centred crystal (BCC) structure (see Figure 2.2 b)).

The amount of δ-ferrite in austenitic stainless steels is a function of the grade composition, and is explored with more details in Section 2.3. In austenitic stainless steels, δ-ferrite may also transform into brittle intermetallic σ-phase between 540 °C and 925 °C under cooling rates below 150 °C/min (Perron et al., 2014). The precipitation of σ-phase causes losses in ductility and toughness, and reduce the corrosion resistance of the alloy by removing Mo and Cr from the austenitic matrix (Villanueva et al., 2006). Under rapid cooling or cold working, martensite can also form in austenitic stainless steels due to the diffusionless nature of the martensitic transformation, which allows austenite to transform into martensite without the need for diffusion of atoms.

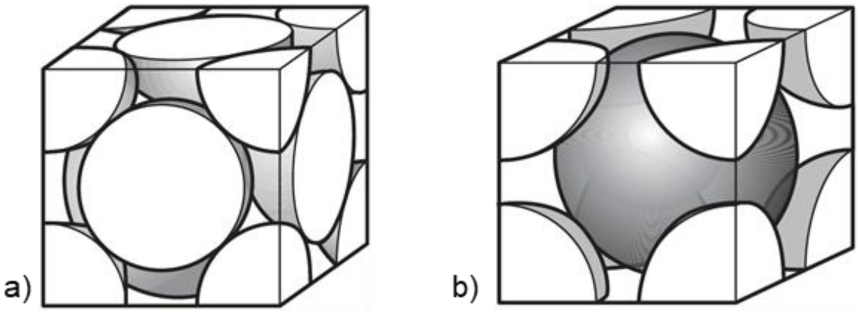

Figure 2.2 : Schematic representation of atoms packing within the unit cells of a) γ austenite (FCC), and b) δ-ferrite (BCC) phases, (Shackelford, 2015).

Table 2.2 : Phases and precipitates in austenitic stainless steels, (Lippold and Kotecki, 2005).

Phase	Crystal structure	Typical composition	Stability temperature range (°C)
MC	FCC	NbC, TiC, TiN	480 to 815
M_2C	FCC	(VTi)C	
M_7C_3	Pseudo hexagonal	Cr_7C_3, $(FeCr)_7C_3$, $(Fe_{0.6}Cr_{0.4})_7C_3$	
$M_{23}C_6$	FCC	$(Cr_{16}Fe_5Mo_2)_6C$, $(FeCr)_{23}C_6$, $(Cr17Fe_{4.5}Mo_{1.5})C_6$	
M_6C	FCC (diamond type)	$(CrCoMoNi)_6C$, $(TiNi)_6C$, $(NbNi)_6C$, $(Fe_3Mo_3)C$	
Boro Carbides	FCC	$M_{23}(CB)_6$	
Borides	Orthorhombic	M_3B_2, M_2B	
Nitrides	FCC / HCP	M(CN), M_2N, MN, M_2NC	
Sigma (σ)	BCC tetragonal	$(FeNi)_x(CrMo)_yFeCr$, $(FeNi)_x(CrMo)_y$	540 to 925
Chi (χ)	BCC	$(FeNi)_{36}Cr_{18}Mo_4$, $Cr_6Fe_{18}Mo_5$, $Fe_{36}Cr_{12}Mo_{10}$	≤ 925
Laves (η)	Hexagonal	Fe_2Mo, Fe_2Ti, Fe_2Nb	

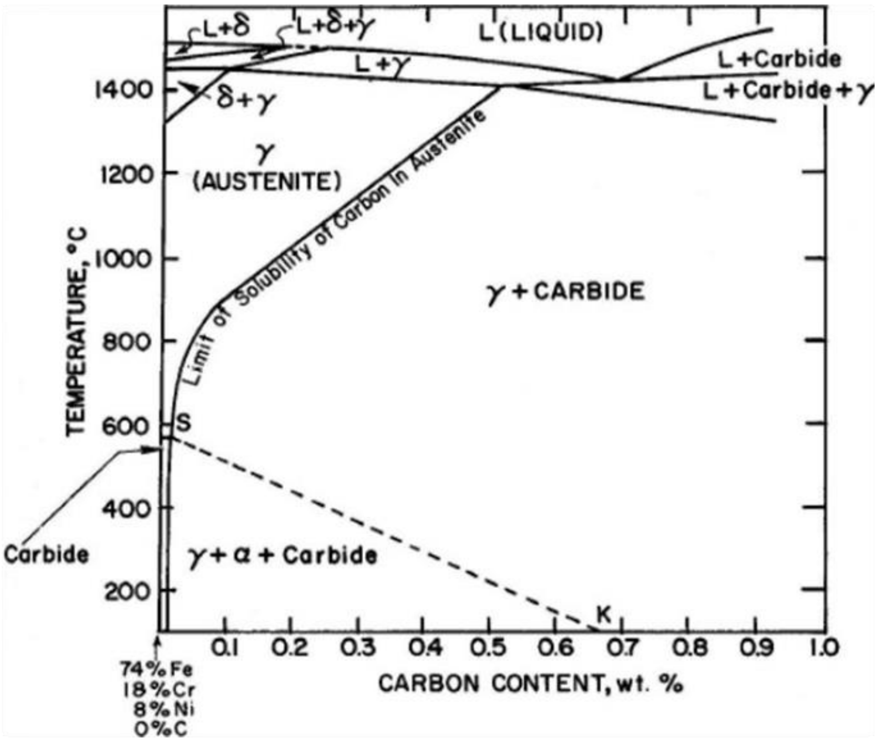

Figure 2.3 : Phase diagram for Fe-18%Cr-8%Ni stainless steel with varying carbon contents, (Sedriks, 1996).

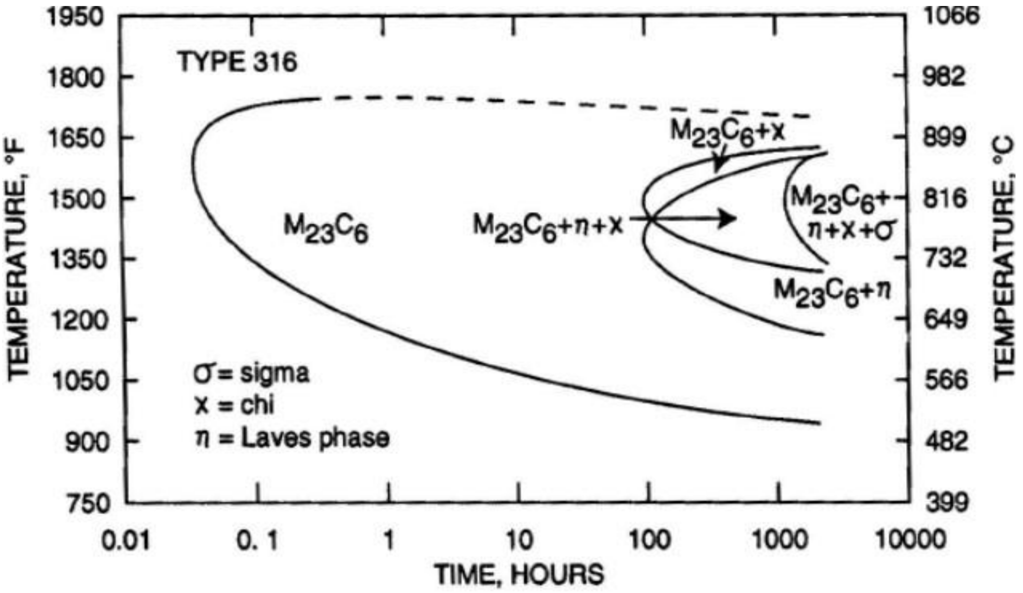

Figure 2.4 : Time-temperature-precipitation (TTP) diagram for type 316 stainless steel containing 0.066% carbon, (Sedriks, 1996).

2.3 CASTING AND INGOT-TO-BILLET CONVERSION PROCESSES

This section provides an overview of the current state-of-the-art industrial processes for casting and the subsequent ingot-to-billet conversion stages of producing wrought products. These are shown schematically in Figure 2.5. The ingot-to-billet conversion process plays an essential role in achieving a refined and equiaxed microstructure from a coarse and directionally grown grains formed during solidification (i.e., casting). One of the key aims of the process is to convert the as-cast structure to fully recrystallised microstructure, by subjecting the ingot to deformation at elevated temperatures, which is typically achieved through a combination of upsetting and incremental cogging operations using open-die forging. The ingots are maintained at elevated temperatures by introducing heating and reheating stages along the deformation process to enhance the workability of the material and allow for the microstructure evolution mechanisms to take place.

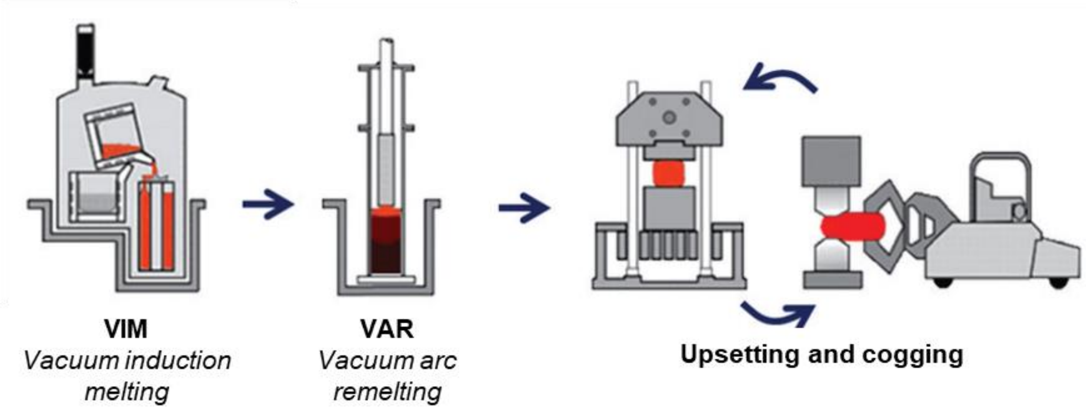

Figure 2.5 : Schematic representations of industrial casting and ingot-to-billet conversion processes of upsetting and cogging (i.e., open-die forging). Adapted from (Beijiang et al., 2015).

Bottom-pouring and vacuum induction melting (VIM) are the primary casting processes to make ingots. The bottom pouring process, schematically shown in Figure 2.6, involves casting of the molten material from the bottom of the moulds. An exothermic powder is dispersed over the molten pool, which forms a protective liquid slag avoiding direct contact of the molten metal with the ambient air, thus reducing the oxidation of the melt. The amount of C in the molten metal can be adjusted prior to casting through Argon-Oxygen decarburisation (AOD) process, during which a mix of Argon and Oxygen gazes are blown into the molten metal to convert C and other impurities to CO and other gases. As can be seen in Figure 2.7, large ingots, weighting over several hundreds of tonnes, can be casted through bottom-pouring. One of the major disadvantages of bottom-pouring is the lack of control of the direction of solidification, leading to the presence of central shrinkage porosities (Wang et al., 2012).

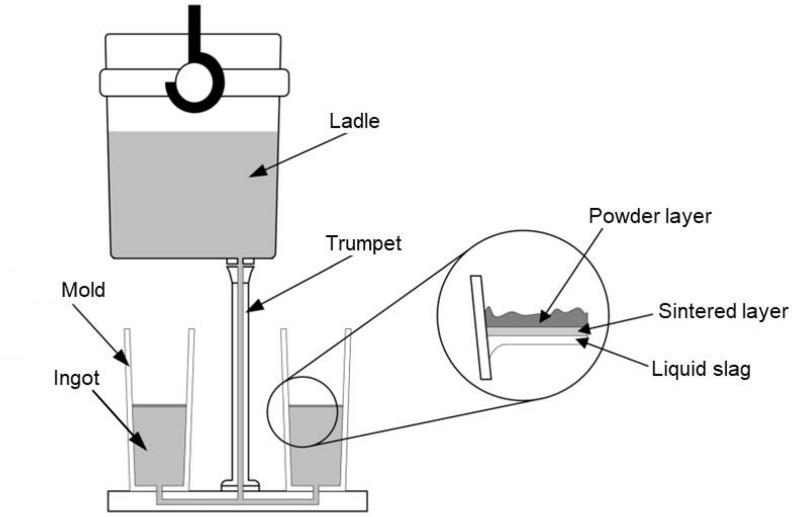

Figure 2.6 : A schematic sketch of bottom pouring casting process to produce ingots, (Eriksson et al., 2004).

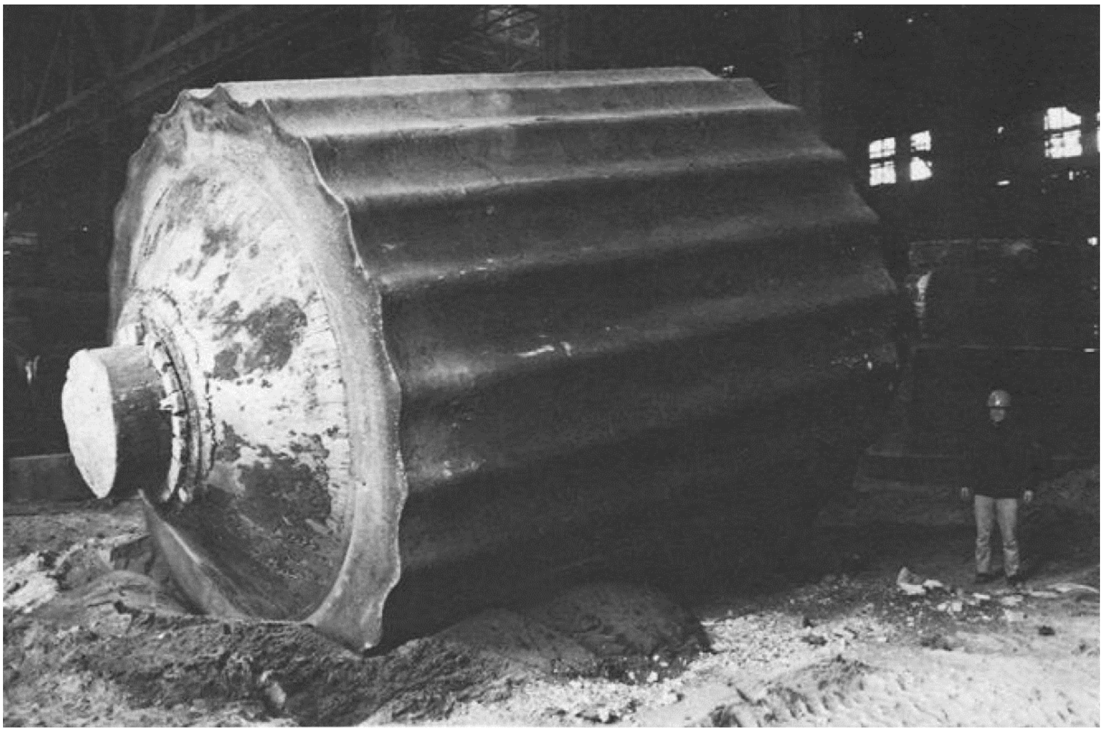

Figure 2.7 : A photograph of a 570 tonnes ingot made of 20MnMoNi 5-5 low-alloy steel. Note the size of the ingot compared to the man standing nearby, (Kawaguchi et al., 1986).

Vacuum induction melting (VIM) process, shown schematically in Figure 2.8, consists of melting raw alloying elements of the alloy under vacuum by induction heating. The vacuum environment prevents oxidation of the molten metal, ensuring the production of clean and high-purity ingots. The composition of the alloy can be adjusted during the process to reach the compositional specification of a certain grade, and the molten alloy is subsequently casted in a crucible having a geometry of the desired ingot (Abrams et al., 2018). A common industrial practice consists of remelting the primary casted ingots (i.e., following bottom-pouring or VIM) using the vacuum arc remelting (VAR) process, which further improves the purity and cleanliness of the ingots. During VAR, an ingot serves as a consumable electrode, undergoing remelting under near vacuum conditions by the effect of a direct current arc generated between the electrode (i.e., the ingot), and a water or nitrogen cooled crucible. A photograph of a 30 tonnes ingot capacity VAR furnace is shown in Figure 2.9, and a schematic sketch of the furnace configuration is shown on Figure 2.10. With appropriate regulation of voltage and current parameters applied to the electrode, the ingot undergoes progressive remelting from one side to the other axially, with accurate control of the rate of remelting and solidification (Abrams et al., 2018). With advantageous control of the directional solidification of the alloy, VAR allows to produce an ingot free of porosities and macro-segregation. An alternative process to VAR is the electro-slag remelting (ESR) process, which uses slag protection instead of vacuum to prevent oxidation in the molten metal, avoiding changes in chemical composition through dissolution of oxygen, hydrogen and nitrogen, which may be removed from the alloy composition while remolten under vacuum during VAR. Superalloy ingots are commonly produced through a three stage casting composed of successive VIM, VAR and ESR castings (i.e., a triplex production).

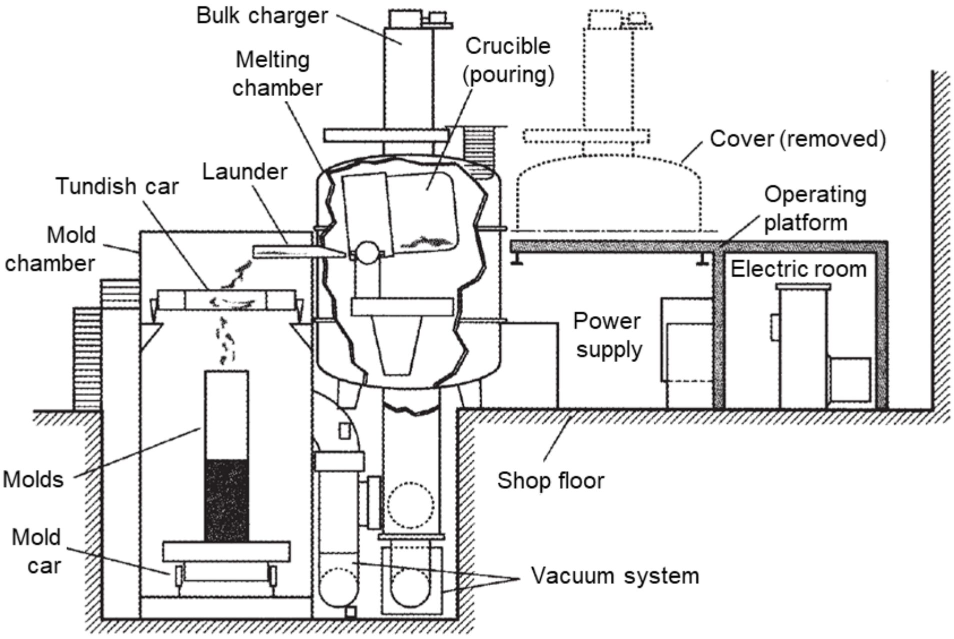

Figure 2.8 : Schematic sketch of a vacuum induction melting (VIM) furnace, (Viswanathan et al., 2008).

Figure 2.9 : Photograph of a 30-tonnes capacity vacuum arc remelting (VAR) furnace, (Reardon, 2011).

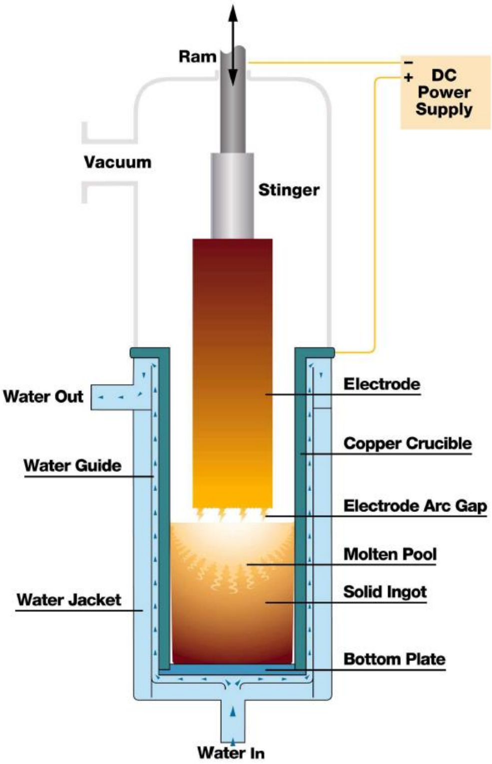

Figure 2.10 : Schematic sketch of a vacuum arc remelting (VAR) furnace, (Kelkar et al., 2007).

Following casting, several thermo-mechanical processes are involved to transform the as-cast microstructure of the ingot to refined recrystallised grains. This typically involves the cogging process, which is incremental open-die forging where a portion of the ingot is incrementally deformed between two opposite dies in a series of press strokes, passes, and eventual intermediate reheating. Cogging allows for an overall reduction of the ingot's cross-section, and increases its length (ASM International, 1990). A photograph of a cogging operation is shown in Figure 2.11, and Figure 2.12 provides a schematic representation of a cogging operation on an ingot (i.e., the workpiece), with forging (green arrows), displacement (blue arrow) and rotation (red arrow) directions highlighted. The following terminology is used to describe different sequences of cogging (i.e., open-die forging) route, which comprises several ***passes***, each of which is executed with a specific orientation of the ingot up to a certain amount of reduction in cross-section (k_s). Within each pass, several forging ***strokes*** are conducted with the ingot successively translated between the anvils, along its entire length.

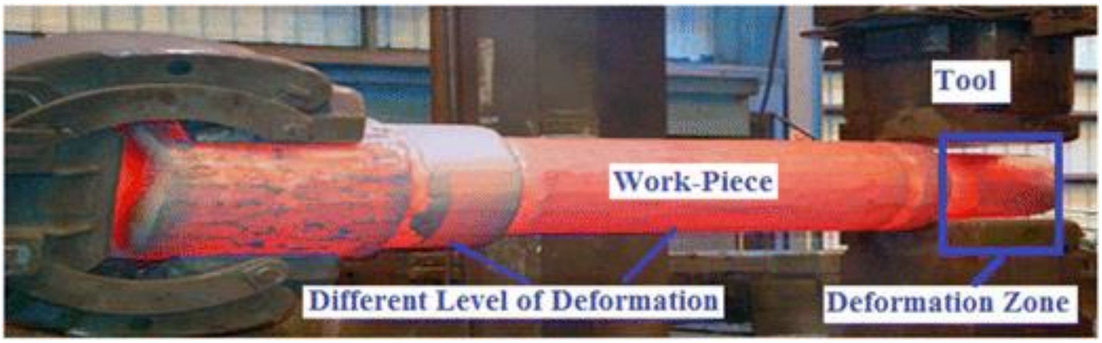

Figure 2.11 : A photograph of cogging operation, (Ramadan et al., 2019).

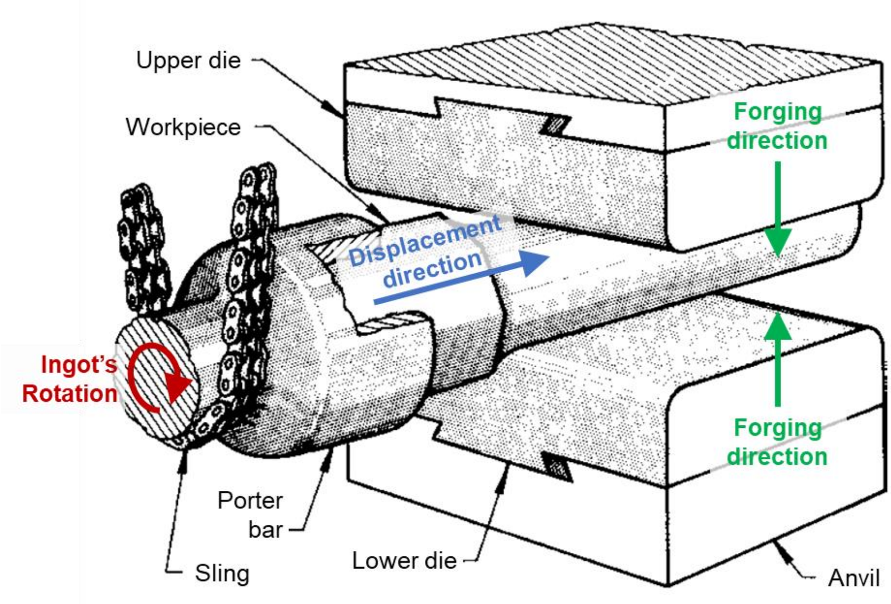

Figure 2.12 : Schematic depiction of cogging process. Adapted from (ASM International, 1990).

Upsetting is another form of open-die forging process exercised during ingot-to-billet conversion, which involves forging the ingot along its height (i.e., axial direction) between two flat dies, resulting in an increase in its transverse cross-section. Photographs of upsetting operations are shown in Figure 2.13. As can be seen from the results of FE simulation in Figure 2.14, deformation is usually localised in the core of the ingot during upsetting, whereas the top and bottom of the ingot experience limited deformation (i.e., known as the dead-zones).

The whole ingot-to-billet conversion process is incremental, composed of several stages of upsetting, cogging and intermediate reheating or heat treatments required to ensure the ingot remains at appropriate temperature for the desired refinement of the as-cast structure through recrystallisation. It is therefore a labour intensive, time and energy consuming process, which can only be performed with heavy duty equipment. As an example, a 10 000 tonnes capacity hydraulic press was used by (Wang et al., 2016b) for cogging a Ø 1700×3166 mm ingot (i.e., ≈ 60 tonnes) into a primary coolant pipe dedicated to nuclear power plant application.

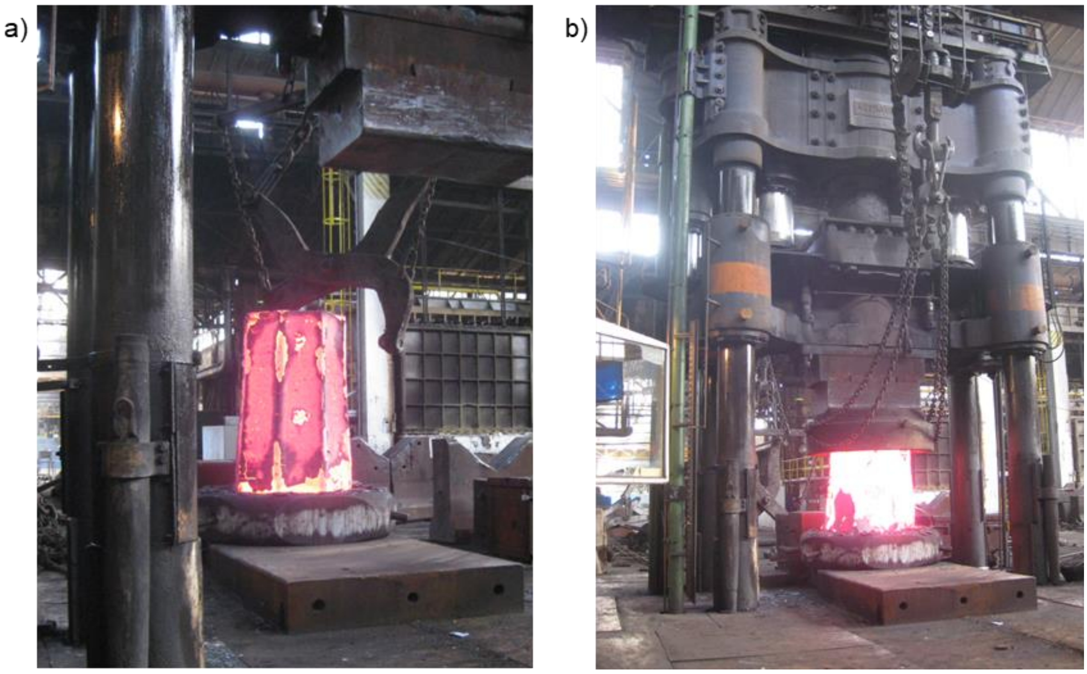

Figure 2.13 : Photographs of an upsetting operation performed on a bottom-poured ingot turned upside-down; a) prior, and b) during the upsetting. Adapted from (Christiansen, 2014).

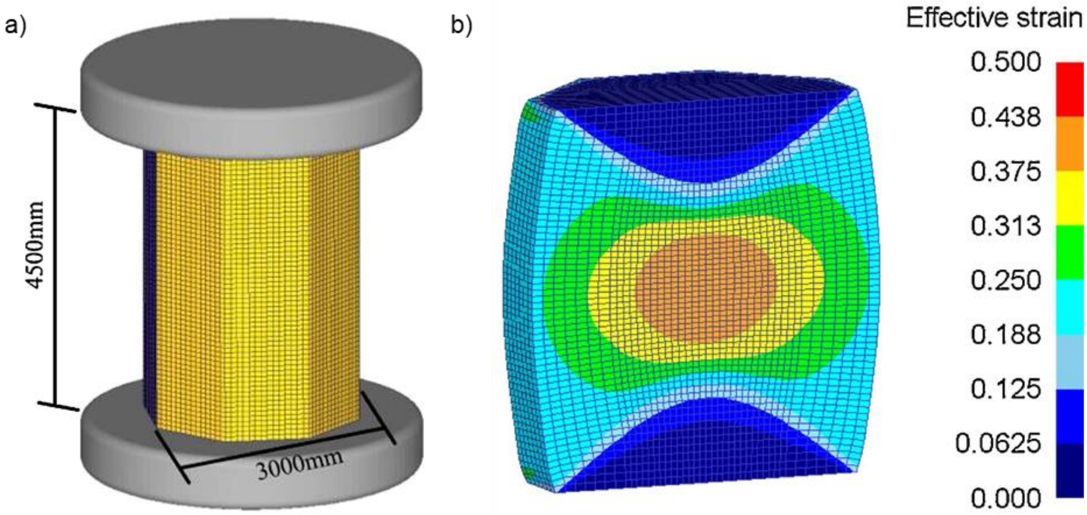

Figure 2.14 : Simulation results for upsetting a Ø3000×4500 mm octahedral billet; a) FE model, and b) effective strain distribution along the longitudinal cross-section following 20% upsetting. Adapted from (Feng et al., 2016).

2.4 AS-CAST MATERIALS

This section aims to introduce basics of solidification and the resulting microstructures. Research on solidification and as-cast material microstructures have been promoted by the development and industrialisation of casting, welding and additive manufacturing processes. Correlations between solidification conditions and the resulting microstructures are now well described in the literature (Kurz and D.J. Fisher, 1992) (Dantzig and Rappaz, 2016). Solidification is the transformation of an alloy from its liquid to solid state, and is achieved by nucleation of small solid particles (i.e., the nuclei) within the liquid metal, which subsequently grow to larger solid grain structures. For a given grade of material (i.e., with a given chemical composition), the morphology and size of the as-cast microstructure are controlled by the growth rate (R) and temperature gradient (G) parameters (Kou, 2003). The growth rate corresponds to the velocity of the liquidus isotherm, and the temperature gradient is the gradient of temperature in the mushy zone (i.e., at the solid/liquid interface).

As illustrated in Figure 2.15, the morphology and the size of the as-cast grains are determined by the G/R ratio, and G×R product, respectively. Both growth rate and temperature gradient parameters are functions of local thermal conditions taking place in the mushy zone. Among others, these are controlled by the material properties (i.e., thermal conductivities of liquid and solid phases, latent heat, etc.), the size and geometry of the ingot, the shape and composition of the mold or crucible, as well as by the casting process (i.e., presence of cooling devices, heat generated by electric arcs, etc.). Typical R and G values are provided in Table 2.3. The condition of solidification (i.e., G and R), and the resulting distribution of as-cast grain morphology, may therefore fluctuate throughout the entire solidification process. An example of which is shown in Figure 2.16, with the presence of a columnar-to-equiaxed transition (CET) (Spittle, 2006).

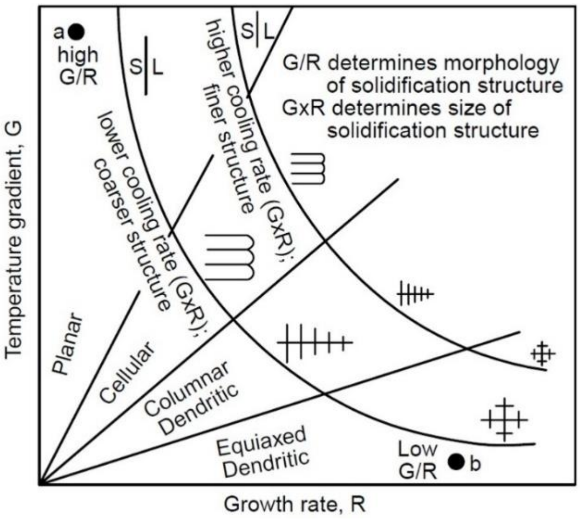

Figure 2.15 : Effect of temperature gradient (G), and growth rate (R) on the morphology and size of as-cast microstructures. (Kou, 2003).

Table 2.3 : Typical values for growth rate (R) and thermal gradient (G) in various casting and welding processes with steels, adapted from (Suutala, 1983).

Processing details		R (cm/min.)	G (°C/cm)	G / R	G×R
Ingot casting	1 ton, surface	2.2	70	32	154
	1 ton, core	0.2	10	50	2
	9 tonnes, surface	1	150	150	150
	9 tonnes, core	0.1	4	40	0.4
Continuous casting	Slab surface	6	330	55	1980
	Slab core	1	40	40	40
Gas tungsten arc welding	Full penetration	6	700	117	4200

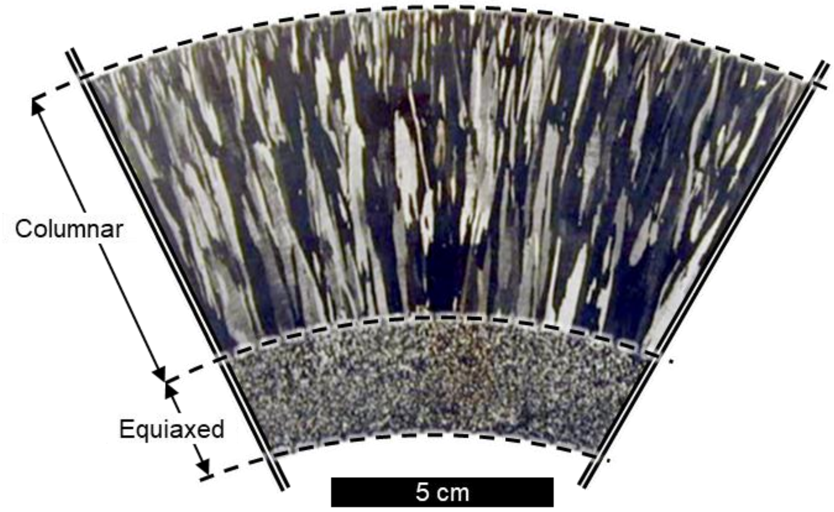

Figure 2.16 : An example of a columnar to equiaxed transition observed along the transverse cross-section of a centrifugally casted pipe made of austenitic stainless steel. Adapted from (Ramuhalli et al., 2009).

As can be seen in Figure 2.17 for as-cast 316L (Mataya et al., 2003a), columnar dendritic microstructures are developed during directional solidification which leads to a strong morphologic texture, with the direction of growth of the columnar grains being parallel to the temperature gradient at the liquidus isotherm (i.e., perpendicular to the liquidus isotherm). Figure 2.18 provides a 3D micrograph of the as-cast microstructure in type 308 austenitic stainless steel, with different morphologies observed depending on the direction of the cross-sectional cut considered for the observations, with regards to the direction of solidification. During solidification of FCC materials, the crystallographic orientation <100> of the grains are oriented parallel to the direction of solidification (i.e., parallel to the long axis of columnar grains), and columnar as-cast microstructures have therefore a strong crystallographic texture (Kurz and D.J. Fisher, 1992).

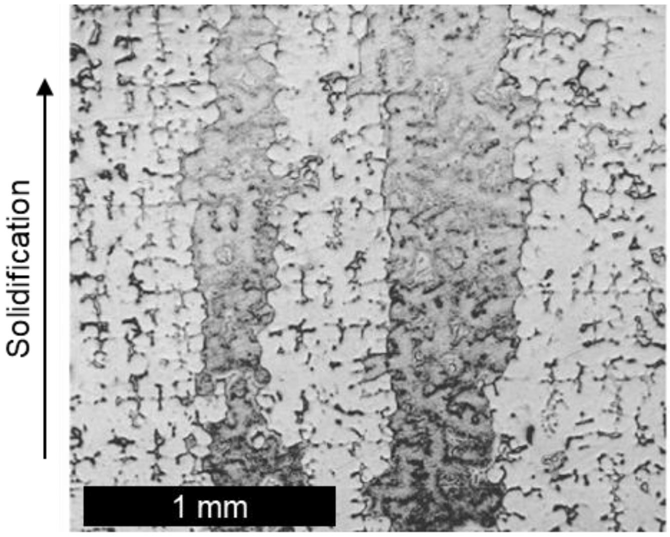

Figure 2.17 : Columnar dendritic grains in an as-cast 316L. Adapted from (Mataya et al., 2003a).

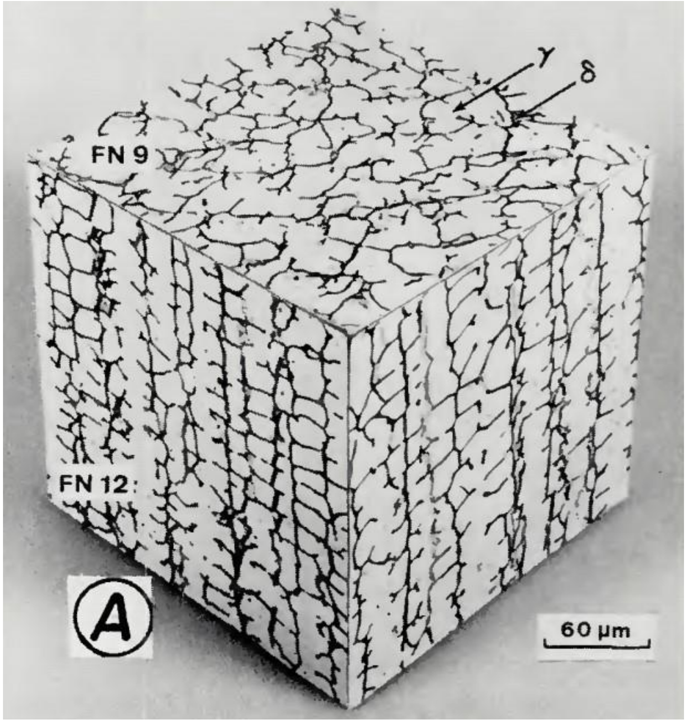

Figure 2.18 : A 3D micrograph of the as-cast type 308 austenitic stainless steel, (David, 1981).

The volume fraction and morphology of the δ-ferrite found in austenitic stainless steels are mainly functions of the grade composition. As can be seen from Figure 2.19, different solidification path can be obtained depending on the Ni and Cr contents of the alloy, which lead to different microstructures shown schematically in Figure 2.20. Calculation of Cr and Ni equivalent concentrations (i.e., Cr_{eq} and Ni_{eq}, respectively) can be performed using different criteria, such as that from "Hammer and Svensson" (see Equation (2.1)) to account for the effect of the alloying elements; some acting as austenite-stabilising elements (e.g., Ni, Mn, C, N, Cu and Co), and some others acting as ferrite-stabilising elements (e.g., Cr, Mo, Si, Nb, Ti, Al, V and T). Depending on the amount of individual alloying elements, or the presence of specific alloying elements, Schaeffler-DeLong and WRC-2 criteria may also be employed for the same purpose (Murugan and Parmar, 1997) (Lippold and Kotecki, 2005). The solidification mode, and the room-temperature phase composition of the stainless steels can then be predicted from the concentration ratio Cr_{eq}/Ni_{eq}. Table 2.4 summarises the solidification sequences for four solidification modes of austenitic stainless steels with corresponding values of Cr_{eq}/Ni_{eq} ratios.

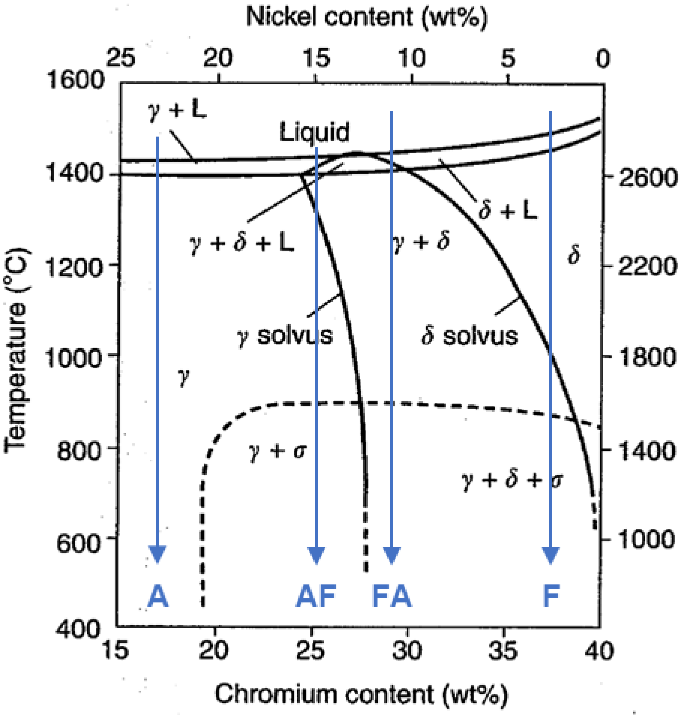

Figure 2.19 : Pseudo-binary section of the Fe- Cr-Ni ternary diagram at 60 % Fe, with different solidification modes superimposed with the blue arrows and annotations: A, Austenite; AF, Austenite – Ferrite, FA, Ferrite – Austenite; and F, Ferrite, see Table 2.4). Adapted from (Lippold and Kotecki, 2005).

As can be seen from Figure 2.21, second phases formed during the solidification process, such as δ-ferrite and σ-phase, result in micro-segregations, manifested in the form of chemical heterogeneities at the scale of the secondary dendritic arms (i.e., usually from 10 to 100 µm). Those second phases can adversely affect the hot-formability of the material (i.e., the ability of the metal to accommodate deformation) by promoting crack initiation during subsequent deformation stages. For instance, (Ledoux et al., 2014) demonstrated that the ductility of 316Nb austenitic stainless steel tensile samples cooled at a rate of 20 °C/min was reduced by ≈ 50 % compared to samples cooled at 200 °C/min. It was also noted that only 2 % of δ-ferrite transformed into σ-phase in the sample cooled at a rate of 20 °C/min. Micro-segregations formed during solidification may under some conditions be removed by performing homogenisation heat treatment, described in Section 2.6.1. Macro-segregations correspond to chemical heterogeneities formed at larger scales (i.e., up to several meters), during casting, and originate from the combination of formation of micro-segregation, and convective displacement of the liquid metal during the solidification. Figure 2.22 schematically show different types of macro segregations which can form in large ingots. In contrast to micro-segregations, macro-segregation cannot be readily removed by homogenisation heat treatment as a consequence of the prohibitive time needed for the solid-state diffusion to be completed at such large scales (Campbell, 2015) (Dantzig and Rappaz, 2016).

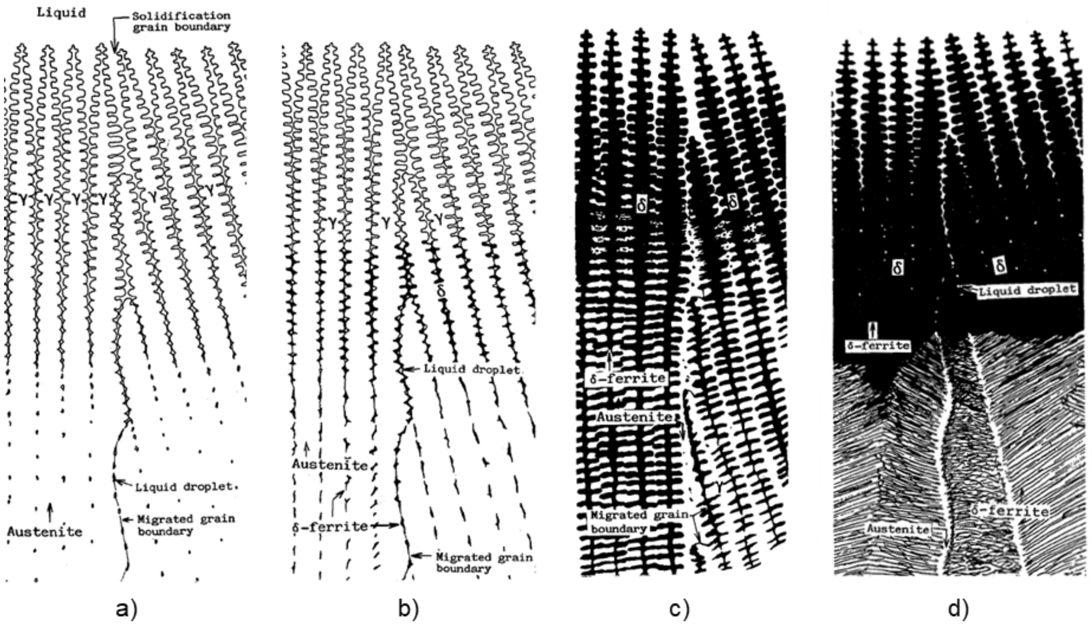

Figure 2.20 : Schematic representation of as-cast microstructure formed through different solidification modes; a) A mode (fully austenite), b) AF mode (austenite/ferrite, intercellular eutectic ferrite), c) FA mode (ferrite/austenite, vermicular ferrite), and d) F mode (acicular ferrite). Adapted from (Katayama et al., 1985).

$$\begin{aligned} Cr_{eq} &= Cr + 1.37\ Mo + 1.5\ Si + 2\ Nb + 3\ Ti \\ Ni_{eq} &= Ni + 0.31\ Mn + 22\ C + 14.2\ N + Cu \end{aligned} \tag{2.1}$$

Table 2.4 : Summary of solidification modes in austenitic stainless steels, with corresponding solidification sequence and values of the Cr_{eq}/Ni_{eq} ratio, (Suutala, 1983).

Solidification mode	Solidification sequence	Cr_{eq}/Ni_{eq} ratio	Illustration
Austenite (A)	$L \rightarrow L + \gamma \rightarrow \gamma$	< 1.37	Figure 2.20 a)
Austenite – Ferrite (AF)	$L \rightarrow L + \gamma \rightarrow L + \delta + \gamma \rightarrow \gamma + \delta \rightarrow \gamma$	$1.37 < Cr_{eq}/Ni_{eq} < 1.5$	Figure 2.20 b)
Ferrite – Austenite (FA)	$L \rightarrow L + \delta \rightarrow L + \delta + \gamma \rightarrow \delta + \gamma \rightarrow \gamma$	$1.5 < Cr_{eq}/Ni_{eq} < 2$	Figure 2.20 c)
Ferrite (F)	$L \rightarrow L + \delta \rightarrow \delta \rightarrow \delta + \gamma$	> 2	Figure 2.20 d)

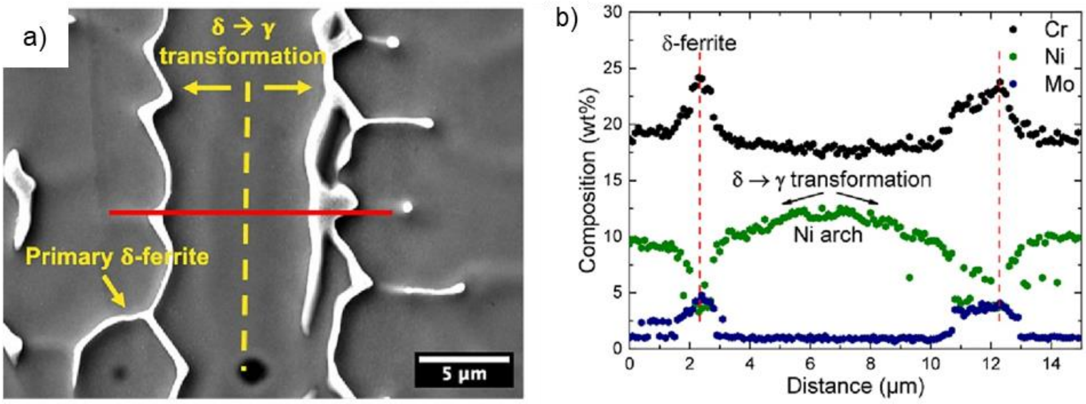

Figure 2.21 : Micro-segregations observed in a 316L austenitic stainless steel sample made by laser wire directed energy deposition, a) a scanning electron microscope (SEM) micrograph, and b) energy-dispersive X-ray spectroscopy (EDS) line scan performed along the red line in a). Adapted from (DeNonno et al., 2024).

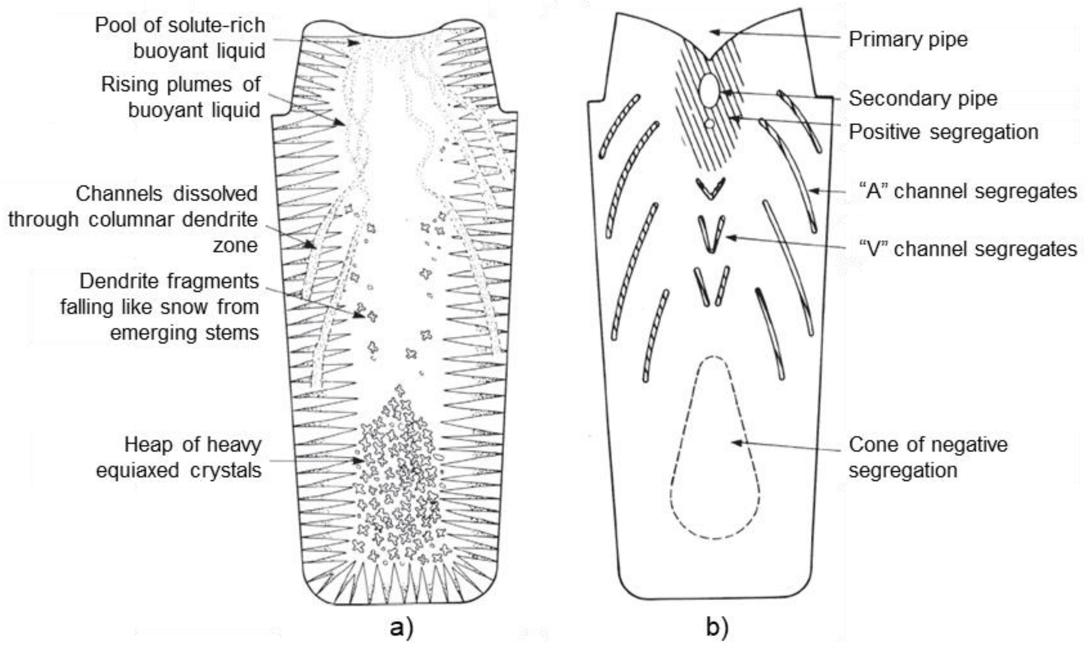

Figure 2.22 : Schematic representation of different types of macro segregations in a large stainless steel ingot, a) during, and b) after solidification, (Campbell, 2015).

A typical microstructure of a Ø 350 mm VAR processed Inconel 718 superalloy ingot is shown in Figure 2.23 a), and a 3D view of the as-cast grains predicted by cellular automata finite element (CAFE) simulation is shown in Figure 2.23 b). A columnar microstructure forms at the core of the ingot, and the orientation of the as-cast grains to the axis of the ingot evolves during the remelting process in response to the direction of thermal gradient, which is perpendicular to the remelting pool profile. The growth of columnar grains occurs parallel to the direction of thermal gradient in the mushy zone, and their orientations to the axis of the ingot is controlled by an equilibrium in heat extraction induced by the colder walls and the bottom surface of the crucible, as well as by the heat generated by the electric-arc used for remelting. As can be seen from Figure 2.23 a), the profile of the remelting pool evolves from a flat surface at the bottom of the ingot, where the thermal gradient is nearly vertical due the influence of the cold bottom surface of the crucible. As the remelting progresses, the thermal gradient gradually rotates towards the axis of the ingot, driven by the increasing influence of the cold walls of the crucible; until the effect of bottom cold surface becomes negligible, and a steady-state remelting regime is established. The grains then grow in a concave way from the bottom to the top, and from the surface to the centre of the ingot (Park et al., 2005). Additionally, the bottom and lateral surfaces of VAR ingots consist of few layers of equiaxed grains due to the significant undercooling of the water-cooled walls of the crucible, providing favourable driving force for nucleation. An advantage of progressive remelting and directional solidification during VAR and ESR processes is the limited size of the volume of the molten pool, reducing therefore the development of macro segregations and formation of porosities within the remelted ingot.

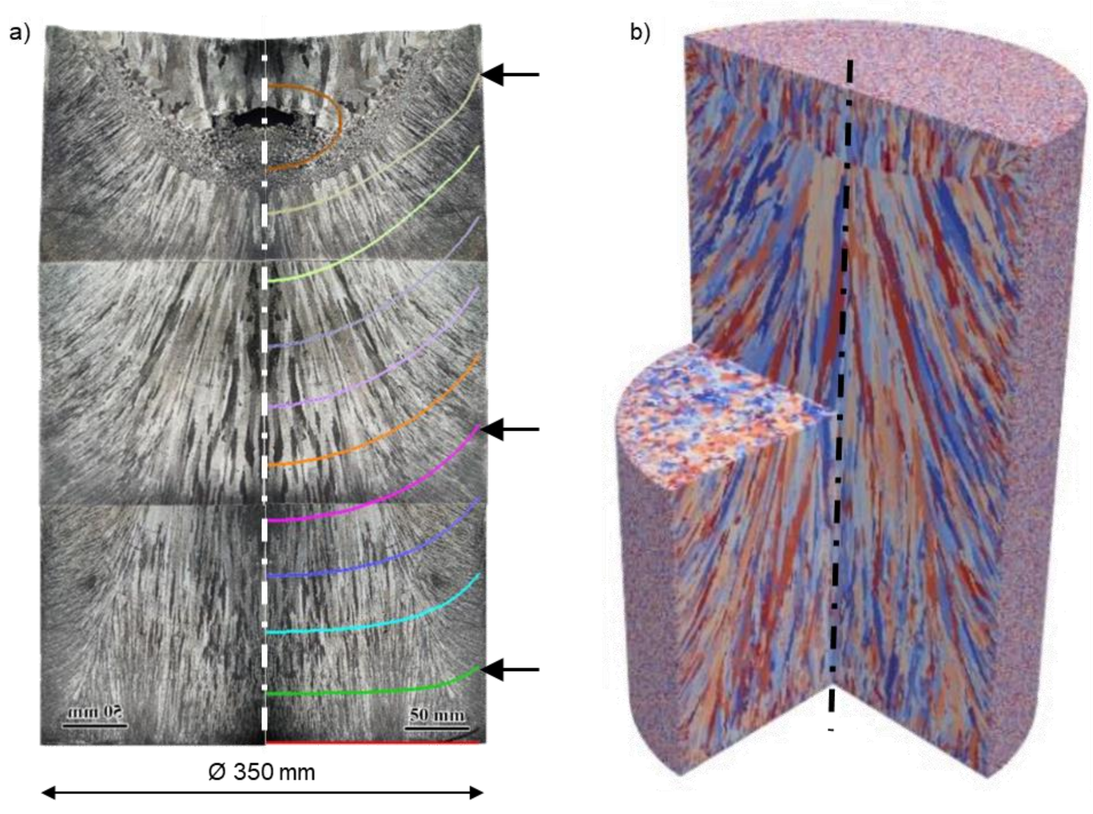

Figure 2.23 : An overview of grain morphology within a Ø 350 mm VAR processed Inconel 718 superalloy ingot; a) microstructure along the longitudinal cross-section of the ingot with the molten pool shape , estimated by a simulation, superimposed (i.e., the black arrows highlight a few), and b) microstructure predicted by cellular automata finite element (CAFE) simulation. Adapted from (X. Li et al., 2023).

2.5 DEFORMATION BEHAVIOUR OF AS-CAST MATERIALS

Wrought FCC materials are made up of a large number of relatively small and equiaxed grains which are uniformly distributed throughout. Thus, they exhibit an isotropic stress-strain behaviour at macroscopic scales. In contrast, directionally solidified materials (i.e., as-cast) have coarse microstructures with preferential crystallographic and morphologic textures induced by the direction of solidification (see Section 2.3). Slip systems of as-cast materials have therefore preferential orientations, which result in anisotropic deformation behaviour.

Investigations of (Terhaar et al., 2012) consisted in the upsetting of Ø 55.6×100 mm cylindrical samples taken out from VAR processed ingots of Inconel 718 from 20 to 50 % reduction in height. The deformed geometry of the cylindrical samples shown in Figure 2.24 allows for a clear illustration of the anisotropic deformation behaviour of the as-cast material, with the samples having elliptical shapes following upsetting. Upsetting were performed by (Semiatin et al., 2004) on double-truncated cone (DTC) samples taken out from a VAR processed waspaloy ingot showed that the samples with the long axis of the columnar grains oriented perpendicular to the direction of upsetting developed a noticeable ovality (see Figure 2.25 a)), whereas those oriented with the long axis of the grains parallel to the direction of upsetting had a relatively circular shape after the tests (Figure 2.25 b)). The irregularities in shape were ascribed to the coarse grain size (i.e., ≈ 5 mm), and the observed anisotropic deformation of samples was associated with anisotropic flow stress of the as-cast microstructures (see Figure 2.26). Free-surfaces irregularities on as-cast samples following upsetting were also observed by (Stamborska and Lapin, 2018). Similar observations of anisotropic deformation were made by (Park et al., 2005) after the upsetting of samples taken from a VAR processed ingots of Inconel 718, and the associated flow curves obtained from the tests showed that the flow stress of columnar microstructure was higher than that of equiaxed one (see Figure 2.27). Hot compression tests were performed by (Wang et al., 2021b) on as-cast super austenitic stainless steel samples, with the compression direction oriented at 0°, 30°, 60° and 90° angle to the long axes of the as-cast columnar grains (see Figure 2.28 a)). An example of results obtained for samples with 60° and 90° grain orientations, at strain rate of 1 s^{-1} are displayed in Figure 2.28 b), which highlights the sensibility of flow stress behaviour to columnar microstructure orientation during hot upsetting. However, the anisotropic behaviour of the deformed samples (i.e., following upsetting) has not been mentioned, and the differences in flow stress evolution throughout the tests was ascribed to different microstructure evolution.

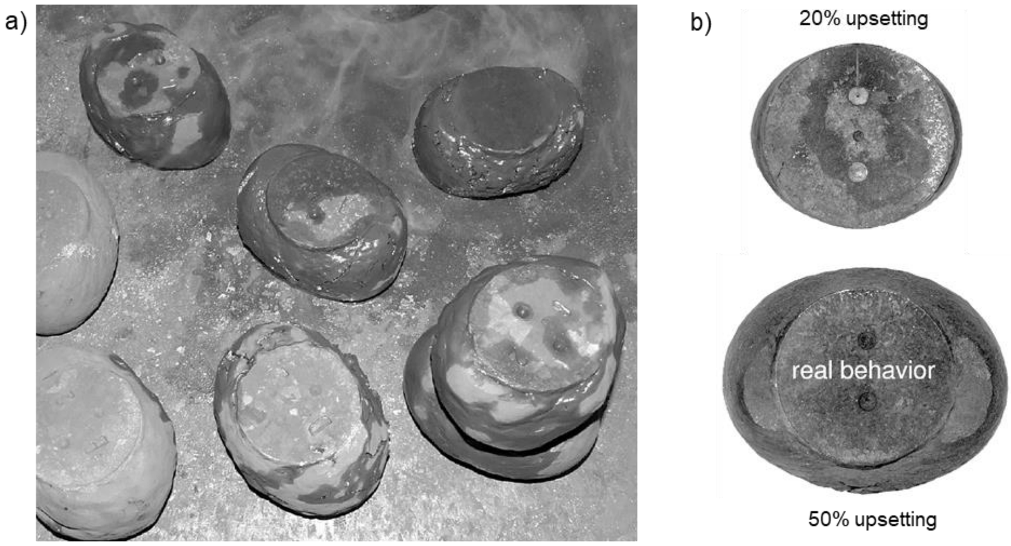

Figure 2.24 : Photographs of Ø 55.6 x 100 mm cylindrical samples taken out from a VAR processed Inconel 718 nickel based superalloy ingot after upsetting to 20 - 50 % reduction in height; a) global view of the deformed samples, and b) top view of the deformed samples showing clear elliptical shapes. Adapted from (Terhaar et al., 2012).

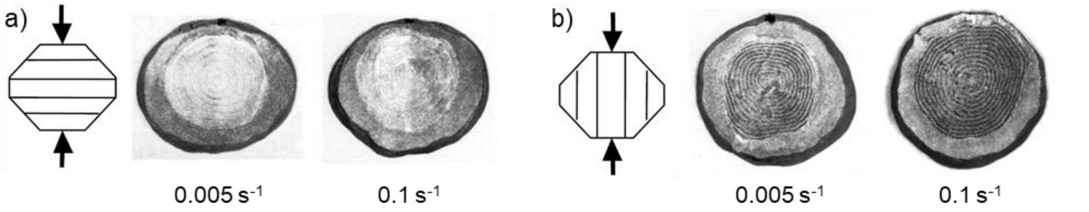

Figure 2.25 : Waspaloy DTC samples after upsetting to 66 % reduction in height at 1177 °C; long axis of the columnar grains oriented a) perpendicular, and b) parallel to the direction of upsetting. Adapted from (Semiatin et al., 2004).

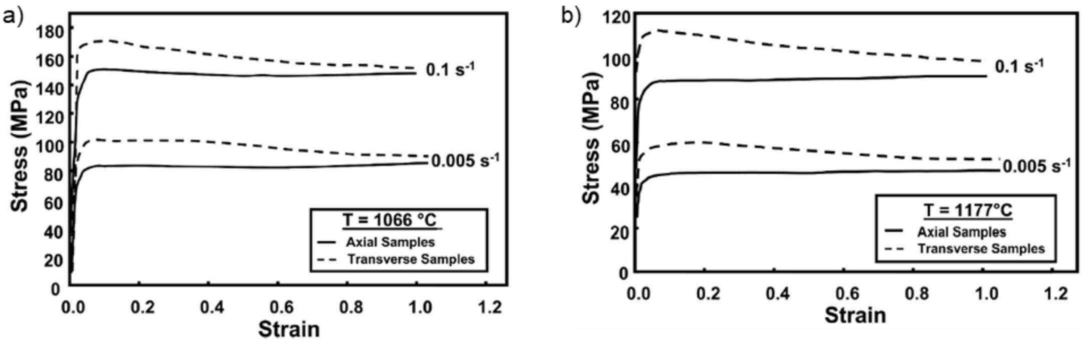

Figure 2.26 : Flow stress sensitivity of Waspaloy ingot to different orientations of columnar as-cast grains to compression direction, at strain rates of 0.005 s^{-1} and 0.1 s^{-1}, and temperatures of a) 1066 °C, and b) 1177 °C. Adapted from (Semiatin et al., 2004).

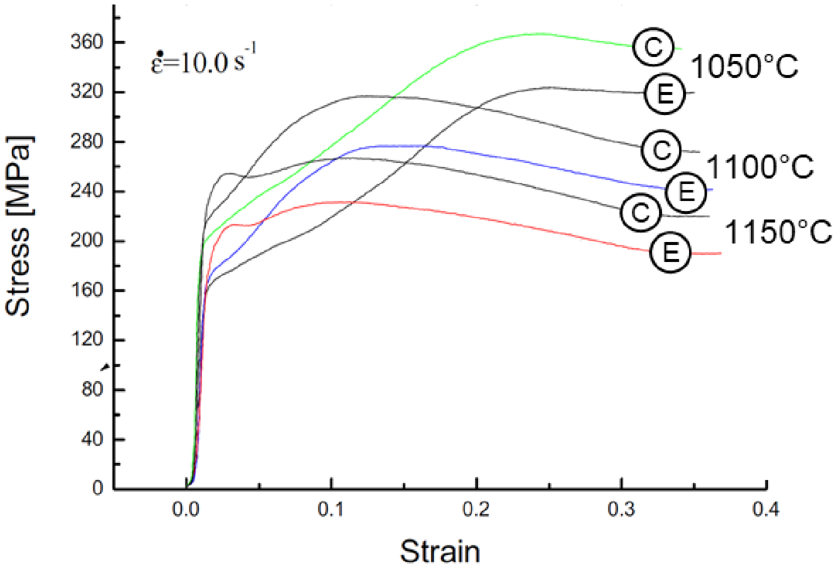

Figure 2.27 : Effect of microstructure on the material flow behaviour during upsetting; "E" and "C" indicate the results obtained for samples with equiaxed and columnar as-cast microstructures, respectively. Adapted from (Park et al., 2005).

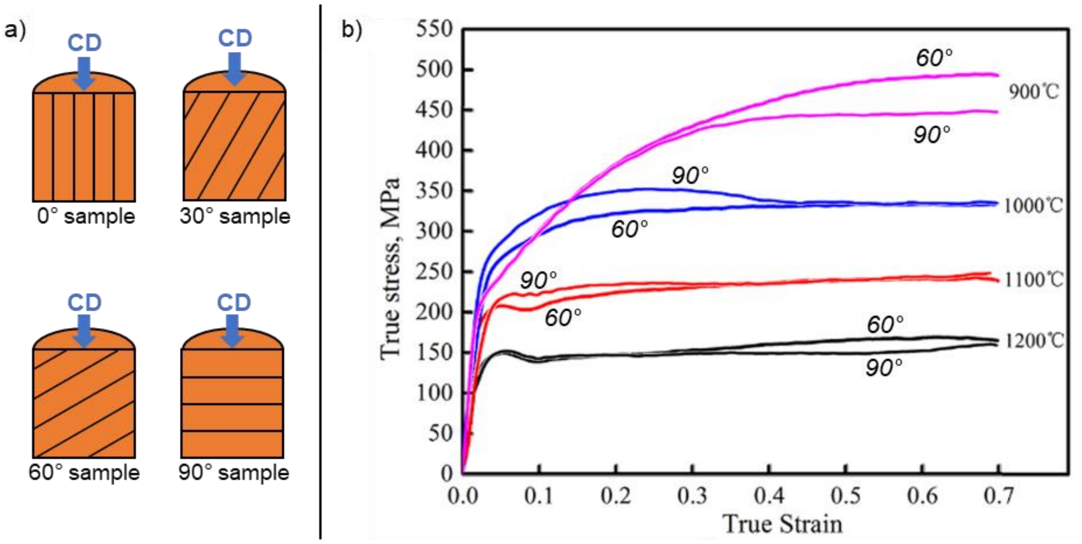

Figure 2.28 : Hot upsetting tests of Ø 8×12 mm as-cast super austenitic stainless steel samples with a) different orientations of columnar grain structure to compression direction (CD), and example of results obtained for samples with 60° and 90° grain orientations, at strain rate of 1 s^{-1}. Adapted from (Wang et al., 2021b).

As a consequence of their coarse size and elongated morphology, as-cast grains are prone to the development of deformation bands, which form when different regions of the same grain undergo slip along different combinations of slip systems. Hence, the grains subdivide at large scale into regions of different orientations, resulting in heterogeneous strain distribution. Deformation bands originate either from inhomogeneous stresses transmitted by neighbouring grains or from intrinsic instability in a grain during plastic deformation to accommodate the change in grain shape (Humphreys and Hatherly, 1995). In as-cast super austenitic stainless steel samples deformed at 900 °C, 10 s^{-1}, (Wang et al., 2021a) observed that deformation bands developed from parent grain boundaries and were oriented nearly perpendicular to the direction of compression of the samples (see the orange arrows in Figure 2.29). As can be seen from Figure 2.30, the EBSD analyses performed by (Poddar et al., 2015) on Fe-30Ni-Nb austenitic model steel showed that non-<011> oriented grains were prone to the development of deformation bands. Relative misorientation of ≈ 15° were found between adjacent deformation bands formed in the parent grain under a relatively low strain deformation of 0.2. Deformation bands were observed by (Wenhui et al., 2011) to promote the formation of micro-cracks (i.e., measuring ≈ 1 µm) in 316LN austenitic stainless steel with 0.05% Nb under deformation conditions of 900 °C, 1 to 10 s^{-1}. Deformation heterogeneities during hot deformation of as-cast Waspaloy were quantified by (Turner and Semiatin, 2011) using isothermal compression tests and crystal plasticity finite element method (CPFEM) simulation. Ø 15×15 mm samples with a coarse and columnar-grain microstructure were used with the long axes of the columnar grains oriented perpendicular to the compression direction. A CPFEM model integrating the initial microstructure of the samples obtained by electron backscatter diffraction (EBSD) was used to simulate the deformation. Simulation results are shown in Figure 2.31 indicating heterogeneity in deformation at grain scale, quantified using the equivalent plastic strain parameter, which is roughly proportional to the stored internal work (i.e., the integration of the sum of the shearing rate of all 12 slip systems over time). As can be seen from Figure 2.31, bands of non-uniform flow crossing several grains were found to form across the microstructure, from the early stage of the upsetting test (see the arrows in Figure 2.31 a)), and heterogeneous deformation occurred both near the grain boundaries and within each grain. Their study also demonstrated that heterogeneous deformation at grain scale was influenced by the crystallographic orientation of the surrounding grains (i.e., first and second layers of neighbouring grains).

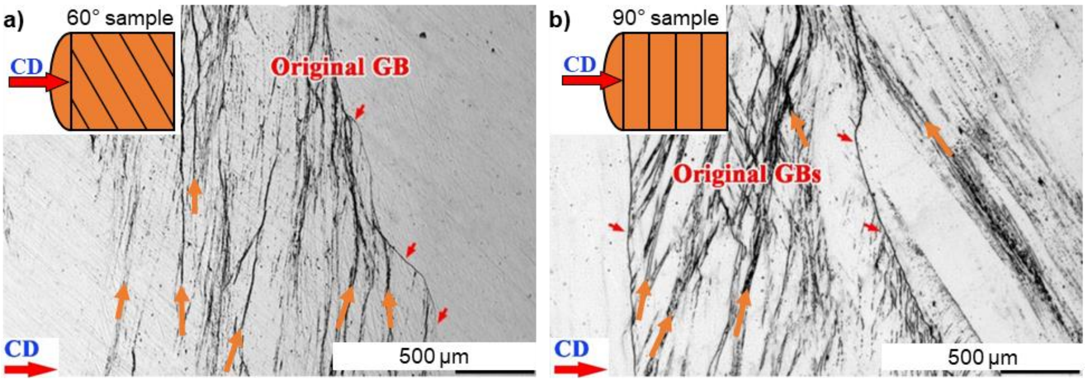

Figure 2.29 : OM appearances of as-cast super austenitic stainless steel microstructures following upsetting at 900 °C, 10 s^{-1}, with the long axes of the columnar grains oriented at a) 60°, and b) 90° to the compression direction (i.e., CD was horizontal). The parent grain boundaries are highlighted by the red arrows, and the orange arrows highlights the deformation bands formed within some parent grains. Adapted from (Wang et al., 2021a).

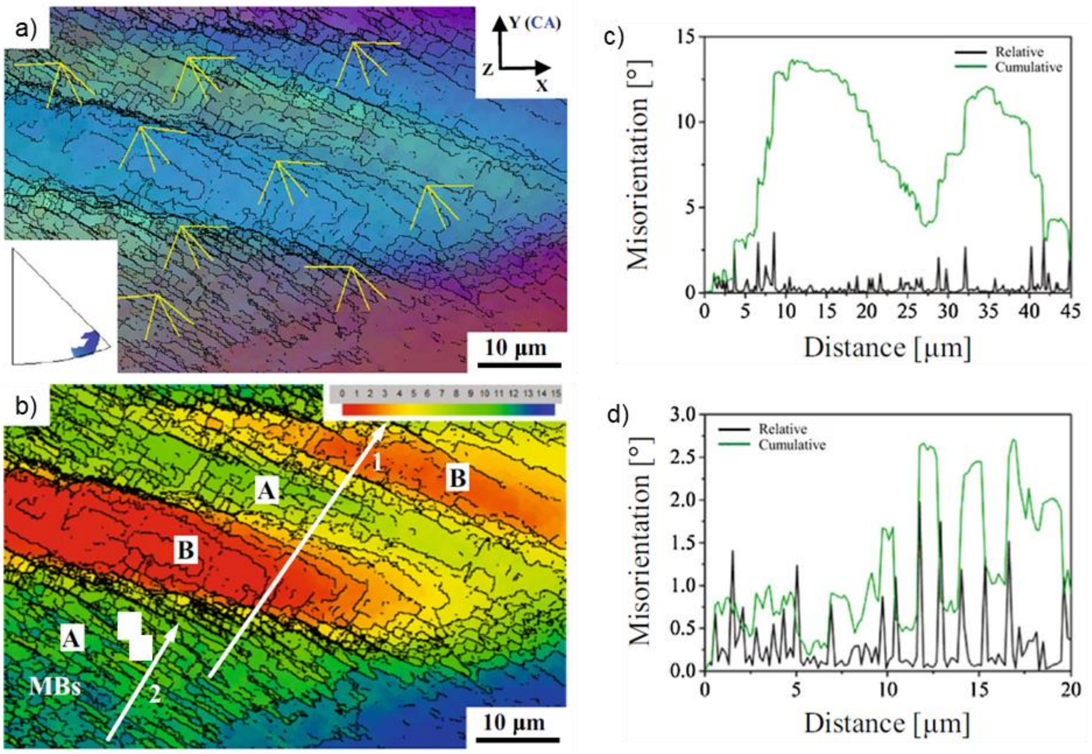

Figure 2.30 : EBSD characteristics of a non-<011> oriented grains following deformation at 925 °C, 1 s^{-1}, up to a strain of 0.2. a) Orientation map in the relative Euler angle colouring with the yellow lines indicating {111} slip plane traces. b) Orientation map coloured according to the angular deviation from the orientation B, where A and B denote the deformation bands. In a) and b), thin and thick black lines denote $0.5° < \theta < 2°$ and $\theta > 2°$ boundaries, respectively. c) And d) displays the point to point (black line) and point to origin (green line) misorientation line scans along the arrows 1 and 2 of b), respectively. Adapted from (Poddar et al., 2015).

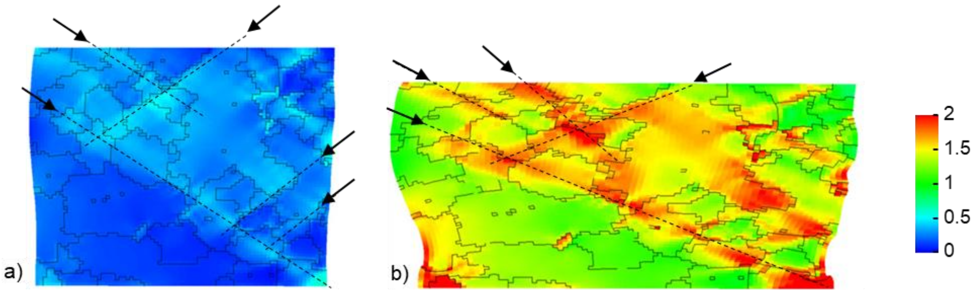

Figure 2.31 : CPFEM-predicted values of the equivalent plastic strain parameter following a) 2 %, and b) 50 % reduction in height, respectively. The arrows and dashed lines indicate the bands of non-uniform flow. Adapted from (Turner and Semiatin, 2011).

2.6 EVOLUTION OF AS-CAST MICROSTRUCTURES DURING THERMOMECHANICAL PROCESSING

Evolution of microstructure characteristics throughout thermomechanical processes, and associated evolution mechanisms are of main interest in this study, and are described in this section.

2.6.1 Homogenisation heat treatments

As detailed in Section 2.4, solidification of liquid metal may lead to the formation of chemical heterogeneities within an ingot (i.e., segregations). Micro-segregation has a length scale of a few microns, and may have detrimental effects on both the corrosion resistance of the alloy, and on the workability of the as-cast material (Czerwinski et al., 1999) (Villanueva et al., 2006) (Perron et al., 2014) (Chu et al., 2024). They can be removed from an ingot after casting by performing a homogenisation heat treatment (Dantzig and Rappaz, 2016). A homogenisation heat treatments consists of heating an ingot to elevated temperatures (i.e., typically above solution annealing temperatures) for a sufficient period of time, allowing solid-state diffusion of chemical elements at the length scale of segregation. At a given temperature, the duration of the homogenisation heat treatment is determined by the length of the secondary dendritic arm spacing (Dantzig and Rappaz, 2016). Table 2.5 provides examples of homogenisation heat treatment conditions reported in the literature for different grades of alloys. In a 316Nb grade containing ≈ 25 % δ-ferrite following casting, (Perron et al., 2014) evaluated that a 1150 °C homogenisation heat treatment would require ≈ 76 days to reach the thermodynamic equilibrium (i.e., corresponding to 3 % δ-ferrite). (Rezayat et al., 2016) showed that homogenisation of austenitic stainless steel consisted of the dissolution of δ-ferrite in the austenitic matrix, which was achieved via lattice diffusion of Cr and Ni in γ-austenite. As can be seen from Figure 2.32, homogenisation heat treatments performed on an as-cast Inconel 718 lead to the removal of the initial dendritic structure.

Table 2.5 : Conditions for homogenisation heat treatment reported in the literature for different grades of alloys.

Grade	Temperature (°C)	Duration (h)	References
Al alloy 7075	480	24	(Park and Kim, 2016)
Inconel 718	1150	0.5 to 60	(Yeom et al., 2007), (Sohrabi et al., 2018), (Sahithya et al., 2019)
GH3535 superalloy	1200	100	(Wang et al., 2018)
Udimet 720Li	1160 to 1170	50 to 70	(Yu et al., 2015) (Fan et al., 2019)
AISI 316L	1240	2	(Chu et al., 2024)
316Nb (0.9 %Nb)	1050 to 1250	5	(Xie et al., 2022)
Super austenitic stainless steel	1250	4 to 50	(DuPont and Farren, 2011), (Wang et al., 2021a), (Zhang et al., 2023)

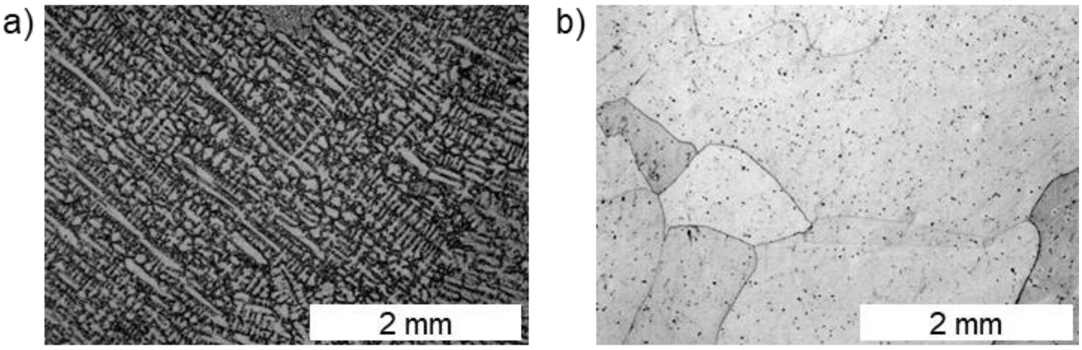

Figure 2.32 : Microstructure of Inconel 718 nickel based superalloy in a) the as-cast, and b) homogenised states. Adapted from (Forbes Jones and Jackman, 1999).

2.6.2 Restoration mechanisms

Restoration mechanisms allow for softening and strain recovery in work hardened materials following deformation, restoring their ductility and making them easier to be deformed in further deformation stages. At the scale of the microstructure, restoration leads to microstructural changes achieved by a combination of recovery, recrystallisation and grain growth mechanisms. Among these restauration process, recrystallisation is of main interest for the investigation of the ingot-to-billet conversion process since it allows for the complete refinement of the initial coarse, elongated as-cast grains into a fine, equiaxed microstructure. The main challenge is to reach a complete recrystallisation of the parent microstructure through different mechanisms. As can be seen from Figure 2.33, all these mechanisms are inter-connected. These are briefly introduced in this section.

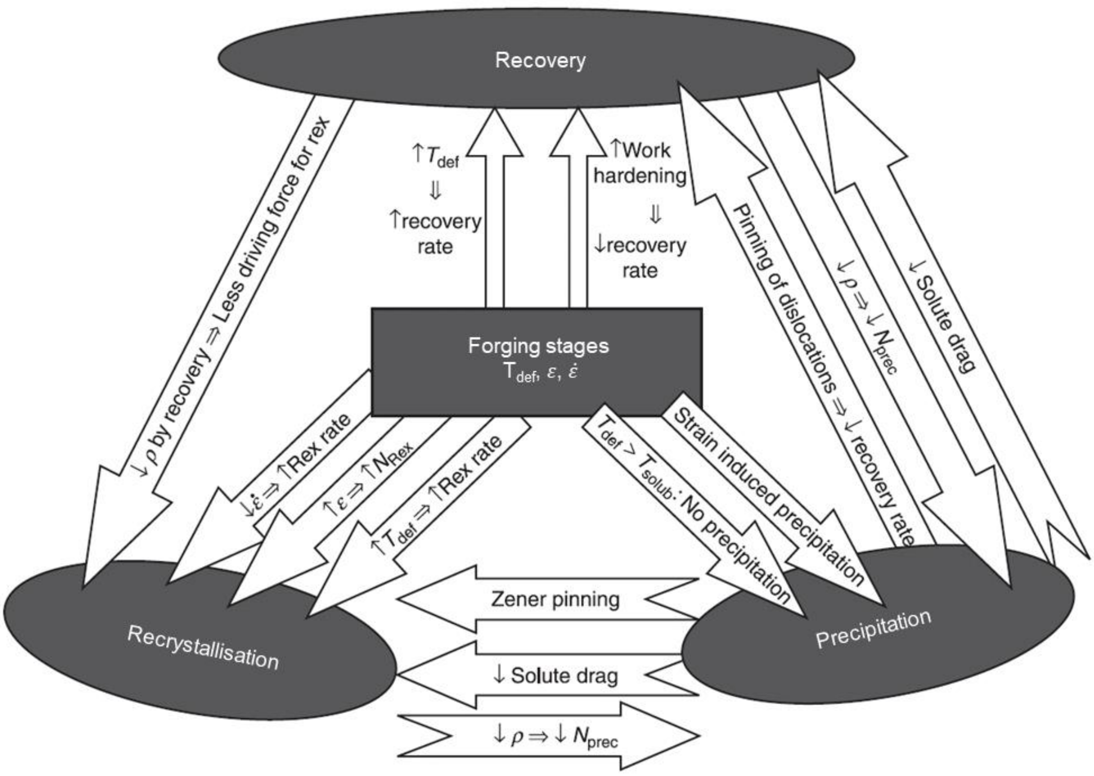

Figure 2.33 : Graphical illustration of inter-dependencies between deformation, recovery, recrystallisation and precipitation. Adapted from (López and Rodriguez-Ibabe, 2012).

2.6.2.1 Recovery

Recovery involves annihilation and rearrangement of dislocations into lower energy configurations and contributes therefore to reducing the strain energy stored in the material. It leads to the formation of LAGBs (i.e., subgrain boundaries) without affecting the boundaries of parent microstructure (Humphreys and Hatherly, 1995). The various stages in the progress of recovery are illustrated schematically in Figure 2.34. Annihilation and rearrangement of dislocations are achieved by glide, climb and cross-slip of the dislocations. The occurrence of recovery depends on the mobility of the dislocation within the material, quantified by the stacking fault energy (SFE, γ_{SFE}) parameter. Recovery can occur either during or after the deformation stages, and is thus referred to as dynamic recovery (DRV) and static recovery (SRV), respectively.

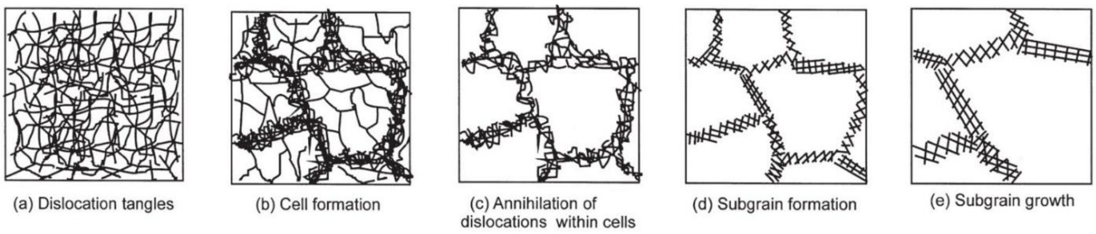
(a) Dislocation tangles
(b) Cell formation
(c) Annihilation of dislocations within cells
(d) Subgrain formation
(e) Subgrain growth

Figure 2.34 : Schematic illustration of the various stages of recovery of a plastically deformed material, (Humphreys and Hatherly, 1995).

2.6.2.2 Recrystallisation and grain growth

Recrystallisation denotes restoration mechanisms based on the evolution or formation of HAGBs (Humphreys and Hatherly, 1995). The propensity of recrystallisation to take place in a plastically deformed microstructure depends on the material properties, the microstructure morphology, and the thermomechanical conditions applied to the material. During recrystallisation or grain growth stages, the migration of grain boundaries is driven by the gradient in the strain energy across the boundary, with a deformed structure on one side and a recrystallised and "dislocation-free" structure on the other. The kinetic of boundary migration is a function of the lattice misorientation of the boundary, the chemistry at the grain boundary, the grain boundary curvature, the deformation gradient across the boundary as-well as the stress and thermal conditions at the boundary (Doherty et al., 1997). Thermomechanical conditions for microstructure evolution mechanisms are commonly related to the Zener-Hollomon parameter, Z, which is calculated using Equation (2.2), (Zener and Hollomon, 1944).

$$Z = \dot{\varepsilon} \cdot \exp\left(\frac{Q}{RT}\right) \tag{2.2}$$

where T is the absolute deformation temperature, Q is the activation energy for the operative thermally activated process, and R is the gas constant.

Recrystallisation has widely been investigated and formulised in the past decades (Sakai and Jonas, 1984) (Humphreys and Hatherly, 1995) (Doherty et al., 1997) (Huang and Logé, 2016); it is commonly described phenomenologically, often referred to as temporal and spatial heterogeneities of microstructural evolutions. The first distinction is made depending on whether or not the recrystallisation occurred while the material was undergoing plastic deformation. Dynamic recrystallisation (DRX) denotes recrystallisation of microstructure while undergoing plastic deformation, meta-dynamic (MDRX) and static (SRX) recrystallisation denote recrystallisation taking place at elevated temperatures following the deformation stages. The second distinction between different recrystallisation mechanisms is made according to the spatial distribution of nucleation events taking place within the microstructure. Recrystallisation is thus termed as "continuous" (e.g., CDRX) when the nucleation events develop homogeneously throughout the entire grain structure, and "discontinuous" (e.g., DDRX) when nucleation events take place preferentially at certain sites. DDRX, CDRX, SRX and MDRX are covered in this section.

Discontinuous dynamic recrystallisation (DDRX) is a "nucleation and growth" process in which dislocation free grains (i.e., the nuclei) nucleates at preferential sites of the crystalline lattice, where elevated levels of energy are stored in the form of dislocations, and where the lattice presents high crystallographic misorientation. Among others, such conditions are reached along grain boundaries, deformation bands or at the vicinity of second phase particles. At high temperatures, it is commonly accepted that DDRX takes place predominantly at low to medium SFE alloys, in which limited extend of DRV allows for development of localised regions with high densities of dislocation (Humphreys and Hatherly, 1995). Based on (Sakai and Jonas, 1984) findings, the flow-softening in a material experiencing DDRX can be identified via a typical shape of the flow curve (i.e., stress vs. strain plot), which can be obtain as a function of the deformation conditions (i.e., Z value), and the grain size (D_0). As can be seen in Figure 2.35, the flow curve displays multiple peaks at low Z deformation and small D_0, and a single peak is observed for high Z deformation and large D_0; and recrystallisation leads to grain coarsening or refinement in those respective conditions. Corresponding microstructure evolution throughout deformation are schematically shown in Figure 2.36 and Figure 2.37, respectively. To highlight the flow softening effect of DDRX, the flow curve of material undergoing predominant DRV is superimposed with the dashed red line in both figures.

In the case of a multi-peak flow curve (i.e., at low Z and small D_0, see Figure 2.36), recrystallisation is achieved through successive cycles of work-hardening, nucleation, and grain growth; and can be described as follow. With heterogeneous work-hardening of the initial microstructure (see Figure 2.36 b)), DDRX grains nucleate and grow at the boundaries of the parent grains (see Figure 2.36 c)). The growth of the DDRX grains is rapidly restrained by their mutual interactions once their size approach that of the initial grains, and the microstructure at this point is composed of soft, dislocation-free DDRX grains (see Figure 2.36 d)) where a local minima in the stress-strain curve is reached. This first generation of DDRX grains undergo work-hardening with further deformation, resulting in a further increase in the stress-strain curve (see Figure 2.36 e)). The whole process is then cyclically repeated until a steady state is reached (see Figure 2.36 f)).

In the case of a single-peak flow curve (i.e., at high Z and large D_0, see Figure 2.37), recrystallisation is achieved through simultaneous work-hardening, nucleation, and grain growth, and can be described as follow. With heterogeneous work-hardening of the initial microstructure (see Figure 2.37 b)), DDRX grains nucleate and grow at the boundaries of the parent grains. As a consequence of the large size of the initial grains compared to that of the recrystallised ones, the DDRX grains form a typical necklace structure at the boundaries of parent microstructure (see Figure 2.37 c)), and their growth into the interior of the work-hardened parent grains induces the progressive material flow-softening observed on the flow curve (see Figure 2.37 d)). Finally, nucleation, growth, and work-hardening simultaneously take place among the microstructure, progressively balancing each other and reaching an equilibrium at the steady-state stress (see Figure 2.37 e)).

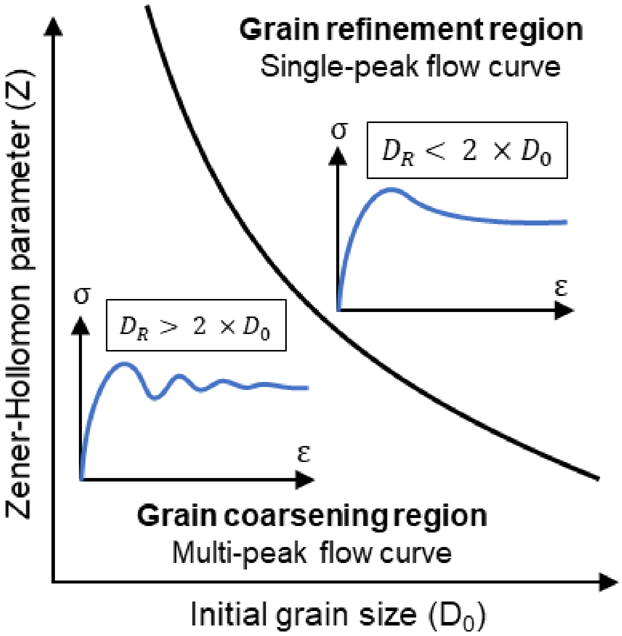

Figure 2.35 : Schematic shape of flow curves obtained as a function of deformation conditions (Z) and initial grain size (D_0); and corresponding trend of microstructure evolution (i.e., refinement or coarsening). Adapted from (Humphreys and Hatherly, 1995).

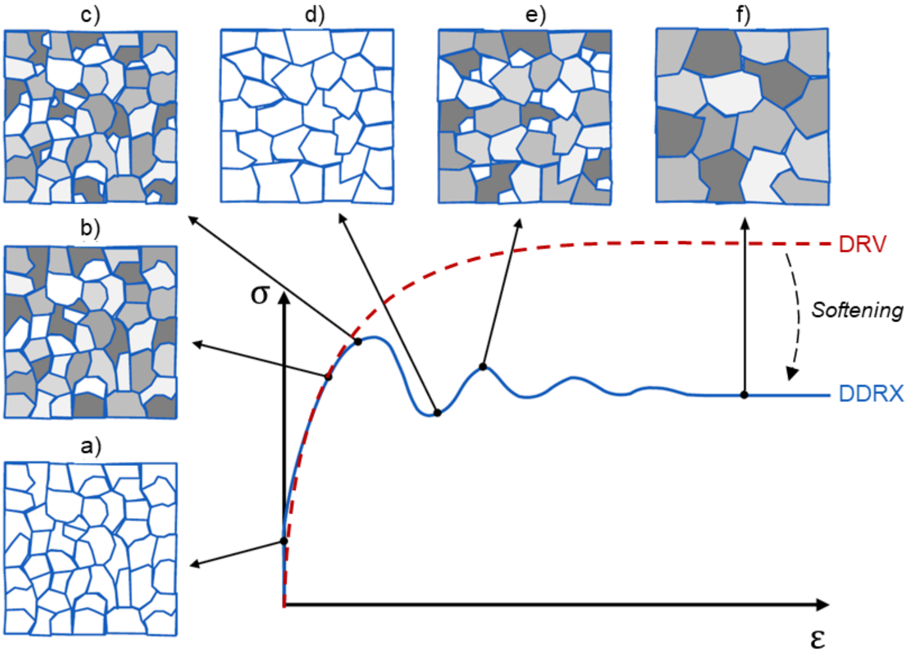

Figure 2.36 : Schematic sketches of microstructure evolution through DDRX leading to growth of the average grain size; a) parent microstructure, free of dislocation, b) work hardened parent grains, c) nucleation of recrystallised grains at boundaries of parent grains, d) limited growth of DRX grains by mutual interactions in the interior of the most work-hardened parent grains, e) subsequent work hardening of latter recrystallised grains and nucleation of new recrystallised grains, and f) steady-state microstructure. Adapted from (Smagghe, 2017).

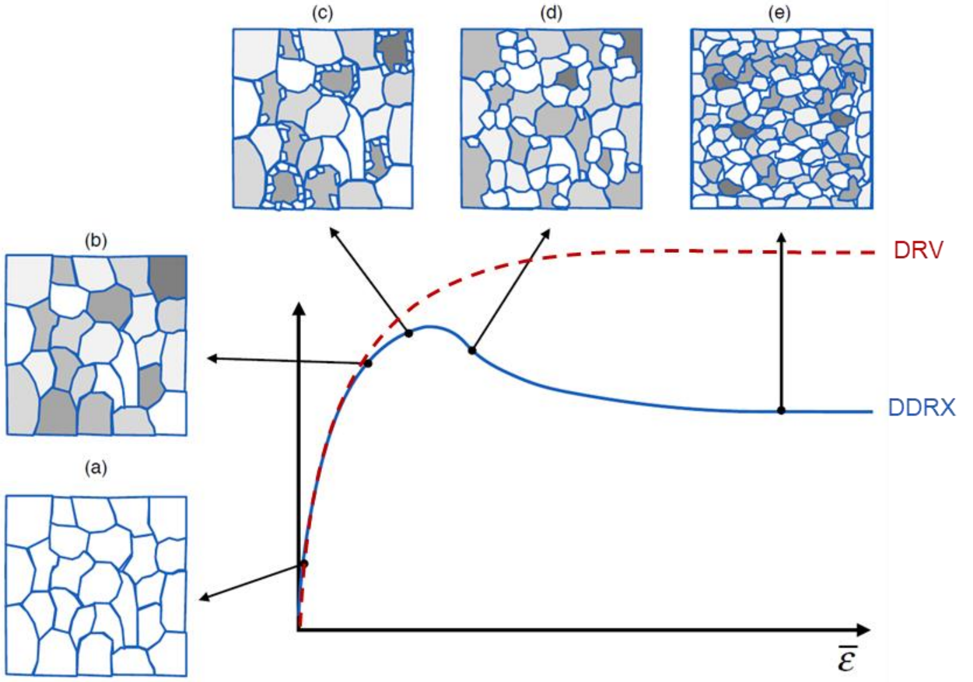

Figure 2.37 : Schematic sketches of microstructure evolution through DDRX leading to reduced average grain size; a) parent microstructure, free of dislocation, b) work hardening of parent grains, c) nucleation of recrystallised grains at boundaries of parent microstructure, d) growth of the recrystallised grains, and e) steady-state microstructure. Adapted from (Smagghe, 2017).

At grain boundaries, DDRX originates from serration and bulging in the boundaries, which is schematically depicted in Figure 2.38. At low strain, the grain boundaries develop serrations, alongside which the substructure develops heterogeneously (see Figure 2.38 a)). Further straining leads to partial grain boundary sliding or shearing, which then leads to the development of localised strain gradients (see Figure 2.38 b)). Nucleus then forms at the locations of bulging out of a segment of the serrated grain boundaries through strain induced subgrain boundary process at low Z deformation conditions (see Figure 2.38 c.1)), and by twinning at high Z (see Figure 2.38 c.2)). Further growth of the DDRX nuclei is then made possible by strain induced boundary migration (SIBM) (see Figure 2.39). Recrystallisation through grain boundary bulging can be identified from partially recrystallised microstructures, where serrated and bulged grain boundaries are visible by means of optical microscopy (OM) (Qin et al., 2017b) (Han et al., 2015) (Liu et al., 2014). Figure 2.40 provides an example of necklace type DDRX observed by (Han et al., 2015) in an as-cast 254SMO super-austenitic stainless steel. Conditions for dislocation (i.e., SIBM) and twining controlled DDRX were investigated by (Qin et al., 2017b) in an as-cast Mn18Cr18N austenitic stainless steel samples during hot upsetting up to a strain level of 0.69. It was found that complete recrystallisation of the as-cast microstructure was obtained through dislocation mechanism following deformation at higher temperatures and lower strain rates (i.e., 1200 °C, 0.001 s^{-1}), and conversely through twining mechanism at lower temperatures and higher strain rates (i.e., 1100 °C, 1 s^{-1}). EBSD maps of recrystallised microstructure obtained through both mechanisms are reproduced in Figure 2.41 a) and b), respectively. It can be seen that the recrystallised grains nucleated and grown by the dislocation mechanism (see Figure 2.41 a)) were composed of recovery, i.e., subgrains with LAGBs (< 15°, green and purple boundaries), whereas those originated from twinning (see Figure 2.41 b)) were composed of twins (Σ3), twin variants (Σ9, Σ27) and dislocation cells (i.e., red boundaries).

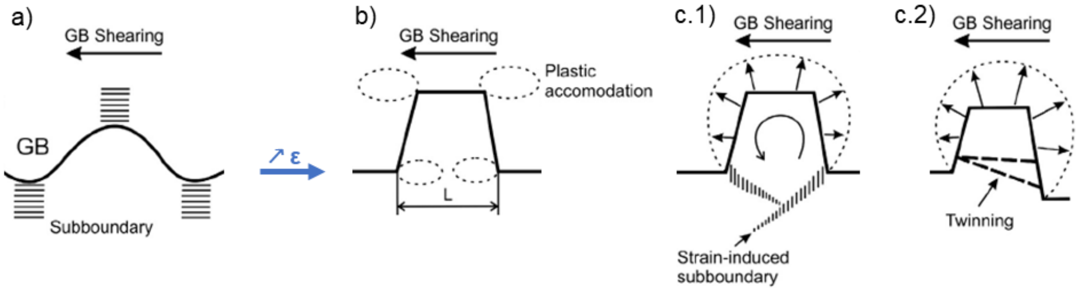

Figure 2.38 : Schematic representation of DDRX nucleation along grain boundaries; a) serration of a parent grain boundary and heterogeneous development of substructure, b) partial grain boundary sliding/shearing and development of strain heterogeneities, and c) nucleation of a recrystallised grain through c.1) strain-induced grain boundary migration, and c.2) twinning processes. Adapted from (Sakai et al., 2014).

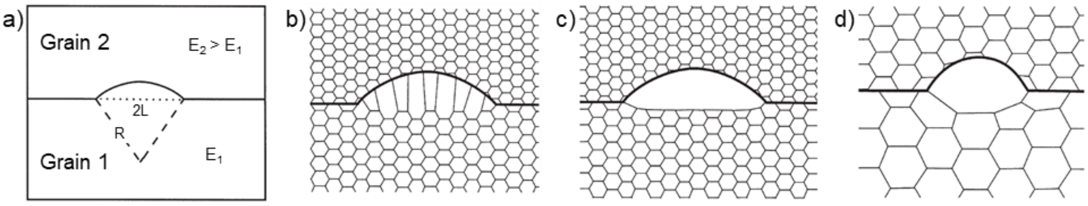

Figure 2.39 : Schematic representation of strain induced boundary migration process; a) initial grain structure where a bulged grain boundary separates grains of low (E1) and high (E2 > E1) stored energy, b) migrating boundary dragging subgrain boundaries, c) the migrating boundary is free from dislocation structure, (Humphreys and Hatherly, 1995).

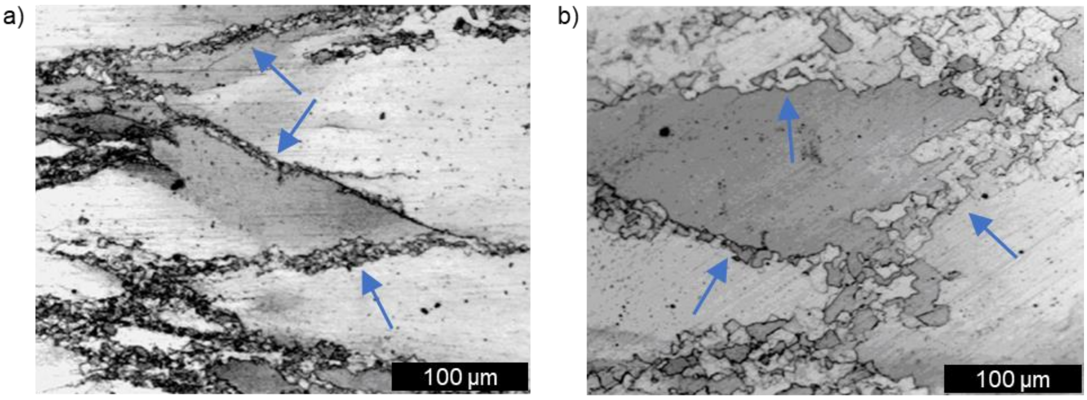

Figure 2.40 : Typical necklace of recrystallised grains at parent grain boundaries highlighted by the blue arrows in as-cast 254SMO super-austenitic stainless steel deformed at a strain rate of 0.01 s^{-1} and temperatures of a) 1000°C, and b) 1050°C. Adapted from (Han et al., 2015).

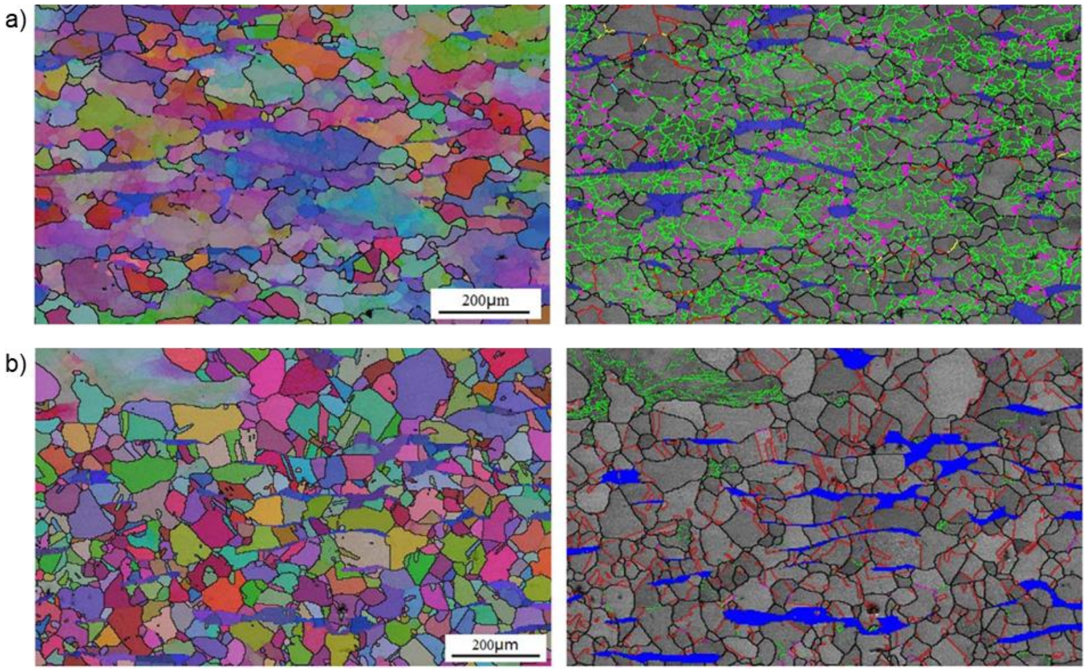

Figure 2.41 : Euler angle (left) and grain boundary (right) EBSD maps of as-cast Mn18Cr18N austenitic stainless steel samples following upsetting up to a strain level of 0.69 at 1200°C under strain rates of a) 1 s^{-1}, and b) 0.001 s^{-1}. The following legend applies to the grain boundary map : 2-10° : green, 10-15° : purple, > 15° : black, Σ3 : red, Σ9 : yellow, Σ27 : aqua, and δ ferrite : blue. Adapted from (Qin et al., 2017b).

DDRX was observed to be incomplete and highly heterogeneous by (Mandal et al., 2012) in an as-cast type 304 austenitic stainless steel following compression up to a strain of 1 at 1000 °C, 0.5 s^{-1}, with clusters of nuclei predominantly located at some boundaries of the parent microstructure. Complete recrystallisation of the as-cast microstructure was obtained following deformation up to a strain of 1 at 1200 °C, 5 s^{-1}. As can be seen from Figure 2.42 for an as-cast Mn18Cr18N austenitic stainless steel, heterogeneous recrystallisation may also be promoted by undissolved secondary phases formed during solidification (Qin et al., 2017b) or by second phase particles dispersed throughout the microstructure (Hermant et al., 2019) which is referred as "particle stimulated nucleation (PSN)". Occurrence of PSN is made possible by the development of local strain heterogeneities at the vicinity of stiff, and non-deformable second phase particles, which depends on the deformation conditions (i.e., on Z value) and on the size of the particles (see Figure 2.43). It is also explained by (Sahithya et al., 2019) that shear bands formed from local adiabatic temperature rise and flow localisation are prone to nucleation of recrystallised grains. The reduced volume fraction of grain boundaries in coarse-grain as-cast materials allow for the formation of high stored energy sites such as deformation bands or twins, which may in turn act as additional sites for nucleation of recrystallisation (Barraclough and Sellars, 1979) (Fernández et al., 2002). Thus, coarse parent grain size is another contributing factor in heterogeneous progress of recrystallisation. Reduced rate of DDRX kinetic was also observed with increasing parent grain size by (Sah et al., 1974) and (El Wahabi et al., 2005).

In (Wang et al., 2021a), the deformation bands highlighted by the orange arrows in Figure 2.29 turned into nucleation sites for recrystallised grains during upsetting at 1200 °C (see Figure 2.44). As detailed in (Semiatin et al., 2004), DDRX kinetics was shown to exhibit a strong sensitivity to the orientation between the direction of compression and the orientation of the long axes of columnar grains in an as-cast waspaloy material (see Figure 2.45), and the rate of recrystallisation of the as-cast material was sluggish compared to that of equivalent wrought material (see the dashed curve in Figure 2.45). As can be seen from Figure 2.46 and Figure 2.47, it is also likely that non-recrystallised grains remain present among almost fully recrystallised areas.

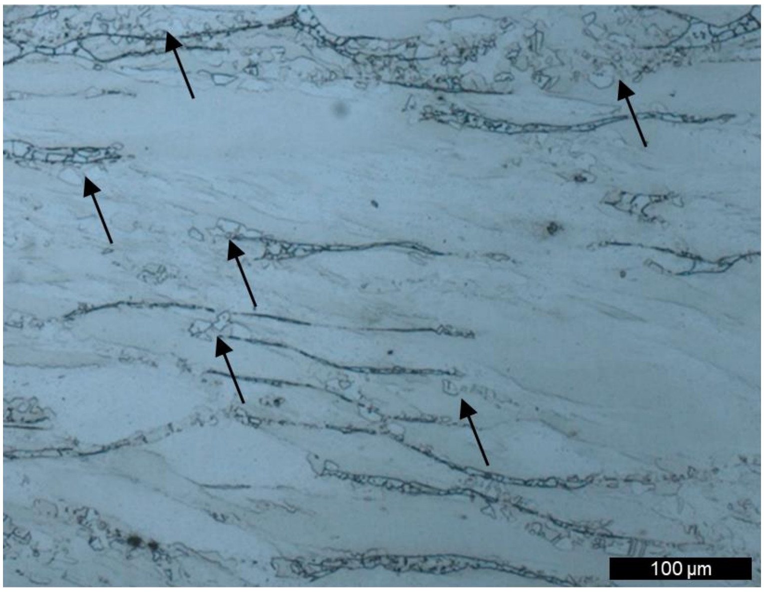

Figure 2.42 : OM appearance of an as-cast Mn18Cr18N austenitic stainless steel microstructure following upsetting at 850 °C, 1 s^{-1} with a few DDRX grains at the interfaces between austenite and secondary phases (see the black arrows). Adapted from (Qin et al., 2017b).

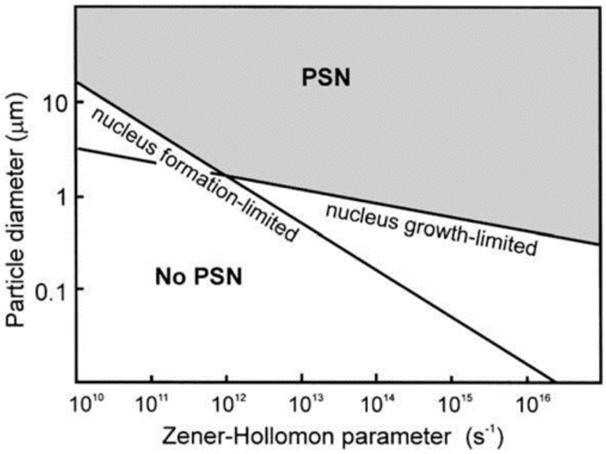

Figure 2.43 : Domain for development of particle stimulated nucleation of recrystallisation, as functions of the second phase particle diameter, and Zener-Hollomon parameter; (Humphreys and Hatherly, 1995).

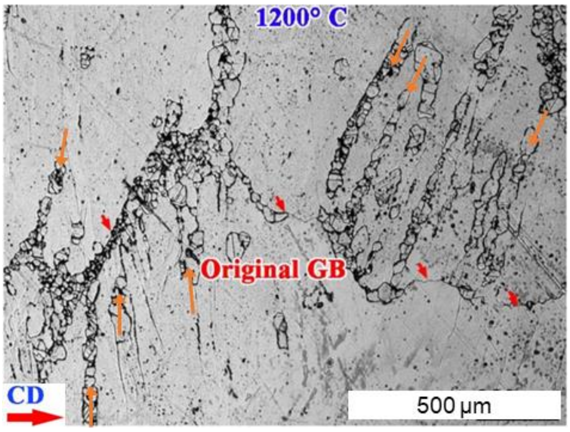

Figure 2.44 : OM appearance of an as-cast super austenitic stainless steel microstructure following upsetting at 1200 °C, 10 s^{-1}, with the long axes of the columnar grains aligned with the compression direction (i.e., CD was horizontal). The parent grain boundaries are highlighted by the red arrows, and the orange arrows highlights the recrystallised grains nucleated along the deformation bands formed within some parent grains. Adapted from (Wang et al., 2021a).

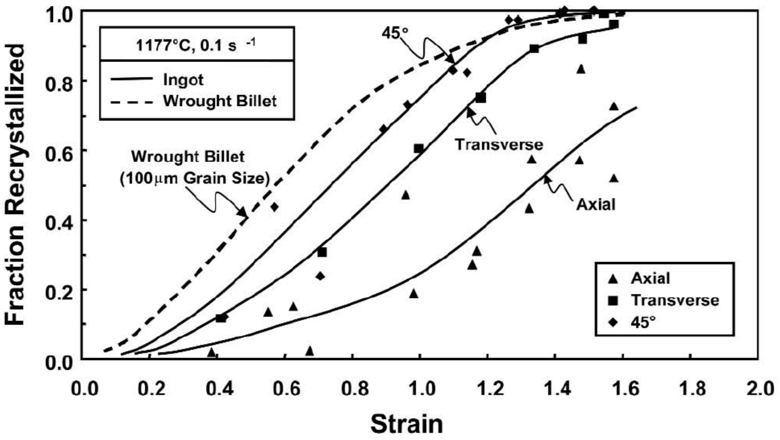

Figure 2.45 : Fractions of DDRX grains measured in waspaloy DTC samples following upsetting performed at 1177 °C, 0.1 s^{-1} with different orientation to the columnar structure orientation (i.e., 0, 45, and 90°), plotted as a function of strain deformation, and compared to that of wrought Waspaloy with a 100 µm grain size (broken line), (Semiatin et al., 2004).

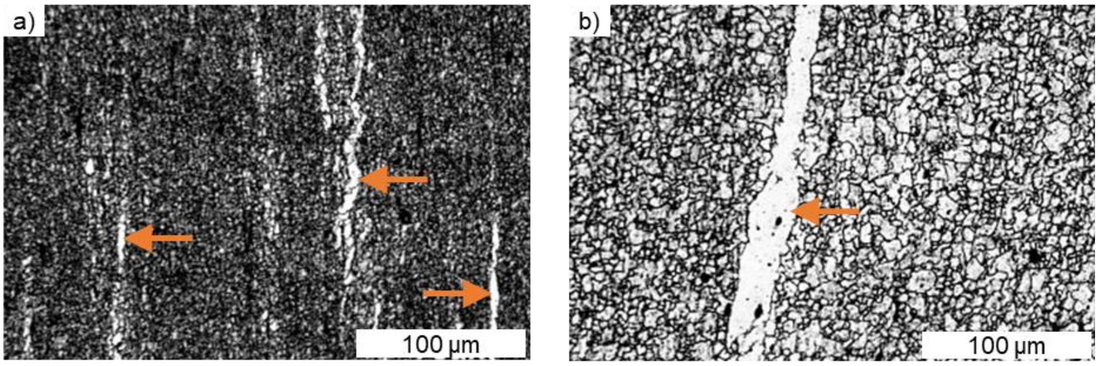

Figure 2.46 : Microstructure appearances of a Nb-containing austenitic stainless steel following deformation up to a strain of 4, at 0.5 s^{-1}, and temperatures of a) 1050 °C, and b) 1100 °C. Note that non-recrystallised isolated grains are highlighted by the orange arrows. Adapted from (Silva et al., 2012).

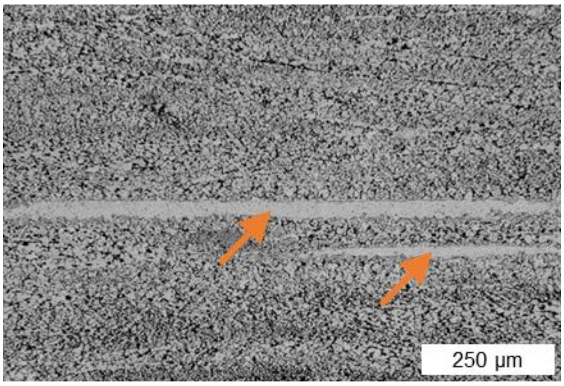

Figure 2.47 : Microstructure appearance of alloy 720 following forging, with non-recrystallised isolated grains highlighted by the orange arrows. Adapted from (Forbes Jones and Jackman, 1999).

In contrast to DDRX, continuous dynamic recrystallisation (CDRX) originates at sub-structure scales and progress homogeneously throughout the microstructure undergoing deformation, without a clear distinction between "nucleation" and "growth" stages. At elevated temperatures, CDRX is known to be promoted in high SFE materials (Humphreys and Hatherly, 1995), prone to recovery, which impedes the formation of regions with high density of dislocations and therefore prevents DDRX to take place. The CDRX mechanism involves rearrangement of dislocations into subgrain boundaries (i.e., LAGB) through DRV, and further transformation of LAGBs into HAGBs, leading to a fully recrystallised microstructure. Transformation of LAGBs into HAGBs can be achieved through homogeneous increase in local misorientation (see Figure 2.48), progressive lattice rotation near grain boundaries (see Figure 2.49), and formation of micro shear bands (see Figure 2.50).

Despite that CDRX and DDRX are based on different types of microstructure evolution mechanisms, they are both likely to take place in austenitic stainless steels, depending on the deformation conditions. Temperature and strain domains for CDRX and DDRX in a type 304H austenitic stainless steel obtained by (Tikhonova et al., 2013) are summarised in Figure 2.51. The transition between CDRX and DDRX mechanisms are primarily temperature dependant, as function of grain boundary mobility and occurrence of DRV. CDRX was observed during multi-pass rolling of type 304 austenitic stainless steel at lower temperatures, in the range 500 °C to 1000 °C (Yanushkevich et al., 2015). In this case, CDRX grain refinement was reached through micro shear bands formation between 500 °C - 700 °C, and progressive increase in misorientation from 800 °C - 1000 °C. As can be seen in Figure 2.52, (Wang et al., 2021a) observed three different recrystallisation processes (see Figure 2.52) during upsetting of super austenitic stainless steels with a columnar as-cast microstructure, involving both DDRX and CDRX recrystallisation mechanisms. The first mechanism (see Figure 2.52 a)) involved the formation of deformation bands within the parent grains, oriented nearly perpendicular to the direction of compression, resulting in a large number of additional LAGBs and HAGBs. These served as nucleation sites for further DDRX, and the recrystallised grains were aligned in strip wise regions formed within the parent grains. The second mechanism (see Figure 2.52 b)) involved CDRX through the formation of subgrains within the parent grains with a further lattice rotation (i.e., increased local misorientation) allowing for recrystallisation. The third mechanism (see Figure 2.52 c)) involved usual DDRX with the recrystallised grains aligned in strip wise regions along the parent grain boundaries.

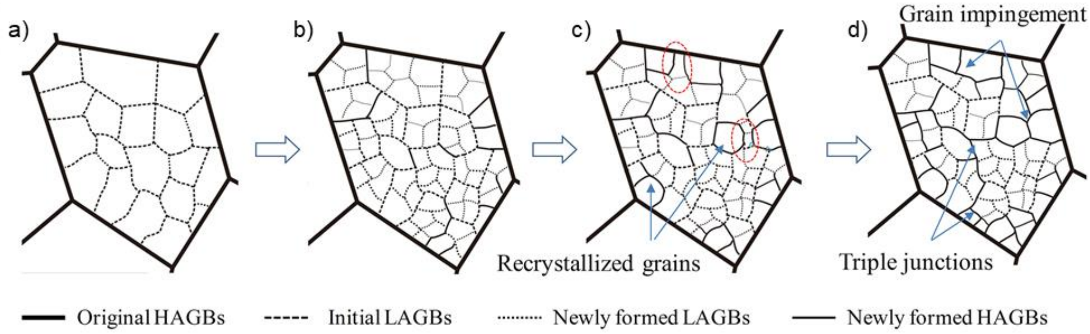

Figure 2.48 : Schematic depiction of CDRX mechanism through homogeneous increase of misorientation; a) starting microstructure with pre-existing substructure, and progressive accumulation of dislocations into b) LAGBs, c) eventually HAGBs, and d) impingement of the newly formed grain boundaries at triple junctions, (Chen et al., 2020).

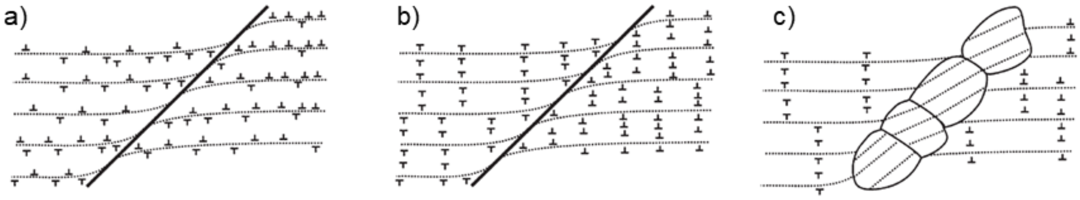

Figure 2.49 : Schematic depiction of CDRX mechanism through progressive lattice rotation near grain boundaries; a) development of localised shearing near grain boundaries, b) DRV and lattice rotation near the boundary, and c) formation of subgrains in the boundary region. Adapted from (Ion et al., 1982).

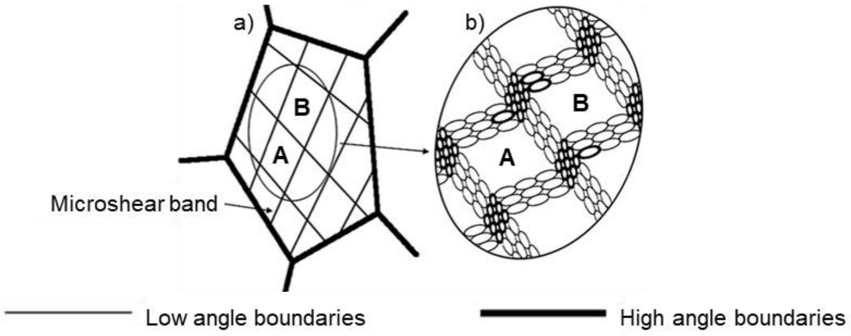

Figure 2.50 : Schematic depiction of CDRX mechanism through micro shear bands formation; a) development of microshear bands at low strain, and b) subsequent formation of CDRX grains at their intersection under large strains. Adapted from (Sakai et al., 2008).

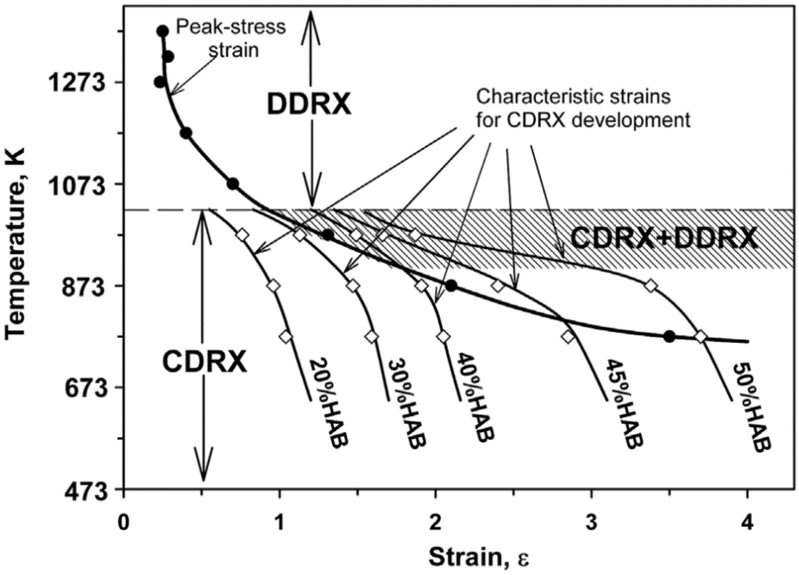

Figure 2.51 : Plot of strain and temperature domains for DDRX and CDRX in a type 304H austenitic stainless steel during warm and hot working, (Tikhonova et al., 2013).

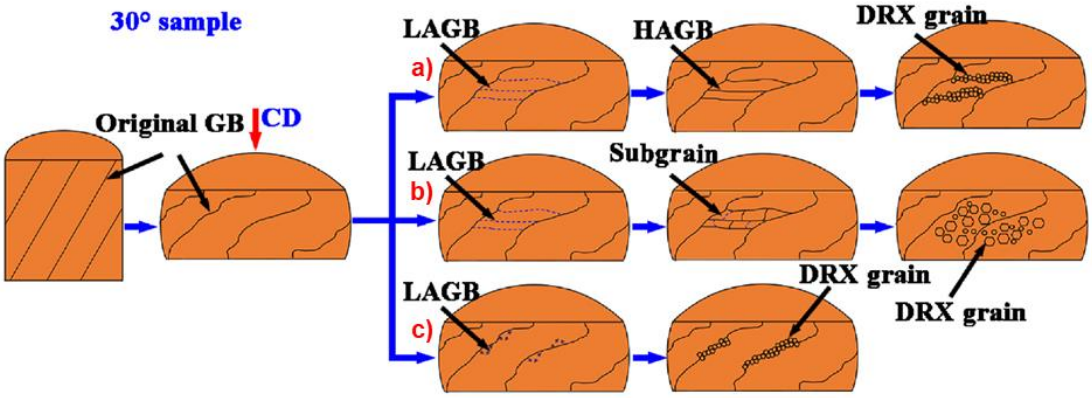

Figure 2.52 : Schematic illustration of three mechanisms identified for the initiation and progress of DRX mechanisms throughout upsetting in a super austenitic stainless steel samples with a columnar as-cast microstructure oriented at 60° to the compression direction, a) CDRX + DDRX, b) CDRX, and c) DDRX. Adapted from (Wang et al., 2021a).

Recrystallisation also occurs during holding at a temperature or slow cooling following deformation, such as inter-pass time during cogging (open-die forging) and reheating stage of the ingot-to-billet conversion process. Deformed or partially DRXed microstructures are very heterogeneous and may contain features such as (i) nuclei of DRX grains almost free of dislocation, (ii) DRX growing grains with a moderate density of dislocation, and (iii) non-recrystallised work-hardened grains with a high dislocation density. The evolution of these types of heterogeneous microstructures during further holding time at an elevated temperature after deformation is summarised in Figure 2.53. These include conditions where (i) the DRX nuclei continue to grow by metadynamic recrystallisation (MDRX), (ii) the non-recrystallised grains experience recovery followed by static recrystallisation (SRX), and (iii) the growing DRX grains undergo either recovery or SRX depending on their level of dislocation density (Humphreys and Hatherly, 1995).

SRX and MDRX are two different types of recrystallisation mechanisms which differ in several ways and need to be distinguished. SRX takes place in microstructures deformed under conditions where no DRX has been initiated and consists of an incubation period during which the rearrangement of dislocation sub-structures allows for new grain nucleation with further growth allowing for the progress of SRX. As shown by (Yang et al., 2015), progress of SRX is mainly promoted by increasing the deformation temperature and strain level. In contrast, MDRX involves uninterrupted continuation in growth of DRX nuclei into DRXed grains with annealing, without any incubation period. High density of DDRX nuclei promote the continuation of recrystallisation through MDRX, which is thus promoted by prior deformation stage to high strain levels at low strain rate. Figure 2.54 schematically show the plots of kinetics of SRX and MDRX mechanisms. It is noteworthy to highlight that MDRX exhibits a rapid onset compared to SRX due to the incubation period required for grain nucleation in SRX. Also, distinct levels of fractional softening are reached with enough annealing duration for each case, attributed to the consumption of deformed grains containing dislocation substructures by the growing DRX grains (i.e., undergoing recovery by SRX or MDRX). Since the onset of MDRX is instantaneous compared to that of SRX, the extent of SRX (i.e., nucleation and growth of new dislocation-free grains) is restrained in DRXed microstructure undergoing MDRX (Tikhonova et al., 2018).

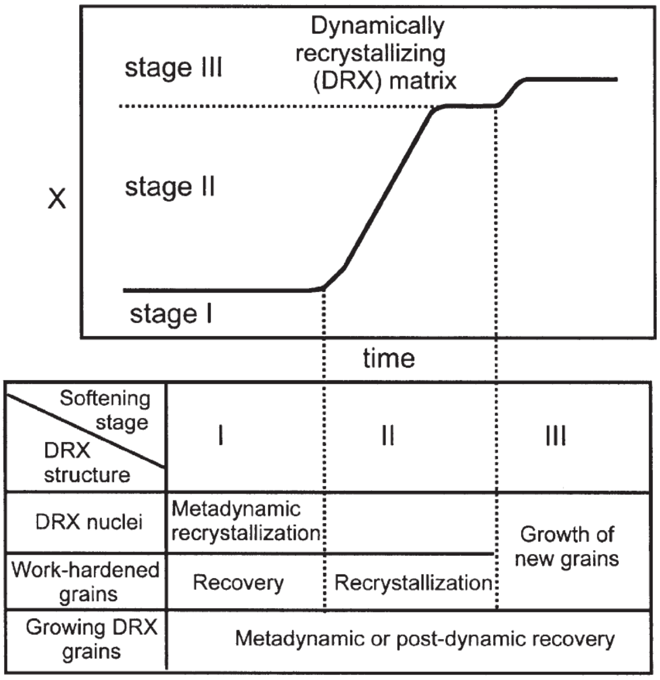

Figure 2.53 : Evolution of fractional softening (X axis) as a function of time, and associated strain recovery mechanisms in partially dynamically recrystallised material during further hold time at high temperature after deformation, (Humphreys and Hatherly, 1995).

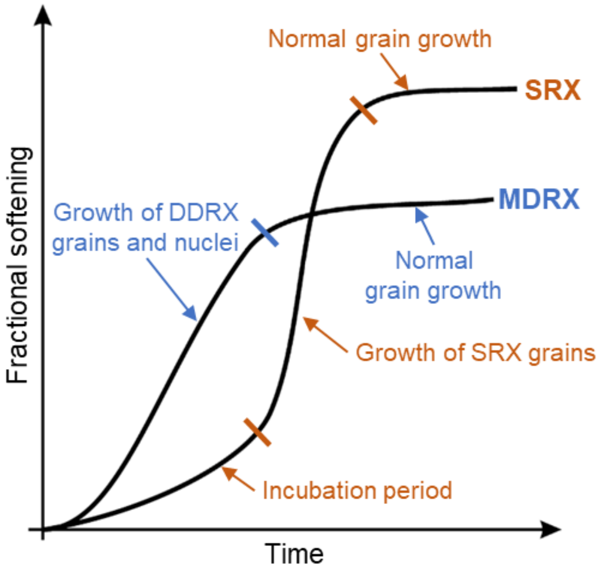

Figure 2.54 : Schematic plots of comparison between softening evolution with time during SRX and MDRX. Adapted from (Tikhonova et al., 2018).

Grain growth (GG) is followed after recrystallisation and involves gradual increase in the average grain size over time while elevated temperature is maintained. This mechanism is achieved though the migration of grain boundaries (Burke and Turnbull, 1952), driven by the reduction in grain boundary energy with the larger grains having a lower total grain boundary area compared to smaller grains. As a result, the grains with higher boundary mobility tend to grow at the expense of the others, leading to grain coarsening in the microstructure. Normal and abnormal grain growth are two different types of GG which have to be considered. Normal GG involves uniform coarsening of the microstructure throughout (see Figure 2.55 a)), whereas in abnormal GG a few grains grow at higher rates and consume the smaller adjacent grains, leading to a sudden development of a bimodal grain size distribution (see Figure 2.55 b)).

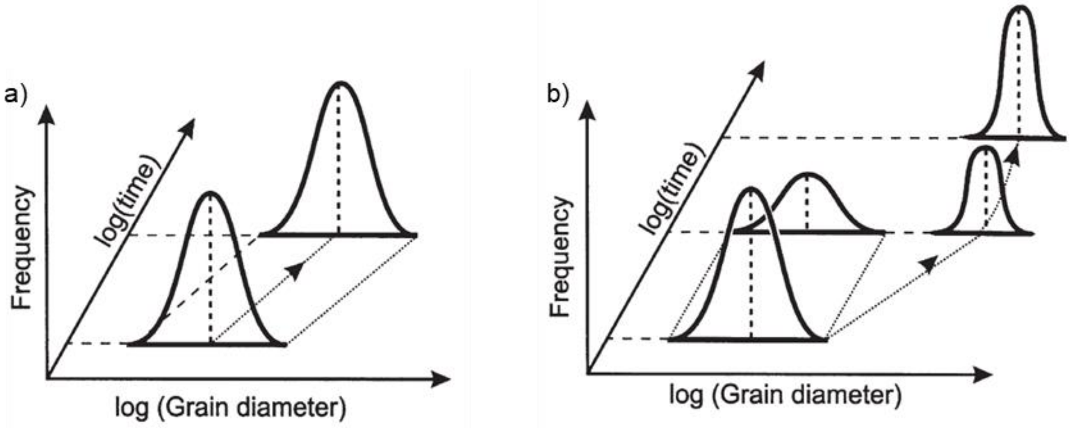

Figure 2.55 : Schematic plots of grain size evolution and distribution during a) normal, and b) abnormal grain growth. Adapted from (Humphreys and Hatherly, 1995).

2.6.2.3 Role of Nb addition

The addition of Nb to the composition of austenitic stainless steel grades not only enhances creep and corrosion resistance properties (see Section 2.2), but also significantly affects the deformation behaviour and recrystallisation mechanisms.

During homogenisation heat treatments, dissolution of primary NbC formed during solidification leads to an increase in C and Nb contents in austenite (Cliche et al., 2021), and thus an increase in SFE (Lu et al., 2011) (Xie et al., 2022) (Vitos et al., 2006). The higher SFE of Nb containing grades may therefore enhance the recovery mechanism during further thermomechanical processing, and thus delaying the onset of DDRX.

As a consequence of synergetic contributions of solute drag and Zener-pining mechanisms, Nb also contributes to of the reduction in grain boundary mobility. This allows for finer microstructures to be attained following recrystallisation compared to grades with no Nb content (Smagghe, 2017) and helps restrain the kinetic of grain growth during hold-on-temperature and reheating stages of the ingot-to-billet conversion processes. The solute drag effect refers to a decrease in grain boundary mobility due to the segregation of solute atoms at grain boundaries (Cahn, 1962) (Lücke and Stüwe, 1971) (Hillert and Sundman, 1976). These solute atoms may either be attracted or repelled by grain boundaries, thus imparting increased resistance to their motion thereby diminishing overall grain boundary mobility. As can be seen from Figure 2.56, the driving force grain boundary mobility increases with increasing concentration of solute atoms and this effect is significantly pronounced at lower kinetic rates of boundary motion. Therefore, solute drag effect has more pronounced influence on mechanisms characterised by lower kinetic rates of boundary motion (i.e., SRX and grain growth) as opposed to those with higher kinetic rates (i.e., DDRX). As highlighted by (Sinclair et al., 2007) in Figure 2.57, a small variation in Nb content leads to a significant effect on controlling the SRX grain size evolution in a α-Fe. In type 304 austenitic stainless steel, (Smagghe, 2017) observed a remarkable $\approx$ 30% reduction in the SRX grain size (i.e., following successive deformation and hold-on temperature stages) with an addition of only 0.15% Nb to the nominal Nb-free grade composition.

The Zener-pinning effect (Smith and Zener, 1948), schematically shown in Figure 2.58, is a mechanism that reduces the mobility of grain boundaries by locally pinning them on closely spaced second-phase particles dispersed throughout the microstructure (e.g., in the form of NbC, Nb(C, N), etc.). The effectiveness of this pinning mechanism is influenced by various factors, including the morphology, size, spacing and volume fraction of the second phase particles (Humphreys and Hatherly, 1995) (Manohar et al., 1998). Most of the studies on the role of Nb in controlling recrystallised grain size in austenitic stainless steels were conducted on thermomechanical conditions prone to predominant solute drag effect. For instance, the preconditioning heat treatment applied by (Hermant et al., 2019) on 316Nb samples prior to torsion test prevented the formation of a high volume fraction of Nb-rich precipitates with the appropriate size. Zener-pinning of grain boundaries by Nb-rich second phase particles was however observed by (Mataya et al., 1996) in a 22Cr-13Ni-5Mn-0.3N austenitic stainless steel containing ≈ 0.2 % Nb. The role of Nb in controlling the rate of recrystallisation through PSN was also shown in this study, with nucleated recrystallised grains observed at Nb-rich second phase particles.

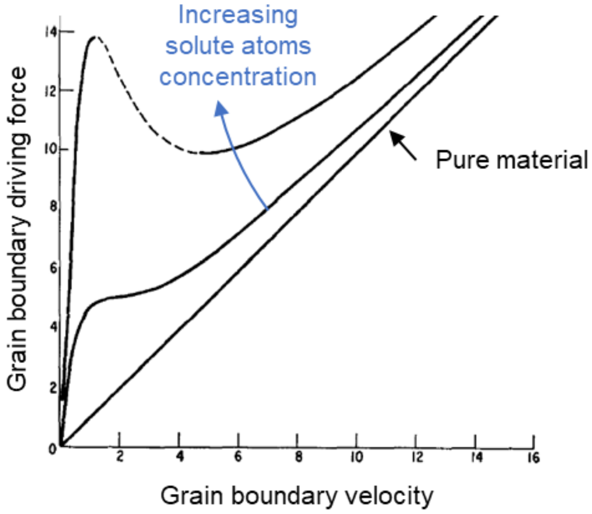

Figure 2.56 : Plots of grain boundary driving force as a function of grain boundary velocity for increasing concentration of solute atoms. Adapted from (Cahn, 1962).

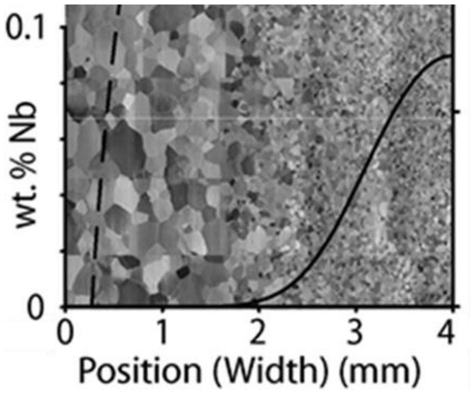

Figure 2.57 : Decreasing grain size observed with increasing Nb concentration (see the black curve) following SRX and grain growth in α-Fe. Adapted from (Sinclair et al., 2007).

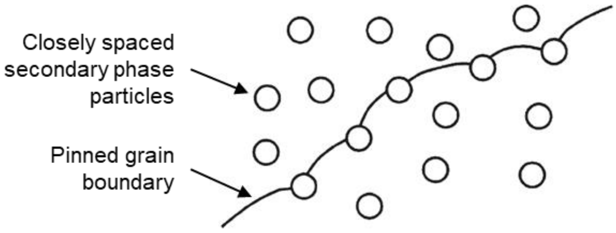

Figure 2.58 : Schematic depiction of the Zener-pinning effect induced by second phase particles on a grain boundary, (Humphreys and Hatherly, 1995).

2.7 MODELLING AND OPTIMISATION OF INGOT-TO-BILLET CONVERSION

The evolution of as-cast microstructure during the ingot-to-billet conversion process has been investigated in the past decades to allow the development and optimisation of manufacturing routes and obtain materials with optimal mechanical properties. Different stages are required for the development and optimisation of ingot-to-billet manufacturing routes, which are introduced in this section. Experimental work are required for a proper understanding and characterisation of the material constitutive behaviour while undergoing thermomechanical processes. It allows for collecting experimental data (e.g., load, displacement, temperature, microstructure, chemical composition, etc.), which are further used for the development and calibration of simulation models. Some of these include homogenisation, stress-strain behaviour, microstructural evolution, etc. These material models are then implemented in simulations, enabling optimisation of manufacturing processes.

Experiments dedicated to the investigation on as-cat material behaviour are based on those developed for wrought materials, such as thermomechanical experiments performed on laboratory-scale samples extracted from larger ingots. Table 2.6 provides details of selected set of studies on the recrystallisation of as-cast materials. Note that the materials used in these investigations are either in as-cast or in homogenised conditions. Thermomechanical experiments are commonly compression tests of laboratory scale samples, performed at elevated temperatures using compressing rigs to provide accurate control and record of the testing process parameters. For instance, the experimental setup developed in (Connolly et al., 2023) allows to replicate cogging and open-die forging processes at laboratory-scale. Despite the advantageous of high control and therefore accuracy of such equipment, their use is restricted to small size samples. These experiments are designed to replicate the thermomechanical conditions of the manufacturing process to be improved (e.g., cogging, upsetting). Most common geometries for samples are cylinders and double-truncated cone (DTC). An example of a DTC sample geometry is shown in Figure 2.59, which is typically upset to a 4:1 height reduction ratio (Semiatin et al., 2004). Upsetting tests performed on DTC samples allow a wide range of strain levels (i.e., from 0 to 2) across a sample, owing to its geometry, and hence cut down the number of experiments. Compression of directionally solidified materials are typically performed with the direction of solidification aligned parallel to the compression direction (Mataya et al., 2003a). Some studies have also investigated the material behaviours with the tests performed with different orientations to the direction of solidification, including 0°, 45° and 90° (Semiatin et al., 2004), and 0°, 30°, 60° and 90° (Wang et al., 2021a) (Wang et al., 2021b), for which different flow-stress and recrystallisation behaviours were observed (see Section 2.5).

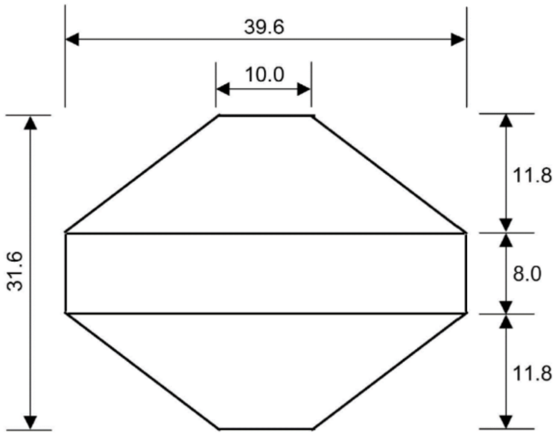

Figure 2.59 : Example of double-truncated cone (DTC) sample geometry used for characterisation of as-cast Waspaloy hot deformation and recrystallisation behaviours. Dimensions in mm. (Semiatin et al., 2004).

Modelling includes mathematically describing material behaviour (i.e., material flow, microstructural evolution, etc.) during thermomechanical processing. Resulting models can then be used to simulate and predict the evolution of material properties at 1:1 scale processing scenarios without the need for extensive and costly trials. Hence, models are essential tools for predicting material behaviour under various thermomechanical processing conditions.

Finite Element (FE) models are powerful tools for predicting the evolution of thermomechanical conditions at macroscopic scale. Models of experimental tests and industrial processes with integrated models for material flow behaviour, heat exchange and friction can hence be used to gain insight on the specificities and characteristics of thermomechanical processes. Anisotropic material flow behaviours can also be integrated into FE models (Terhaar et al., 2012). Crystal plasticity finite element method (CPFEM) can introduce an additional layer of complexity to FE models by incorporating crystallographic and morphologic description of a microstructure. With appropriate constitutive materials models integrated, CPFEM allow to simulate material deformation behaviour at grain scale, and predict microstructural evolution such as texture development, grain rotation, and strain localisation. Among others, CPFEM models allows to account for heterogeneous material deformation behaviour (Turner and Semiatin, 2011). However, due to significant computational time required for CPFEM simulations, their application is restricted to small representative volume element (RVE), consisting of a limited number of grains. Together, FE and CPFEM offer complementary approaches for predicting material behaviour from microscopic to macroscopic scales during deformation (e.g., forging).

As graphically summarised in Figure 2.60, various modelling approaches and models were developed for describing microstructure evolution and recrystallisation in metallic materials during thermomechanical processing (Miodownik, 2002) (Hallberg, 2011) (Orend et al., 2015) (Aghajani Derazkola et al., 2022).

Table 2.6 : Experimental details of selected studies on recrystallisation of as-cast materials.

Grade of material	Material condition	Sample geometry	Sample dimensions (mm)	Type of test	Testing conditions (°C ; s^{-1})	Reference
AISI 304	As-cast	Specific	35×35×5	Plane strain compression	850 to 1200 °C ; 0.5 and 5 s^{-1}	(Mandal et al., 2012)
AISI 316L	As-cast	Cylindrical	Ø 12.7×19.05	Isothermal compression	1000 to 1150 °C ; 1 s^{-1}	(Mataya et al., 2003a)
AISI 317L	As-cast	Cylindrical	Ø 12.7×19.05	Isothermal compression	1000 to 1150 °C ; 1 s^{-1}	(Mataya et al., 2003b)
AISI 904L	As-cast	Cylindrical	Ø 8×12	Isothermal compression	1000 to 1150 °C ; 0.01 to 10 s^{-1}	(Han et al., 2013)
AISI 904L	As-cast	Cylindrical	Ø 8×12	Isothermal compression	950 to 1150 °C ; 0.05 to 5 s^{-1}	(Zhang et al., 2016)
Mn18Cr18N austenitic stainless steel	As-cast	Cylindrical	Ø 8×12	Isothermal compression	950 to 1200 °C ; 0.001 to 10 s^{-1}	(Qin et al., 2017a) (Qin et al., 2017b)
Super austenitic stainless steel	Homogenised	Cylindrical	Ø 8×12	Isothermal compression	900 to 1200 °C ; 10 s^{-1}	(Wang et al., 2021a) (Wang et al., 2021b)
Super austenitic stainless steel S31254	As-cast	Cylindrical	Ø 8×12	Isothermal compression	900 to 1200 °C ; 0.01 to 10 s^{-1}	(Han et al., 2015) (Liu et al., 2014)
Inconel 718	Homogenised	Cylindrical	Ø 10×15	Compression	950 to 1130 °C ; 0.01 to 10 s^{-1}	(Yeom et al., 2007)
Inconel 718	Homogenised	Cylindrical	Ø 55.6×100	Forging (Upsetting)	1075°C ; Upsetting to 20 and 50% reduction in height	(Terhaar et al., 2012)
Inconel 718	As-cast	Cylindrical	Ø 12.7×19	Isothermal compression	950 to 1150 °C ; 0.01 to 1 s^{-1}	(Weis et al., 1989)
Nickel-Base Superalloy	As-cast	DTC	See Figure 2.59	Isothermal compression	1066 to 1177 °C ; 0.05 to 0.1 s^{-1}	(Semiatin et al., 2004)
Nickel-Base Superalloy	Homogenised	Cylindrical	Ø 15×15	Isothermal compression	1065 °C ; Upsetting to 50% reduction in height; 0.005 s^{-1}	(Turner and Semiatin, 2011)
Nickel-Base Superalloy	Homogenised	Cylindrical	Ø 8×12, Ø 10×15, Ø 12×18	Isothermal compression	1000 to 1150 °C; 0.0001 to 0.1 s^{-1}	(Sahithya et al., 2019)
Nickel-Base Superalloy	Homogenised	Cylindrical	Ø 14×20	Isothermal compression	1070 to 1190 °C; 0.01 to 0.5 s^{-1}	(Yu et al., 2015)

Johnson-Mehl-Avrami-Kolmogorov (JMAK) type of recrystallisation models are part of the so-called "constitutive models for process control" in Figure 2.60, and are named after the authors of the studies which led to development of the model (Johnson and Mehl, 1939) (Avrami, 1941) (Kolmogorov, 1937). JMAK models provide phenomenological, simplified and averaged description of recrystallisation mechanisms, and their use is well developed in academic and industrial research compared to other type of models. They have relatively simple mathematical formulation in the form of Equation (2.3), and assume homogeneous nucleation of recrystallisation. For modelling time-dependant recrystallisation mechanisms (i.e., SRX and MDRX), Equation (2.3) is adapted in the form of Equation (2.4), and in the form of Equation (2.5) for strain-dependant recrystallisation mechanisms (i.e., DDRX). The determination of numerous parameters involved in such JMAK-type models however require extensive experimental data.

$$X(t) = 1 - exp(-k\ t)^n \tag{2.3}$$

$$X = 1 - exp\left[-0.693\left(\frac{t}{t_{50}}\right)^n\right] \tag{2.4}$$

Where n is time dependant exponent (i.e., a constant), and t_{50} is the time at which 50% of a microstructure is recrystallised ($X = 50\%$). As expressed in Equation (2.6), t_{50} can be expressed as a function of additional parameters to account for its sensibility of different material or thermomechanical conditions.

$$X_{DRX} = 1 - exp\left[-k\ \left(\frac{\varepsilon - \varepsilon_c}{\varepsilon^*}\right)^m\ \right] \tag{2.5}$$

Where k and m are material constants, ε is strain, ε_c is critical strain for onset of DDRX and $\varepsilon^*$is strain for maximum softening rate. ε_c and ε^* can be expressed in the power-law form of Equation (2.7).

$$t_{50} = A_{50}\ \dot{\varepsilon}^p \varepsilon^q D_0^r exp\left[\frac{Q}{RT}\right] \tag{2.6}$$

Where A_{50}, p, q and r are material constants, $\dot{\varepsilon}$ is strain-rate, ε strain level, D_0 is the initial grain size, Q is activation energy required for SRX or MDRX, R is the gas constant, and T is temperature.

$$Parameter = p_1 \cdot \left(\frac{Z}{A}\right)^{p_2} \tag{2.7}$$

Where A, p_1 and p_2 are additional material constants and Z is the Zener-Hollomon parameter (see Equation (2.2)).

A first method for the determination of JMAK recrystallisation model is based on the correlation of the thermomechanical processing conditions with measurements of the fraction of recrystallised grains or grain size in the final microstructure. Example of such studies for the characterisation and model calibration of static recrystallisation kinetic in as-cast 316L and 317L stainless steel grades can be found in (Mataya et al., 2003a) and (Mataya et al., 2003b), respectively. The as-cast Ø 12.7×19.05 mm samples, taken out from a larger ingot, were subjected to upsetting to strains ranging from 0.1 to 1, following which they were kept in the thermomechanical simulator at the test temperature for a post-deformation heat treatment prior to water quenching. No homogenisation heat treatments were performed on the samples prior to the tests, and a 10 minutes heating stage was used to heat the samples to the testing temperature, ranging from 1000 to 1150 °C. The samples were then prepared for microstructure characterisation and measurements of the fraction of recrystallised grains. The parameters of the JMAK model for SRX were finally determined by least squares fitting of the JMAK function to the experimental results. An overview of these results are shown in Figure 2.61 for the 316L grade. Correlation of thermomechanical processing conditions to measurements of the fraction of recrystallised grains was also performed by (Fan et al., 2019) and (Freund et al., 2020) for wrought material. This last study aimed at investigating the DRX behaviour of wrought Ø 70×200 mm billets made of Inconel 625 during cogging, and the results were presented in the form of a map of the progress of DRX as function of strain and deformation conditions (i.e., Z).

The double-hit interrupted isothermal compression experiment is another method used for the determination of JMAK equations for SRX and MDRX kinetic (Jin et al., 2013) (Zhang et al., 2016). As shown schematically in Figure 2.62, the tests consist of interrupted compression stages to different deformation levels, with intermediate heat treatments at different temperatures for 1 to 100 s duration. The effects of recovery are neglected, and the fraction of recrystallised grains (X_{RX}) is determined for each experimental condition from the flow softening measured between the first and second compression stages using Equation (2.8). Finally, the parameters for the JMAK model are obtained by linear-fitting.

$$X_{RX} = \frac{\sigma_m - \sigma_1}{\sigma_m - \sigma_2} \tag{2.8}$$

Where σ_m is the stress reached following the first compression stage, and σ_1 and σ_2 are the 2% offset stress measured following first and second compression stages, respectively (see Figure 2.62 b)).

Additional methods for determination of JMAK DRX models rely on the analysis of the stress-strain curves obtained from isothermal compression tests. The JMAK equation for DRX is solved from the determination of flow softening effect induced by the initiation of recrystallisation during compression tests (see Figure 2.37). Study of dynamic recrystallisation behaviour of as-cast 254SMO super-austenitic stainless steel by (Han et al., 2015) provides a well detailed step-by-step example of the method. It is based on the identification of a set of stress and strain parameters from the flow curves using the double-differentiation method proposed by (Poliak and Jonas, 1996), on the determination of the activation energy parameter of the Zener-Hollomon equation (see Equation (2.2), (Zener and Hollomon, 1944)), and of the hyperbolic-sine Arrhenius type constitutive equation for the material (Sellars and McTegart, 1966). It is noteworthy that

JMAK models developed from the analysis of flow softening induced by the onset of recrystallisation provide macroscopic prediction of recrystallisation, as considerate is assumed that the material deforms homogeneously.

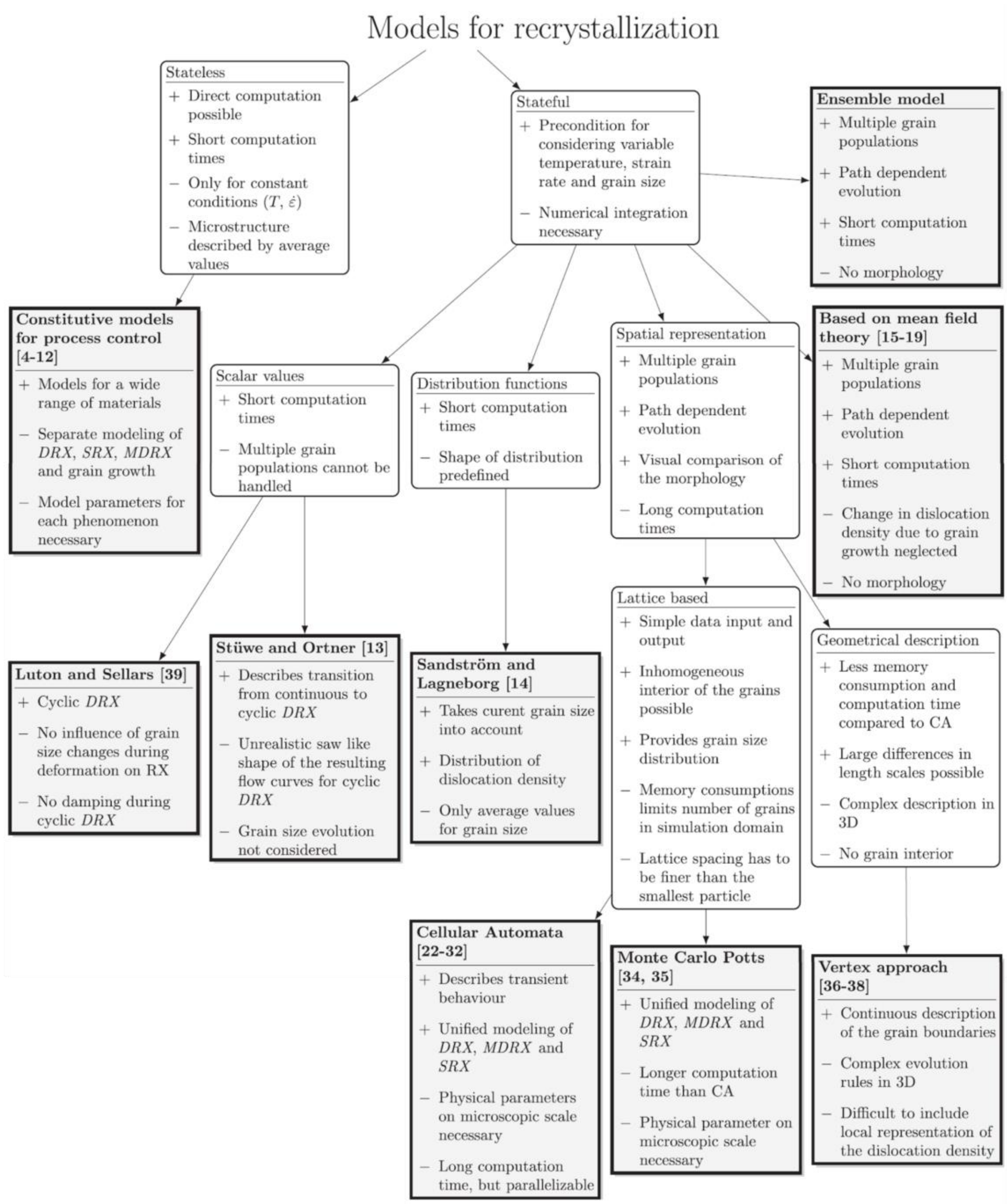

Figure 2.60 : Overview of some modelling approaches and microstructure evolution models (highlighted with a bold borders) available in the literature, (Orend et al., 2015).

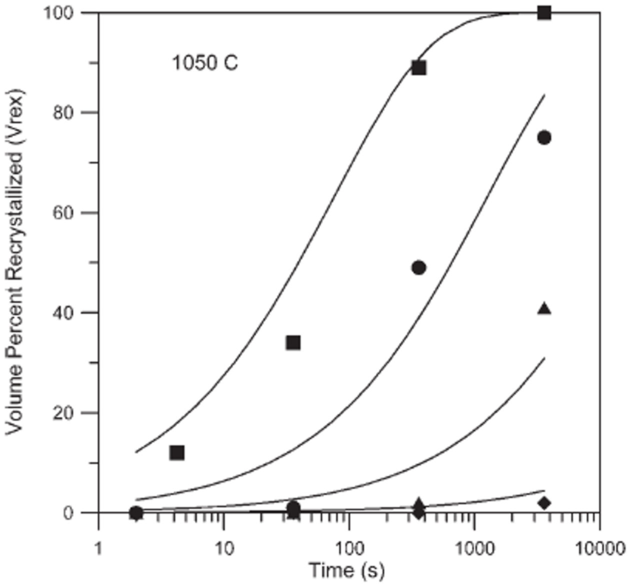

Figure 2.61 : Example of JMAK model for SRX obtained by correlation of experimental thermomechanical processing conditions and measurements of the fraction of recrystallised grains following upsetting and hold on temperature tests. Adapted from (Mataya et al., 2003a).

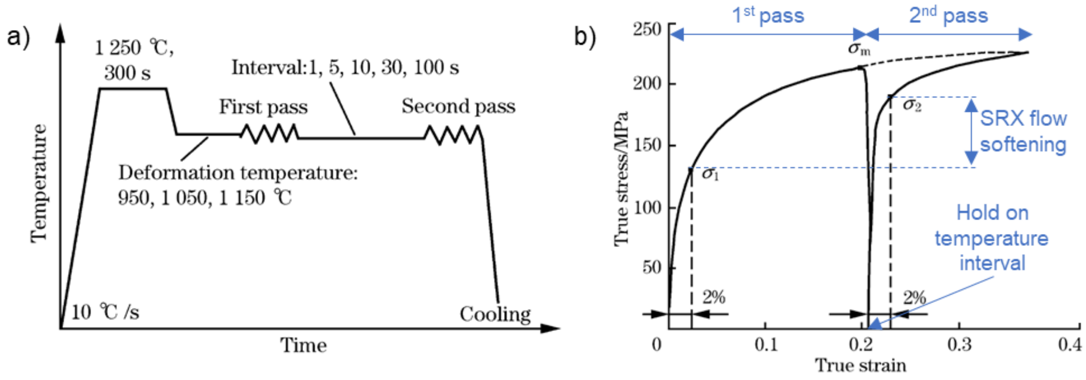

Figure 2.62 : Characterisation of SRX kinetic in 316LN austenitic stainless steel; a) deformation schedule including an interrupted compression stage performed at 950 °C to 1150 °C with hold on temperature intervals of 1 to 100 s, and b) exploitation of stress-strain curves for determination of flow-softening fraction. Adapted from (Jin et al., 2013).

The ability of JMAK approach to accurately predict the progress of recrystallisation throughout experiments with increasing complexity of thermomechanical loading history (see Figure 2.63 a)) was investigated by (Bylya et al., 2017). As depicted in Figure 2.63 b), the main results from this study is that increasing the thermomechanical loading history complexity of the tests leads to a decrease in accuracy. This is explained by two main factors: (i) the unknown area of applicability of the models, and (ii) poor calibration methodology used for their development. It is shown that conventional uniaxial laboratory-scale experiments remains insufficient for appropriate calibration of JMAK models. It is also stated by (Bandar et al., 2007) that JMAK models are typically not sensitive to variation in grain morphology, and face some challenges at determining the dominant recrystallisation mechanisms throughout cyclic deformation and heat transfer stages. Those aspects related with intrinsic characteristics of as-cast microstructure and ingot-to-billet conversion processes therefore limit the ability of JMAK models to accurately predict the evolution of as-cast microstructure throughout the ingot-to-billet conversion process.

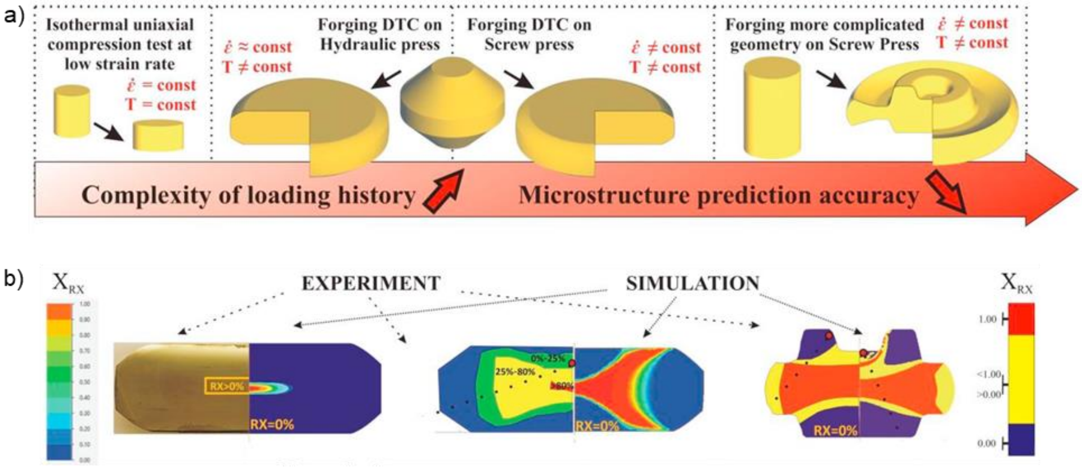

Figure 2.63 : Overview of experimental and simulation work performed to demonstrate the effect of thermomechanical loading history on the accuracy of JMAK microstructure prediction models. Adapted from (Bylya et al., 2017).

In contrast to JMAK models, which provide phenomenological, simplified and averaged description of recrystallisation mechanisms, cellular automata (CA) models offer a more detailed approach by simulating recrystallisation at microstructural level. In CA models, the material is spatially discretised into a grid of cells, each of which representing a microstructural feature, such as grain orientation, boundary characteristics, or dislocation density; and a set of local rule is used to govern the evolution of the state of each cell. CA models are hence able to account for spatial and temporal evolution of microstructure characteristics, and were developed for both wrought (Chen et al., 2014) (De Jaeger et al., 2015) and as-cast (Li et al., 2015) (Guo et al., 2018) materials. As an example, Figure 2.64 provides a comparison of experimental and CA simulated microstructure obtained by (Li et al., 2015) following isothermal compression and annealing of an as-cast Ni-based single crystal superalloy. Further analyses of the recrystallisation kinetics performed in this study with the CA model revealed the inhomogeneous nature of recrystallisation nucleation in the dendritic as-cast microstructure, demonstrating the limits of JMAK recrystallisation models for accurately predict the kinetic of recrystallisation in such materials. As depicted in Figure 2.65, CA models can also be coupled with CPFEM models to capture complex interactions between thermomechanical response of a material and its microstructural evolution (Li et al., 2016) (Majta et al., 2016). This approach allows for predicting nucleation and progress of recrystallisation in materials undergoing heterogeneous deformation. Although CA models have significant ability to accurately predict the evolution of microstructure, they require extensive computational and storage resources due to the need to simulate a large number of cells. This complexity grows significantly for three-dimensional simulations or when fine spatial and temporal resolutions are required (Svyetlichnyy, 2023).

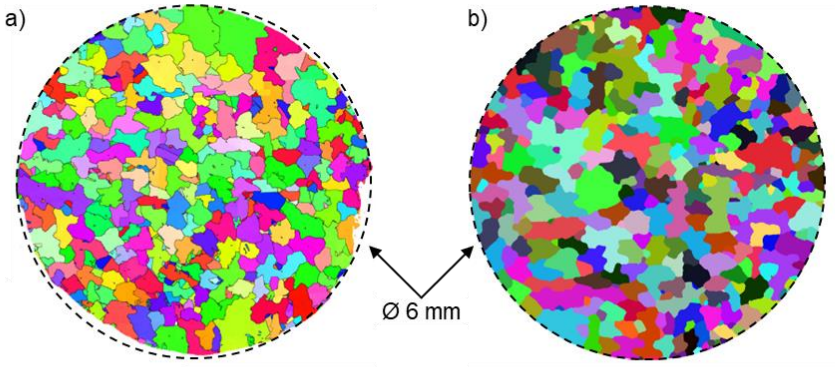

Figure 2.64 : Comparison of a) experimental (EBSD), and b) CA simulated microstructure of an as-cast Ni-based single crystal superalloy after isothermal compression (980 °C, 3×10^{-3} s^{-1}) and annealing (1300 °C, 4 h). Observation performed along the transverse cross-section of the sample. Adapted from (Li et al., 2015).

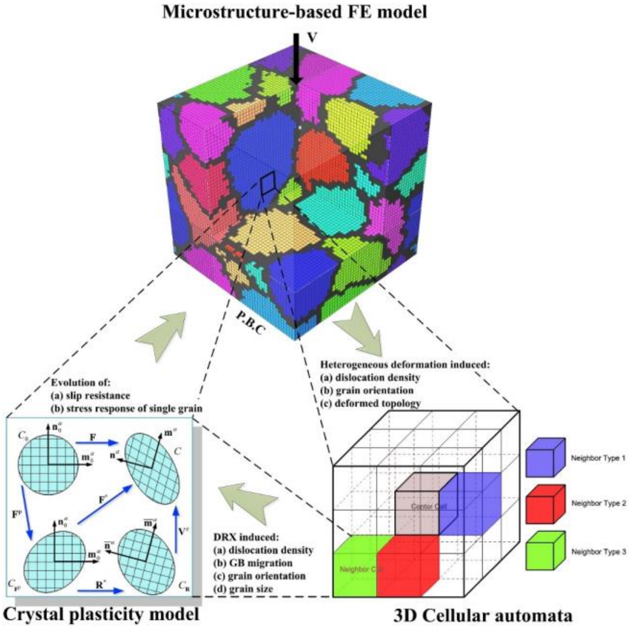

Figure 2.65 : Illustration of the modelling approach of the full coupling of FE, CPFEM and 3D CA models, (Li et al., 2016).

Another common method developed for the determination of optimised processing conditions for efficient recrystallisation is the generation of processing maps such as that proposed by (Prasad et al., 1984). This approach is based on dynamic material model concept, considering the absorption of power by the tested sample during hot working, expressed as the sum of the plastic deformation energy, the generation of heat, and the energy required for microstructure evolution including recovery, recrystallisation, flow localisation and phase transformation. Additional details on processing map theory can be found in (Prasad and Seshacharyulu, 1998), (Prasad, 2003), (Anitha Lakshmi et al., 2017), and (Anoop et al., 2020). A processing map is a graphical representation which illustrates a relationship between the thermomechanical processing conditions (i.e., temperature and strain rate), and the material deformation and microstructural evolution behaviours. It superimposes both power dissipation and instability maps, allowing to identify the optimal processing conditions to obtain the desired material properties while avoiding defects such as micro-cracking, heterogeneous deformation, formation of shear bands, and localised adiabatic heating. Processing maps are developed from the analysis of the hyperbolic-sine Arrhenius type constitutive equation, obtained from isothermal compression tests performed on laboratory scale samples. The study from (Han et al., 2013) on as-cast 904L austenitic stainless steel details a methodology for generating a processing map. This study demonstrated the power dissipation (see Figure 2.66 a)), and instability (see Figure 2.66 b)) maps of the material deformed at the true strain of 0.75. The high efficiency processing conditions for DRX are highlighted as domains #1 and #2 in the power dissipation map reproduced in Figure 2.66 a), and the instability map (see Figure 2.66 b)) provides indications of suitable thermomechanical processing conditions for avoiding any deleterious phenomena. An example of severe flow localisation observed following deformation in a fully instable region of the processing map is provided in Figure 2.66 c). Some controversy however exist about the use of processing maps, with questionable rigorousness of the analytical approach used for their development, and correctness of the predicted results (Ghosh, 2000) (Ghosh, 2002).

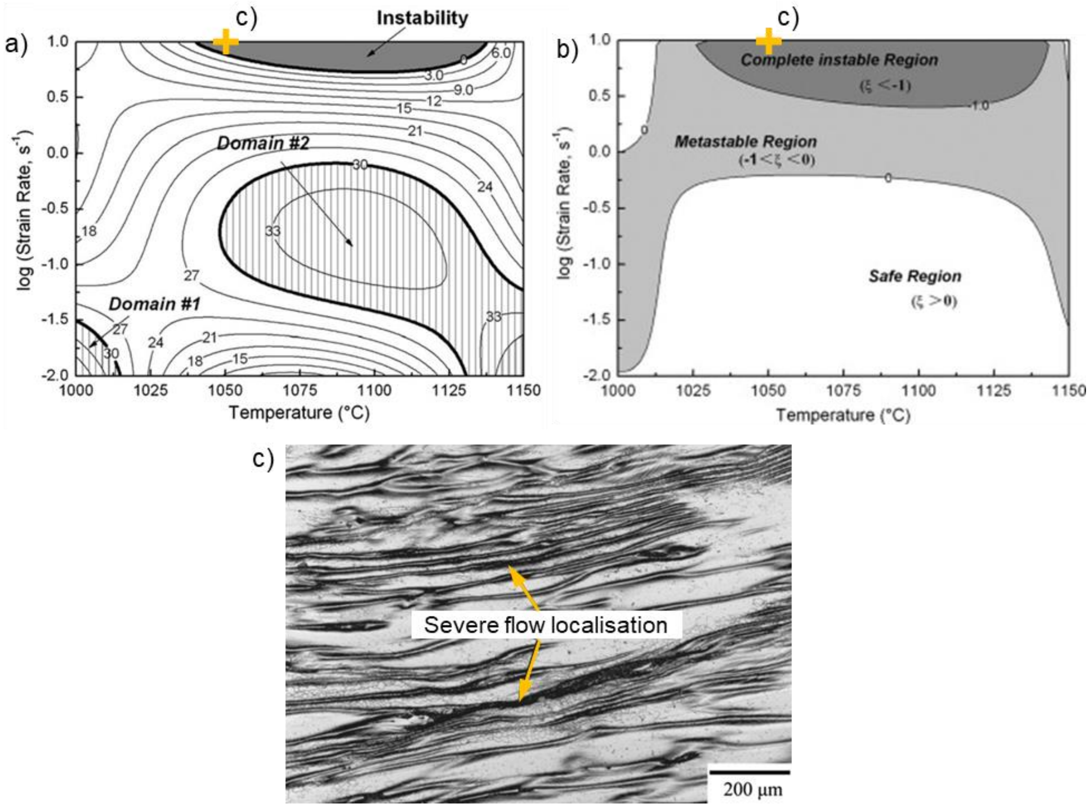

Figure 2.66 : Processing map of as-cast super-austenitic stainless steel predicted using Prasad's criterion, a) power dissipation, and b) instability map for a deformation up to the true strain of 0.75, c) an optical microstructure appearance of an instable region at 1050 °C deformed under a strain rate of 10 s^{-1} (see the yellow crosses in a) and b)). Adapted from (Han et al., 2013).

Optimisation of ingot-to-billet conversion process was promoted by the development of FE models, allowing to predict the evolution of thermomechanical properties of the material throughout the whole process (Cho et al., 1992) (Dandre et al., 1999). For instance, the cogging schedule and the shape of the dies used for cogging can be optimised to ensure effective closure of void porosities formed during the solidification of large bottom-poured ingots (Kim et al., 2011) (Lee et al., 2011) (Feng et al., 2016) (Pondaven et al., 2021) (Kukuryk, 2023). The cogging schedule was also subjected to various studies to ensure homogeneity of thermomechanical evolution across the transverse cross-section of ingots, hence improving the homogeneity of recrystallisation progress (Choi et al., 2006) (Kukuryk, 2018). Such work was performed by (Tamura and Tajima, 2004) for cogging a 500×500 mm ingot into a ≈ Ø 33 mm bar, and the ability of the optimised pass schedule in promoting full recrystallisation across the transvers cross-section of an ingot was validated by performing 1:1 scale experiments. As described in (Terhaar et al., 2012) and (Kukuryk, 2020), manufacturing routes with reduced susceptibility of material fracture can also be developed by integrating a damage criteria in FE model of the cogging process. Deep neural network regression models and the Taguchi optimisation method were used by (Park et al., 2023) for the optimisation of a cogging pass schedule. Fast calculation models developed by (Rosenstock et al., 2013) (Wolfgarten et al., 2019) are based on a semi-empirical approach to allow for the prediction of thermomechanical and microstructure evolution with short calculation times compared to conventional FE models, hence allowing to perform in-process optimisation. Note that the anisotropic characteristic of as-cast materials is not considered in most of those studies, although aiming at the optimisation of the ingot-to-billet conversion process.

Optimal hot working conditions for manufacturing (i.e., forging and ring-rolling) a ≈ Ø 3m×Ø2.8 m×0.4 m ring from a 6.5 tonnes GH3535 superalloy ingot were determined by (Wang et al., 2018) using a processing maps developed from laboratory-scale experiments. A 1:1 scale trial of the whole manufacturing process was conducted, including 7 reheating stages. The test allowed to manufacture a ring free of cracks, and microstructure analyses performed on the final product validated its homogeneous refinement, hence highlighting the advantages of using processing maps developed from laboratory-scale experiments for appropriate definition of hot processing conditions for large scale manufacturing routes.

In (Dandre et al., 2000c), JMAK relationships for microstructure evolution (i.e., DRX, SRX and GG) of Inconel 718 were determined from isothermal compression tests performed on samples taken out from a Ø 200 mm wrought billet; and the study aimed at determining an optimised manufacturing route for this billet from the as-cast ingot. Several cogging scenarios were proposed based on an analysis of the constitutive relationships for microstructure evolution. Corresponding FE simulations with the JMAK models implemented were carried out and compared to the actual cogging route. The optimal cogging route was identified as a route to achieve a uniformly refined grain size distribution across the transverse cross-section of the billet. It was shown to predict a grain size of ASTM 4 to 7, compared to ASTM 3 to 6 measured in the initial billet (see Figure 2.67). However, this work was carried out on wrought material, and the optimised cogging route was not validated through 1:1 scale experiments. This was made in (Dandre et al., 1999), but no details were provided on how the parameters of the JMAK recrystallisation model were evaluated. (Yeom et al., 2007) also developed a JMAK recrystallisation model for an as-cast Inconel 718, using small-scale experiments, which was then used to predict the average grain size in a cogged ingot. A similar method was used by (Jia et al., 2017) for the development of a predictive FE model of the hot extrusion process of as-cast P91 alloy steel. (Zhang et al., 2010) also used the same method for the optimisation of hot die forging of superalloy Inconel 718 in wrought condition. Laboratory-scale experiments were used to develop a JMAK recrystallisation model and a processing map of the material. The processing map was used to define several scenarios which were compared to each other with the help of FE simulation with the JMAK recrystallisation model integrated, hence allowing to choose one with optimal results. No 1:1 scale experiment was however included in this study to validate the ability of the developed JMAK model in accurate prediction of the resulting microstructure.

To account for the limitations of JMAK models in predicting the kinetic of recrystallisation in coarse, columnar as-cast materials, (Bandar et al., 2007) used a conventional FE model of the cogging process to estimate the evolution of thermomechanical properties (i.e., ε, $\dot{\varepsilon}$ and T) at key locations in an ingot. Those data were further used as input parameters in a CA model to predict the evolution of microstructure throughout cogging, hence accounting for the variation of the initial microstructure (i.e., grain size and geometry) in those key locations. Validation of the microstructure evolution model at industrial scale was not performed in this study, which stated that it will be conducted over the second phase of the project.

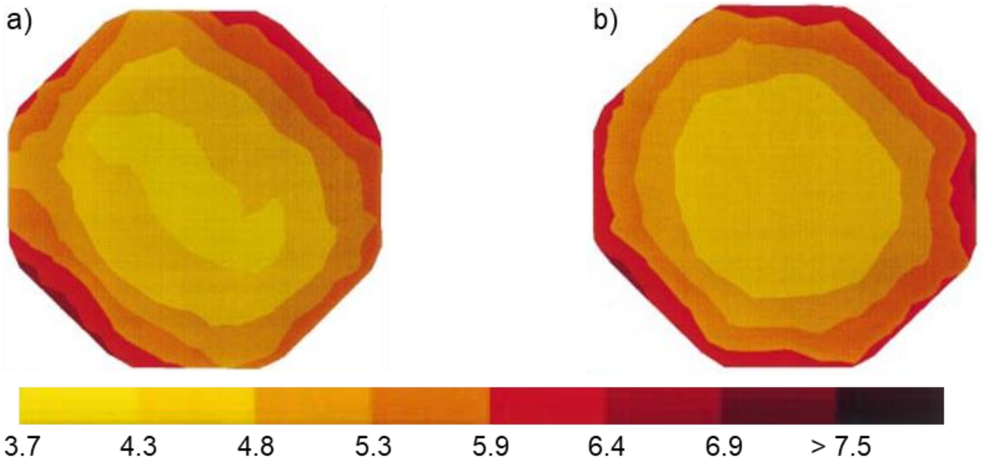

Figure 2.67 : FE simulation of ASTM grain size distribution in the transverse cross-section of a billet obtained following cogging with a) initial, and b) optimised cogging routes. Adapted from (Dandre et al., 2000a).

All studies reviewed for the investigation of the as-cast material behaviours involved thermomechanical experiments performed on small scale samples, and a limited number of studies reviewed in the following were found to investigate the evolution of as-cast microstructure through industrial scale forging tests. In the study of (Wang et al., 2016a), microstructure evolution models for DRX, SRX, MDRX and GG of wrought 316LN austenitic stainless steel were taken from literature, and implemented in an FE model of the conversion of a Ø 1700×3200 mm ingot. The grain size predicted by FE simulation was compared to experimental measurements performed at various location of the component following cogging, and the results showed a good correlation between FE and experimental results. This work remains however questionable from several aspects since the microstructure evolution models chosen from the literature were developed for different grades of wrought steels such as C-Mn steel, having thus different recrystallisation kinetics compared to the 316LN grade, which was also in as-cast condition. Moreover, the comparison of grain size distribution between experimental and FE predictions was performed at the end of the cogging process, and no comparisons were performed at intermediate stages.

Improvements of ingot-to-billet manufacturing process are strongly supported by investigations focused on the evolution of as-cast material during thermomechanical processing, allowing for deeper understanding and modelling of microstructure evolution and recrystallisation mechanisms (see Section 2.6.2.2 and Table 2.6). FE software packages have also been significantly improved to reduce computation time required for simulation of the cogging process, which incremental characteristics require long duration of computation, and thus reduce the ability at performing numerous simulations of the process (Ramadan et al., 2014) (Ramadan et al., 2019).

Although numerous studies were focused on the optimisation of ingot-to-billet manufacturing routes and recrystallisation of as-cast materials, very few studies provide validation of their findings (i.e., optimised cogging schedule, microstructure evolution model) at industrial scale. Moreover, validation stages proposed in those few studies were performed at the end of the ingot-to-billet conversion stage, i.e., after several deformation and reheating stages. No intermediate characterisation was made to support the validity of the developed recrystallisation models in predicting when the initial as-cast structure was fully recrystallised. Validation stage remains however crucial to ensure that findings issued from small-scale experiments can effectively be up-scaled for industrial processing conditions.

2.8 SUMMARY

This literature review introduced the key concepts related to the material, processes and investigation methods involved in the ingot-to-billet conversion process. The heterogeneous and anisotropic deformation behaviours of as-cast materials, owing to the size, orientation and morphology of the as-cast grains, compared to those in wrought condition were described. The existing available literature on microstructure evolution and recrystallisation mechanisms of as-cast FCC-type materials were reviewed, covering the effects of Nb composition on austenitic stainless steels. This literature review also provided a global overview of experimental and modelling methods currently available for the investigation of as-cast material behaviours and microstructure evolution mechanisms, which can be used for the optimisation of the ingot-to-billet conversion.

Most of the reviewed methods were derived from wrought materials, including laboratory-scale experimentations and the development of JMAK models, which have drawbacks when applied to as-cast materials. For instance, as a consequence of their coarse, elongated and dendritic microstructure, as-cast materials show heterogeneous deformation when subjected to thermomechanical processing, hence leading to heterogeneous nucleation and progress of recrystallisation. Columnar as-cast materials are also subject to anisotropic deformation behaviour owing to their strong preferential crystallographic texture. Also, due to high costs and efforts required for 1:1 scale experimentation, very few studies provided an industrial scale validation of their findings. Hence, despite extensive laboratory-scale studies on the constitutive flow behaviours and progress of recrystallisation in as-cast material during the ingot-to-billet conversion, there remain a significant gap in understanding how these mechanisms effectively operate during the industrial scale conversion process.

In light of these statements, it appears that upsetting and cogging experiments are required at intermediate scales, i.e., between laboratory and industrial scales, aiming at providing an overview of the evolution of microstructure in the early stages of the ingot-to-billet conversion process, under conditions closer to those encountered during industrial processing. This approach not only enhances the reliability of laboratory findings when applied at a larger scale but also contributes to optimising manufacturing processes by tailoring them more precisely to the specific needs and challenges of as-cast material processing. The insights gained through this scale of testing ultimately support more efficient, cost-effective, and quality driven ingot-to-billet conversion processes.

Chapter 3: MATERIALS AND METHODS

CONTENT

3.1 INTRODUCTION

This chapter deals with the experimental protocol developed in this PhD study to investigate at different scales the as-cast material behaviour and microstructure evolution during the industrial ingot-to-billet conversion process. To begin with, the different grade of materials, the ingots and the specimen geometries used for the investigations are presented with the associated thermo-mechanical processes implemented. The FE models of the experiments, accounting for the anisotropic as-cast material behaviour, are then described. Finally, the metallurgical analysis procedures are introduced, including material preparation, microstructure observations and quantitative measurements methods. Figure 3.1 displays a graphical abstract of the experimental, characterisation and simulation methods involved in this PhD study.

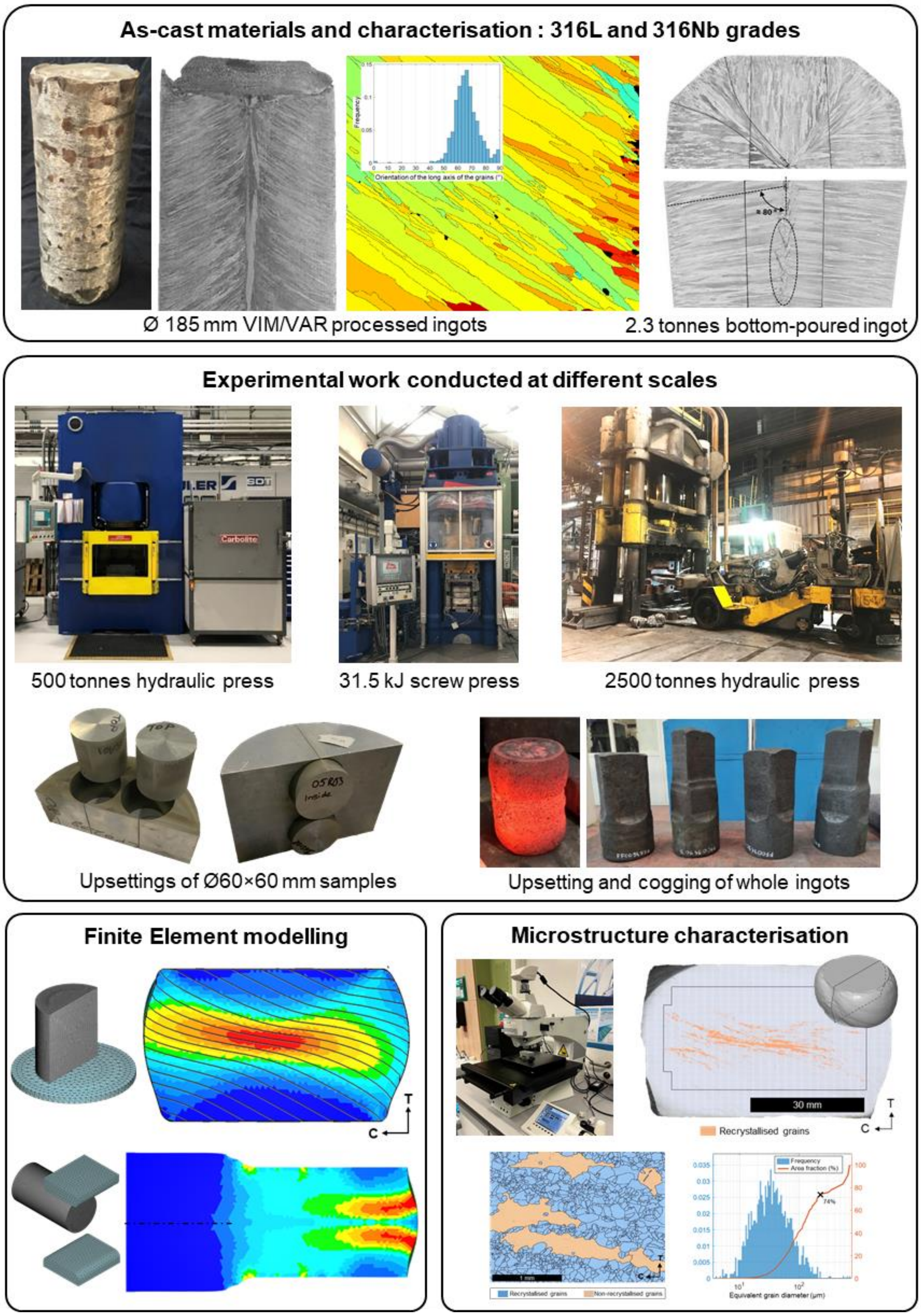

Figure 3.1 : Graphical abstract of experimental, characterisation and simulation methods involved in the present study.

3.2 MATERIALS

The materials used in the present work were two different grades of type 316 austenitic stainless steel, in the form of as-cast ingots, supplied by Aubert & Duval[1] as the industrial sponsor for this PhD thesis. Alloys production, including sequential specialised remelting processes (i.e., VIM, VAR) were all carried out at Aubert & Duval's factory in Les Ancizes, France. Photographs of the provided ingots are shown in Figure 3.2. Alloy designation and the nominal chemical compositions for both grades of type 316 austenitic stainless steel investigated in this thesis are given in Table 3.1. The chemical compositions of these materials were adjusted during production processes to comply with the standard specifications necessary for these grades of materials. As can be seen from Table 3.1, the difference between these grades was in the amount of Niobium content.

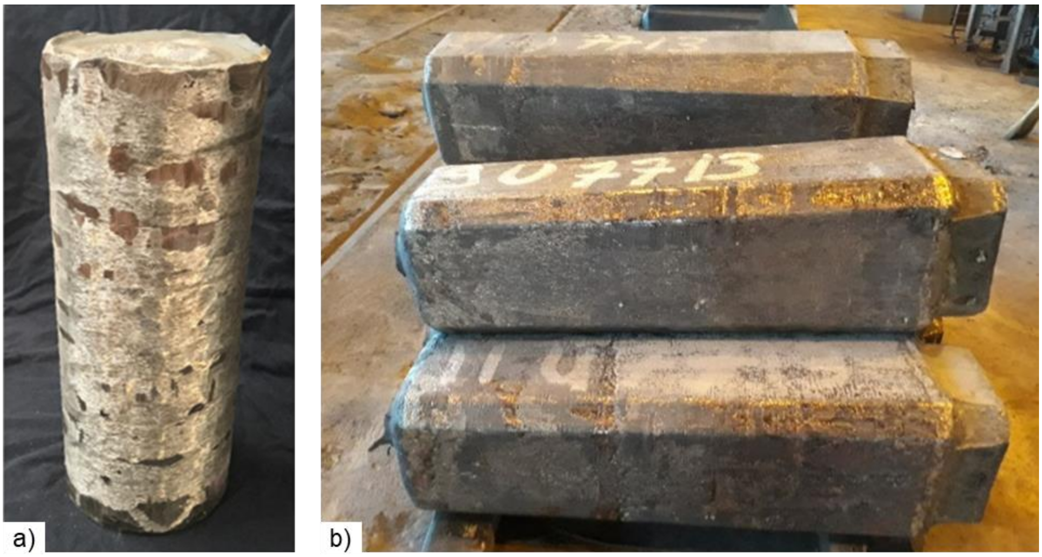

Figure 3.2 : Photographs of a) an intermediate scale b) industrial scale ingots after casting.

Table 3.1 : Designation and chemical compositions of the two grades of type 316 austenitic stainless investigated in this thesis. The chemical compositions of type 316L and 316Nb recommended by ASTM standard are also provided for comparison.

Grade designation	Alloying element and amount (wt.%)								
	C	Nb	Mn	Ni	Cr	Mo	Si	N	Fe, other
ASTM 316L *	0.03	x	2	10 - 14	16 - 18	2 - 3	0.75	0.1	Balance
316L	< 0.1	< 0.05	< 2	12 - 13	18 - 20	2.5 - 2.7	0.3 - 0.5	< 0.05	Balance
ASTM 316Nb *	0.08	10×C - 1.1	2	10 - 14	16 - 18	2 - 3	0.75	0.1	Balance
316Nb	< 0.1	≈ 0.7	< 2	12 - 13	18 - 20	2.5 - 2.7	0.3 - 0.5	< 0.05	Balance

* ASTM standard as per (ASTM A240/A240M-22, 2022)

---

[1] Aubert & Duval is a French metallurgist with fully integrated set of processes and facilities from steel and alloy-making through to pre-machined and machined parts.

Intermediate industrial size ingots (see Figure 3.2 a)), having a cylindrical shape with approximate dimensions of Ø 190×550 mm (≈ 125 kg), were casted through consecutive VIM and VAR processes. The industrial scale 2.3 tonnes ingot, shown in Figure 3.2 b), was casted through bottom pouring; and its schematic sketches and dimensions are presented in Figure 3.3. After casting, the surface of both ingots were cleaned by rough grinding to remove surface imperfections which might lead to crack initiation during forging (see Figure 3.2 a)). Ingots of both geometry were used for characterisation of the as-cast microstructure, and thermo-mechanical experiments were performed on the intermediate industrial size ingots. A summary of the ingots used in the present study is presented in Table 3.2, including a description of their elaboration process, geometry, dimension and available grade.

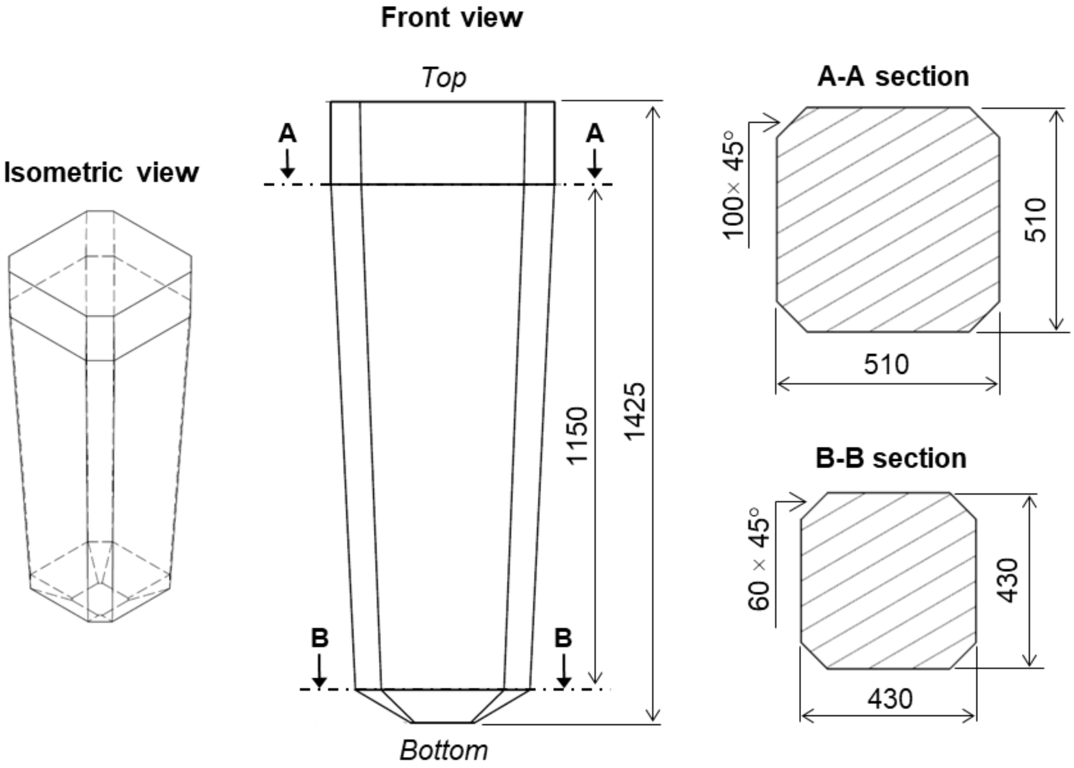

Figure 3.3 : Geometry and dimensions of the "L2300" industrial scale 2.3 tonnes ingot, casted through bottom pouring.

Table 3.2 : Summary of the ingots manufactured for the present study.

Casting process	Geometry	Grade	Number of ingots	
			Characterisation	Experiments
VIM + VAR	Ø 190×550 mm	316L	1	2
		316Nb	1	3
Bottom pouring	"L2300"	316Nb	1	-

3.2.1 Characterisation of the as-cast materials

Sufficient number of samples were cut from the ingots considered for this study to investigate the effect of alloy composition (i.e., different grades) and ingot size on microstructure characteristics, such as the size and morphology of grains, in the as-cast condition. Characterisations were performed along the longitudinal and the transvers cross-sections of the as-cast ingots. Due to the large size of the bottom poured ingots, instead of the entire cross-sections, only representative sections were characterised. The overall macrostructures of the ingots along transverse and longitudinal cuts were revealed by chemical etching after their surfaces were machined by milling to an Arithmetic Roughness (Ra) below 0.6 µm. The etching solution was composed of 40% ferric chloride ($FeCl_3$) and 30% of hydrochloric acid (HCl), and for each case etching was performed at 50 °C for several minutes until the microstructure was properly revealed. A conventional digital camera was then used to capture the microstructures.

The microstructure of the 316Nb ingot is presented in Figure 3.4, where “top” and “bottom” indications were defined according to the orientation of the ingot during the bottom-pouring casting process. It can be seen that the grains were columnar. In the transverse cross-section, the grains were perpendicular to the skin of the ingot, forming a specific pattern along the diagonals of the transverse cross-section (see the dashed lines in Figure 3.4 a)). As can be seen in Figure 3.4 b), the grains were oriented at about 80° to the axis of the ingot in the longitudinal cross-section of the ingot, and “V” shaped shrinkage porosities (i.e., voids) were formed along the axis of the ingot during solidification (see the dashed circle in Figure 3.4 b)).

The microstructures of the VIM/VAR processed ingots for both grades of materials (316L and 316Nb) are presented in Figure 3.5, where “top” and “bottom” indicate the orientation of the ingots during remelting. The as-cast microstructures composed of coarse and elongated grains, similar overall, but with different morphologies at three zones. In the chill zone (i.e., at the bottom of the ingots, where the remelting process was initiated) the grains were aligned with the direction of remelting and progressively converged towards the axis of the ingot, at a distance of 15 to 20 cm away from the bottom of the ingot. Once the remelting process reached a steady-state regime, the grains become parallel to the axis of the ingot within a ≈ Ø 20 mm zone around the core, and oriented at about 60° to the axis of the ingot in the surrounding areas towards the exteriors. Thin layers of equiaxed grains were also observed along the skin of the ingots which formed due to the fast cooling rate and abundant nucleation sites in this area (i.e., close to the mold wall). It can also be seen from the transverse sections that the microstructure is symmetrical around the axis of the ingot.

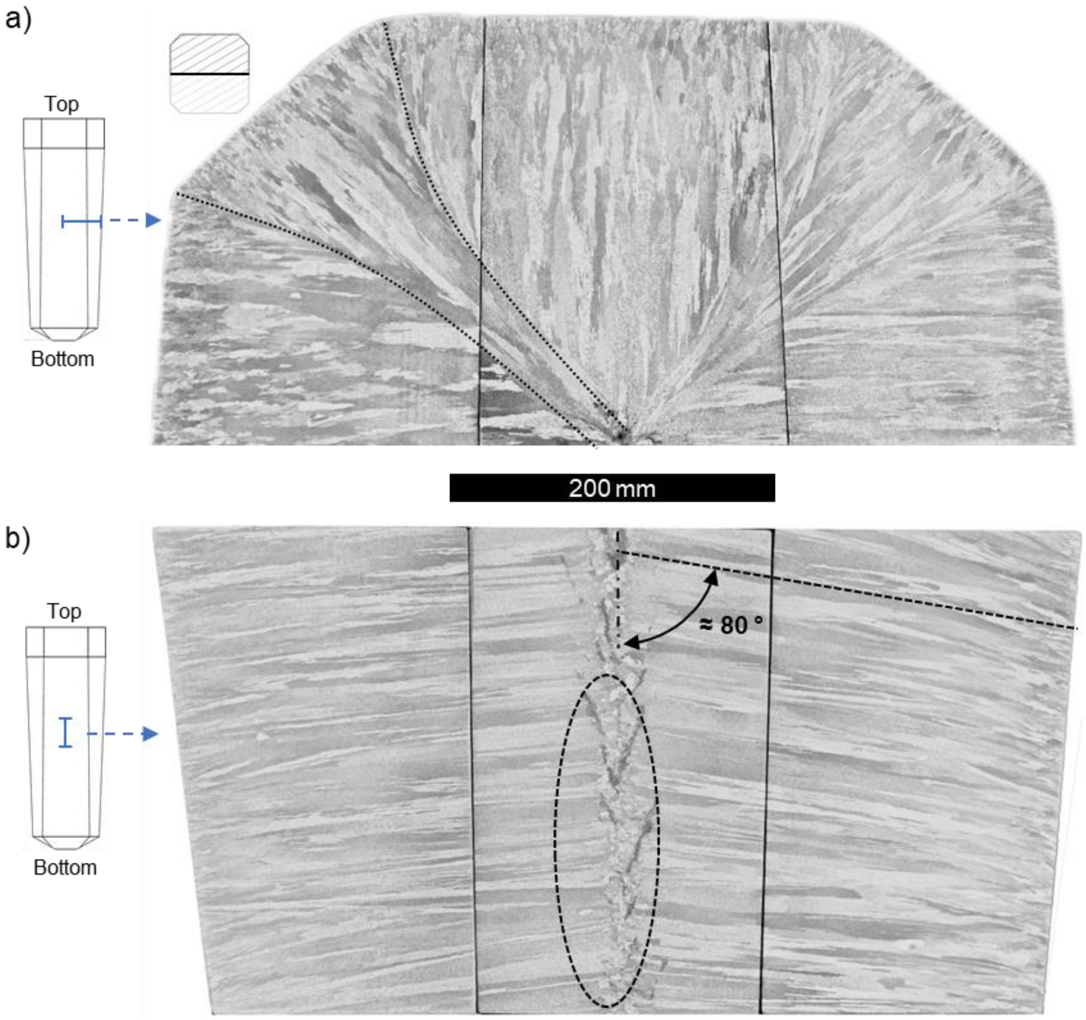

Figure 3.4 : Microstructures of the 2.3 tonnes 316Nb ingot produced through bottom-pouring; a) half-transverse, and b) a portion of the longitudinal cross-section.

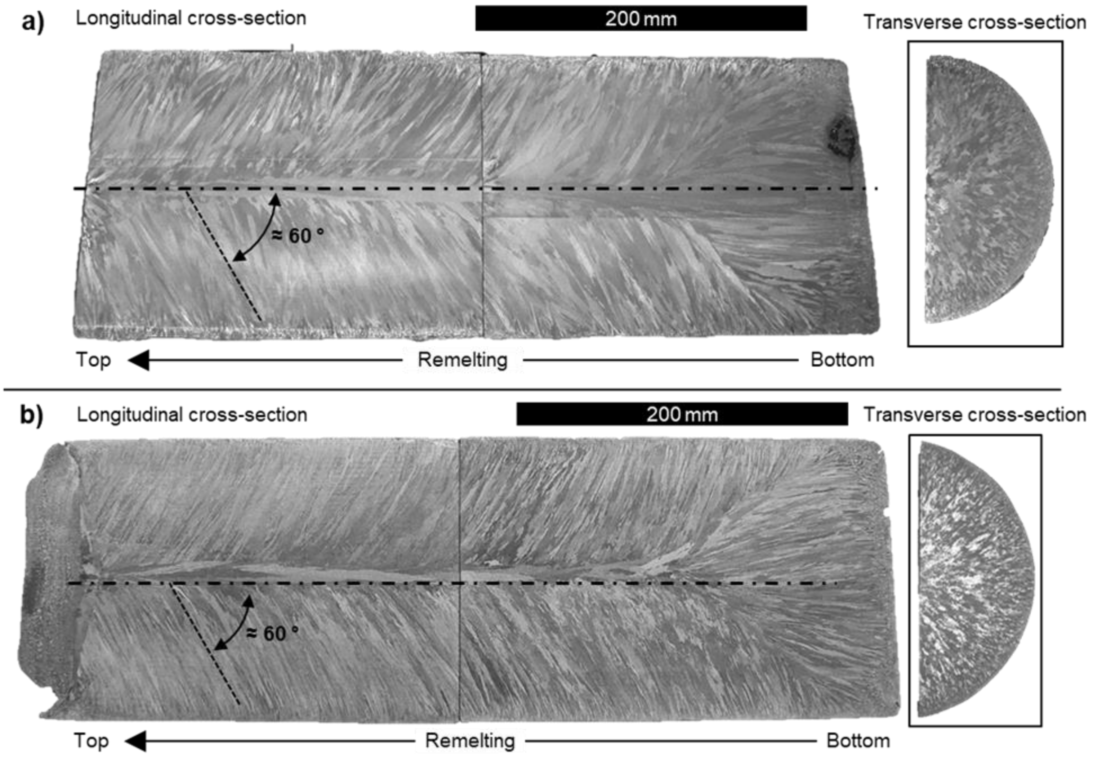

Figure 3.5 : Microstructures of the ≈ 120 kg ingots a) 316L, and b) 316Nb grades in as VIM/VAR processed conditions. Observations performed along longitudinal and transverse cross-sections.

Measurements of grain size (i.e., minor diameter) and their orientations with respect to the axis of the ingots were performed for both the 316L and 316Nb grades, on specimens extracted from the VIM/VAR processed ingots, homogenised for 24 h at 1250 °C. The locations of the specimens in the initial ingots are schematically shown in Figure 3.6. For each case, the microstructure of the sample was then revealed by etching, and optical microscopy images were captured (see Figure 3.7 a)) from the whole cross-section of the sample using a Leica® DM12000-M optical microscope. The acquired individual micrographs from the cross-sections of the samples were then stitched together to reconstruct a larger micrograph of the investigated areas. Grain boundaries were traced manually over the micrographs (see Figure 3.7 b)) using GIMP® image editing software, and exported as a binary image (see Figure 3.7 c)) for post-processing using an in-house developed routine in Matlab® software, which was used for quantitative analyses of the as-cast microstructures characteristics. An elliptical shape was fit to each grain, using the best-fit approach, and the orientation of their long axis to the axis of the ingot was then measured. The thicknesses of the grains were estimated using their minimum Ferret diameter the grain. Colour maps of the grain orientations (i.e., the angle between the long axis of the grain and the axis of the ingot) and their thicknesses are displayed in Figure 3.8 and Figure 3.10, respectively; and corresponding histograms showing their distributions are shown in Figures 3.9 and 3.11, respectively. The average orientations of the long axes of the grains were measured at ≈ 58° and

≈ 66° to the axis of the 316L and 316Nb ingots, respectively, and the average grain thicknesses were measured at ≈ 0.8 and ≈ 0.4 mm for 316L and 316Nb grades, respectively.

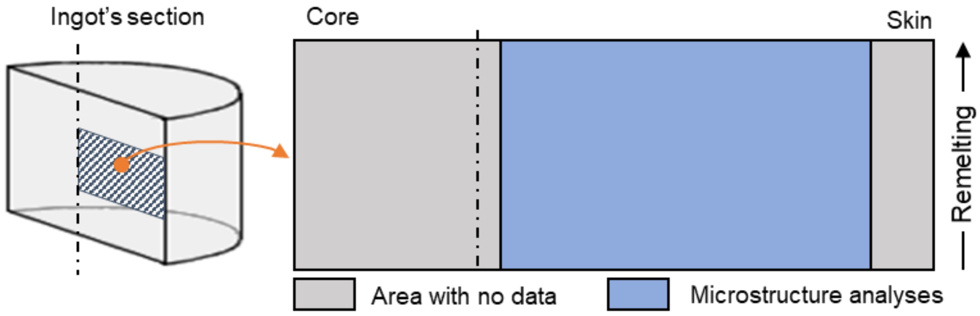

Figure 3.6 : Schematic representations of the location of the specimens taken from the ingots for characterisations of as-cast microstructures of 316L and 316Nb VIM/VAR ingots.

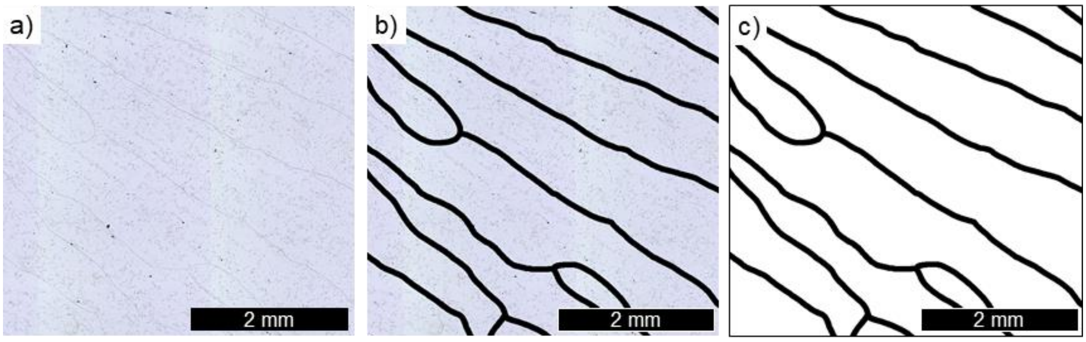

Figure 3.7 : a) Optical microscopy appearance of the as-cast microstructure, with b) the grain boundaries traced manually, and c) resulting binary image of the grain boundaries for further analyses with Matlab.

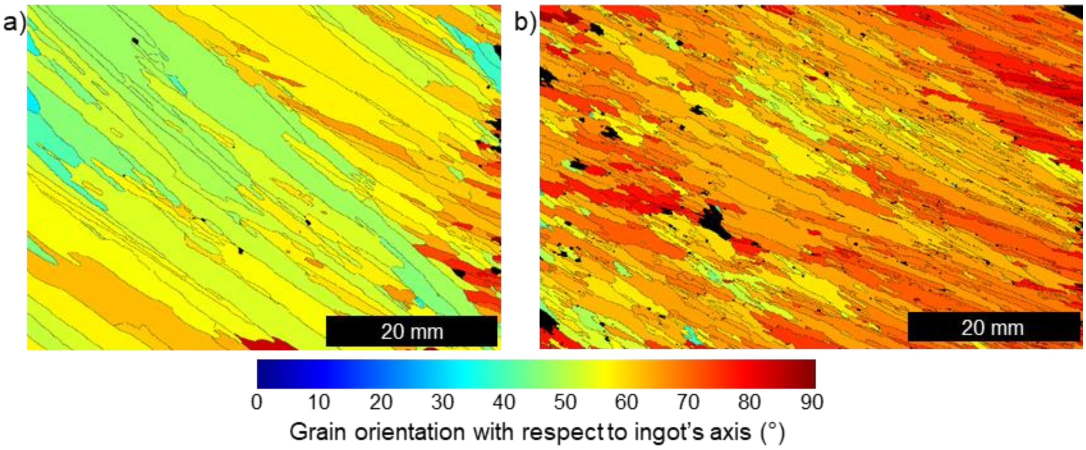

Figure 3.8 : Microstructures of the homogenised VIM/VAR produced ingots with the grains coloured according to their orientations (°) to the axis of the ingot; a) 316L, and b) 316Nb grades.

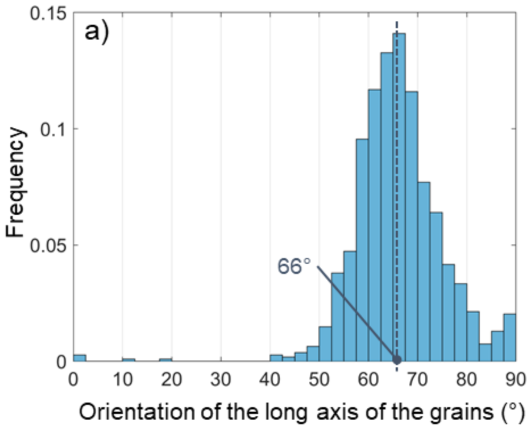

Figure 3.9 : Histogram plots showing distributions of the orientations of the grains with respect to the axis of the VIM/VAR produced ingots; a) 316L and b) 316Nb grade.

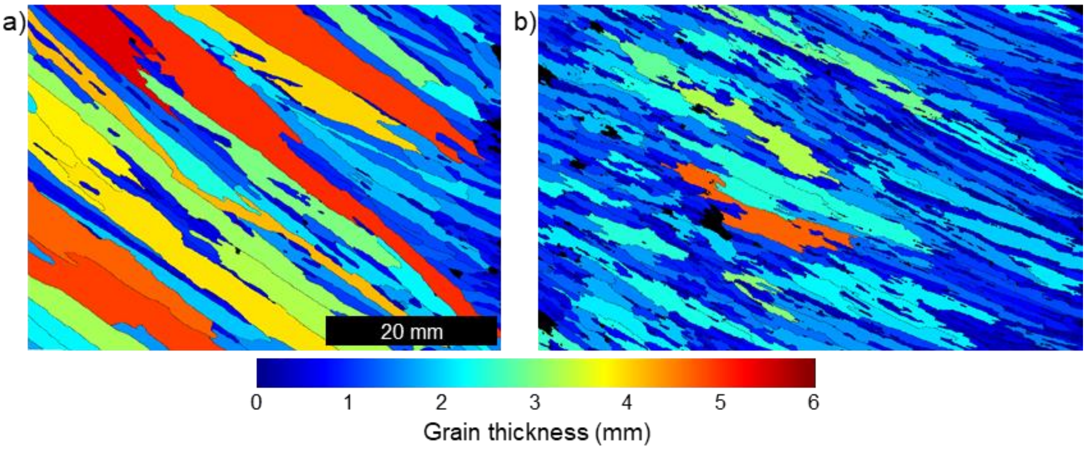

Figure 3.10 : Microstructures of the homogenised VIM/VAR produced ingots with the grains coloured according to their thicknesses (mm); a) 316L, and b) 316Nb grades.

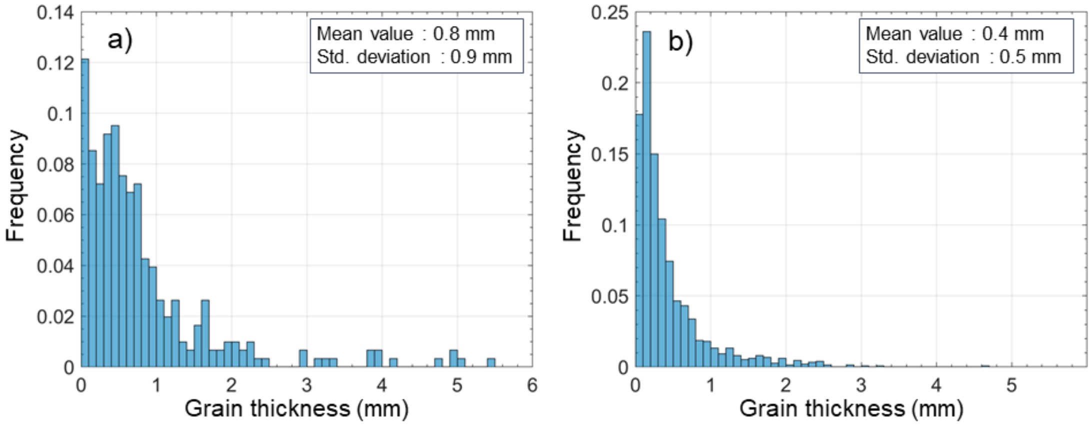

Figure 3.11 : Histogram plots showing distributions of the grain thickness (mm) in the VIM/VAR produced ingots; a) 316L and b) 316Nb grades.

3.2.2 Thermomechanical processing

The evolution of the as-cast microstructure during ingot-to-billet conversion process was investigated. For this purpose, a set of experimental trials were designed and executed to understand the likely mechanisms of microstructure evolution using a combination of characterisation techniques and mechanical works. Experiments were conducted on the VIM/VAR processed ingots (see Table 3.2). The experimental works conducted on smaller-scale samples taken from the ingots, as well as upsetting and cogging operations performed on the entire ingots. The following sections aim to describe these experiments in details:

3.2.2.1 Small scale hot upsetting tests

For this part of the work, the effects of grade composition, orientation of the sample in the ingot and two different levels of strain rates were investigated on the as-cast materials. Different steps of the experimental processes are summarised in Figure 3.12.

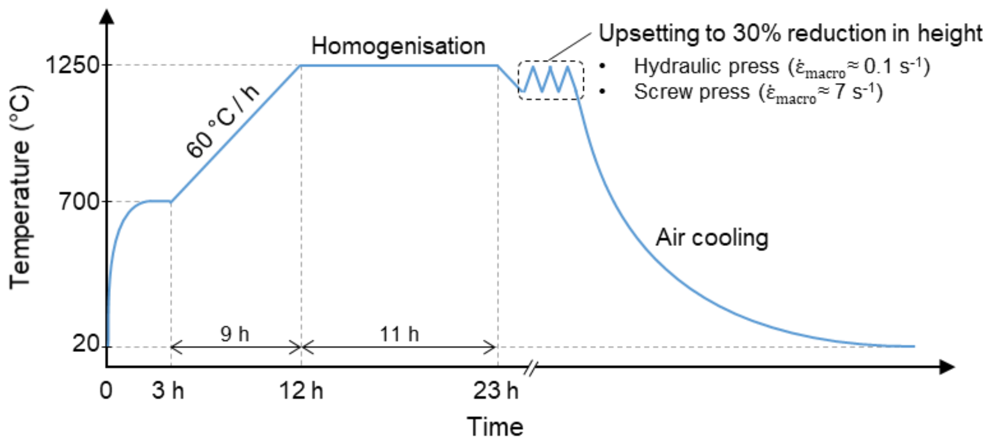

Figure 3.12 : Hot upsetting experiments performed on the small scale samples taken from the VIM/VAR ingots.

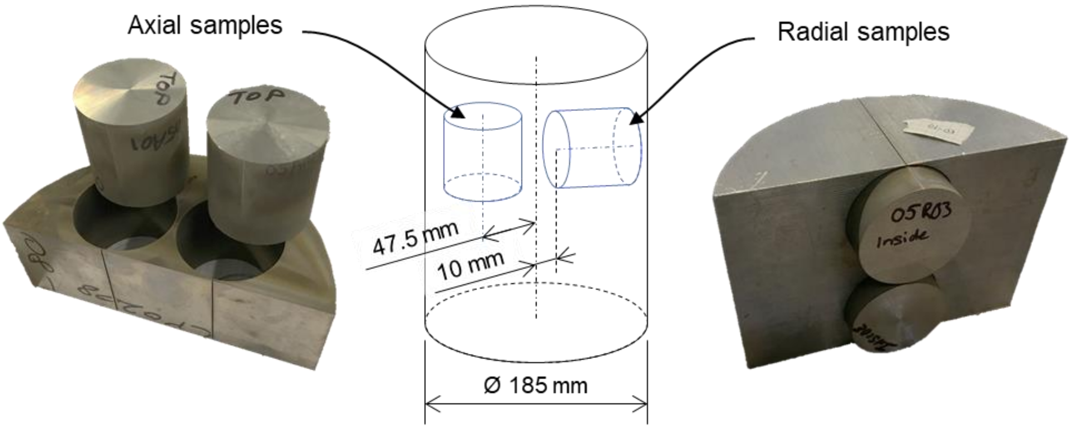

Figure 3.13 : Locations and orientations of the samples taken axially and radially from the starting as-cast ingots.

The cylindrical Ø 60×60 mm samples were machined out from the 316L and 316Nb VIM/VAR processed ingots. Their axes were taken either parallel or perpendicular to the axis of the ingot to study the influence of the upsetting direction with respect to the as-cast ingot orientation, i.e., replicating the direction of deformation during cogging operation which is parallel and perpendicular to the ingot axis (see Figure 3.13). These samples are respectively described as "axial" and "radial" samples hereafter. The 1:1 height to diameter ratio of the samples was taken to minimise temperature gradient prior to the upsetting tests, and to obtain samples with the same dimensions regardless their orientations in the ingot, aiding comparisons between axial and radial directions. The samples were initially heated to 1250 °C gradually (see Figure 3.12) and homogenised for 11 h to replicate the heating stage involved in the industrial forging process. A refractory coating, acting as a thermal insulation and protecting the samples from oxidation, was applied on the surfaces of the samples prior to heating. The experimental plan developed to conduct these works are summarised in Table 3.3. Table 3.4 summarises the number of grains from the transverse cross-sections of axial and radial samples based on the average grain thicknesses measured on as-cast and homogenised material (see Figure 3.11). Note that the grains were oriented at 60° and 30° to the axes of the samples, i.e., axial and radial samples, respectively.

Table 3.3 : Material and the forming parameters investigated during the hot upsetting tests.

	Parameters	No. of levels	Investigated condition
Material parameters	Orientation within the ingot	2	Axial ; Radial
	Grade composition	2	316L ; 316Nb
Forming parameters	Heating temperature	1	1250 °C
	Heating stage	1	Including a homogenisation heat treatment
	Forging equipment	2	Hydraulic press ($\dot{\varepsilon}_{\mathrm{macro}} \approx 0.1\ \mathrm{s}^{-1}$) Screw press ($\dot{\varepsilon}_{\mathrm{macro}} \approx 7\ \mathrm{s}^{-1}$)
	Upsetting ratio	1	30 %
	Thermal condition	1	Non-isothermal

Table 3.4 : Evaluated number of grains from the transverse cross-sections of the Ø 60×60 mm samples used for the upsetting tests (i.e., reduced to 30% in height).

Sample orientation	Grade	Angle between the long axes of the grain and the upsetting direction (°)	Estimated number of grains on the transverse cross-section of the sample
Axial	316L	60	11 250
	316Nb	60	45 000
Radial	316L	30	6 500
	316Nb	30	26 000

The hot upsetting tests were performed using two different presses to investigate the material behaviour under different strain rates. A 500 tonnes capacity hydraulic press (see Figure 3.14), controlled with a constant strain rate of 0.1 s^{-1}, and a screw press (see Figure 3.15) with 28.9 kJ capacity at its maximum ram speed of 680 $mm.s^{-1}$ were used. Using the screw press characteristics and Equation (3.1), the equivalent mass of the screw press was calculated to be 125 tonnes (i.e., 125 000 kg). 50% of the available energy of the screw press, corresponding to a ram speed of 480 $mm.s^{-1}$ on impact with the samples, was used for the experiments when using the screw press. The height of the samples at the end of the upsetting (at ≈ 1250 °C) was set to 42 mm (i.e., ≈ 30 % reduction in height) using a set of calibration gauges placed on the tooling set. The tests were performed using flat dies heated to 400 °C lubricated using a water and graphite slurry, which was applied on upper and lower dies using a paintbrush prior to each upsetting. Following the upsetting, the samples were transferred and placed on a refractory brick for slow air cooling.

$$E = \frac{1}{2} M_{eq} V^2 \tag{3.1}$$

Where E is the energy of the press (J), M_{eq} is the equivalent mass characteristic of the press (kg) and V is the speed of the forging die ($m.s^{-1}$).

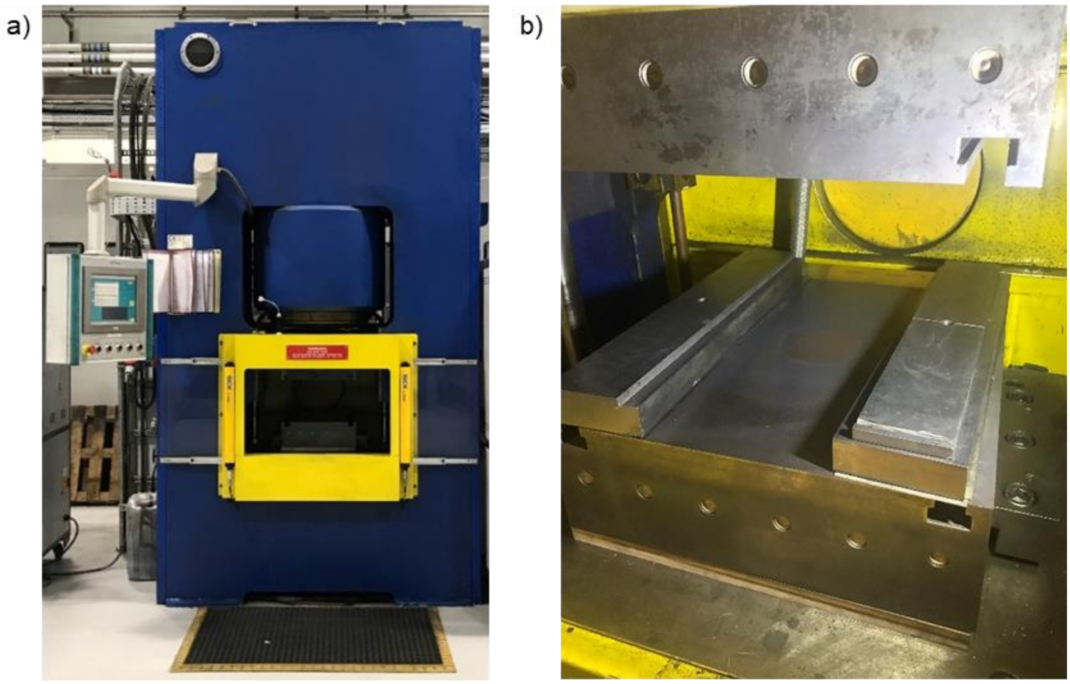

Figure 3.14 : a) The 500 tonnes hydraulic press, and b) the associated tooling set used for the hot upsetting tests using this press.

The load and position data, recorded by the embedded sensors and program of the presses, were used to analyse the forging conditions applied during the experiments. For instance, the data obtained from the screw press were used to evaluate different levels of energy delivered to the samples (see Figure 3.17). As can be seen in Figure 3.16, these data also allowed to point out the similarities and differences between both presses. In both cases, the ram speed gradually decreased during upsetting. However, on the hydraulic press, which was operated under constant strain-rate control at 0.1 s^{-1}, the ram speed progressively reduced to 4.3 $mm.s^{-1}$ by the end of the test. In contrast, the screw press was characterised by an impact-type loading mode, with the ram motion decelerating more abruptly until reaching a final speed of 0 $mm.s^{-1}$ at the end of the stroke.

Figure 3.15 : a) The Lasco® SPR 400 screw press (28.9 kJ at 680 $mm.s^{-1}$), and b) the associated tooling sets used for the upsetting tests conducted using this press.

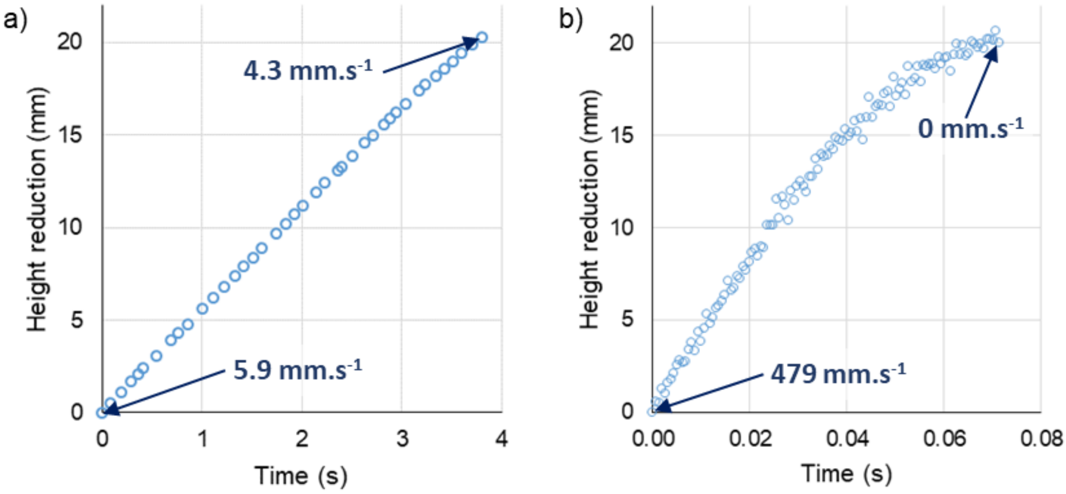

Figure 3.16 : Plots of height reduction vs. time recorded by the presses for the upsetting of the axial 316Nb samples forged by a) hydraulic, and b) screw presses, respectively. The ram speed is indicated in both case at the beginning and end of the stroke.

The transfer and hold/dwell durations before forging were measured using video recording of the experiments and are presented in Figure 3.18. A 3D optical scanner, GOM ATOS®, was used to capture 3D shape (see Figure 3.19) of the samples after forging and cooling, to evaluate accurately their dimensions. Traceability of sample locations and orientations in the initial ingots were achieved by marking a notch on the edge of the samples, highlighted with dashed circles in Figure 3.19, and the direction of the "top" and "core" of the ingot are indicated with "T" and "C". These are shown on the geometries and micrographs presented in this thesis hereafter. The results of height measurements performed on the forged samples are summarised in Figure 3.20, with the calculated height at 1250 °C, i.e., considering thermal expansion, also provided. The upsetting tests were not limited to the press capacity (i.e., load or energy) as all samples were smaller than expected after upsetting (i.e., 42 mm at 1250 °C), owing to the calibration gauges used during forging.

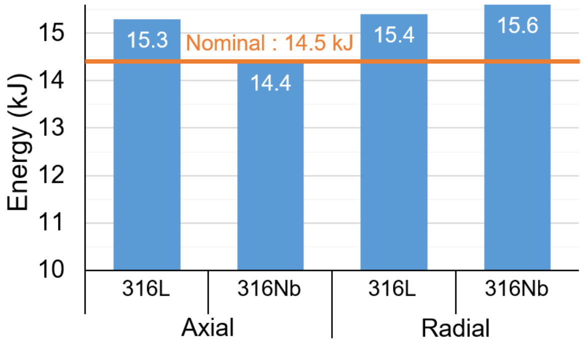

Figure 3.17 : Measurements of the screw press energy at the point of impact with the samples.

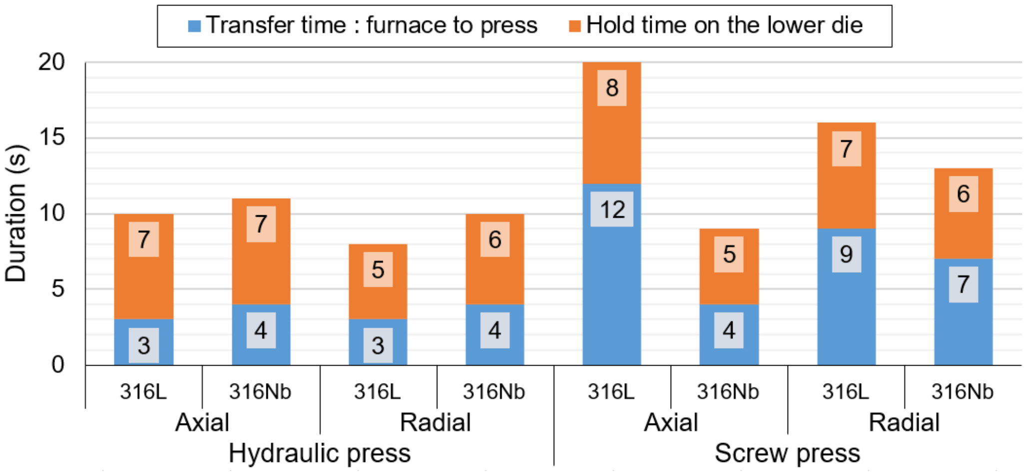

Figure 3.18 : Transfer and hold/dwell times measured using the video records of the experiments.

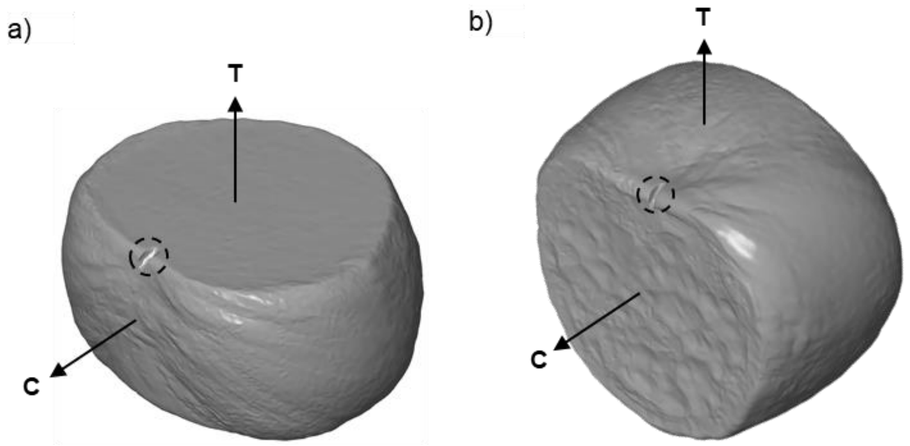

Figure 3.19 : 3D models obtained by GOM ATOS® of the a) axial, and b) radial 316Nb samples forged by hydraulic press. The notches highlighted with the dashed circles were used for the traceability of the initial orientation of the as-cast ingot, and the orientation of the samples within the initial as-cast ingot are indicated by the directions of "core" (C) and "top" (T).

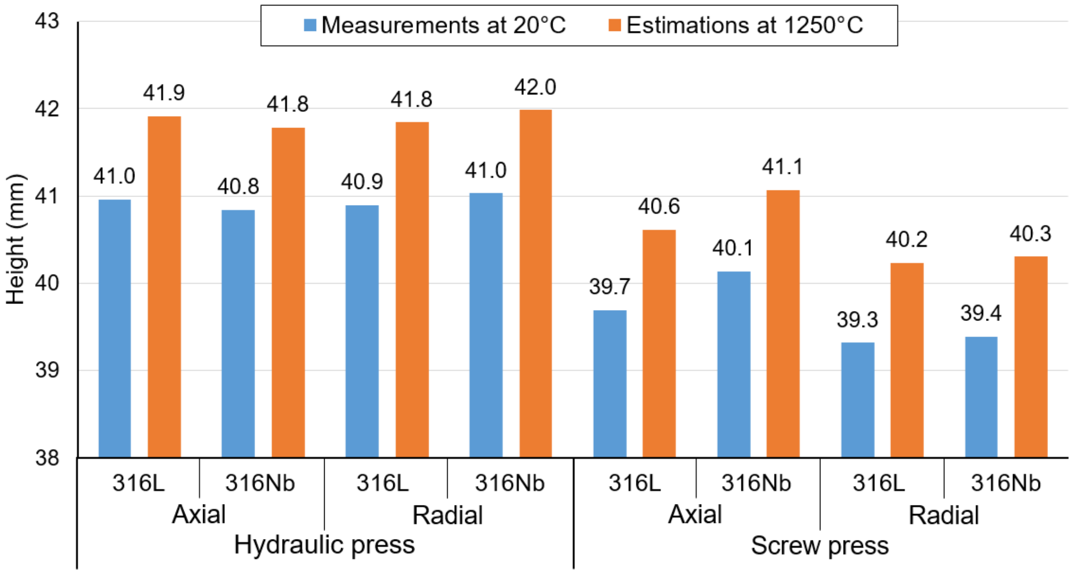

Figure 3.20 : Heights of the samples after 30% upsetting at 1250 °C. The measurements at 20 °C were performed on the 3D models of the samples obtained by GOM ATOS®, and were then used to evaluate the likely height at 1250 °C using the thermal expansion coefficient.

The load and die position data recorded by the presses were used to compare the deformation behaviours of the samples. The load and position records were individually fitted with a 6-order polynomial function, except for the records of position for the hydraulic press (i.e., fitted with linear curve). An example of experimental load and position records obtained for the 316L axial samples as a function of time are presented in Figure 3.21 with their corresponding fits. The plots of load-position are presented in Figure 3.22.

The stress-strain curves for the samples were determined from the small-scale upsetting trials. The measured flow stress (i.e., σ_{exp}) and strain (i.e., ε) were calculated for each deformation increment using Equations (3.2) and (3.3). Note that Equation (3.2) assumes that a sample is deformed without barrelling and keeps its cylindrical shape throughout upsetting. The methodology developed by (Evans and Scharning, 2001) and (Gholamzadeh and Karimi Taheri, 2009) was used to convert the load-position records into stress-strain curves, and the corrected stress (i.e., σ) was calculated using Equation (3.4) to account for the effect of friction. The friction factor (i.e., m) was determined for each test with Equation (3.5) based on the methodology of (Ebrahimi and Najafizadeh, 2004), which involves the determination of the barrelling parameter (i.e., b, see Equation (3.6)) as a function of measurements performed on the sample after the test. To account for the specific deformed geometry of the small-scale samples, the radius R_M and R_T were determined from the best fit circles (see the green arrows in Figure 3.23) to the cross-sections positioned at the vicinity of their upper and lower surfaces, as well as at a mid-height plane (see the orange arrows in Figure 3.23), respectively. As an example, the stress-strain plots of the 316L axial samples (i.e., derived from the load-position plots of Figure 3.21) are presented in Figure 3.24.

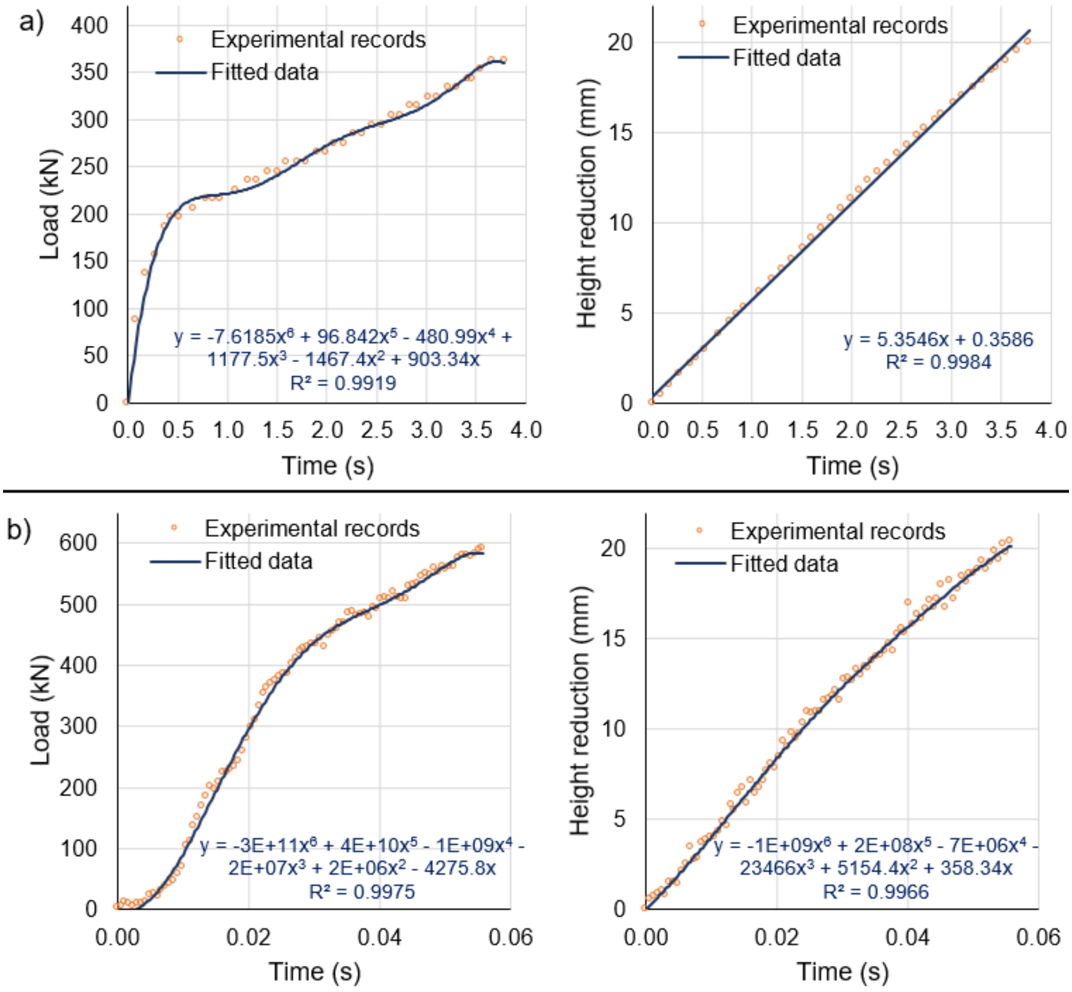

Figure 3.21 : Plots of load and die position data recorded by the presses, with fitted curves, for the upsetting of the axial 316L samples forged by a) hydraulic, and b) screw presses, respectively.

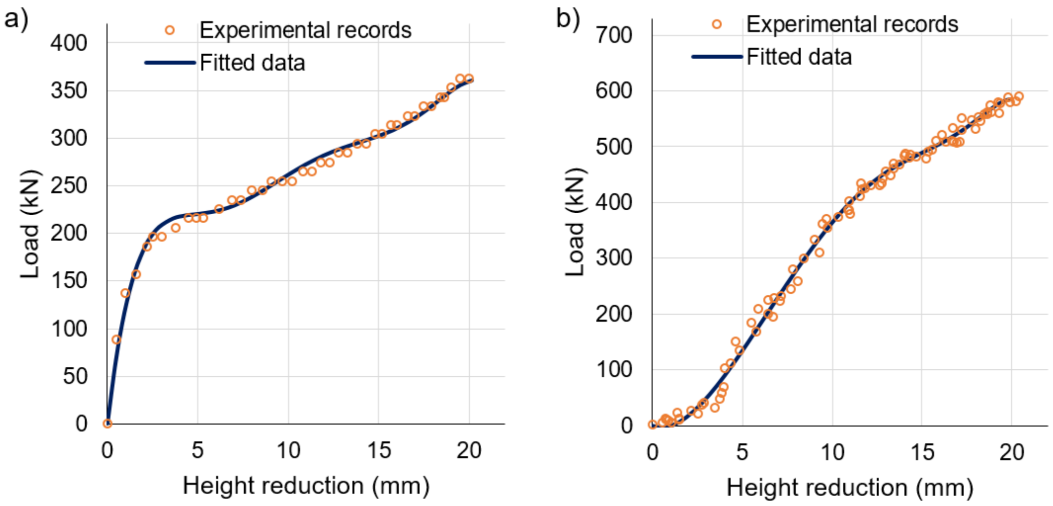

Figure 3.22 : Plots of load vs. die position data recorded by the presses, with their associated fitted curves for the upsetting of the axial 316L samples forged by a) hydraulic, and b) screw presses, respectively.

$$\sigma_{\text{exp}} = \frac{F\,h}{\pi\, r_0^2 h_0} \tag{3.2}$$

where F is the recorded compression load, h_0 and h are the initial and recorded height of the sample, respectively, and r_0 is its initial radius.

$$\varepsilon = \ln\left(\frac{h_0}{h}\right) \tag{3.3}$$

$$\sigma = \frac{\sigma_{\text{exp}}}{1 + \frac{2}{3\sqrt{3}} m \frac{r_0}{h_0} exp\left(\frac{3\varepsilon}{2}\right)} \tag{3.4}$$

where σ_0 and ε are the measured flow stress and strain, respectively, m is the friction factor, r_0 is the initial radius of the sample, and h_0 is the initial height.

$$m = \frac{\frac{R}{h} \times \mathrm{b}}{\frac{4}{\sqrt{3}} - \frac{2\mathrm{b}}{3\sqrt{3}}} \tag{3.5}$$

where b is the barrelling parameter, R and h are the average radius (see Equation (3.7)) and height of sample after deformation, respectively.

$$\mathrm{b} = 4 \cdot \frac{\mathrm{R_M} - \mathrm{R_T}}{\mathrm{R}} \cdot \frac{\mathrm{h}}{\mathrm{h_0} - \mathrm{h}} \tag{3.6}$$

where $\mathrm{R_M}$ is the radius of the best-fit circle to the transverse cross-section of the sample, and $\mathrm{R_T}$ is the average radius of best-fit circles positioned at the vicinity of upper and lower surfaces of the sample (see Figure 3.23).

$$R = r_0\sqrt{\frac{h_0}{h}} \tag{3.7}$$

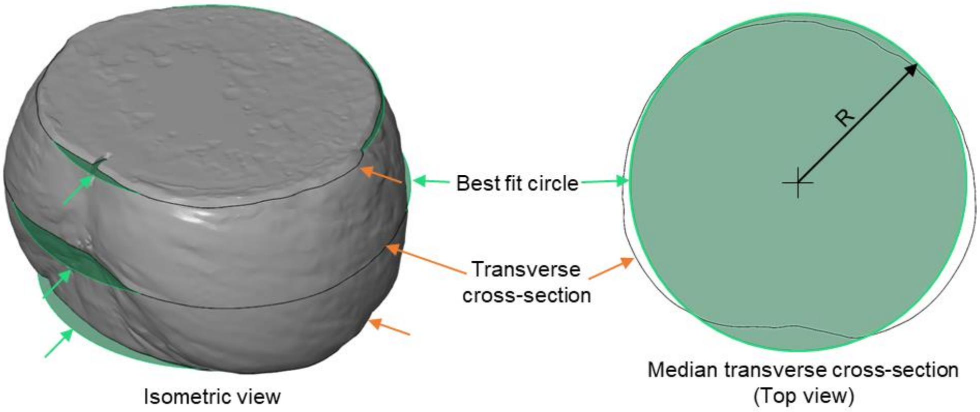

Figure 3.23 : The methodology followed to evaluate the radius R_M and R_T of the samples following upsetting to 30% in height. The orange arrows indicate the position of the cross-sections considered for the determination of the best-fit circles, which are indicated by the green arrows. Example provided for the 316L axial sample deformed by the hydraulic press.

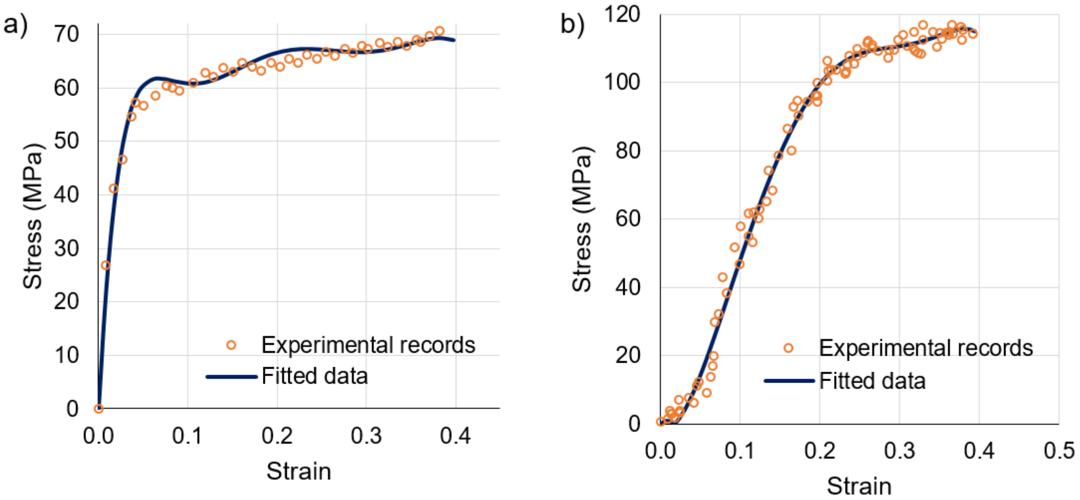

Figure 3.24 : Stress-strain plots derived from the load-position records of the upsetting of the axial 316L samples using a) the hydraulic, and b) the screw presses, respectively.

3.2.2.2 Forging trials on entire ingots

Upsetting and cogging experiments were conducted on VIM/VAR processed ingots with different Niobium composition to investigate the evolution of the as-cast microstructure during the ingot-to-billet conversion process. The experiments were performed using hydraulic and screw presses for upsetting and cogging experiments, respectively. The upsetting was performed using the 2 500 tonnes capacity hydraulic press available at Aubert & Duval's plant in Les Ancizes, France, and in laboratory condition, using the 28.9 kJ capacity screw press at Arts et Métiers in Metz, France. The general experimental process involved for the upsetting and cogging tests on the entire ingots is presented in Figure 3.25 and example of ingots after upsetting and cogging are presented in Figure 3.26.

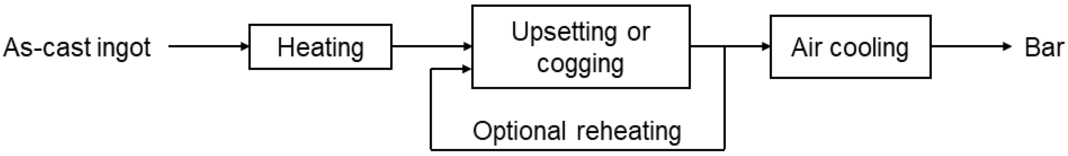

Figure 3.25 : Experimental process of the upsetting and cogging experiments performed on intermediate industrial scale ingots.

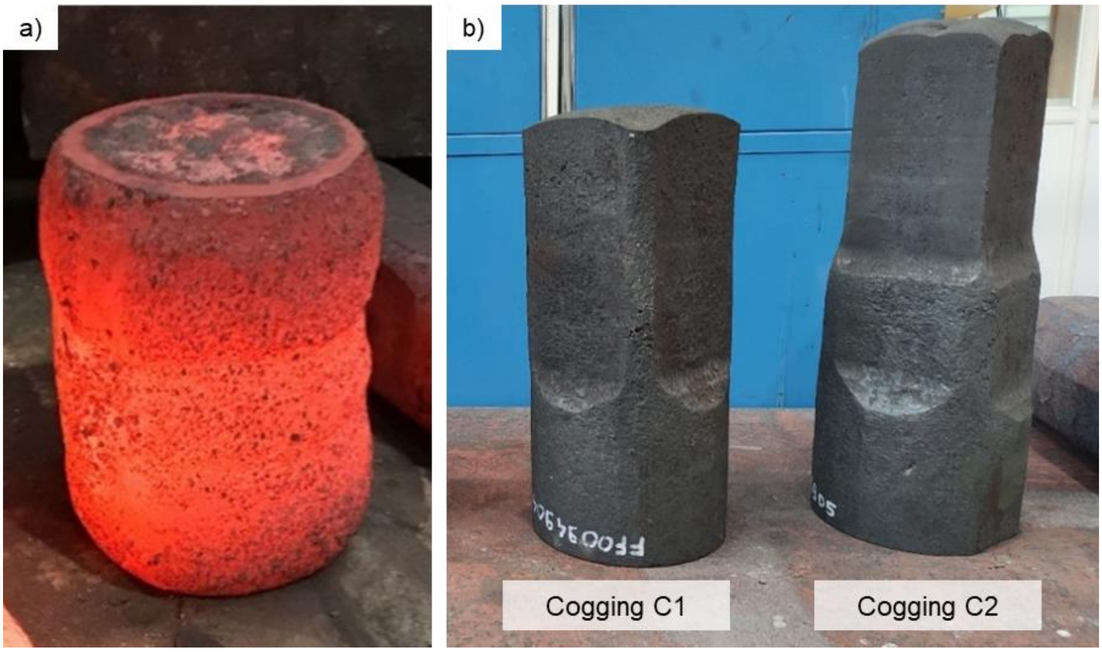

Figure 3.26 : Photographs showing the ingots after the a) 40% upsetting, and b) 1st (C1) and 2nd (C2) cogging.

The ingots were heated to 1250 °C using the same cycle as that used for the small scale Ø 60×60 mm samples (see Figure 3.12), including a progressive temperature raise to prevent the risk of hot tapping and followed by a homogenisation heat treatment. Prior to heating, a refractory coating acting as thermal insulation was applied on the surface of the ingots dedicated to cogging to limit the heat losses within the ingots during the incremental cogging operations. The forging route designed to study the evolution of the as-cast microstructure during the ingot-to-billet conversion process consists of one upsetting to a 40% reduction in height, and cogging to 33% and 50% section reduction ratios (k_s), including an intermediate reheating. The dimension of the starting ingots are provided in Table 3.5, and the geometry of the ingots after forging are provided in Figure 3.27.

Table 3.5 : Summary of the forging experiments performed on the intermediate scale industrial ingots.

Forging press	Forging route	Grade	Dimension of the ingot (mm)	
			At 20 °C	At 1250 °C
Hydraulic press	Upsetting : 40% height reduction	316Nb	Ø 185×520	Ø 189×532
Screw press	Cogging C1 : $k_s \approx 33\%$	316L	Ø 186×340	Ø 190×348
		316Nb	Ø 186×344	Ø 190×352
	Cogging C2 : $k_s \approx 33\%$ and 50% Including an intermediate reheating	316L	Ø 186×345	Ø 190×353
		316Nb	Ø 185×340	Ø 189×348

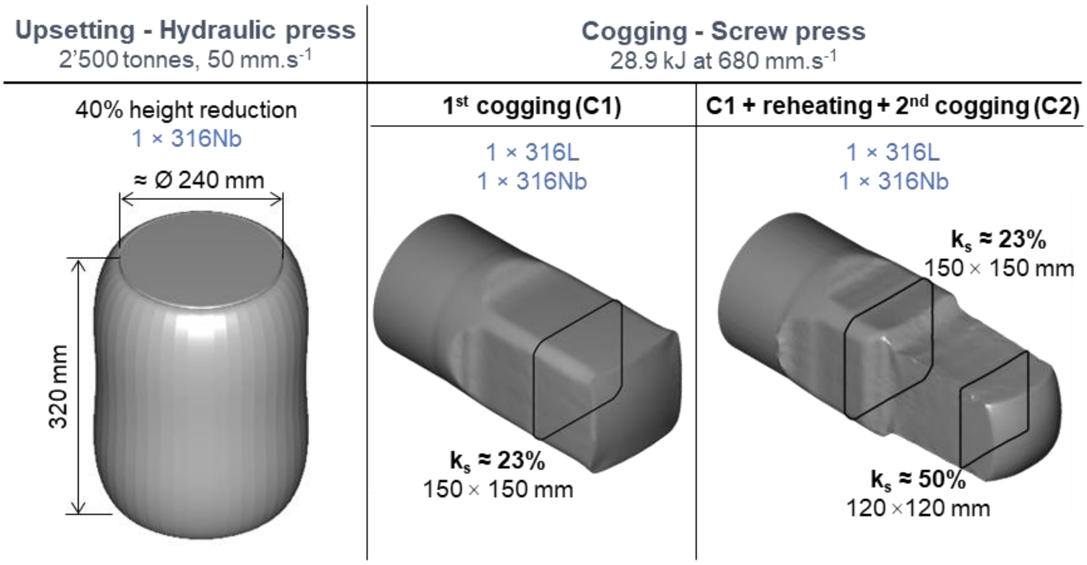

Figure 3.27 : Summary of upsetting and cogging tests performed on the 5 available ingots made of 316L and 316Nb grade of material. k_s denotes the section reduction ratio reached after cogging.

The upsetting test was performed on a 316Nb ingot in one operation to a 40% upsetting ratio with a ram speed of 50 mm.s^{-1}. The ingot was handled using a wheel-mounted manipulator for the transfer from the furnace to the press (see Figure 3.28 a)), which lasted around 60 seconds. The non-lubricated dies used for forging were composed of a 300 mm width flat forging surface (see Figure 3.28 b)), and were heated up to ≈ 300 °C prior upsetting using gas burners. The bottom of the ingot was placed on the lower anvil.

The cogging experiments were carried out using a Lasco® SPR-400 screw press, which was also used for the small upsetting tests (see Figure 3.15 a)). The press was coupled with a 6-axis robot, on which a manipulator was mounted to handle the ingots during the forging operations (see Figure 3.29). To account with the load capacities of the manipulator, the ingots dedicated to cogging were cut to reduce their weight to 75 kg, and the 150 mm zone held by the gripper was not forged (see Figure 3.26 b)). To avoid the enlargement of the bar at its extremities and calibrate the dimensions of the forged product, several passes were repeated at the end of each section reduction step. The non-lubricated dies used for forging were composed of a 160 mm width flat forging surface and two 30 mm radius on each side. The dies were heated up to 450 °C prior forging using the embedded heating cartridges. The length of the ingots were measured at the end of each pass using the back-door safety light curtain of the press so that their position was correctly adjusted during the cogging experiments.

The designed forging routes used for the cogging experiment are schematically illustrated in Figure 3.30. The cogging schedule "C1" aimed to reduce the section of both 316L and 316Nb grades ingots to a 145×145 mm square ($k_s \approx 23\%$), with intermediate passes forming 170×170 mm ($k_s \approx 0\%$) and 160×160 mm ($k_s \approx 13\%$) square sections, see Table 3.6. The cogging schedule "C2" aimed to continue C1 cogging schedule on both grade ingots with an intermediate reheating (90 minutes, 1250 °C) followed by a subsequent cogging along the half length of the partially-forged ingot. This was designed to evaluate the effects of both intermediate reheating and subsequent forging on the microstructure obtained after the first forging route. The section of the partially-forged half-length of the ingots were finally reduced to a 120×120 mm square ($k_s \approx 50\%$), with an intermediate pass forming a 135×135 mm square ($k_s \approx 38\%$), see Table 2.6. In order to account for the effects of the orientation of the directionally solidified microstructure of the ingots, the bottom of the ingots were placed on the lower die during upsetting, and in the manipulator during cogging. However, the 316Nb ingot forged with C1 was mistakenly forged in reverse direction.

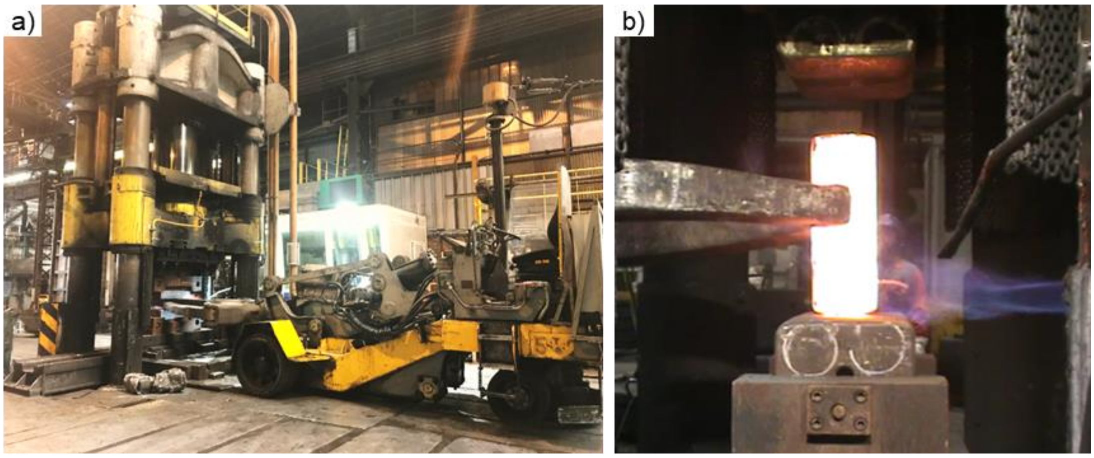

Figure 3.28 : Photographs showing the a) 2500 tonnes hydraulic press and wheel-mounted manipulator used for the 40% upsetting, and b) the ingot placed between the anvils at the beginning of the upsetting.

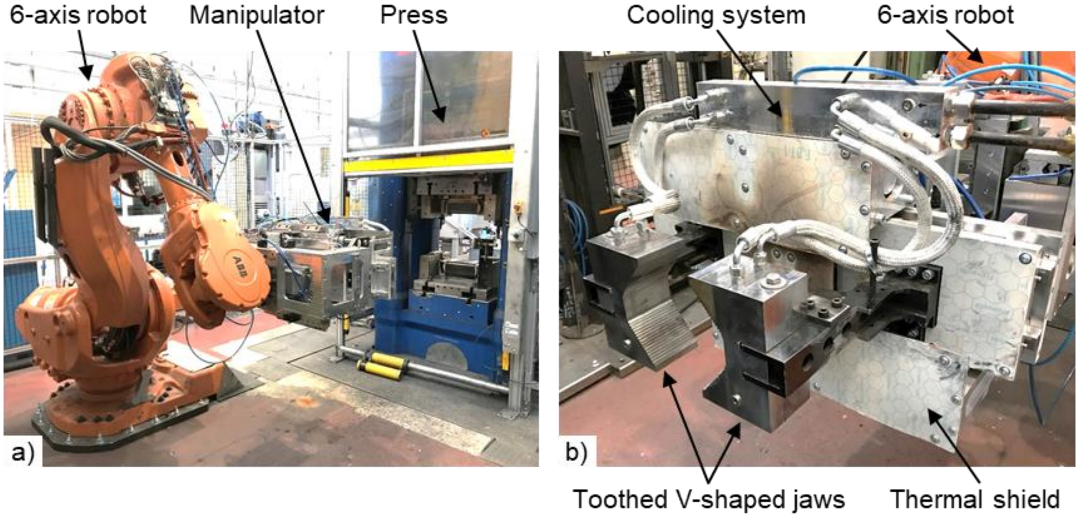

Figure 3.29 : Setup used for cogging operation in laboratory conditions. a) Overview of the experimental setup, and b) detail of the tailor-made manipulator used to handle the ingots during the forging experiments.

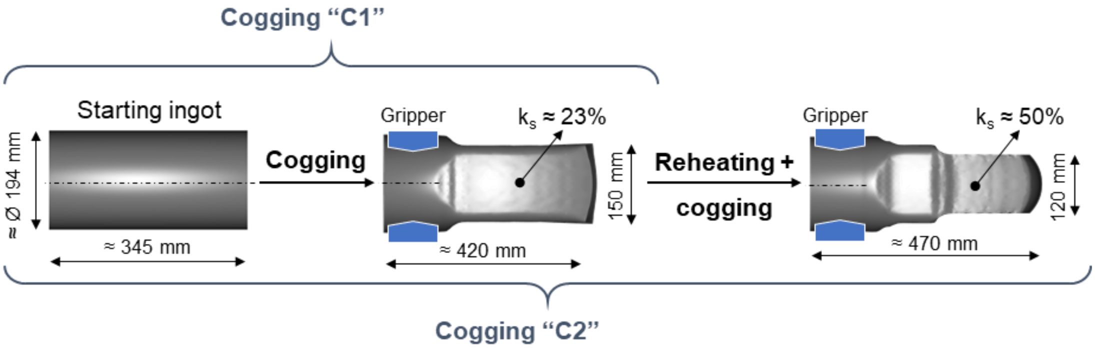

Figure 3.30 : Schematic illustration of the cogging experiments designed for the study of the as-cast material evolution during cogging. "K_s" denotes the section reduction ratio reached at the end of each cogging sequence.

Table 3.6 : Processing parameters of C1 cogging schedules.

Step of section reduction	Section dimension mm	k_s %	No. of passes -	Initial feed mm	Following feed* mm
1	170×170	≈ 0	2	110	60
2	160×160	≈ 13	2	80	30
Final	150×150	≈ 23	316L : 3 316Nb : 4	80	30

* : The last feed of each pass was adjusted by the control unit of the manipulator to forge the maximal length of the bar.

Table 3.7 : Processing parameters of C2 cogging schedules.

Step of section reduction	Section dimension mm	k_s %	No. of passes -	Initial feed mm	Following feed* mm
1	170×170	≈ 0	2	110	60
2	160×160	≈ 13	2	80	30
3	150×150	≈ 23	316L : 3 316Nb : 2	80	30
Reheating : 90 minutes at 1250 °C					
4	135×135	≈ 37	2 (half length)	60	30
Final	120×120	≈ 50	4 (half length)	60	30

* : The last feed of each pass was adjusted by the control unit of the manipulator to forge the maximal length of the bar.

After cogging and cooling to room temperature, the ingots were scanned after cooling by an GOM ATOS® system (see Figure 3.31 a)) to generate a 3D model of each bar, which were compared in a subsequent step to the FE predicted geometry of the ingots to evaluate their representativeness. As example, the 3D model of the 316L ingot after the 1st cogging route is presented in Figure 3.31 b).

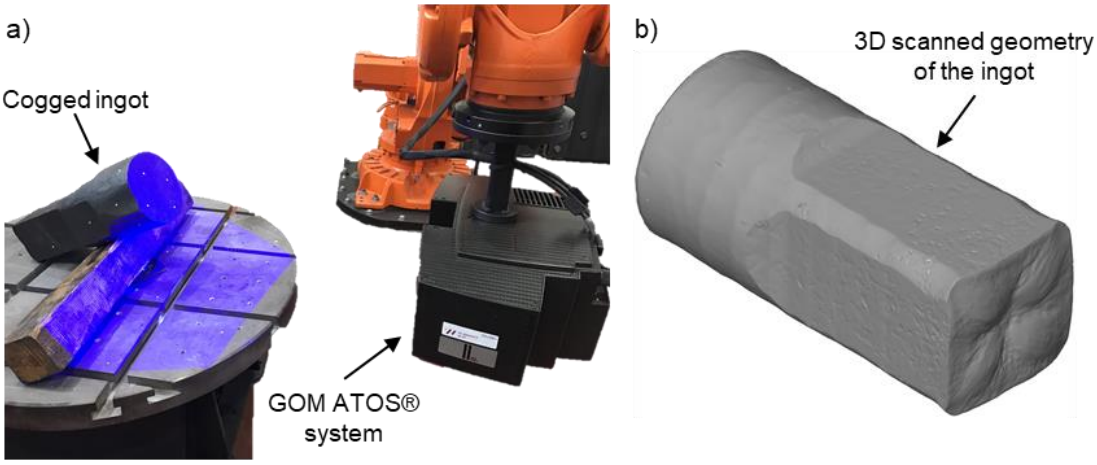

Figure 3.31 : a) Scan operation using a GOM ATOS® system, and b) resulting scanned geometry, of the 316L ingot after the C1 cogging schedule.

The data involved in the cogging sequences, such as the time-position records of the upper ram of the press were recorded by the program controlling the robot and the press during the experiments. Figure 3.32 displays the experimental time records of the forging operations performed on the 316L ingot during the cogging C1, where the strokes highlighted by the green rectangles were achieved after several hits from the press, as a consequence of its energy limitation. Different number of passes and strokes were involved for each case (i.e., for both grades and cogging schedules, see Figure 3.32, Table 3.6 and Table 2.6) owing to the manual definition of the energy instruction set into the screw press, which was required to avoid overpassing the maximal load allowed by the press, of 400 tonnes. The energy instructions given to the press during the cogging operation of that same ingot are presented in Figure 3.33, with the calculated energies that were actually delivered by the press, at each hit. It can be seen that the available forging energy was limited at ≈ 20 kJ as a consequence of the limited travel distance required for the upper ram to reach the target travel speed prior the impact with the ingot. Conversely, the press delivered more energy than required for energy instructions below ≈ 20 kJ as a consequence of the inaccurate in-line prediction of the position of the ingot between the dies. The time and energy records of all cogging experiments are summarised in Appendix A, and showed similar observations.

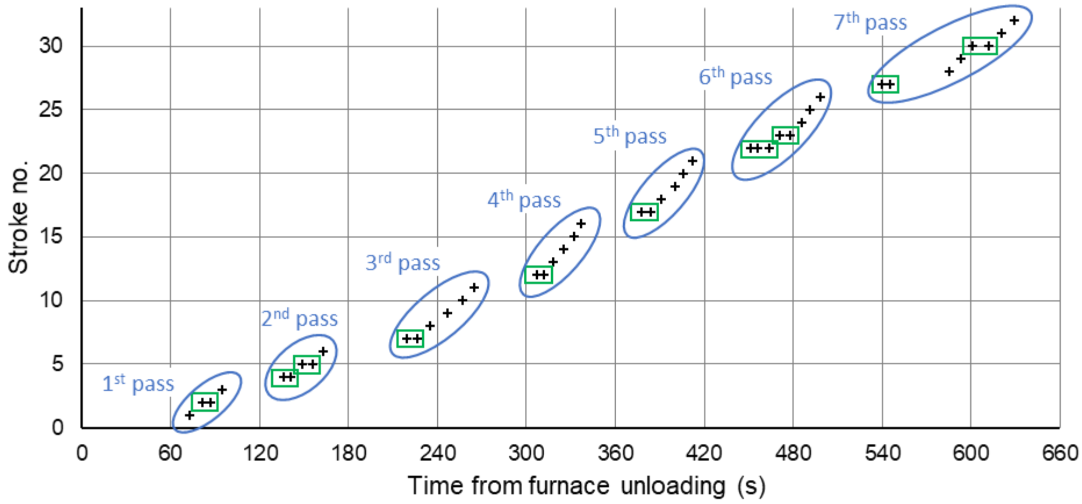

Figure 3.32 : Experimental time records of the forging operations performed on the 316L ingot during C1 cogging schedule; with the different passes highlighted by the blue circles, and the strokes achieved after several hits by the green rectangles.

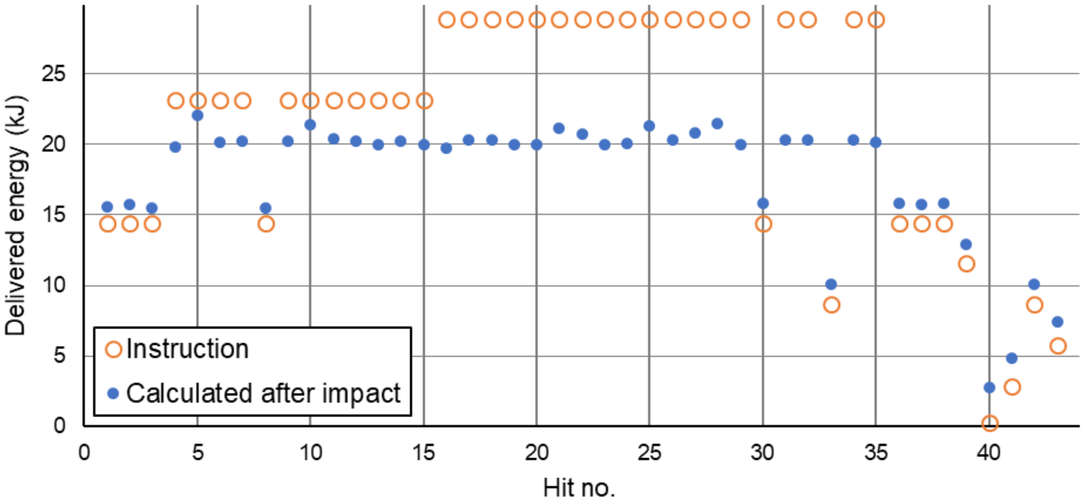

Figure 3.33 : Plots of the energy instructions and post-forging calculations for the 316L ingot during C1 cogging schedule. The calculated values were calculated using the speed records of the press, at the impact with the ingot.

The macroscopic average strain rate applied by the press on the ingots was calculated as the ratio between the average speed of the upper die during the deformation, and the height of material being forged (i.e., the vertical dimensions of the ingot's section between the dies). The histogram plot of the macroscopic strain rate calculated for all cogging experiments is displayed in Figure 3.34, and shows that most of the hits were applied with a macroscopic strain rate between 1 and 2 s^{-1}. These relatively low values, in comparison to the average ram speed of ≈ 530 $mm.s^{-1}$ used for cogging, represents an average strain rate applied by the press across the whole section of the material being deformed. Local strain rate values may significantly exceed these averaged values and will be estimated by means of Finite Element simulation of the experiments.

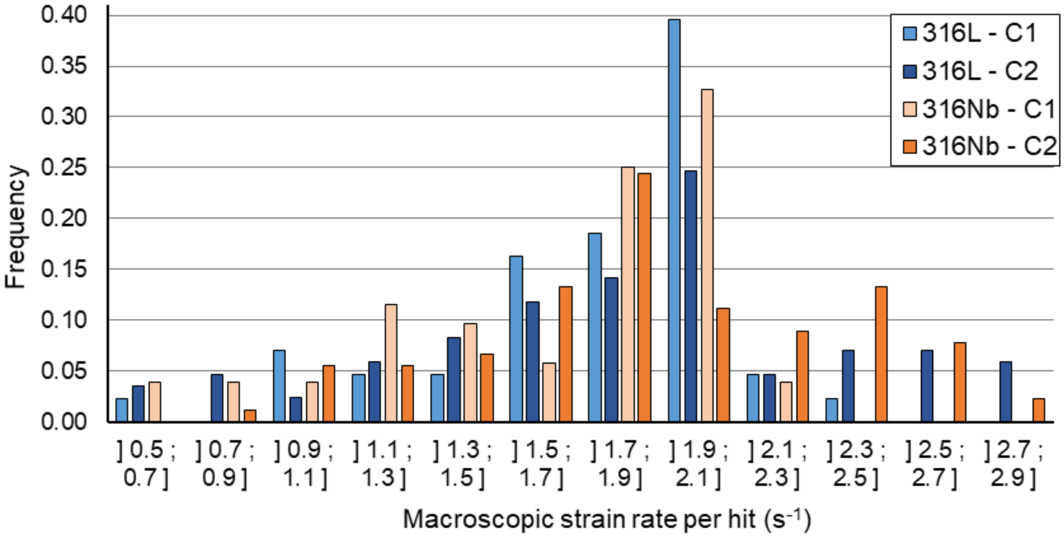

Figure 3.34 : Histogram plot of the calculated macroscopic strain rate applied by the press during the cogging experiments.

3.3 FINITE ELEMENT MODELLING

Finite Element (FE) method models of the experiments were developed using the commercial software FORGE NxT 3.0® by Transvalor® to estimate the evolution of temperature, strain and strain rate within the forged samples and ingots throughout the experimental processes.

Material behaviours were modelled by the simplified Hensel-Spittel thermo-viscoplastic law (see Equation (3.8)) with the material properties data for 316L and 316Nb alloys taken from the FORGE® database (see Table 3.8).

$$\sigma = \mathrm{A} \cdot e^{m_1 T} \cdot \varepsilon^{m_2} \cdot \dot{\varepsilon}^{m_3} \cdot e^{\frac{m_4}{\varepsilon}} \tag{3.8}$$

Table 3.8 : Material parameters used in the simplified Hensel-Spittel equation taken from the FORGE® database for 316L and 316Nb alloys.

Parameter	A	m1	m2	m3	m4
316L	8905.3400	- 0.00383	0.012460	0.09912	- 0.02413
316Nb	4660.0156	- 0.00311	- 0.09996	0.09794	- 0.06481

Following the work presented in (Terhaar et al., 2012), an orthotropic anisotropic material behaviour was considered for the as-cast materials, and the orthotropic Hill-48 yield criterion (Hill and Orowan, 1948) was implemented in the FE models. The Hill criterion is expressed in the anisotropic frame described hereafter, in which the surface equation is given by Equation (3.9). The values of the Hill parameters can be expressed as a function of the material behaviour ratios in axial and transverse directions using Equation (3.10) and Equation (3.11), and are usually obtained experimentally from stress-strain data of representative compression, tensile and shear tests performed in the directions of the anisotropic frame (Hill and Orowan, 1948). As can be seen from Figure 3.5, the specific orientation and symmetry of the as-cast microstructure investigated in this work impedes however to extract representative specimens from the as-cast ingots and therefore perform such tests. In the present case, the values of the Hill parameters were obtained by “trial and error” optimisation, allowing the best fit between the experimental and predicted deformed geometries of the Ø 60×60 mm samples. The optimised values of the Hill parameters are summarised in Table 3.9.

As required by FORGE® software to handle material properties data, *.tmf files were generated for each grade, and included the parameters of the simplified Hensel-Spittel equation (see Table 3.8) as well as the optimised values of the Hill parameters (see Table 3.9). The temperature dependence of several key material properties were also incorporated in both *.tmf material files using a point-by-point (i.e., tabulated) description. These properties include Young’s modulus, Poisson’s ratio, density, specific heat capacity, thermal conductivity, and the coefficient of thermal expansion. The data for these parameters were provided by Aubert & Duval and are not disclosed in this thesis due to confidentiality agreements. Figure 3.35 provides an overview of the structure of the *.tmf material file implemented in the FE models.

$$\begin{aligned}\sigma_0{}^2 = F\cdot(\sigma_{22}-\sigma_{33})^2 + G\cdot(\sigma_{11}-\sigma_{33})^2 + H\cdot(\sigma_{11}-\ \sigma_{22})^2 \\ + 2L\cdot\sigma_{23}{}^2 + 2M\cdot\sigma_{13}{}^2 + 2N\cdot\sigma_{12}{}^2\end{aligned} \tag{3.9}$$

Where F, G, H, L, M and N are the Hill parameters.

$$f_{ij} = \frac{\sigma_{11}}{\sigma_{ij}} \tag{3.10}$$

Where σ_{11} is the yield stress measured in the main anisotropy direction, and σ_{ij} the yield stress measured in other directions.

$$\begin{aligned} F &= \frac{\sigma_0}{2}\times\left(\frac{1}{\sigma_{22}{}^2}+\frac{1}{\sigma_{33}{}^2}-\frac{1}{\sigma_{11}{}^2}\right) & L &= \frac{3}{2}\times\frac{\sigma_0^2}{\sigma_{23}{}^2} \\ G &= \frac{\sigma_0}{2}\times\left(\frac{1}{\sigma_{11}{}^2}+\frac{1}{\sigma_{33}{}^2}-\frac{1}{\sigma_{22}{}^2}\right) & M &= \frac{3}{2}\times\frac{\sigma_0^2}{\sigma_{13}{}^2} \\ H &= \frac{\sigma_0}{2}\times\left(\frac{1}{\sigma_{11}{}^2}+\frac{1}{\sigma_{22}{}^2}-\frac{1}{\sigma_{33}{}^2}\right) & N &= \frac{3}{2}\times\frac{\sigma_0^2}{\sigma_{12}{}^2} \end{aligned} \tag{3.11}$$

Where σ_0 is the reference yield stress and σ_{ij} are the yield stresses in the i and j directions.

Table 3.9 : The optimised Hill parameters values obtained via best-fit approach.

Parameter	F	G	H	L	M	N
Isotropic case	0.5	0.5	0.5	1.5	1.5	1.5
Anisotropic case	0.5	0.5	0.5	0.68	0.68	1.5

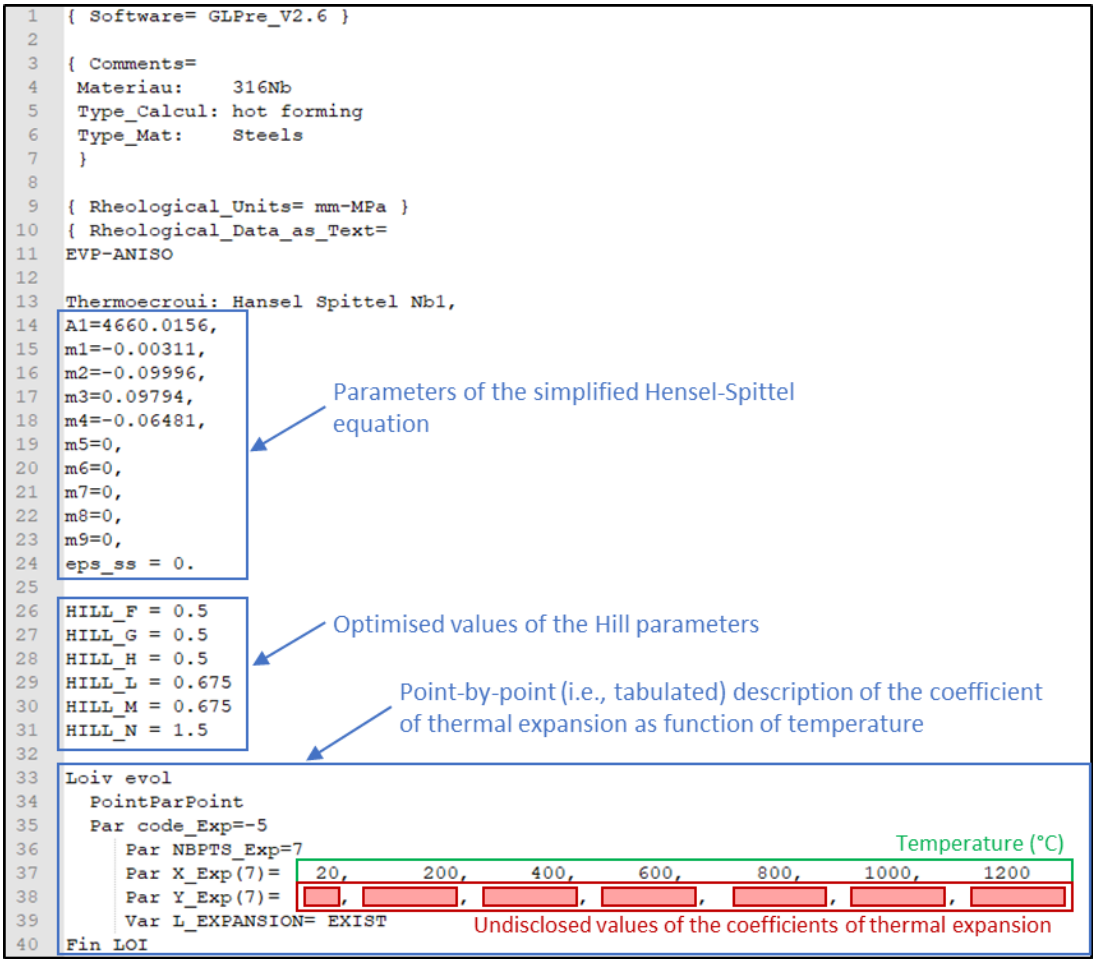

```
{ Software= GLPre_V2.6 }

{ Comments=
 Materiau:    316Nb
 Type_Calcul: hot forming
 Type_Mat:    Steels
 }

{ Rheological_Units= mm-MPa }
{ Rheological_Data_as_Text=
EVP-ANISO

Thermoecroui: Hansel Spittel Nb1,
A1=4660.0156,
m1=-0.00311,
m2=-0.09996,
m3=0.09794,
m4=-0.06481,
m5=0,
m6=0,
m7=0,
m8=0,
m9=0,
eps_ss = 0.

HILL_F = 0.5
HILL_G = 0.5
HILL_H = 0.5
HILL_L = 0.675
HILL_M = 0.675
HILL_N = 1.5

Loiv evol
  PointParPoint
  Par code_Exp=-5
     Par NBPTS_Exp=7
     Par X_Exp(7)=  20,     200,      400,      600,      800,     1000,     1200
     Par Y_Exp(7)=  [redacted], [redacted], [redacted], [redacted], [redacted], [redacted], [redacted]
     Var L_EXPANSION= EXIST
Fin LOI
```

Figure 3.35 : Annotated screenshot of the *.tmf material file used in FORGE® to implement the material properties of the 316Nb grade. The additional material parameters implemented are described in the same way, in the following lines of the *.tmf material file. Note that the values of the coefficients of thermal expansion are undisclosed for confidentiality reasons.

The anisotropic frame to be implemented for the as-cast material must match with the morphologic distribution of the microstructure, i.e., with a frame oriented at 60° to an axis of revolution located at the centre of the ingots. By default, FORGE® software features Cartesian or cylindrical implementations of anisotropic frames, which do not allow to describe the anisotropic configuration required to model the deformation behaviour of the as-cast material. A dedicated user-variable was hence developed on request by Transvalor® to account for the specificities of this work. Figure 3.36 illustrates the implementation of the anisotropic frame in FORGE® software for the axial Ø 60×60 mm sample subjected to 30% upsetting, and Figure 3.37 illustrates an overlap of the anisotropic frame with the as-cast microstructure. The anisotropic frame $(\overrightarrow{A1}, \overrightarrow{A2}, \overrightarrow{A3})$ was defined at each point of the ingot with $\overrightarrow{A3}$ set parallel to the long axes of the grains (i.e., at a 60° angle to the axis of the ingot), $\overrightarrow{A1}$ perpendicular to $\overrightarrow{A3}$ along the short axes of the grains, and $\overrightarrow{A2}$ orthogonal to both $\overrightarrow{A1}$ and $\overrightarrow{A3}$ directions. Note that the anisotropic frame displayed in Figure 3.36 is intentionally superposed to the reference frame of the FE model.

This idealised implementation of the anisotropic material behaviour does not account for local deviations of morphologic and crystallographic orientation of the as-cast microstructure. The anisotropic deformation behaviour of the as-cast material was implemented in the FE model of the ingots subjected to upsetting and cogging following the same methodology, with the revolution axis of the anisotropic frame matching with that of the ingot.

It can be seen from Table 3.9 that the value of two of the Hill parameters differ from the isotropic case when considering anisotropic behaviours. According to Equations (3.9) and (3.10), and within the reference frame demonstrated in Figure 3.37, this suggest that shearing was restricted in the planes perpendicular to the growth axis of the as-cast grains (i.e., normal to $\overrightarrow{A3}$). For simplification, the central section of the ingot with the long grains oriented parallel to the axis of the ingot was modelled with the same material behaviours as that for the rest of the ingot where the grains were oriented at 60° to the axis of the ingot.

The computation time required to run the FE model was optimised using geometrical symmetry for each type of the experiments, and the entire samples and ingots were reconstructed from the reduced shapes using the "mirroring" feature of FORGE® software. The plane of symmetry defined for each type of experiment accounts for the symmetric properties of the sample or ingot to be modelled, as well as for the distribution of the anisotropic frame implemented in the model (see Figure 3.37). As can be seen from Figure 3.38, half cylinders were used to model the small-scale samples dedicated to the upsetting tests, with the plane of symmetry of the half cylinders aligned with the longitudinal cross-section of the sample to account for the symmetry of the anisotropic frame. It is noteworthy to state that 2D simulations could not be applied in this scenario due to the misalignment of the axis of revolution of the anisotropic frame with that of the sample. The small-scale samples were meshed with tetrahedral elements of size ≈ 1.5 mm.

For the upsetting experiment conducted on the whole 316Nb ingot, the axis of the ingot matched that of the anisotropic frame, and 2D simulation could have been used. However, 2D simulation could not be handled via the user-variable developed by Transvalor® for the consideration of the anisotropic frame. Instead, the ingot was modelled using a 3D quarter cylinder with two orthogonal planes of symmetries (see Figure 3.39 a)).

A 3D quarter cylinder with two orthogonal planes of symmetries was also used to model the ingots during the cogging experiments (see Figure 3.39 b)), and the successive positions of the ingot during the first couple of passes are schematically shown in Figure 3.40 for clarity. The quarter ingot is rotated between each pass according to the cogging route, and only one anvil is modelled in the FE model as the median plane between the anvils corresponds to a plane of symmetry of the simulation. The ingots were meshed with tetrahedral elements of size ≈ 6.5 mm.

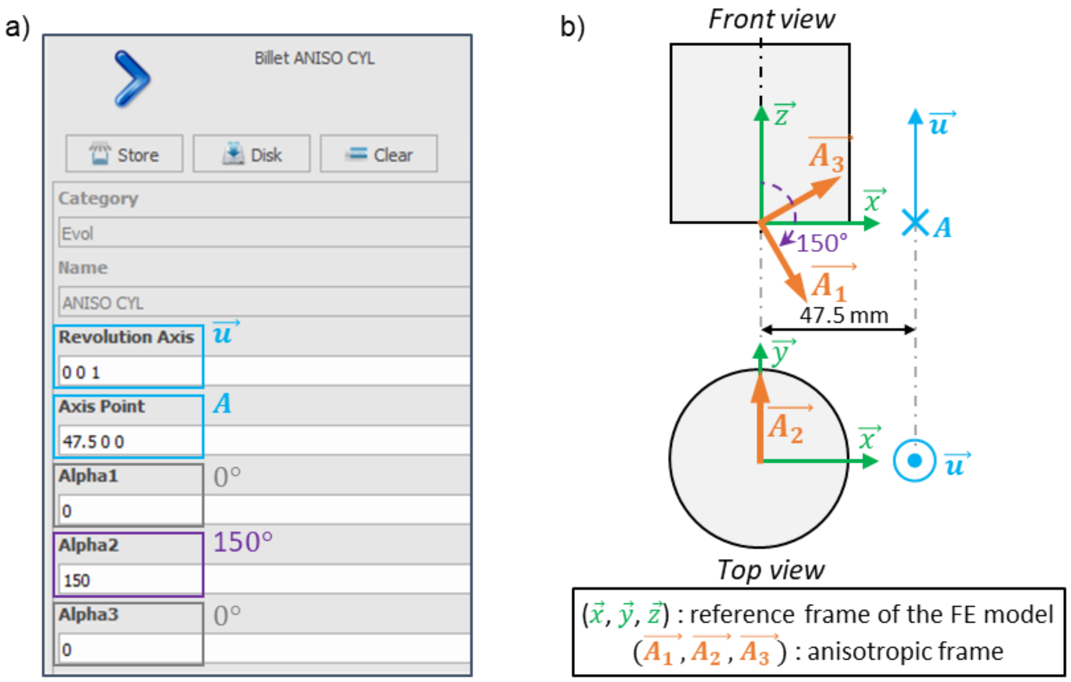

Billet ANISO CYL

Category

Evol

Name

ANISO CYL

Revolution Axis

0 0 1

Axis Point

47.5 0 0

Alpha1

0

Alpha2

150

Alpha3

0

Figure 3.36 : Implementation of the anisotropic frame $(\overrightarrow{A1}, \overrightarrow{A2}, \overrightarrow{A3})$ in FORGE® software; a) a screenshot from FORGE® software interface showing the parameters to be set for the implementation of the anisotropic frame, and b) schematised configuration of the anisotropic frame for the upsettings performed on the axial samples. Note that Alpha1, Alpha2 and Alpha3 are the angle of rotation of $(\overrightarrow{A1}, \overrightarrow{A2}, \overrightarrow{A3})$ around $\vec{x}$, $\vec{y}$ and $\vec{z}$ directions, respectively

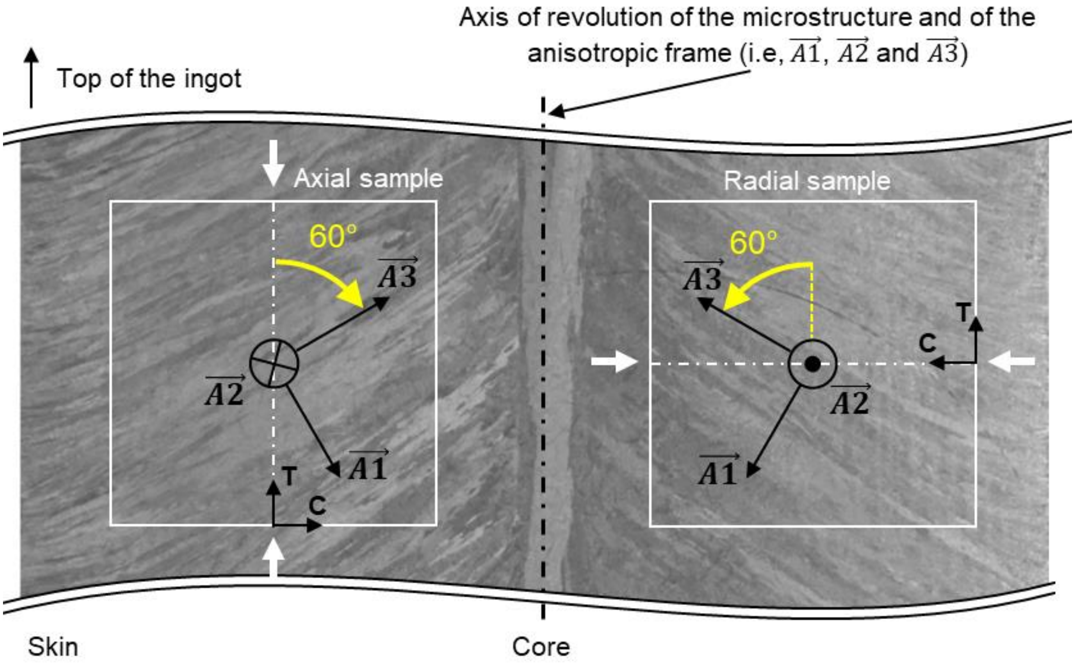

Figure 3.37 : Anisotropic frame $(\overrightarrow{A1}, \overrightarrow{A2}, \overrightarrow{A3})$ defined for the as-cast microstructure. Note that the axis of revolution of the ingot's microstructure matches with that of revolution of the axis of revolution of the anisotropic frame. The position and orientation of the axial and radial samples are schematically shown with the white arrows indicating the direction of upsetting for each case.

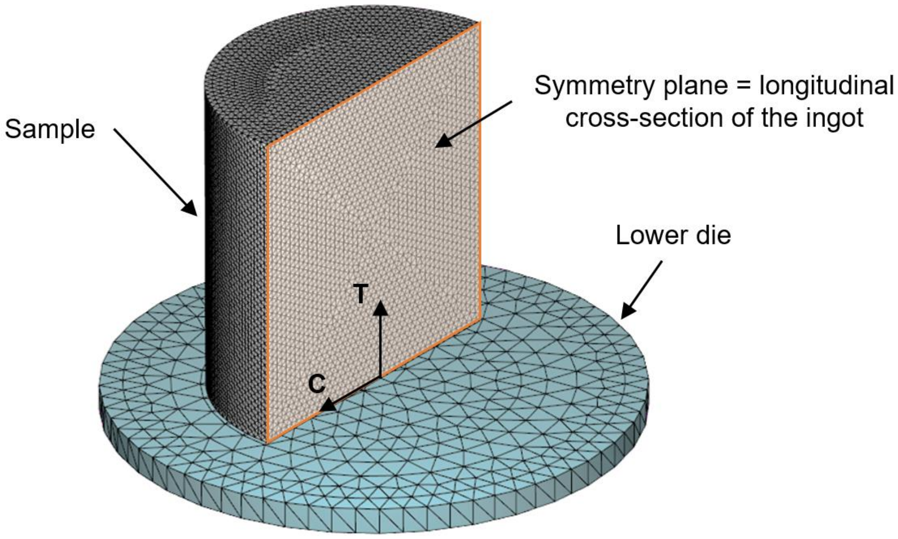

Figure 3.38 : The half cylindrical meshed geometry used in the FE model for the Ø 60×60 mm samples dedicated to upsetting. For visualisation convenience, only the lower die is displayed.

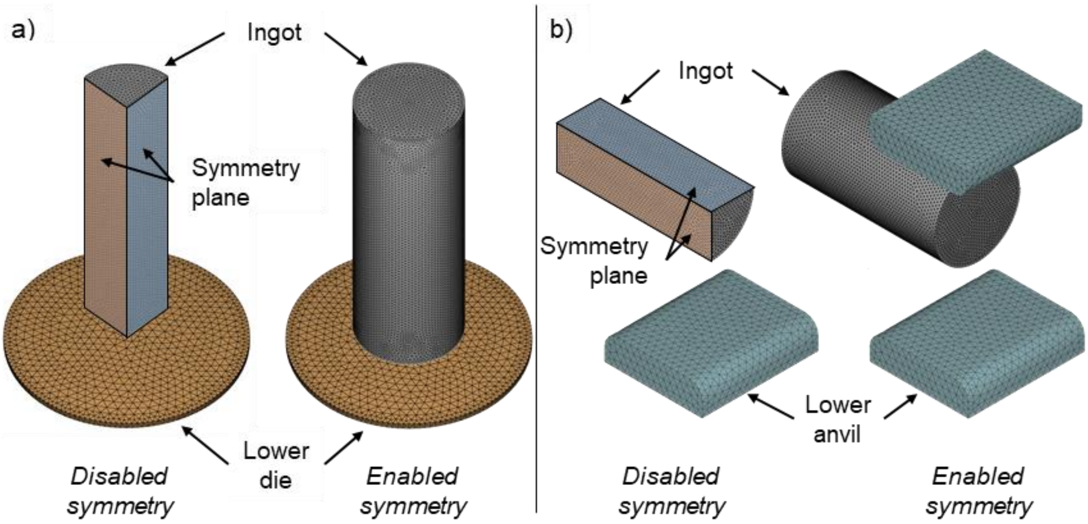

Figure 3.39 : A screenshot of the meshed ingots (elements) used for the FE simulation of the forging processes, including a) upsetting, and b) cogging. Note that in both cases the left view depicts the model with symmetry considerations implemented in the FE, and the right view displays a full 3D visualisation of the FE model reconstructed from the quarter model in left.

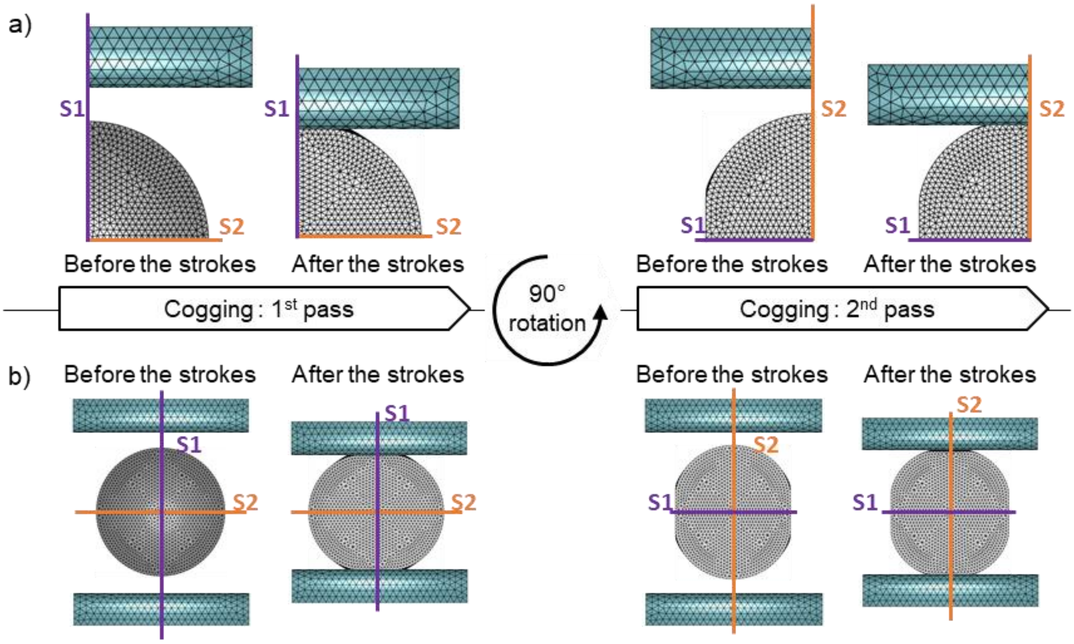

Figure 3.40 : Front view of the ingot's position during the first couple of cogging passes with visualisation of symmetries a) disabled, and b) enabled. S1 and S2 denotes the considered planes of symmetries.

The transfer time and holding/dwelling times used in the FE models were those measured from the video records of the experiments. Dies kinematic were implemented using FORGE® embedded features to model the hydraulic and screw presses, according to their characteristics (i.e., energies, speed, symmetry of the FE model, …), and to the experimental data records (i.e., dimensions of the samples or ingot following upsetting and cogging, …).

In cogging FE models, the die kinematics was set to ensure the final height was achieved at each stroke, regardless of the differences in material behaviour between the experiment and the simulation. Consequently, the model was set with the maximum energy available by the press (i.e., 28.9 kJ), which differ from the energy level measured during the experiments. Dedicated *.mpfx files were used to model the kinematic of the press and ingots for the cogging FE model, including the forging route parameters issued from the analysis of the experimental forging routes records (see Figures 3.31 and 3.32). Figure 3.41 provides an example of the structure of the *.mpfx file implemented in the FE models for modelling the kinematic of the screw press and of the 316L grade ingot during C1 cogging.

The *.mpfx file starts with a header section (see Figure 3.41 a)), which is used to declare the number of passes to model. In this work, each hit from the press is individually described as a "pass" in the *.mpfx files, with a single hit from the press. This allows to account for the real experimental cogging schedule (e.g., case of the strokes achieved via successive hits from the press to different final height, see Figure 3.32). Then, the *.mpfx files consists in a succession of sections used to describe the kinematic parameters for each hit from the press (see Figure 3.41 b) to d)). These parameters includes:

- The initial and final positions of the upper die, which accounts for the symmetry considered in the FE model (e.g., see the rectangle "**B**" in Figure 3.41 b)),
- The position of the ingot, described with its maximal position along the $\vec{x}$ axis (e.g., see the rectangle "**C**" in Figure 3.41 b)),
- The energy efficiency for each hit from the press, set to 50% to account for the for the symmetry considered in the FE model (e.g., see the rectangle "**D**" in Figure 3.41 b)),
- The wait time to be considered prior the deformation stage, which corresponds to the duration between successive hits from the press (e.g., see the rectangle "**E**" in Figure 3.41 b) to d)). Note that no wait time was declared in Figure 3.41 b) since it was integrated in the previous stage of the FE model, corresponding to the transfer from the furnace to the press.
- The rotation of the ingot between each pass, by an angle of ±90° around its axis (e.g., see the rectangle "**F**" in Figure 3.41 d)).

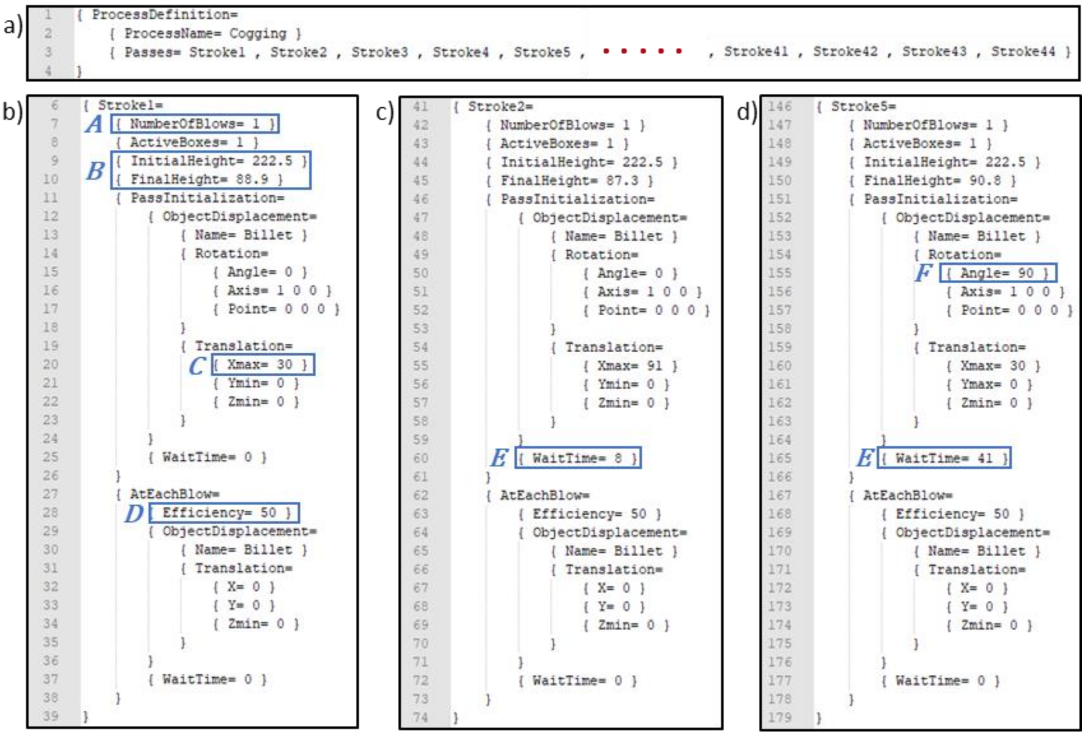

a)

```
{ ProcessDefinition=
    { ProcessName= Cogging }
    { Passes= Stroke1 , Stroke2 , Stroke3 , Stroke4 , Stroke5 , • • • • • • , Stroke41 , Stroke42 , Stroke43 , Stroke44 }
}
```

b)

```
{ Stroke1=
    { NumberOfBlows= 1 }
    { ActiveBoxes= 1 }
    { InitialHeight= 222.5 }
    { FinalHeight= 88.9 }
    { PassInitialization=
        { ObjectDisplacement=
            { Name= Billet }
            { Rotation=
                { Angle= 0 }
                { Axis= 1 0 0 }
                { Point= 0 0 0 }
            }
            { Translation=
                { Xmax= 30 }
                { Ymin= 0 }
                { Zmin= 0 }
            }
        }
        { WaitTime= 0 }
    }
    { AtEachBlow=
        { Efficiency= 50 }
        { ObjectDisplacement=
            { Name= Billet }
            { Translation=
                { X= 0 }
                { Y= 0 }
                { Zmin= 0 }
            }
        }
        { WaitTime= 0 }
    }
}
```

c)

```
{ Stroke2=
    { NumberOfBlows= 1 }
    { ActiveBoxes= 1 }
    { InitialHeight= 222.5 }
    { FinalHeight= 87.3 }
    { PassInitialization=
        { ObjectDisplacement=
            { Name= Billet }
            { Rotation=
                { Angle= 0 }
                { Axis= 1 0 0 }
                { Point= 0 0 0 }
            }
            { Translation=
                { Xmax= 91 }
                { Ymin= 0 }
                { Zmin= 0 }
            }
        }
        { WaitTime= 8 }
    }
    { AtEachBlow=
        { Efficiency= 50 }
        { ObjectDisplacement=
            { Name= Billet }
            { Translation=
                { X= 0 }
                { Y= 0 }
                { Zmin= 0 }
            }
        }
        { WaitTime= 0 }
    }
}
```

d)

```
{ Stroke5=
    { NumberOfBlows= 1 }
    { ActiveBoxes= 1 }
    { InitialHeight= 222.5 }
    { FinalHeight= 90.8 }
    { PassInitialization=
        { ObjectDisplacement=
            { Name= Billet }
            { Rotation=
                { Angle= 90 }
                { Axis= 1 0 0 }
                { Point= 0 0 0 }
            }
            { Translation=
                { Xmax= 30 }
                { Ymax= 0 }
                { Zmin= 0 }
            }
        }
        { WaitTime= 41 }
    }
    { AtEachBlow=
        { Efficiency= 50 }
        { ObjectDisplacement=
            { Name= Billet }
            { Translation=
                { X= 0 }
                { Y= 0 }
                { Zmin= 0 }
            }
        }
        { WaitTime= 0 }
    }
}
```

Figure 3.41 : Annotated screenshots of the *.mpfx file used in FORGE® for modelling the kinematic of both the screw press and the 316L grade ingot during C1 cogging; a) header section, and b) to c) the parameter sections for the 1st, 2nd and 5th hits from the press, respectively. Note that this *.mpfx kinematic file describe 44 individual hits from the press, along 1545 lines.

Sensors were implemented into the FE models to record the evolution of thermomechanical properties at various locations of the samples or ingots throughout the experiments. They were defined prior to the computation of the FE models so that results are recorded for each computed increment, including those for which the computation results were not stored. Marking grid features, consisting of a network of parallel lines oriented parallel to the long axes of the grains (i.e., oriented at 60° to the axis of the ingot, see Figure 3.42), were also added to the FE model of the Ø 60×60 mm samples to track the deformation of the initial parent grains.

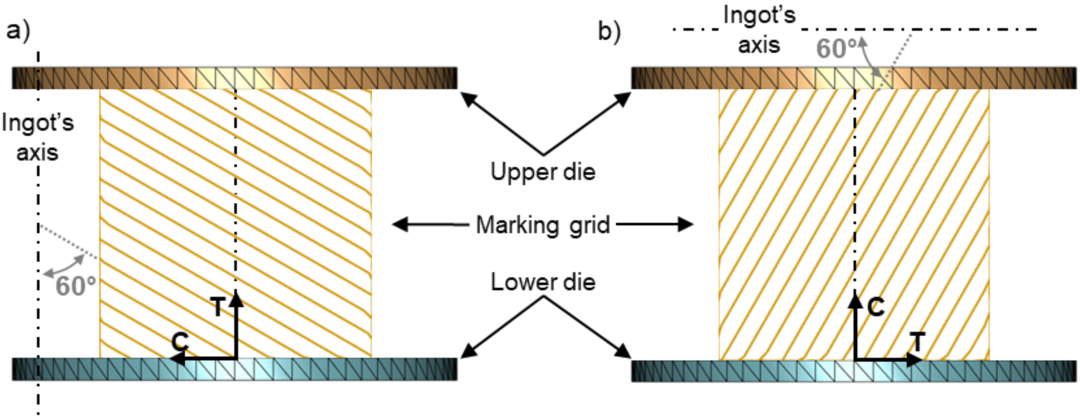

Figure 3.42 : Marking grids implemented in the FE model of the Ø 60×60 mm samples to track the deformation of the initial grain boundaries orientations; a) axial, and b) radial sample orientations. The position of the axis of the ingot (i.e., axis of symmetry of the as-cast microstructure) is displayed for each case.

Additional parameters, computation and storage settings used in the FE models are summarised in Tables 3.10 and 3.11 for the experiments conducted on the Ø 60×60 mm samples and entire ingots, respectively. The friction with the dies was modelled using the "Coulomb's law limited to Tresca" friction model, with the values of both $\bar{m}$ and μ parameters indicated in Tables 3.10 and 3.11 for each case. According to the experimental conditions, the values of these parameters were taken from the FORGE® database for lubrication conditions using (i) a water and graphite slurry in the case of the 30% upsetting in height performed on the Ø 60×60 mm samples, and (ii) no lubricant in the case of the upsetting and cogging experiments.

Table 3.10 : Summary of the parameters and computation settings used in the FE modelling of the hot upsetting tests performed on the Ø 60×60 mm samples.

		Heat transfer coefficient			Settings	
	Material emissivity	with ambient medium	with the dies	Friction coefficients	Max. temp. variation (°C)	Storage
Stage	-	(W.m^{-2}.K^{-1})	(W.m^{-2}.K^{-1})	-	-	-
Transfer : press to lower die	0.3	10	/	/	10	Δt = 0.5 s
Holding time on the lower die	0.3	10	/	/	10	Δt = 0.5 s
Forging	0.88	10	7 500	$\bar{m} = 0.3$ $\mu = 0.15$	10	ΔH = 0.5 mm + Final height
Air cooling on the refractory bricks	0.88	10	400*	/	10	Δt = 30 s

* Defined experimentally from the records of temperature evolution at the interface between the sample and the refractory brick.

Table 3.11 : Summary of the parameters and computation settings used in the FE modelling of the upsetting and cogging experiments on intermediate scale industrial ingots.

		Heat transfer coefficient			Computation settings	
Stage	Material emissivity -	with ambient medium ($W.m^{-2}.K^{-1}$)	with the dies ($W.m^{-2}.K^{-1}$)	Friction coefficients -	Max. temp. variation (°C) -	Storage -
Transfer furnace ⇔ press	0.3 or 0.88	10	/	/	10	Δt = 10 s
Forging (upsetting)	0.88	10	10 000	$\bar{m} = 0.4$ $\mu = 0.8$	10	ΔH = 10 mm
Forging (cogging)						End blow storage
Final air cooling	0.88	3 700	/	/	10	Δt = 60 s

The validity of the FE modelling, including the anisotropic material model, was assessed by comparing the experimentally measured geometries of the Ø 60×60 mm samples, scanned using GOM ATOS® after upsetting and cooling (e.g., see Figure 3.19), with those predicted by the FE model. Experimental and predicted geometries were compared using GOM Inspect® software, and the variance was evaluated using the average absolute surface distance between them. As an example, the results obtained for the axial and radial 316Nb samples forged using the hydraulic press are presented in Figure 3.43. Examples of FE results obtained for a Ø 60×60 mm sample following upsetting, and for an entire ingot following cogging are displayed in Figures 3.43 and 3.44, respectively.

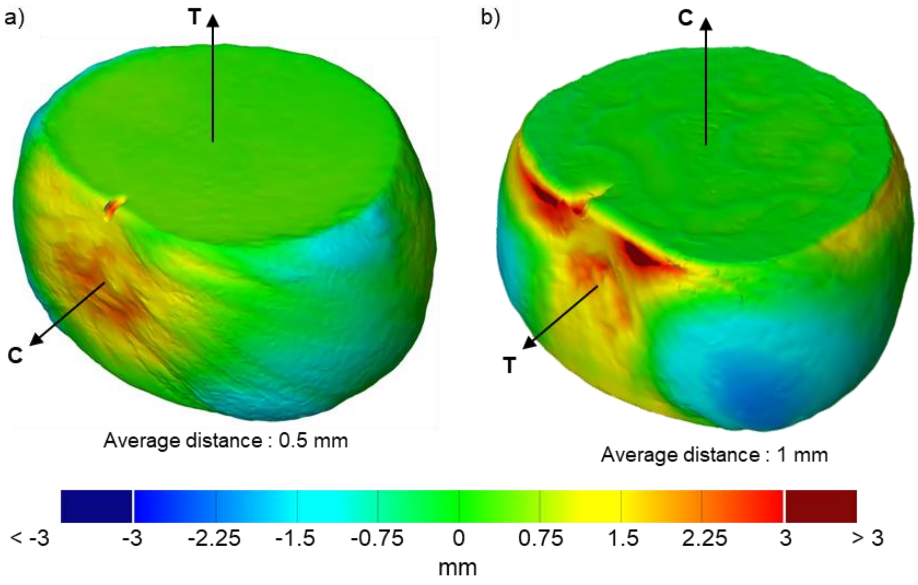

Figure 3.43 : Surface distance (mm) measured for a) axial and b) radial 316Nb samples between experimental and FE model geometries.

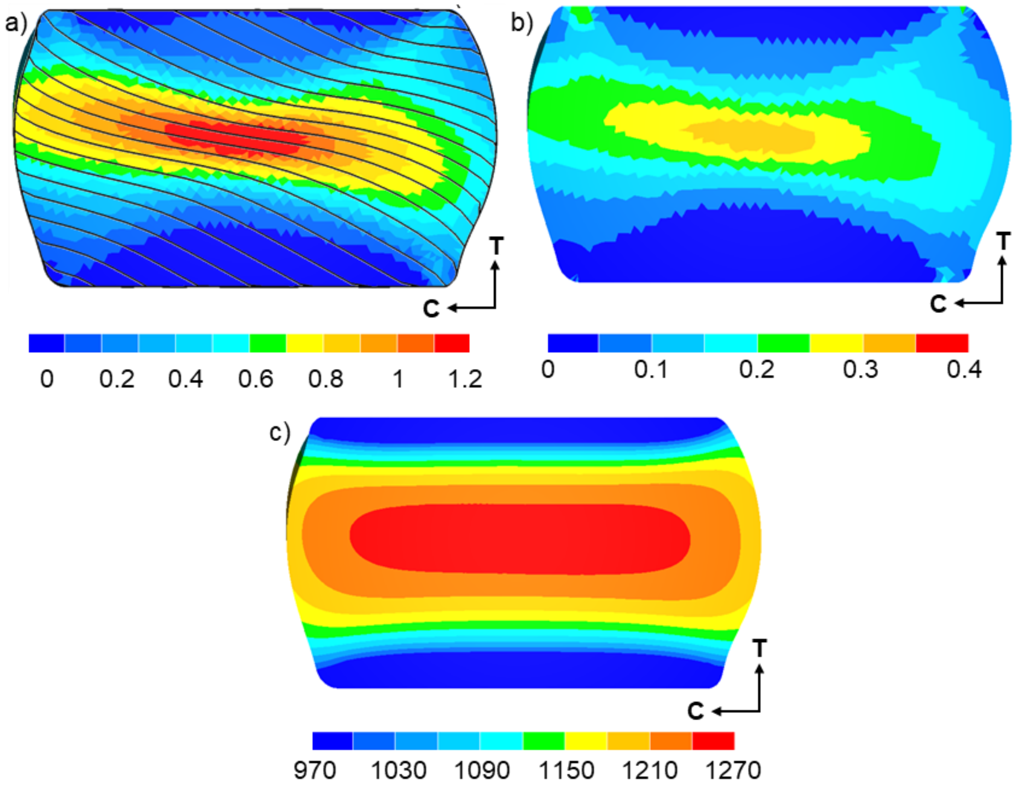

Figure 3.44 : FE predicted results for the axial 316L sample forged by the hydraulic press; a) strain (-), b) strain rate (s^{-1}), and c) temperature (°C) distributions. The deformed marking grids in a) showing deformation of the lines overlaid along the parent grains, which initial orientation and spacing (i.e., prior to upsetting) are depicted in Figure 3.42.

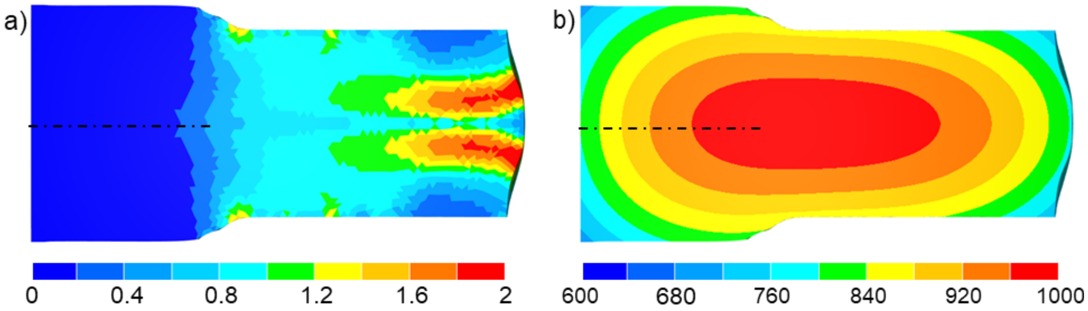

Figure 3.45 : FE predicted results for the 316L ingot after the cogging C1; a) strain (-), and b) temperature (°C) distributions.

3.4 METALLOGRAPHIC INSPECTION

3.4.1 Sample preparation

After upsetting, the Ø 60×60 mm samples were cut along their longitudinal cross-section using a water-cooled cut-off wheel. As can be seen from Figure 3.46, the inspected cross-sections of the Ø 60×60 mm samples was defined to match the longitudinal cross-section of the starting as-cast ingots to obtain a clear overview of the evolution of the elongated as-cast grains. Note that the longitudinal cross-section defined for microstructural analyses match with that used for the analyses of thermomechanical properties predicted by simulation (see Figure 3.44).

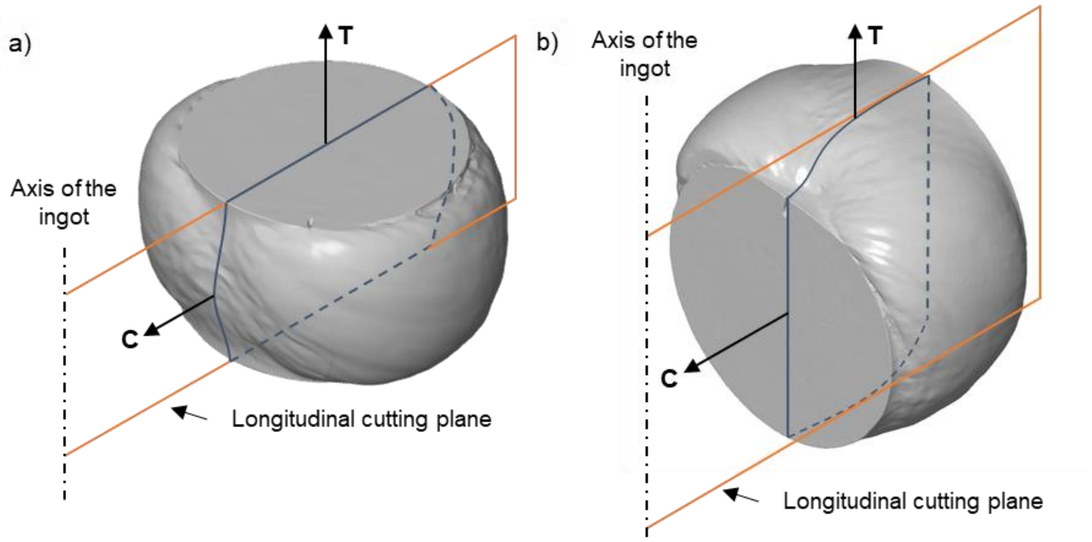

Figure 3.46 : Schematic sketches of Ø 60×60 mm sample after upsetting with the position of longitudinal cuts for microstructure characterisations highlighted; a) axial and b) radial samples.

The forged ingots were cut along their longitudinal cross-section using a band saw to extract specimens dedicated to microstructure analysis. The large specimens dedicated to the overall characterisation of the macrostructure evolution, shown in Figure 3.47 c) were prepared following the same methodology as those used for the characterisation of the as-cast materials (see Section 3.2.1). Specimens dedicated to microstructure characterisations were extracted from the longitudinal cross-sections of the ingots using a water-cooled cut-off wheel in the areas presented in Figures 3.44 and 3.43 d) for the ingots forged by upsetting and cogging, respectively.

The surface of the extracted specimens were prepared for metallographic characterisations using a Buehler EcoMet 300 grinding/polishing machine. Silicon carbide grit paper with a grit size varying from 80 to 1200 were used with water as lubricant/coolant to flatten the surface of the specimens. Final polishing was achieved with polishing cloths and successive 9, 3 and 1 μm diamond solutions. The microstructure was revealed on the prepared surface by electro-etching using the experimental setup presented in Figure 3.49. The specimens were placed on a stainless-steel grid connected to the DC power supply. The cathode was composed of a massive stainless-steel part covering the whole surface of the specimens to ensure a uniform current density along its surface and thus obtain uniform electro-etching results. The electrolyte was composed of 10% oxalic acid in distilled water as per (ASTM E 407, 1999), and the electro-etching were performed at 0.3 A, 2 V for 3 to 5 minutes.

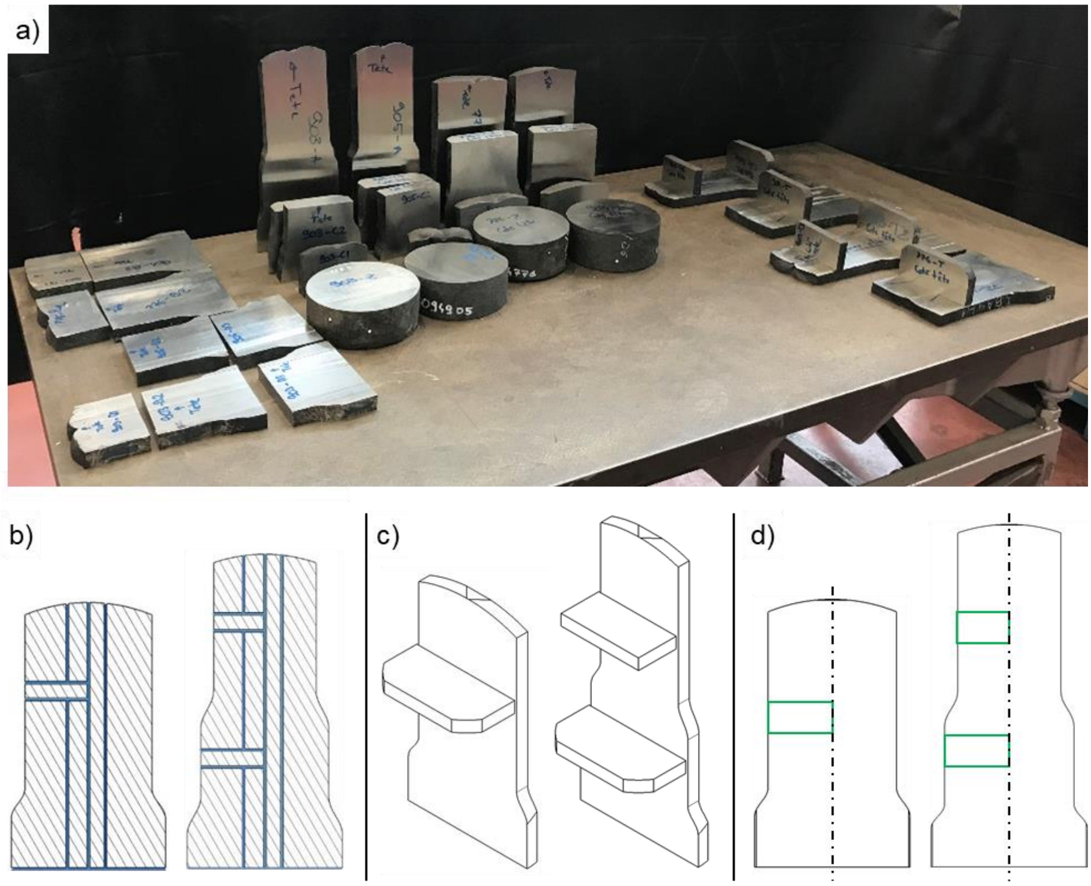

Figure 3.47 : Cutting operations performed on the cogged 316L and 316Nb ingots forged by the screw press for microstructures characterisation; a) parts after cutting, b) cutting operation performed on the forged ingots, c) longitudinal and transverse sections dedicated to macro etching, d) locations of specimens dedicated to quantitative OM analysis.

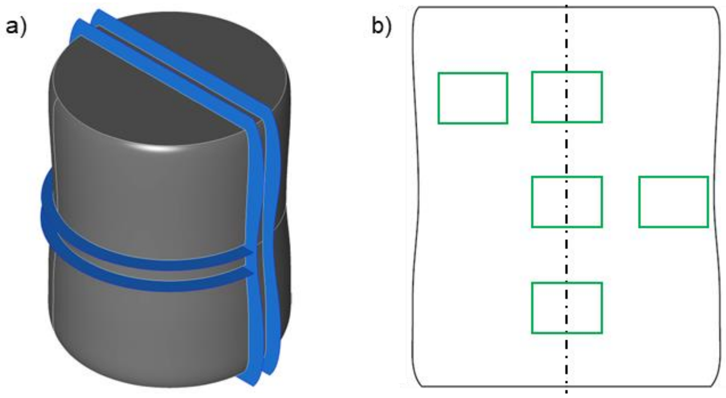

Figure 3.48 : Schematic sketches of the cutting operations performed on the 316Nb ingot after upsetting to extract the specimens dedicated to a) macrostructure observation, and b) quantitative OM characterisations.

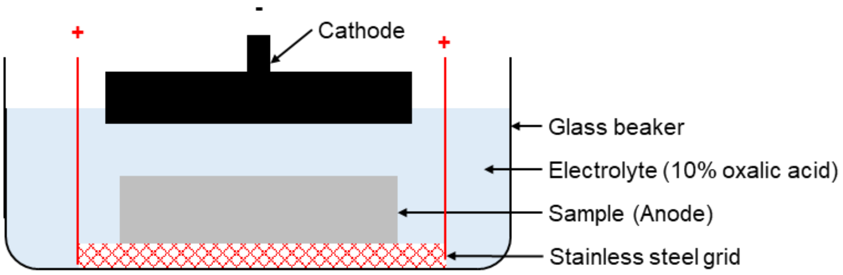

Figure 3.49 : Schematic cross-section of the experimental setup used for electro-etching.

3.4.2 Optical microscope observation and analysis

A Leica® DM12000-M optical microscope with an automated positioning table (Leica® STP6000) was used to observe and capture the microstructure across the large surface area of the specimens (see Figure 3.50). The collected micrographs were stitched together to obtain a global overview of the specimen microstructure, shown as example in Figure 3.51 a). As can be seen from Figure 3.51, the orientation of the micrographs (and specimens) within the initial as-cast ingot are provided in each case with “T” and “C” arrows, corresponding to the position of the top and core of the ingot, respectively. This convention is used for each micrograph presented in this manuscript.

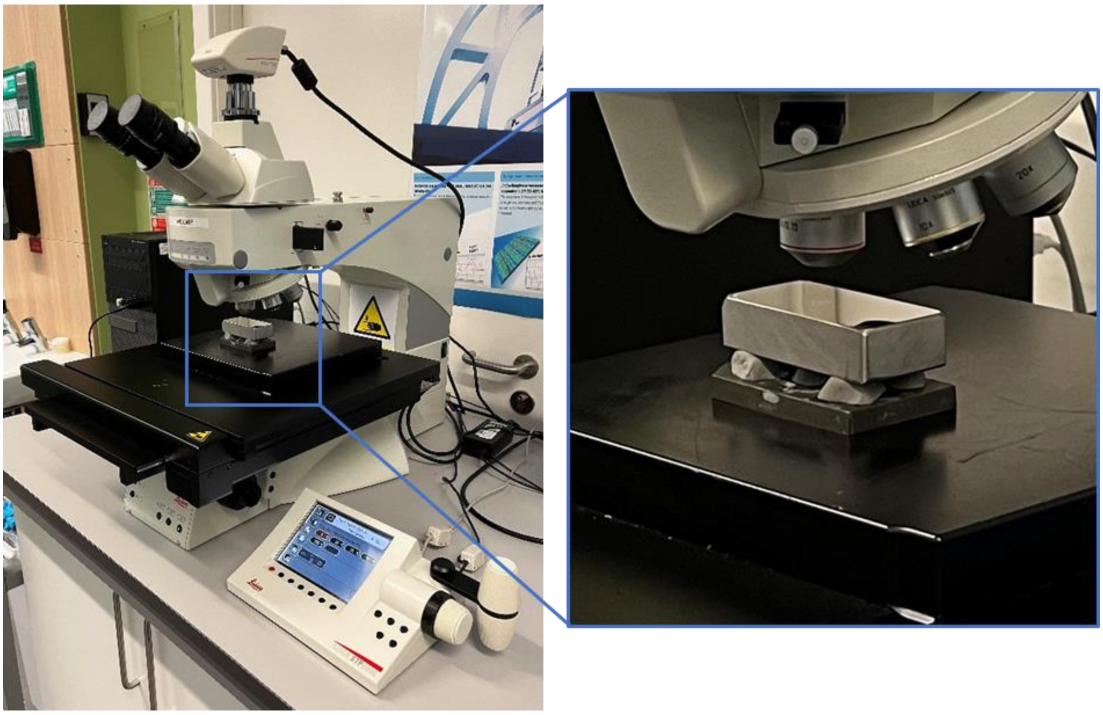

Figure 3.50 : Leica® optical microscope used for microstructure observation. The photographs shows the surface of a ≈ 40×80 mm specimen extracted from an ingot after cogging being mapped by the microscope.

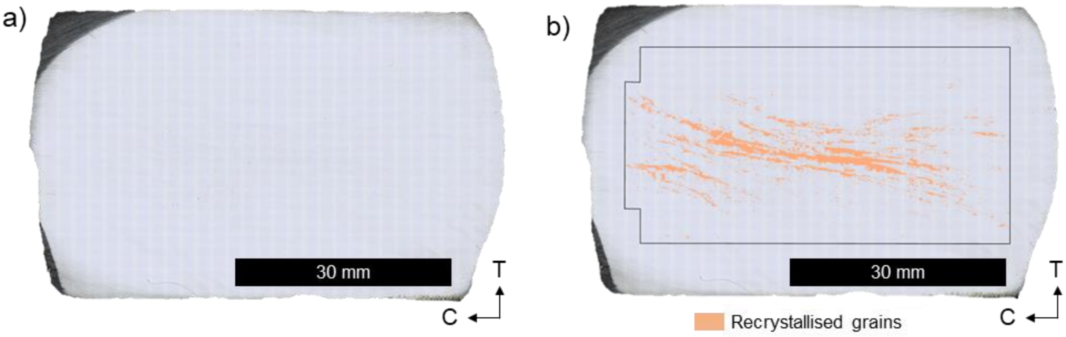

Figure 3.51 : a) Reconstructed image of a specimen cross-section with b) the areas underwent recrystallisation superimposed. Example taken from the axial 316L Ø 60×60 mm sample after upsetting using the hydraulic press.

To meet the specific requirements of this study, which are to (i) perform quantitative measurements of the grain size and fraction of recrystallised grains, and (ii) highlight the progress of recrystallisation at the scale of the samples (see Figure 3.51 b)), an in-house image processing analysis software was developed using the commercial software Matlab R2018a®. The schematic process integrated to the software and followed to obtain the results presented in Figure 3.51 b) is illustrated in Figure 3.52. Screenshots from this innovative quantitative image analysis software are provided in Appendix B. The features integrated to the software are listed and briefly described as follow:

- **Scaling:** A dedicated scaling feature was implemented to enable accurate measurements on OM micrographs, independent of the magnification or image resolution used during acquisition. This functionality required a micrograph to be exported from the microscope with a scale-bar overlaid, which was used for calibration; and allowed for the conversion of distances and areas from pixels or pixels^2 into real-world units (µm and µm^2).
- **Pre-processing of the input micrographs:** Various micrographs quality were collected throughout all samples, depending from sample preparation (i.e., polishing, etching homogeneity, etc.), observation conditions (i.e., specimen levelling, focus, illumination, etc.), and camera settings (brightness, contrast, etc.). To ensure appropriate segmentation of the grain boundaries, a "pre-processing" stage consisting in applying a set of prelaminar filtering and image enhancement techniques to the micrographs was incorporated to the software. Figures 3.52 a) and b) provide examples of a micrograph prior and after pre-processing, respectively.
- **Pre-processing of input micrographs**: The quality of collected micrographs varied across samples due to differences in sample preparation (e.g., polishing, etching uniformity), observation conditions (e.g., specimen levelling, focus, illumination), and camera settings (e.g., brightness, contrast). To ensure reliable grain boundary segmentation, a dedicated pre-processing stage was implemented in the software. This stage applied a sequence of filtering

and image enhancement techniques to optimise the input micrographs for segmentation. Figures 3.52 a) and b) illustrate a representative micrograph before and after the pre-processing stage, respectively.

- **Segmentation of grain boundaries:** The software incorporated an algorithm dedicated to identifying grain boundaries within the micrographs, using the marker-based watershed segmentation method proposed by (Debayle and Pinoli, 2006). This approach, combined with built-in MATLAB® functions (e.g., "regionprops", etc.), enabled the extraction of valuable properties for each grain detected in a micrograph, including its position and surface area. The capabilities of the integrated segmentation method are demonstrated in Figure 3.53, showing a micrograph collected at ×5 magnification alongside the corresponding segmented grains and delineated boundaries.
- **Quantitative analyses**: with proper scaling of the micrographs and the use of the segmentation algorithm, quantitative analyses were made possible by the software, which was developed to allow the measurement of grain size and of the fraction of recrystallised grains. The fraction of recrystallised grains was evaluated as the area fraction of the recrystallised grains measured across the observation plane. In this work, the recrystallised grains were identified using a grain area threshold value below which the grains were considered as recrystallised, and the others were considered as non-recrystallised. The grain area threshold value was manually defined and adjusted on the basis of the plots of cumulative area fraction as function of the equivalent grain diameter (see Figure 3.54 a)), and the recrystallised grains were highlighted in the micrograph (see Figure 3.54 b)).
- **Automation**: To address the need for processing large sets of micrographs collected over extensive sample areas, the features highlighted within the blue rectangle in Figure 3.52 were automated. This enabled semi-automated quantitative analyses to be performed across all micrographs within a selected region of the sample's cross-section.
- **Stitching**: Following processing, the results were available for each individual micrograph. To retrieve a global overview of the progress of recrystallisation along the large length-scale cross-section of the sample, as shown in Figure 3.51 b), a stitching feature was implemented to the software.
- **Storage and export of results**: The software incorporated dedicated functionalities for storing results obtained from both individual micrographs and the stitched results. These included automated path management and a consistent naming convention to ensure organised and traceable data handling.

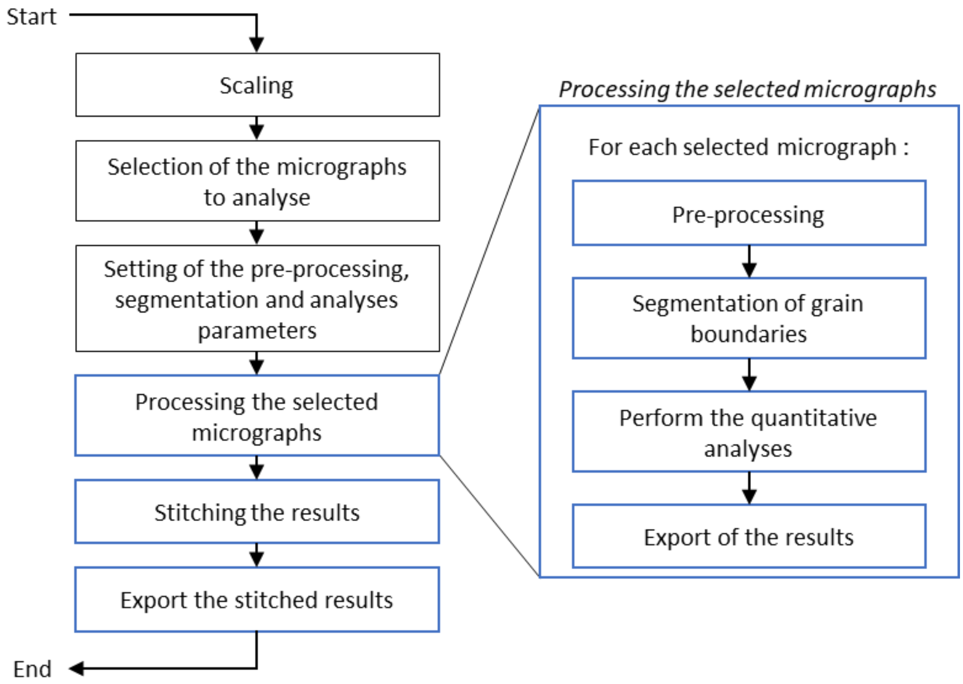

Figure 3.52 : Schematic process used for conducting the quantitative analyses on the OM micrographs collected from a sample. The automated stages of the whole process are highlighted by the blue rectangles.

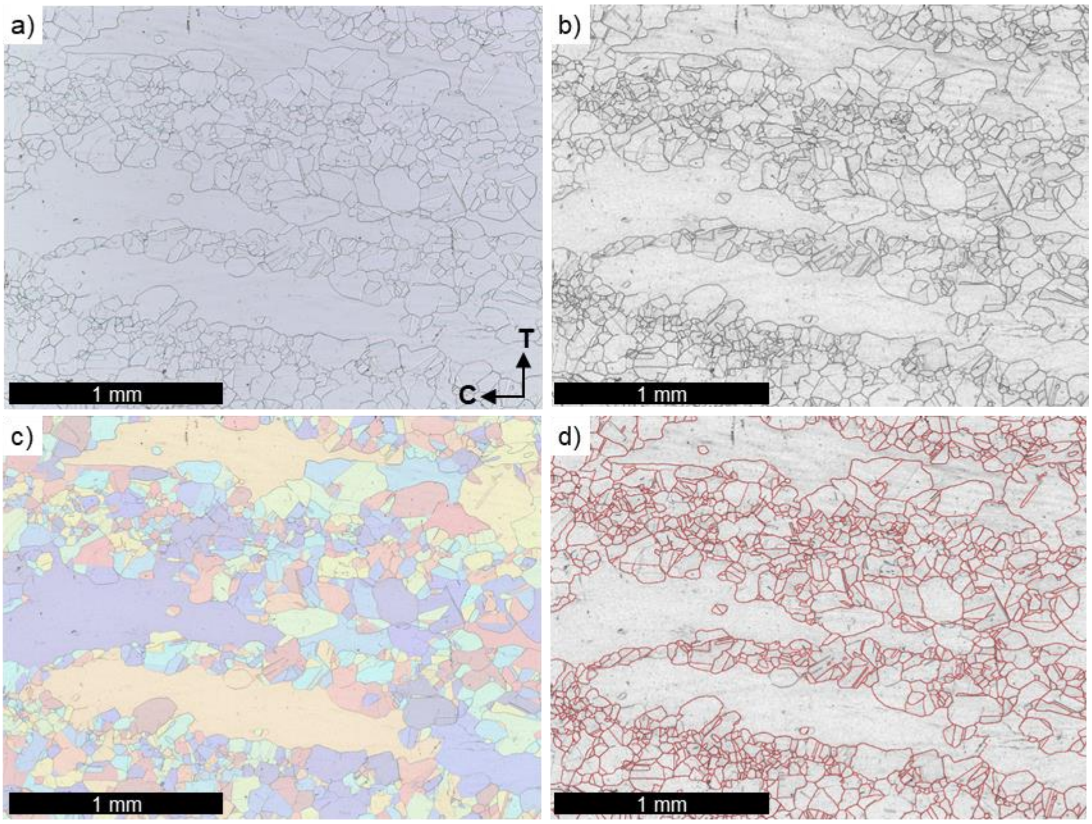

Figure 3.53 : Illustration of the image processing capabilities integrated to the software: a) an optical micrograph is scaled and b) pre-processed prior to segmentation of the grain boundaries. Following segmentation, the identified c) grains and d) grain boundaries are highlighted on the pre-processed image.

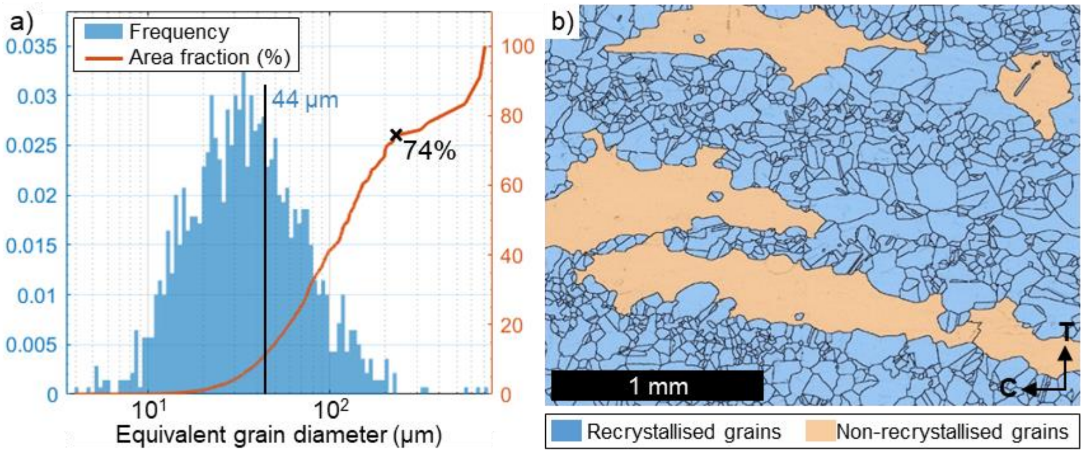

Figure 3.54 : a) Plots of equivalent grain diameters and cumulative area fraction and b) micrograph with recrystallised (blue) and non-recrystallised (orange) grains highlighted. The fraction of recrystallised grains is evaluated at 74% in this micrograph and the average diameter of recrystallised grains is 44 µm.

3.5 SUMMARY

An experimental methodology has been developed to investigate the as-cast material behaviour during the ingot-to-billet conversion process. To begin with, the as-cast microstructure of the intermediate size ingots used for the thermo-mechanical experiments is characterised and compared to that of industrial size ingots to gain an initial overview of the materials used in this study. The experiments designed to study the as-cast material behavior during thermo-mechanical processing were described with the associated manufacturing equipments, and consist of upsetting tests on small Ø 60×60 mm samples extracted from the intermediate size ingots, and upsetting and cogging performed on entire ≈ Ø 185×550 mm ingots. A finite element model of the experiments, considering the anisotropic as-cast material behavior was developed to provide additional data on the evolution of material thermomechanical properties throughout the experiments, such as the temperature, strain and strain rate. Characterisation and methods for the analysis of the experimental results were also introduced. Specimens were extracted from the samples and ingots after forging, prepared with conventional metallography techniques and the microstructure was revealed by electro etching with a 10% oxalic acid solution as electrolyte. The microstructure of the specimens was captured with an optical microscope and quantitative measurement of the fraction of recrystallised grains and of the size of the recrystallised grains were performed over the surface of the specimens using a tailor-made image analysis routine. This allowed to highlight the occurrence of recrystallisation at large scale and provide local measurements of the fraction of recrystallised grains.

Chapter 4 : HOT UPSETTING TRIALS ON SMALL-SCALE SAMPLES

CONTENT

4.1 INTRODUCTION

This chapter presents the results obtained for the hot upsetting trials performed on the Ø 60×60 mm samples extracted from the as-received ingots. The as-cast 316L and 316Nb (0.7%Nb) austenitic stainless steel grades were investigated, the former was with no Nb and the latter had 0.7% Nb (wt%) in its chemical composition. Two sets of cylindrical samples with their axes along the axial and radial directions of the as-cast billet were extracted to replicate industrial-scale upsetting and cogging operations. As explained in Section 3.2.2.1, the 30% height reduction upsetting tests were performed on the Ø 60×60 mm samples after homogenisation heat treatment using hydraulic and screw presses, to investigate microstructure evolution under different strain rates (i.e., ≈ 0.1 and 7 s^{-1}). The geometry of the samples following upsetting were measured and compared with the results of finite element (FE) predictions. The evolution and microstructure and thermo-mechanical properties of the samples are quantified and the results are presented.

Similarly to the previous chapter, the Ø 60×60 mm samples are referred to as "axial" and "radial" samples hereafter according to the orientation of their axis in the starting as-cast ingot, and the direction of the "top" and "core" of the ingot are indicated with "T" and "C" arrows when required.

4.2 DEFORMATION BEHAVIOUR OF THE AS-CAST SAMPLES

The 3D scanned geometries of the samples after upsetting and air cooling are presented in Figure 4.1, highlighting the anisotropic deformation behaviour (i.e., asymmetrical shape) of the as-cast material during upsetting. Higher magnification images of Figure 4.1 are provided in Appendix A. Both axial and radial samples show similar anisotropic behaviour regardless of the grade of the materials and the equipment (i.e., strain rate) used for the test. However, different deformed geometries were obtained depending on the sample's orientation (i.e., axial or radial), suggesting measurable impacts of crystallographic and grain morphology distributions in the as-cast microstructure on deformation behaviour (i.e., the nature of anisotropic deformation). As highlighted by the red arrows in Figure 4.2, the free-surfaces of the samples show irregularities in a direction aligned with the major axis of the as-cast grains. The surface irregularities can be ascribed to the different deformation behaviours in individual grains due to their respective crystallographic orientations.

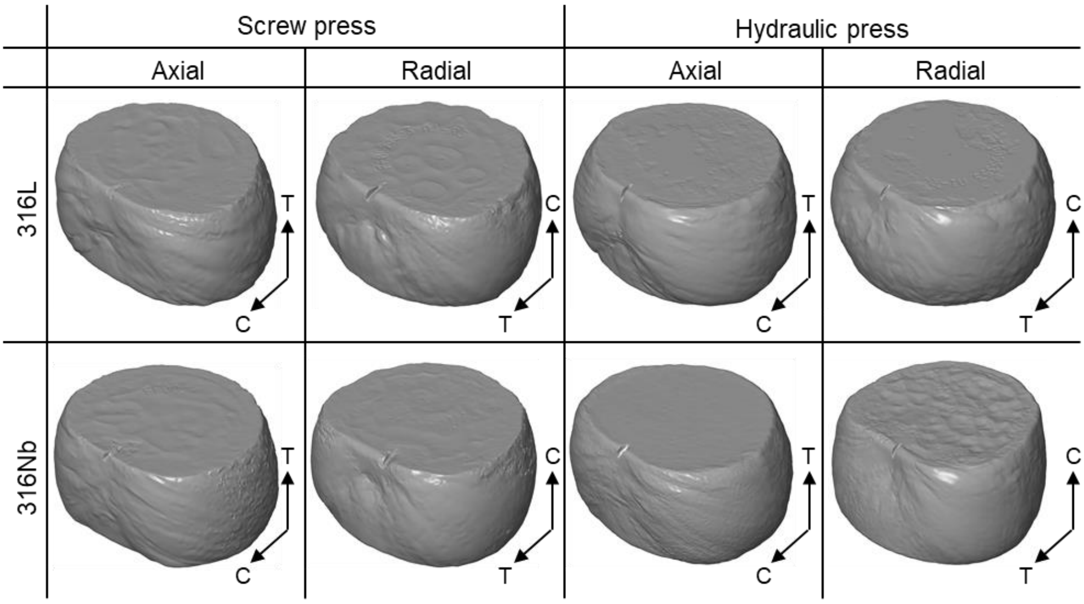

Figure 4.1 : 3D scanned geometries of the Ø 60×60 mm samples after upsetting. Note that the orientation of the samples within the initial as-cast ingots are indicated (“core” (C) and “top” (T)) in each image.

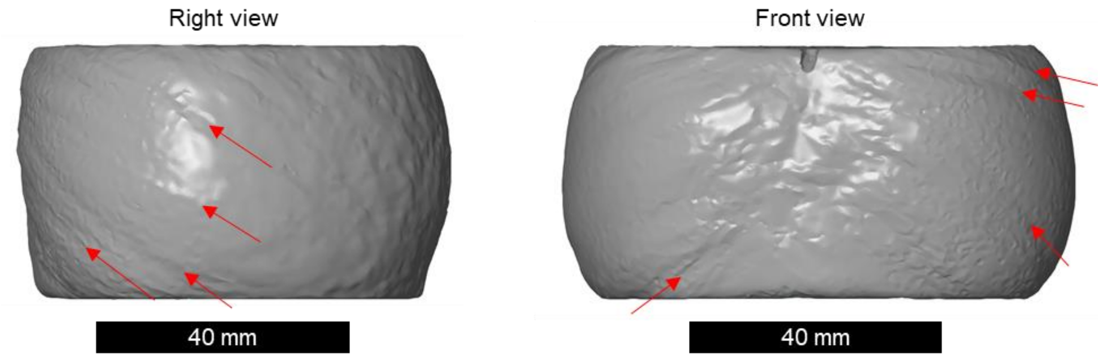

Figure 4.2 : 3D scanned geometry of the 316Nb Ø 60×60 mm samples after upsetting by the hydraulic press with the surface irregularities highlighted by the red arrows aligned with the major axis of the grains.

Figure 4.3 shows colour maps of the difference between the 3D scanned geometries with those predicted by FE simulation. The 2D cross-sections of both are shown in Figure 4.4 for the ease of comparison. A good agreement can be seen between the results of the FE predictions and the measured geometries. Note that in Figure 4.4 the significant difference between the results of FE and the measurements on the bottom of some samples (highlighted by arrows) was due to the remnant of refractory brick in the furnace, which got stuck to the samples during upsetting.

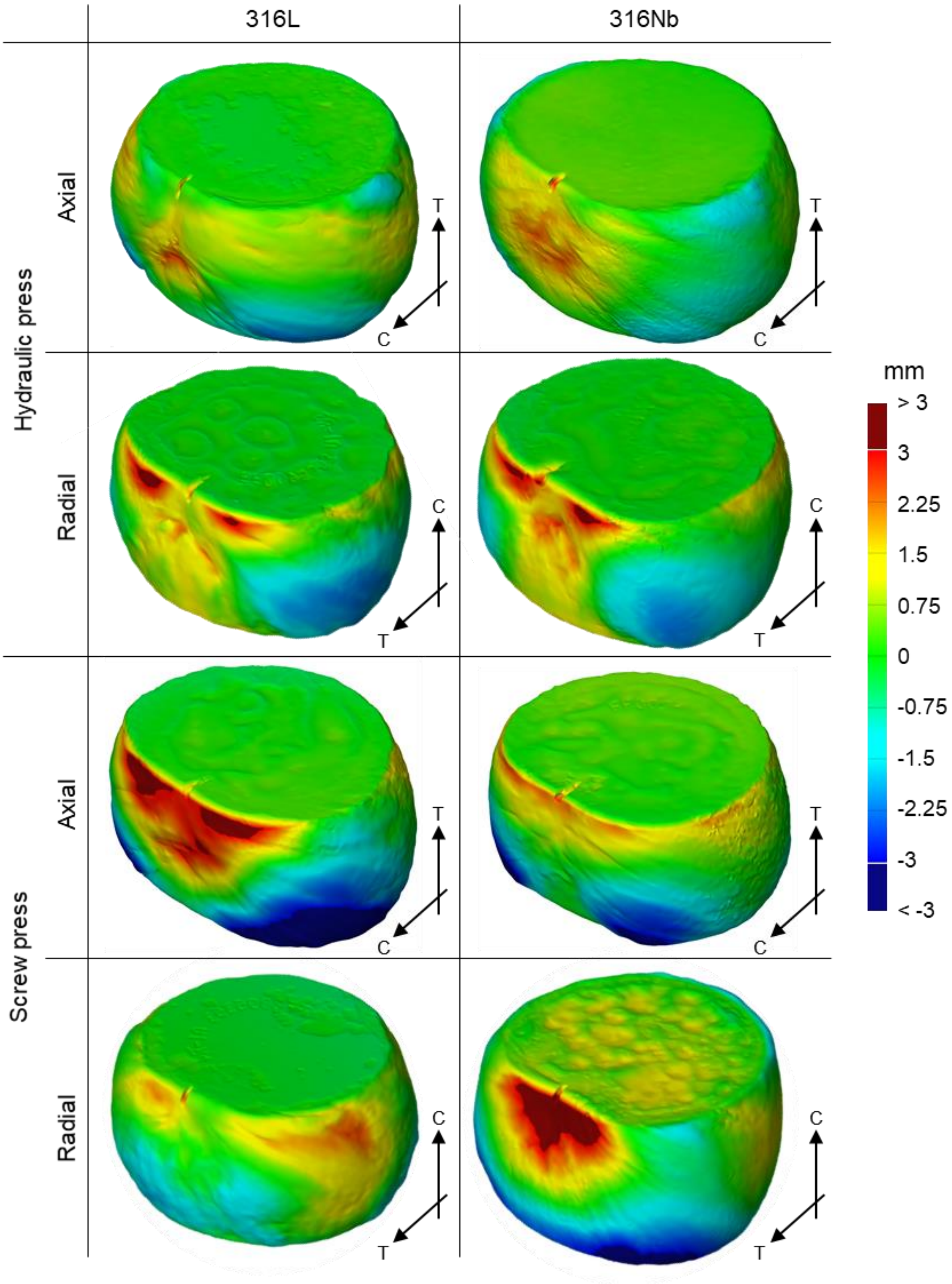

Figure 4.3 : Differences between the surfaces of the deformed samples scanned in 3D by GOM ATOS and the predicted shapes of the Ø 60×60 mm samples after 30% upsetting. Legend limits are set to ± 3 mm.

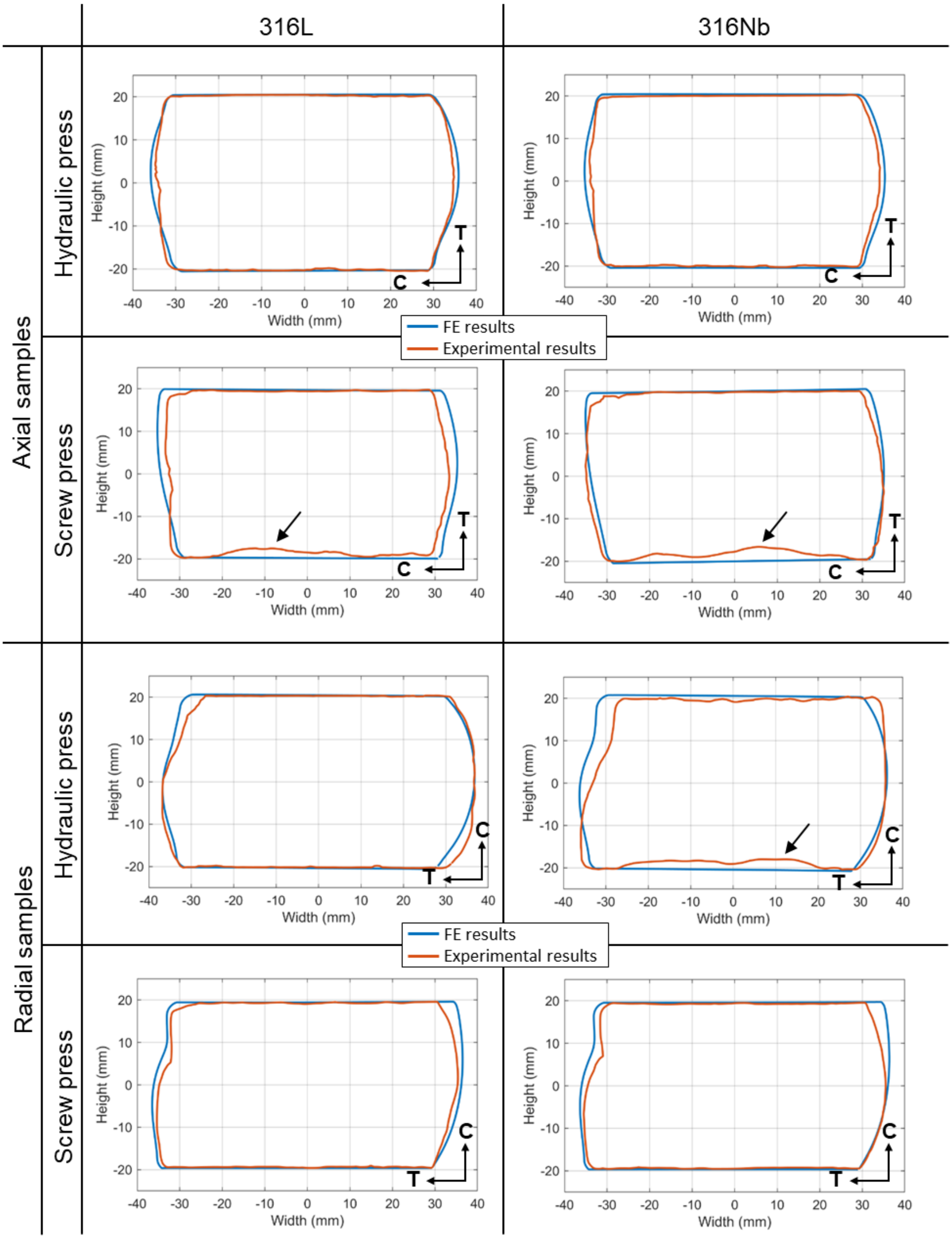

Figure 4.4 : Comparison between 3D GOM scans and FE predicted longitudinal cross-sections of the Ø 60×60 mm samples after 30% upsetting. The arrows are pointing at locations where refractory bricks stuck to the samples which led to deviation of the measured contour with FE results. The orientations of the samples within the initial as-cast ingot are indicated by “core” (C) and “top” (T) in each case.

The measured shear angles (i.e., the misalignment between upper and lower surfaces of the samples) presented in Figure 4.5 appear to have a similar trend for both grades, with those of 316Nb samples being higher.

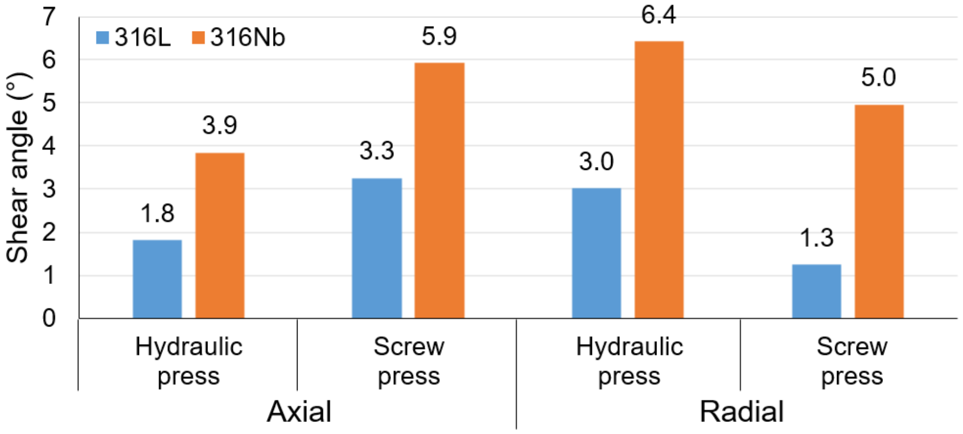

Figure 4.5 : Measured shear angle (°) of the small-scale samples after 30% upsetting. Measurements performed on the scanned 3D geometries (i.e., using GOM ATOS) of the samples.

The radius measurements performed on the samples, using the methodology described in Section 3.2.2.1 and shown in Figure 3.23, are presented in Figure 4.6. The results show the radius measured for the radial samples exhibited higher difference for both grades of materials compared to the axial samples. These differences in radius measurements had significant impact on the barrelling parameter (see Figure 4.7 a)) and friction coefficient (see Figure 4.7 b)) calculated for these samples with the methodology described in Section 3.2.2.1. The friction coefficient was in the range of 0.45 - 0.55 for the axial samples compared to 0.3 - 0.71 range for the radial samples.

The load-displacement and stress-strain curves obtained for the small-scale samples, i.e., evaluated from the upsetting tests, are presented in Figures 4.8 and 4.9, respectively. Note that no results are provided for the radial 316L sample forged by hydraulic press due to incomplete records of the load-displacement data. The flow-curves evaluated for the samples with the same orientation in the ingot (i.e., axial or radial) exhibited a similar shape, regardless of the grade composition. For both grades, different flow curves were obtained for the axial and radial samples, hence highlighting the sensibility of the material deformation behaviour to the microstructure orientation.

All flow-curves exhibited a continuous increase in stress with strain, which is explained as a result of the non-isothermal testing conditions, which led to material strengthening simultaneously with cooling throughout the upsettings. Because (i) the hydraulic press was controlled with a constant strain rate of 0.1 s^{-1} (see Section 3.2.2.1), and (ii) the ram speed decreased as function of the height reduction during the upsetting performed using the screw press (i.e., from 480 $mm.s^{-1}$ on impact with the samples to 0 mm.s^{-1} at the end of the upsetting), the strain-rate sensitivity of the material could not explain such behaviour in the present case.

As can be seen from Figure 4.9 a), the flow curves of the axial samples forged by the hydraulic press displayed multiple peaks, whereas that of the 316Nb radial sample exhibited more homogeneous strengthening with strain. Higher loads were required to achieve the nominal upsetting using the screw press compared to the hydraulic press owing to the higher ram speed (i.e., strain rate) of the former, which consequently higher the flow stresses measured for these samples.

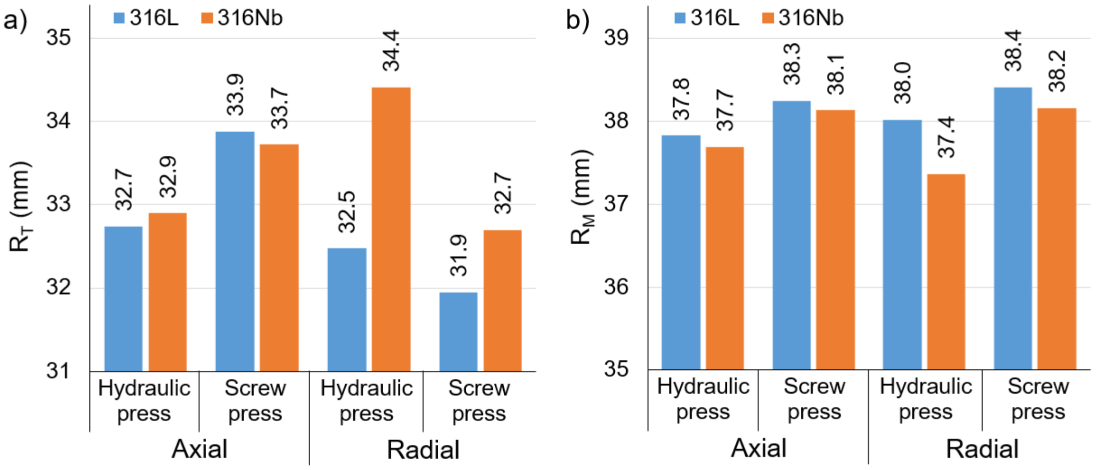

Figure 4.6 : Measured a) average top and bottom (R_T), and b) middle (R_M) radius of the small-scale samples after 30% upsetting. Measurements performed on the scanned 3D geometries of the samples using GOM ATOS.

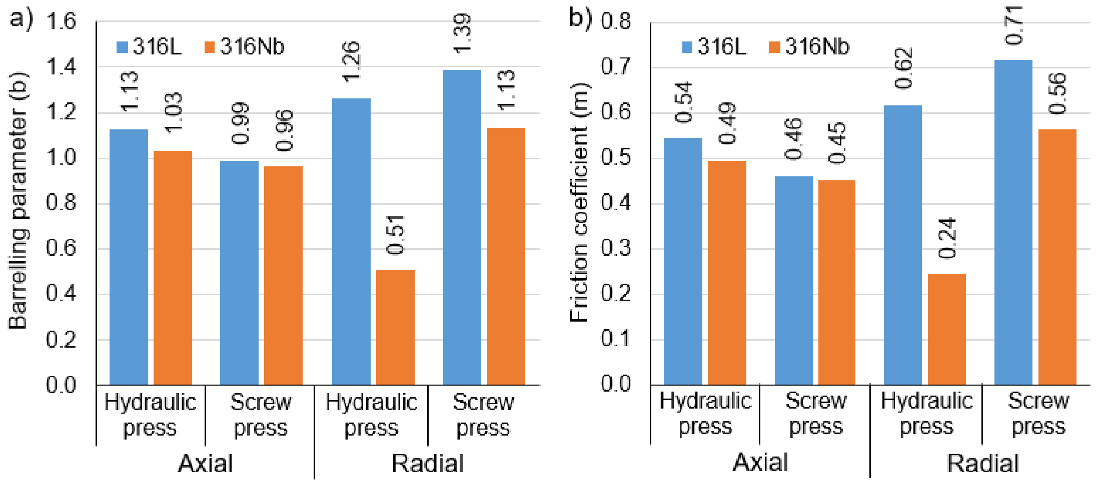

Figure 4.7 : Calculated a) barrelling parameter, and b) friction coefficients for the small-scale samples subjected to upsetting to 30% of reduction in height. Measurements performed on the 3D scans of the deformed samples.

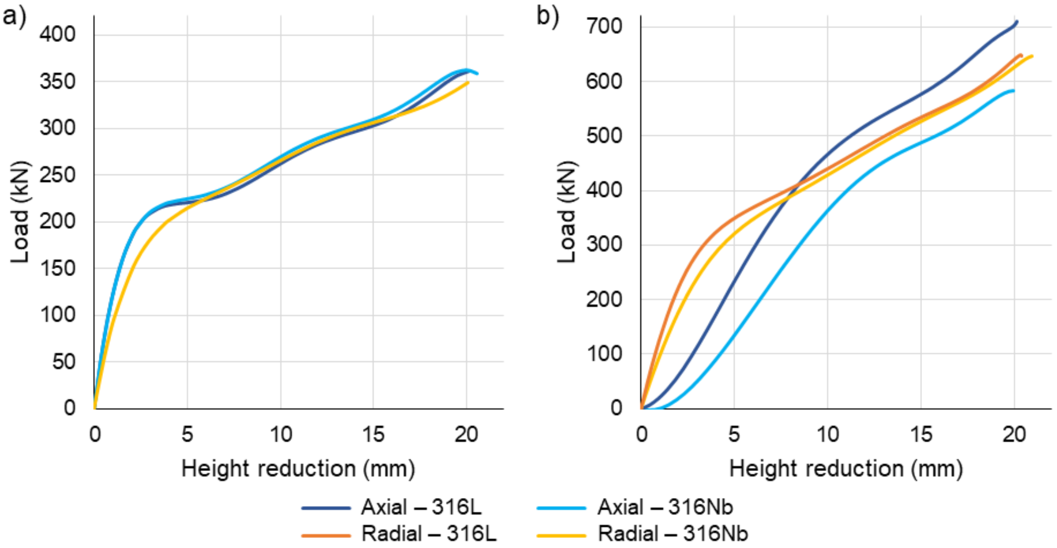

Figure 4.8 : Load-displacement plots recorded for the small-scale samples during upsetting to 30% reduction in height using the a) hydraulic, and b) screw presses. Note that the data for the radial 316L sample forged using the hydraulic press are not presented due to incomplete recording.

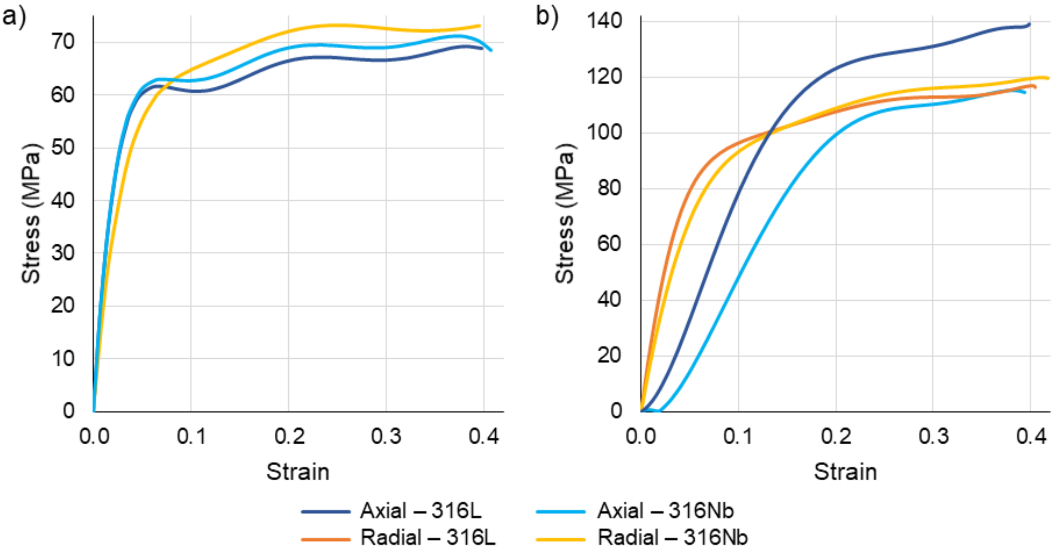

Figure 4.9 : The evaluated stress-strain curves (i.e., flow stress) for the small-scale samples subjected to upsetting to 30% reduction in height using the a) hydraulic, and b) screw presses. Data reconstructed from the Load-Displacement data presented in Figure 4.8.

4.3 THERMOMECHANICAL PROPERTIES

Plots of temperature distributions predicted by FE simulations just at the beginning of upsetting, after transfer from the furnace to the press, are presented in Figure 4.10. Plots of temperature, strain and average strain rate distributions predicted by FE at the end of upsetting are presented in Figures 4.11, 4.12 and 4.13, respectively. The high strain zone, corresponding to the area where maximum strain was reached at the end of the upsetting, are highlighted by a solid rectangle for each case in these figures. Plots of temperature and strain profiles as a function of % of deformation (i.e., upsetting ratio) in the high strain zones are presented in Figure 4.14. Also, the plots of cooling curves in the high strain zones, during post deformation air cooling stage are presented in Figure 4.15.

The predicted temperature distributions just before the initiation of forging (see Figure 4.10) show higher temperatures (≈ 1240-1250 °C) in the central regions of the samples. For the samples forged by the screw press the higher temperature zone was relatively smaller, because they were lying on the bottom die of the press for longer times before forging starts (see Figure 3.18). The lower temperature of the axial 316L sample compared to the axial 316Nb led to the higher flow-stress recorded for that sample (see Figure 4.9 b)).

The temperature distributions predicted at the end of upsetting (see Figure 4.11) show that the higher temperature zone (≈ 1240-1250 °C) was relatively larger for the cases of the screw press compares to those forged by the hydraulic press. This can be due to firstly the faster deformation rate of the former compared to the latter, which takes shorter time and hence there is no enough time for temperature to dissipate; secondly, the higher deformation rate can lead to the generation of adiabatic heating which further increase the temperature of the part. Temperature profiles for the high strain areas of the samples presented in Figure 4.14 show the occurrence of adiabatic heating during upsetting, which was more pronounced for the samples forged by the screw press (i.e., + 16 to 21 °C) compared to those forged by hydraulic press (i.e., + 6 to 10 °C). Cooling curves for the high strain zones presented in Figure 4.15 show different cooling rates for the samples forged by the hydraulic (- 9 °C/sec.) and screw (- 4 °C/sec.) presses. The higher cooling rates observed for the former can be due to the large temperature gradients along the surface in contact with the dies during upsetting, which accelerated the heat dissipation from the hotter core upon removal from the press. The high strain zones, highlighted by rectangles in Figure 4.12, were observed to displace for both axial and radial samples of both 316L and 316Nb grades as a consequence of the different deformation behaviour of these samples (see Figure 4.1).

The predicted strain level in the high strain zone was in the range 1.15 to 1.2 and 0.9 to 1 for the samples forged by the hydraulic and screw presses, respectively (see Figure 4.12). The difference in deformation behaviours of the samples forged by the hydraulic and screw presses are highlighted by deformation grids implemented on their longitudinal cross-sections shown in

Figure 4.11 and Figure 4.12. Figure 4.11 show that the curvature of the deformed marking grids were more pronounced in the high temperature area, which were narrower for the samples forged by the hydraulic press. As shown in Figure 4.13, average strain rate reached ranges from 0 to 0.35 s^{-1} and from 0 to 20 s^{-1} for upsetting by the hydraulic and screw presses, respectively. These values were higher than the nominal strain rate values of 0.1 and 7 s^{-1} estimated for the hydraulic and screw presses, respectively (see Table 3.3). In Figures 4.12 and 4.13, low strain and strain rate zones were observed along the upper and lower surfaces of the samples forged by the hydraulic press, as well as along the bottom surface of those forged by the screw press, in places where the temperature was predicted to be relatively low at the end of upsetting (i.e., < 1150 °C, see Figure 4.14).

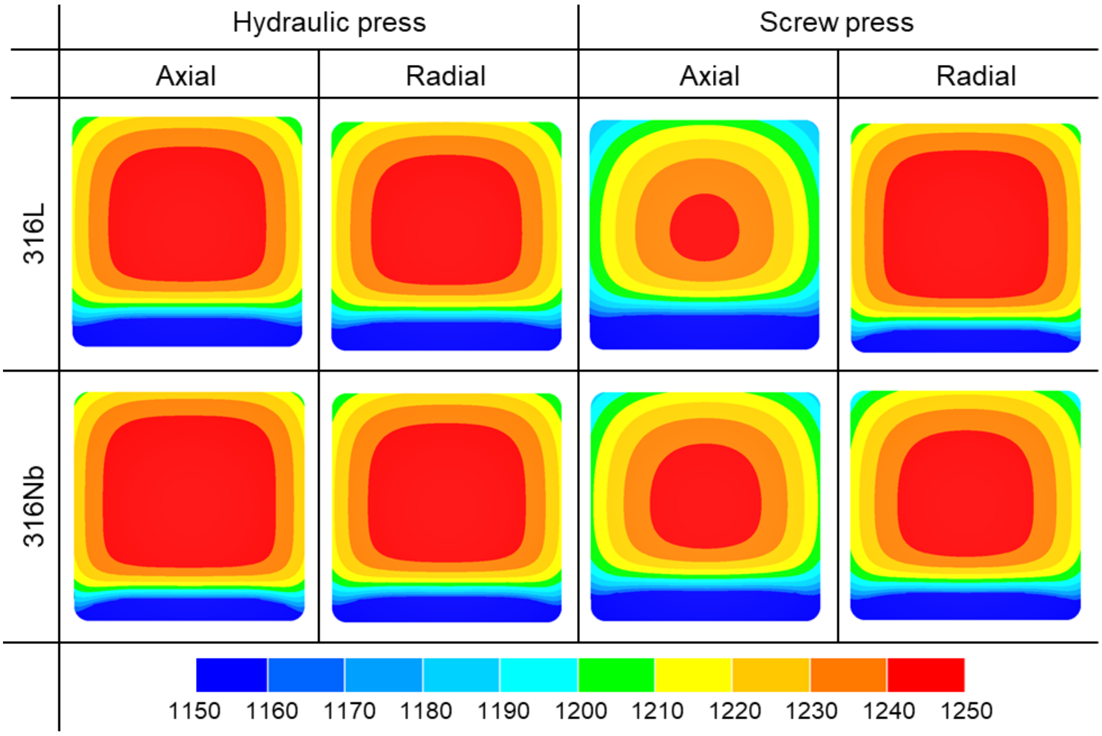

Figure 4.10 : Temperature distributions predicted by FE simulation at the beginning of upsetting of Ø 60×60 mm samples, taking into consideration the transfer from furnace to the press. The scale is set to the temperature range 1150-1250 °C to highlight temperature gradients and differences between samples. Upsetting was performed in the vertical direction.

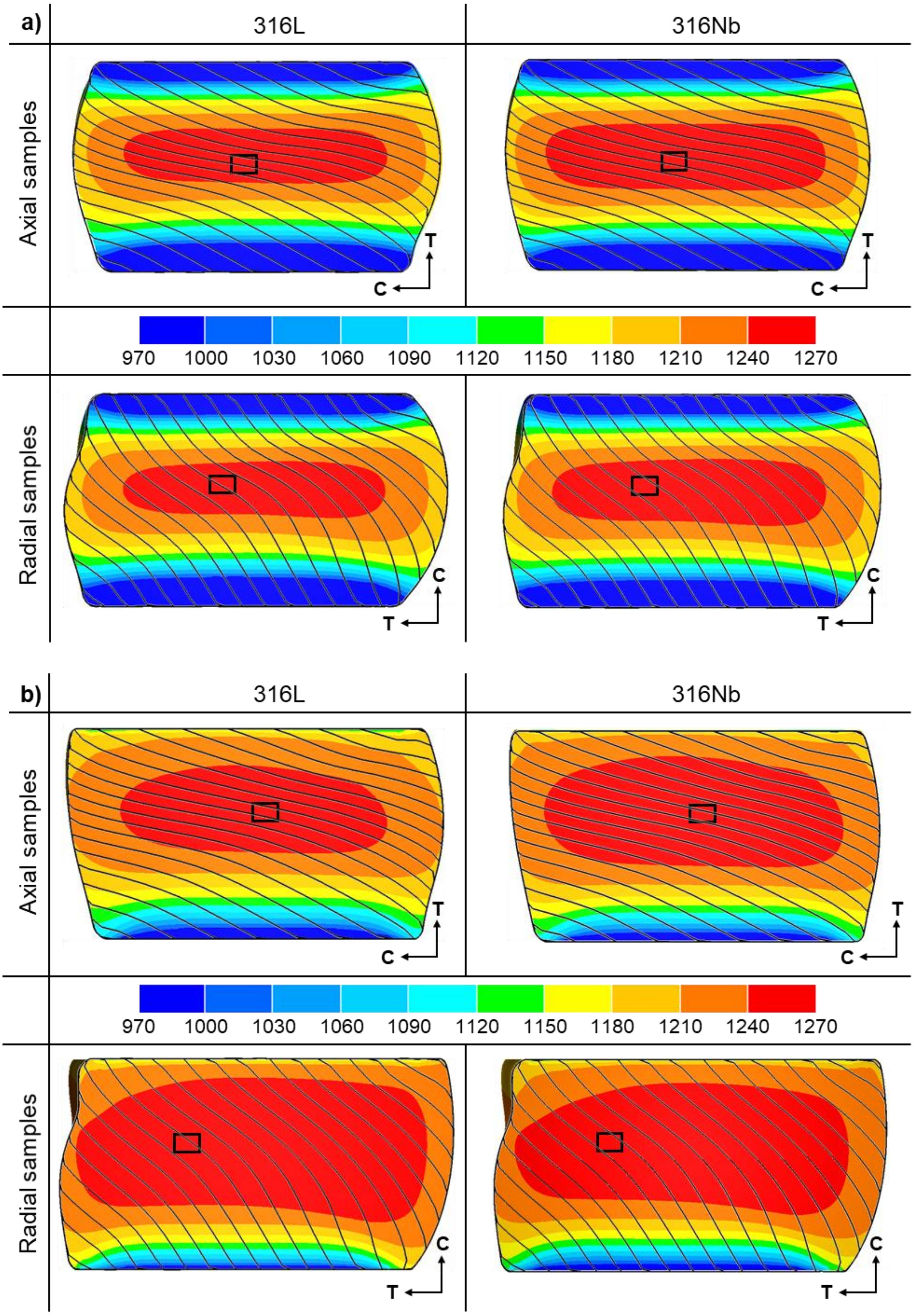

Figure 4.11 : Temperature distributions (°C) predicted by FE simulations at the end of upsetting to 30% reduction in height with deformed marking grids superimposed in Ø 60×60 mm samples forged by a) hydraulic, and b) screw presses. Note that the high strain areas are highlighted by the solid rectangles. The initial orientation and spacing of the marking grid (i.e., prior to upsetting) are depicted in Figure 3.42. Upsetting performed in the vertical direction.

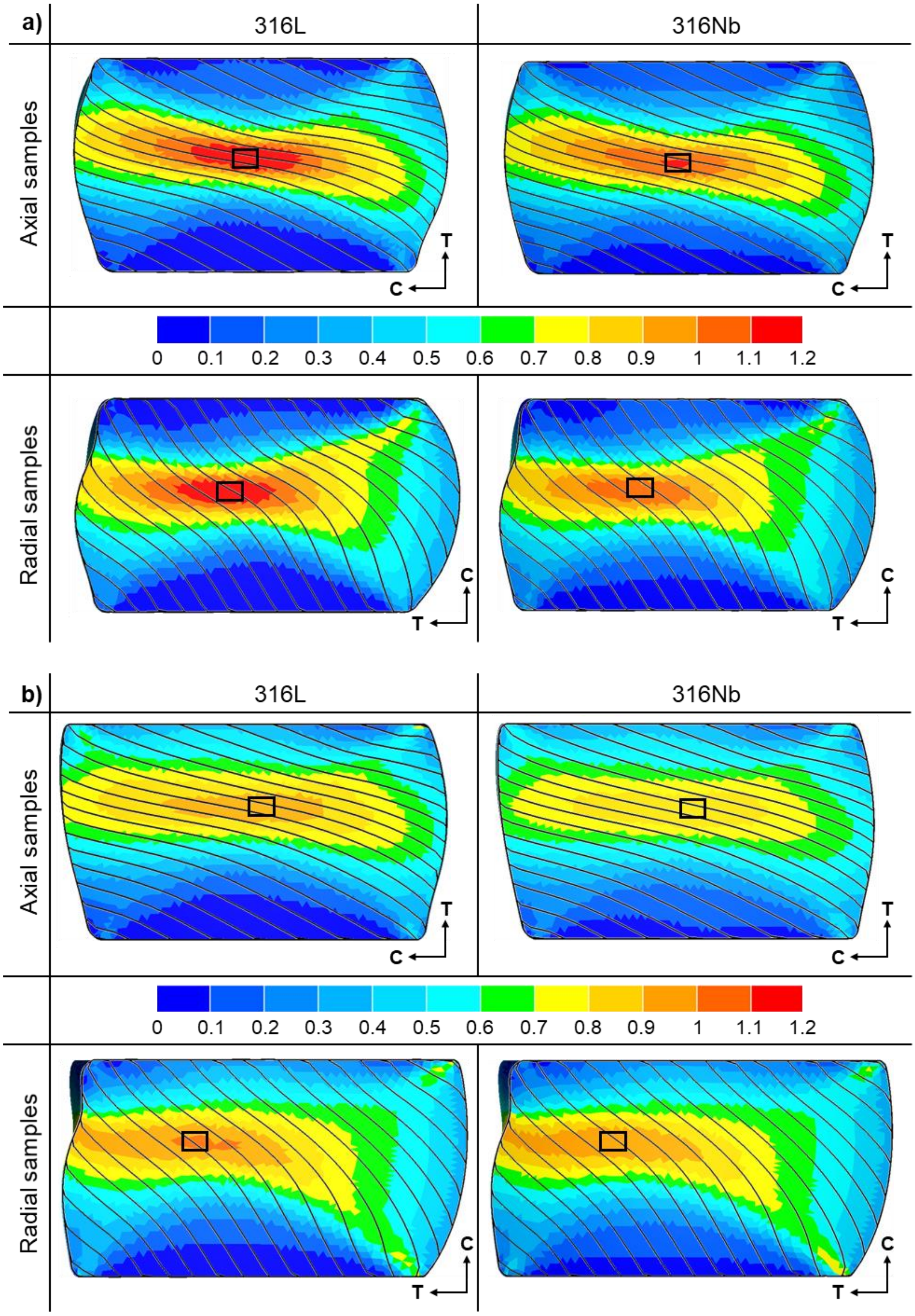

Figure 4.12 : Equivalent strain (-) distributions predicted by FE simulations at the end of upsetting to 30% reduction in height with deformed marking grids superimposed in Ø 60×60 mm samples forged by a) hydraulic, and b) screw presses. Note that the high strain areas are highlighted by the solid rectangles. The initial orientation and spacing of the marking grid (i.e., prior to upsetting) are depicted in Figure 3.42. Upsetting performed in the vertical direction.

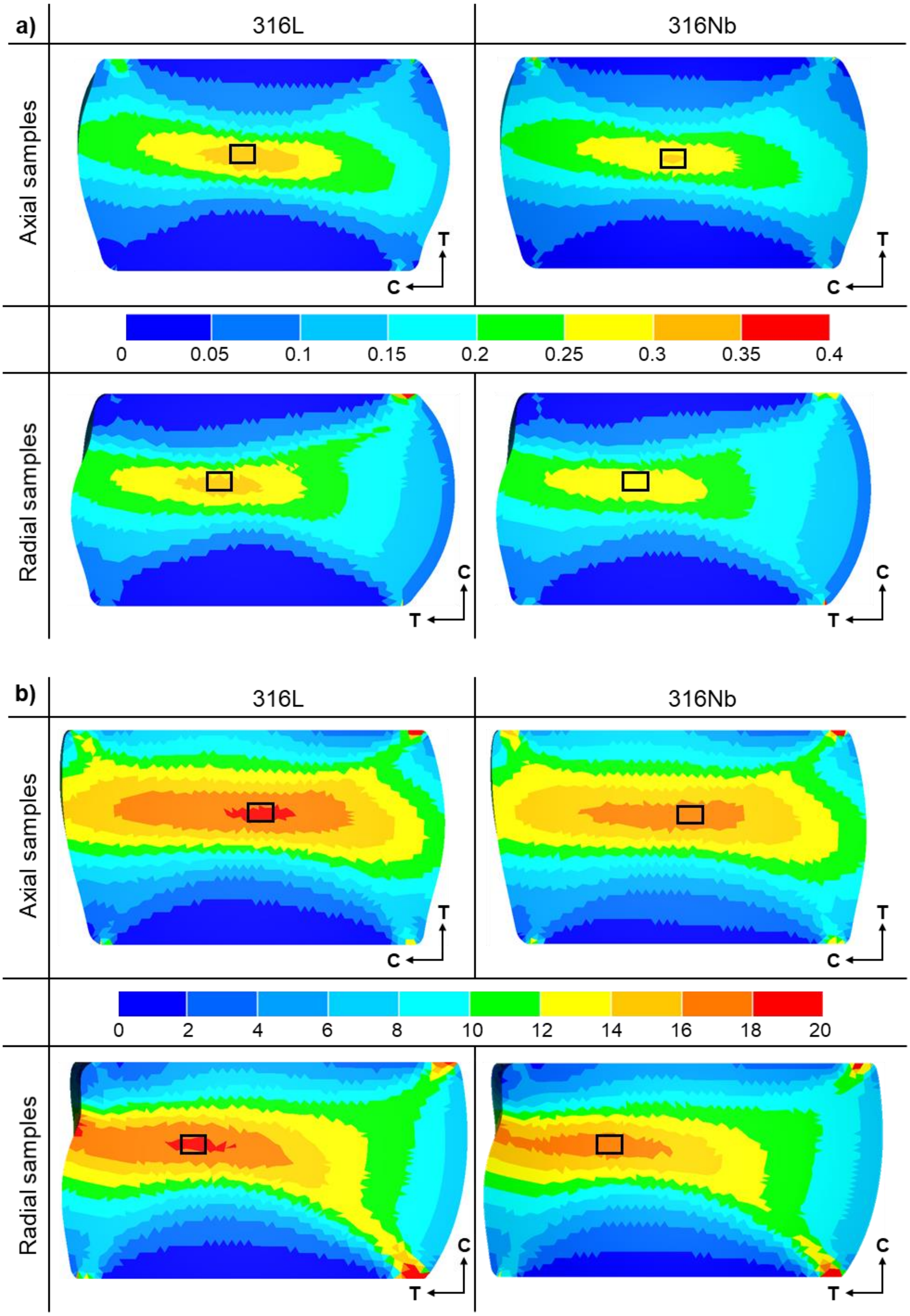

Figure 4.13 : Average strain rate distributions (s^{-1}) predicted by FE simulations at the end of upsetting to 30% reduction in height in Ø 60×60 mm samples forged by a) hydraulic, and b) screw presses. Note that the high strain areas are highlighted by the solid rectangles. Upsetting performed in the vertical direction.

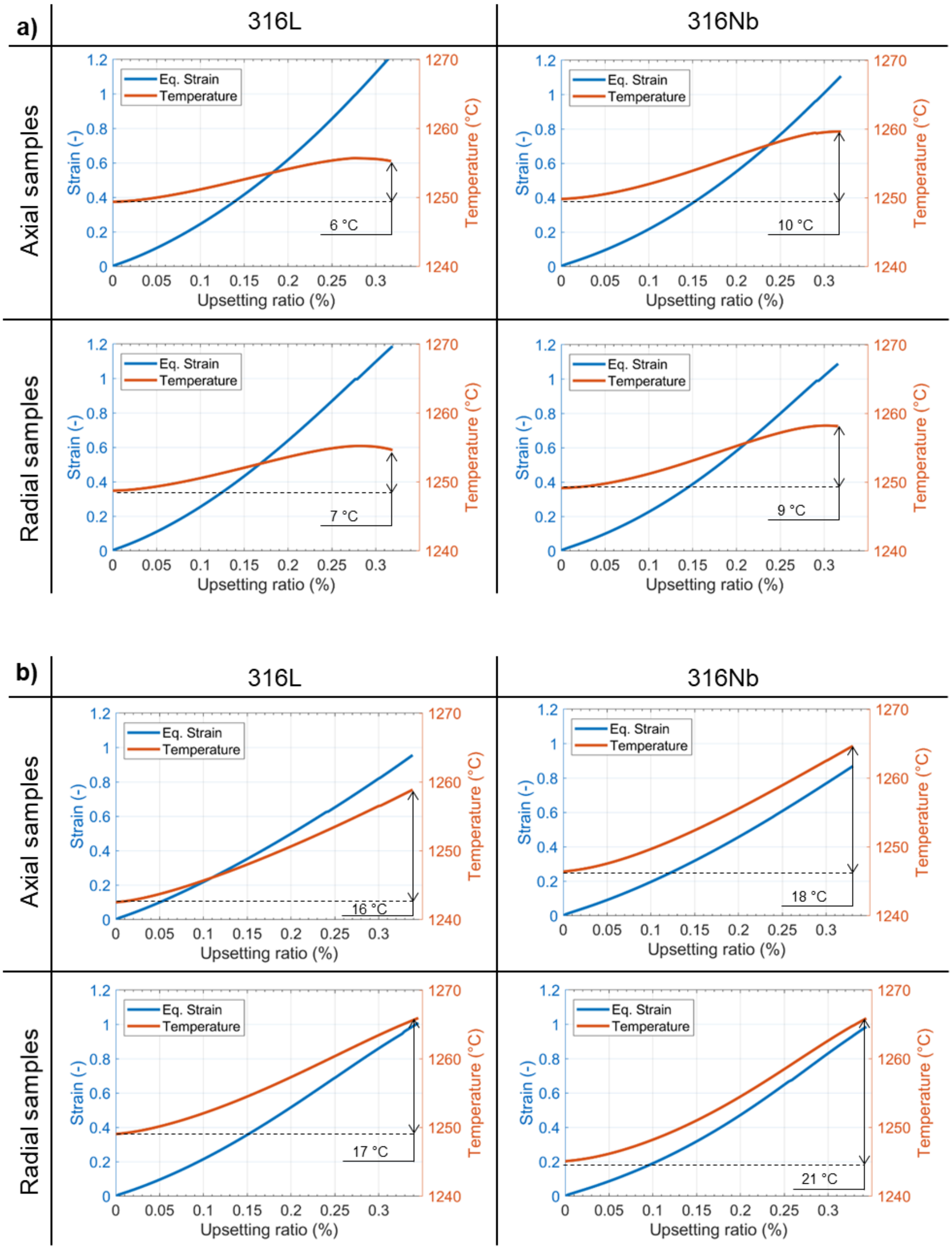

Figure 4.14 : Evolution of equivalent strain (-) and temperature (°C) in the high strain zones during upsetting to 30% reduction in height in Ø 60×60 mm samples forged by a) hydraulic, and b) screw presses.

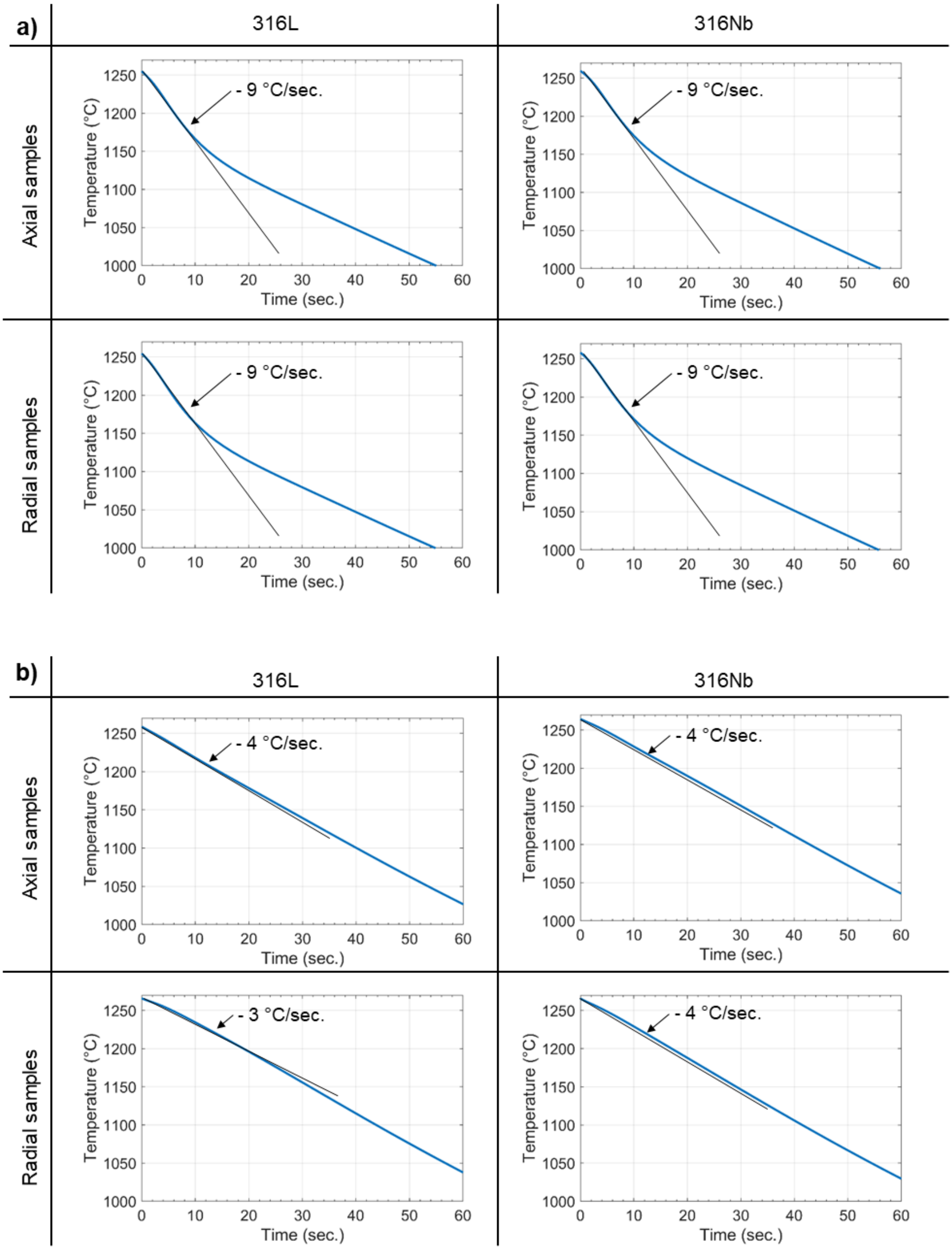

Figure 4.15 : Plots of cooling curves in the high strain zone during air cooling stage, following upsetting to 30% reduction in height in Ø 60×60 mm samples forged by a) hydraulic, and b) screw presses.

4.4 MICROSTRUCTURE EVOLUTION IN THE AS-CAST MATERIAL

This section summarises the results of microstructural observations made on the Ø 60×60 mm samples subjected to the hot upsetting trials described in Section 3.2.2.1. Figures 4.16 and 4.17 show optical microscopy appearances of both materials on the longitudinal cross-sections of the samples, following hot upsetting to 30% at 1250 °C using hydraulic and screw presses, respectively. Following the methodology described in Section 3.4.2, the areas underwent recrystallisation (i.e., recrystallised grains) were extracted and superimposed on the longitudinal cross-section of the samples for each case. Higher magnification images of Figures 4.16 and 4.17 are provided in Appendix D. Though, the progress of recrystallisation was observed to be at different levels depending on strain rate (i.e., press type). Recrystallisation appear to occur predominantly around the centre of the samples, where the material experienced deformation at high strain, strain-rate and temperature (see Section 4.3). The as-cast samples forged by hydraulic press demonstrated a clear evolutionary trend at the early stage of recrystallisation. For instance Figure 4.16 show partially recrystallised microstructures. These samples showed that recrystallisation occurs along strip-wise regions, termed as "recrystallised bands" in this thesis hereafter, which were matching with the deformed marking grids implemented in the FE simulations to track the location of virtual grain boundaries with ≈ 60° to the axis of the ingot (see Figure 4.18). On the other hand, the core of the samples forged using the screw press were almost fully recrystallised (see Figure 4.17). In Figure 4.16 a) and b), the cross-section of the axial and radial 316L samples forged by the hydraulic press presented a similar level of recrystallisation, whereas the axial and radial 316Nb samples are the opposite (see Figure 4.16 c) and d)). The different progress of recrystallisation observed between the samples forged by the hydraulic and screw presses is ascribed to the different temperature evolution between each case, owing to the adiabatic heating generated by the high strain rate deformation on the screw press (see Section 4.3). Hence, partial DRX occurred in all samples, and recrystallisation may significantly extended with MDRX in the samples forged by the screw press, compared to those forged on the hydraulic press.

Representative high resolution micrographs taken from the central region of the forged samples (see the solid rectangle in Figures 4.16 and 4.17), which underwent high strain levels (≈ 0.9 to 1.2, see Figure 4.12) are shown in Figures 4.19 and 4.22. The higher magnification micrographs obtained from the samples forged on the hydraulic press (see Figures 4.19 and 4.20) demonstrate the heterogeneous nature of recrystallisation and a clear difference in the range of grain size being observed. It is apparent that recrystallisation was initiated predominantly from the parent grains boundaries (i.e., as-cast microstructure) where in some cases the initial parent grains were fully recrystallised. Bands of small recrystallised grains were observed at the boundaries of parent microstructure, where recrystallisation tends to progress into the adjacent parent grains, orthogonally to the traces of the grain boundaries (see the arrows in Figure 4.19). The preferential recrystallisation at grain boundaries of the parent grains was consistent with the orientation relationship previously highlighted at the scale of the samples between the starting microstructure and the recrystallised bands (see Figures 4.16 and 4.18). The fully recrystallised microstructures observed in both 316L and 316Nb samples forged using the screw press are shown in Figures 4.21 and 4.22, respectively. Grain size heterogeneities were observed in these samples, with the presence of smaller recrystallised grains aligned along the direction of the former parent grain boundaries. A noticeable amount of undissolved secondary phases were also observed within all the 316Nb samples (see Figures 4.20 and 4.22), even though they were subjected to a homogenisation heat treatment prior to forging. Microstructure observations performed in additional locations of the longitudinal cross-sections of the samples revealed the presence of serrated grain boundaries (see Figure 4.23), remnant non-recrystallised grains in recrystallised areas (see Figure 4.24), deformation bands (see Figure 4.25) and heterogeneities in grain size (see Figure 4.26).

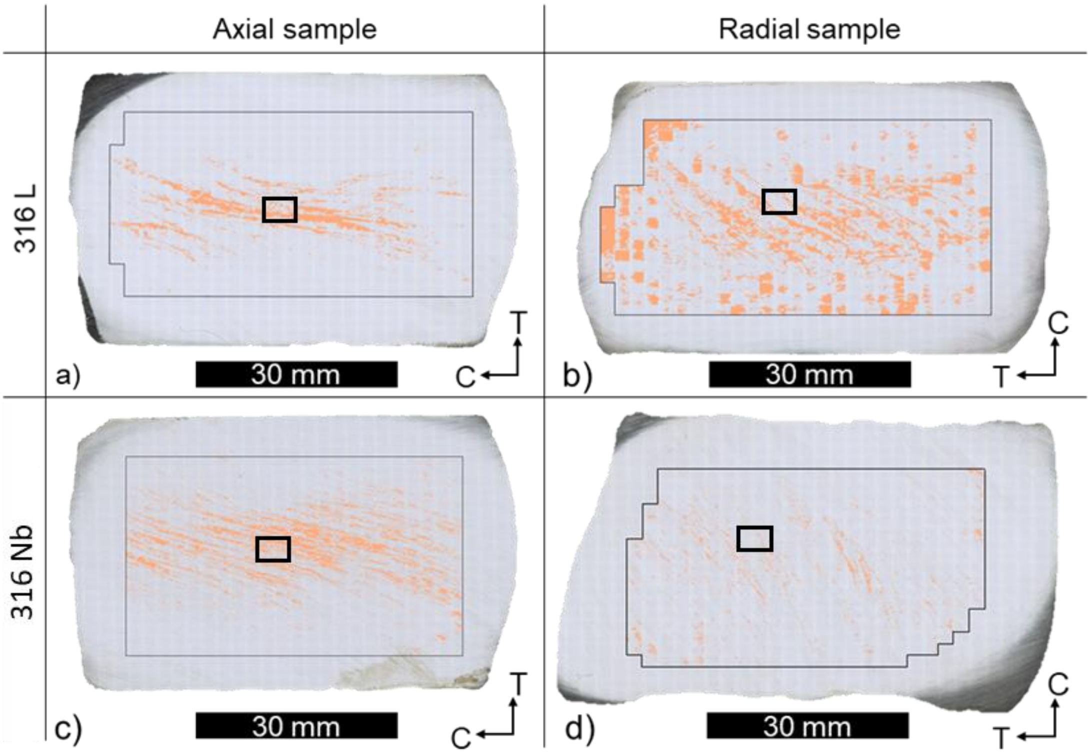

Figure 4.16 : Plots of recrystallised grains imposed on the longitudinal cross-sections of the samples after 30% upsetting at 1250 °C using the hydraulic press; a) axial 316L, b) radial 316L, c) axial 316Nb, and d) radial 316Nb samples. The solid rectangles highlight the high strain areas from which high magnification micrographs were taken and shown in Figures 4.19 and 4.20.

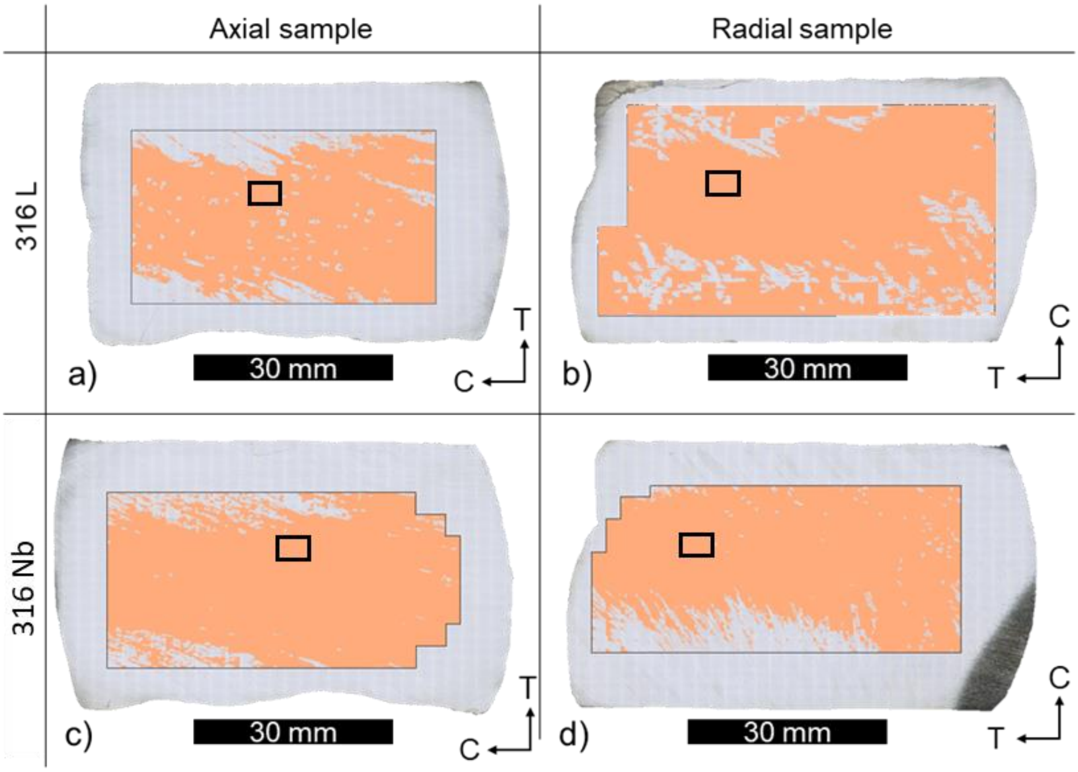

Figure 4.17: Plots of recrystallised grains imposed on the longitudinal cross-sections of the samples after 30% upsetting at 1250 °C using the screw press; a) axial 316L, b) radial 316L, c) axial 316Nb, and d) radial 316Nb samples. The solid rectangles highlight the areas from which high magnification micrographs were taken and shown in Figures 4.21 and 4.22.

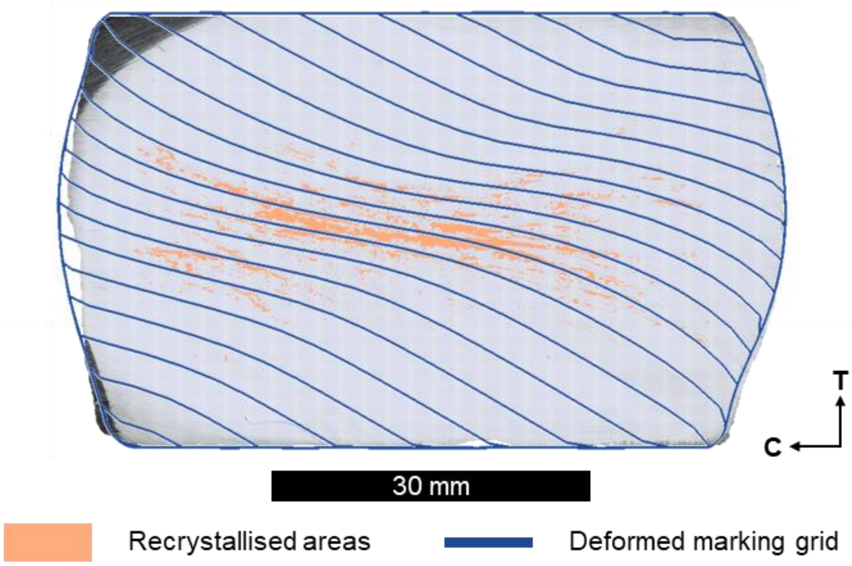

Figure 4.18: Superposition of the deformed marking grid (blue lines), initially aligned parallel to the long axes of the grains in the FE model, with the plots of recrystallised grains (orange areas) imposed on the longitudinal cross-sections of the 316L sample after 30% upsetting at 1250 °C using the hydraulic press.

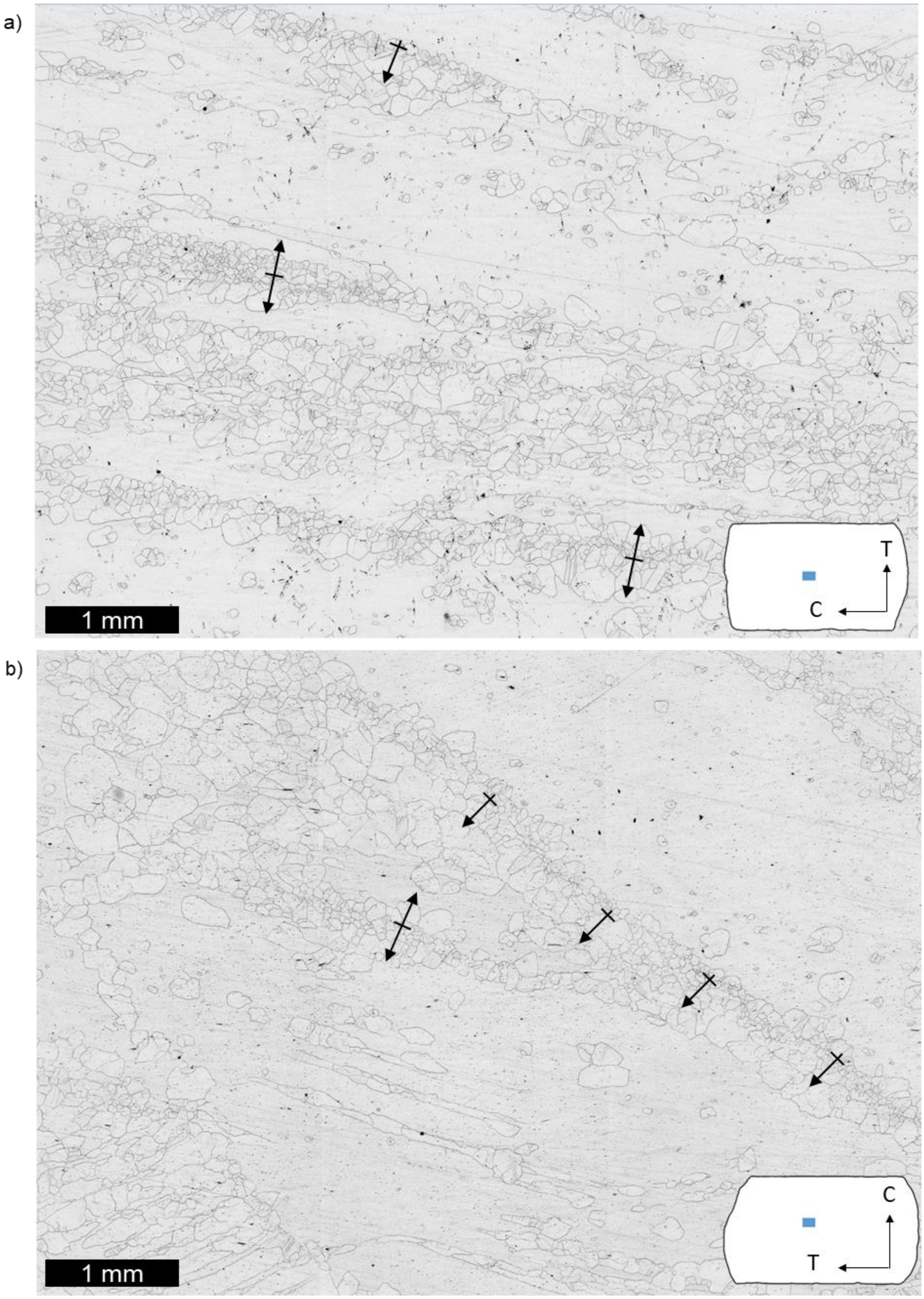

Figure 4.19 : Optical microscopy appearances of the a) axial and b) radial 316L samples after upsetting to 30% at 1250 °C using the hydraulic press, taken from the high strain zone (ε ≈ 1.1 to 1.2). The formation of necklace structure (i.e., small recrystallised grains) and the direction of progress of recrystallisation are highlighted. The micrographs were obtained by stitching 3×3 smaller micrographs together. Upsetting was performed in the vertical direction.

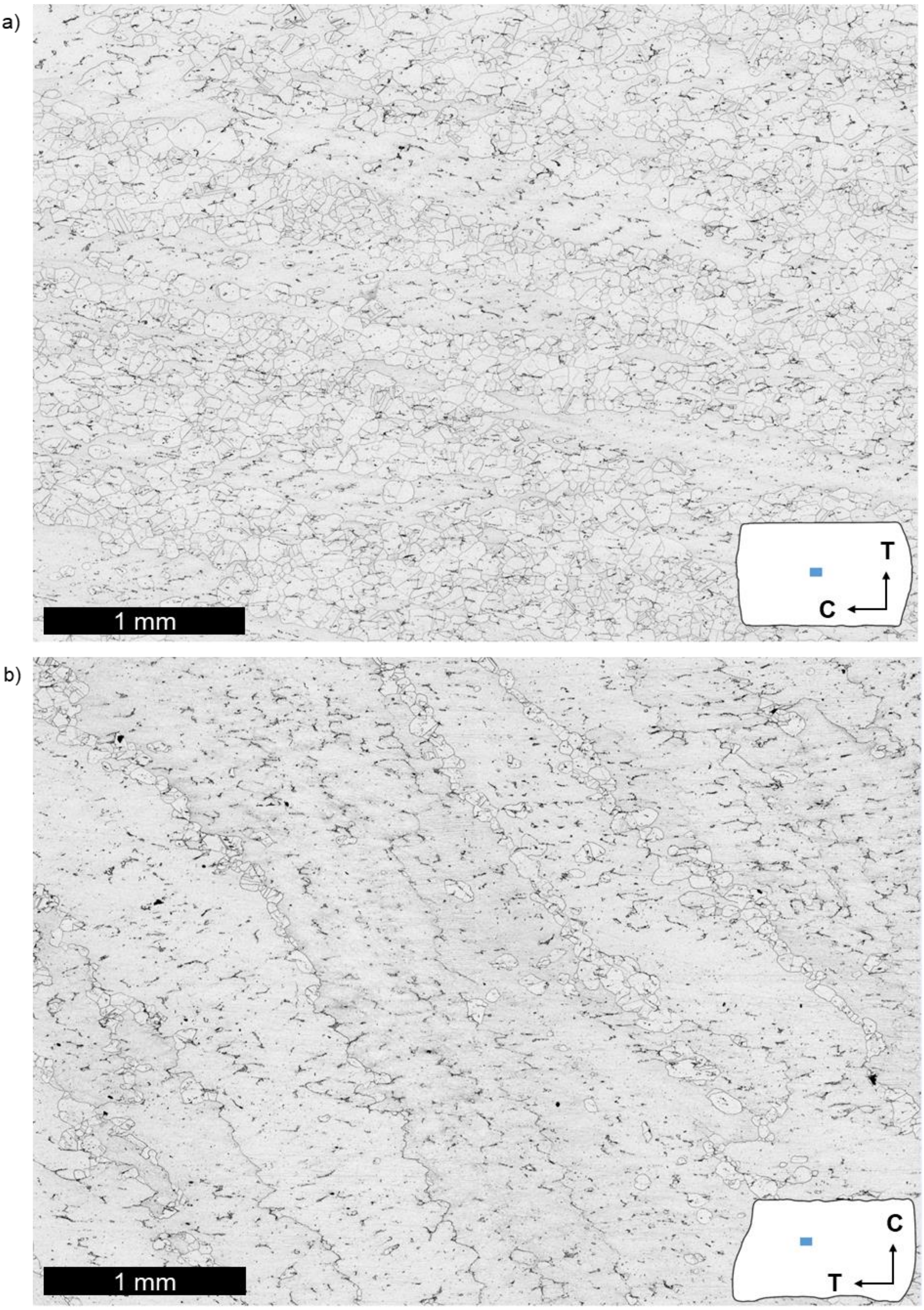

Figure 4.20 : Optical microscopy appearances of the a) axial and b) radial 316Nb samples after upsetting to 30% at 1250 °C using the hydraulic press, taken from the high strain zone ($\varepsilon \approx 1.1$ to 1.2 and 1 to 1.1, respectively). The micrographs were obtained by stitching 2×2 smaller micrographs together. Upsetting was performed in the vertical direction.

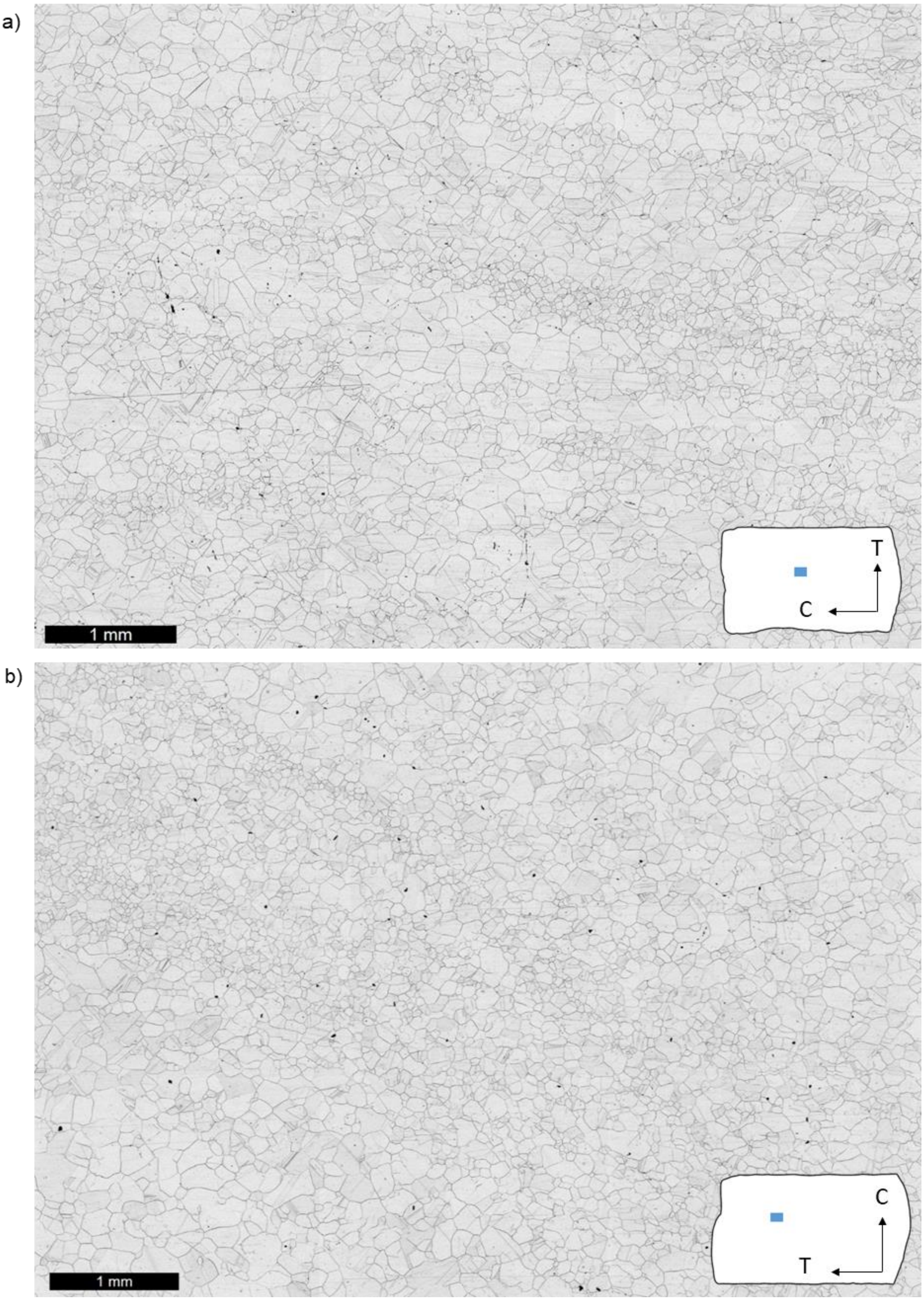

Figure 4.21 : Optical microscopy appearances of the a) axial and b) radial 316L samples after upsetting to 30% at 1250 °C using the screw press, taken from the high strain zone ($\varepsilon \approx 0.9$ to 1 and 1 to 1.1, respectively). The micrographs were obtained by stitching 3×3 smaller micrographs together. Upsetting was performed in the vertical direction.

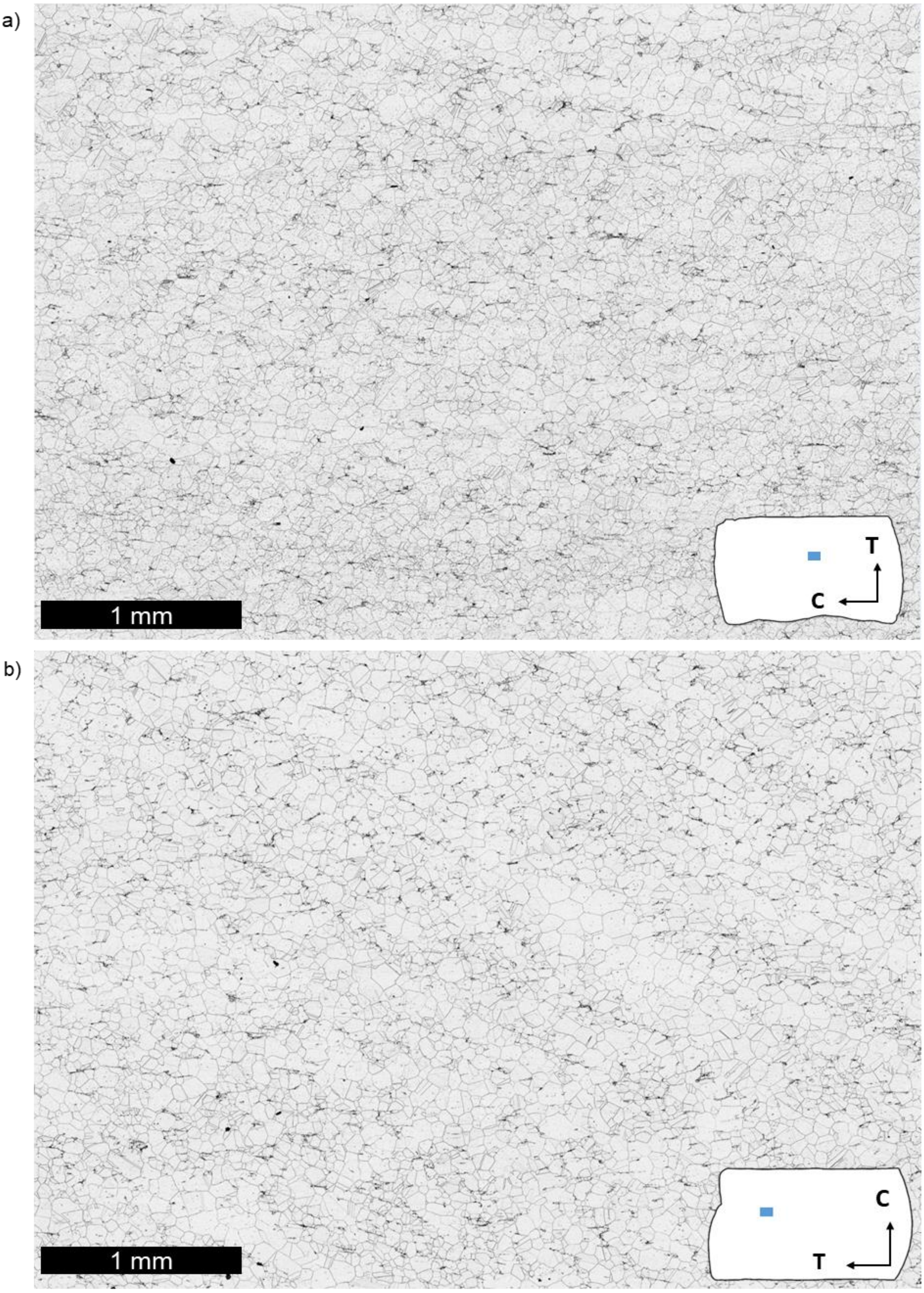

Figure 4.22 : Optical microscopy appearances of the a) axial and b) radial 316Nb samples after upsetting to 30% at 1250 °C using the screw press, taken from the high strain zone (ε ≈ 0.8 to 0.9 and 0.9 to 1, respectively). The micrographs were obtained by stitching 2×2 smaller micrographs together. Upsetting was performed in the vertical direction.

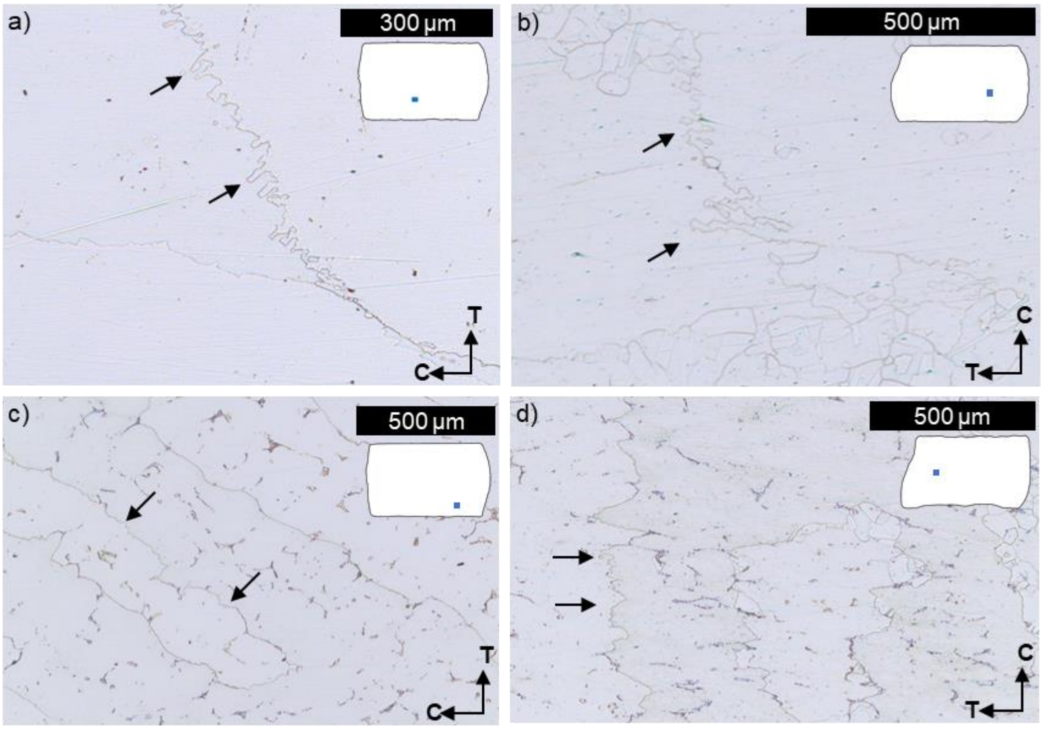

Figure 4.23 : Microstructure details of serrated grain boundaries observed in samples forged on the hydraulic press, a) and b), axial and radial 316L samples, respectively, and c) and d), axial and radial 316Nb samples, respectively.

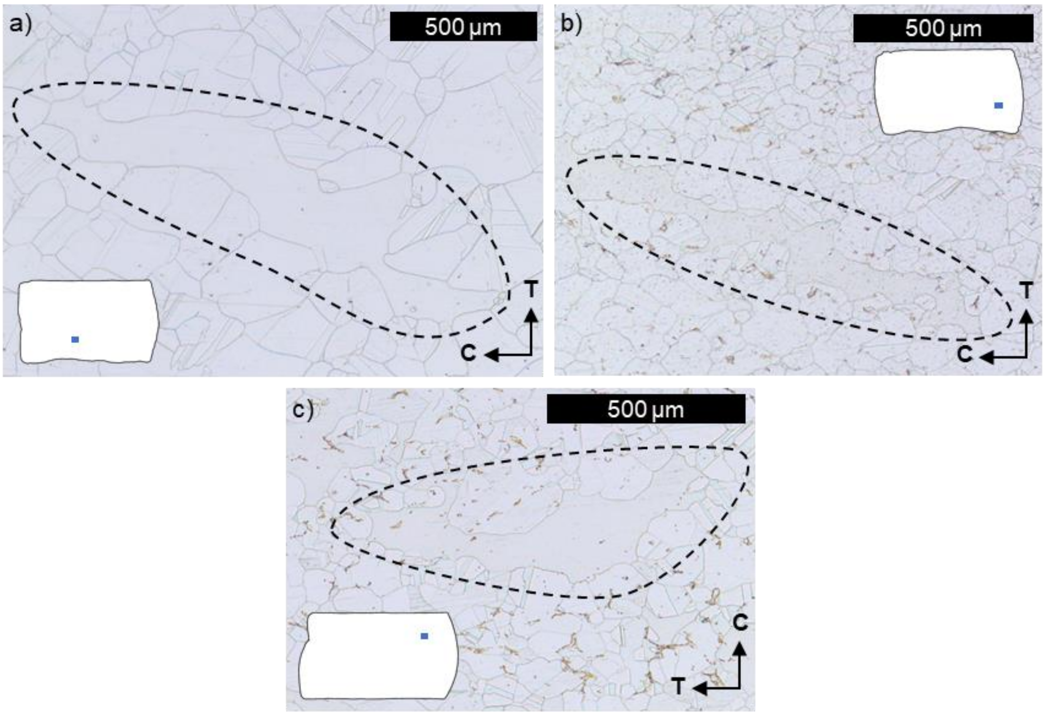

Figure 4.24 : Microstructure details of non-recrystallised grains observed in recrystallised areas of the samples forged on the screw press, a) axial 316L sample, b) and c) axial and radial 316Nb samples.

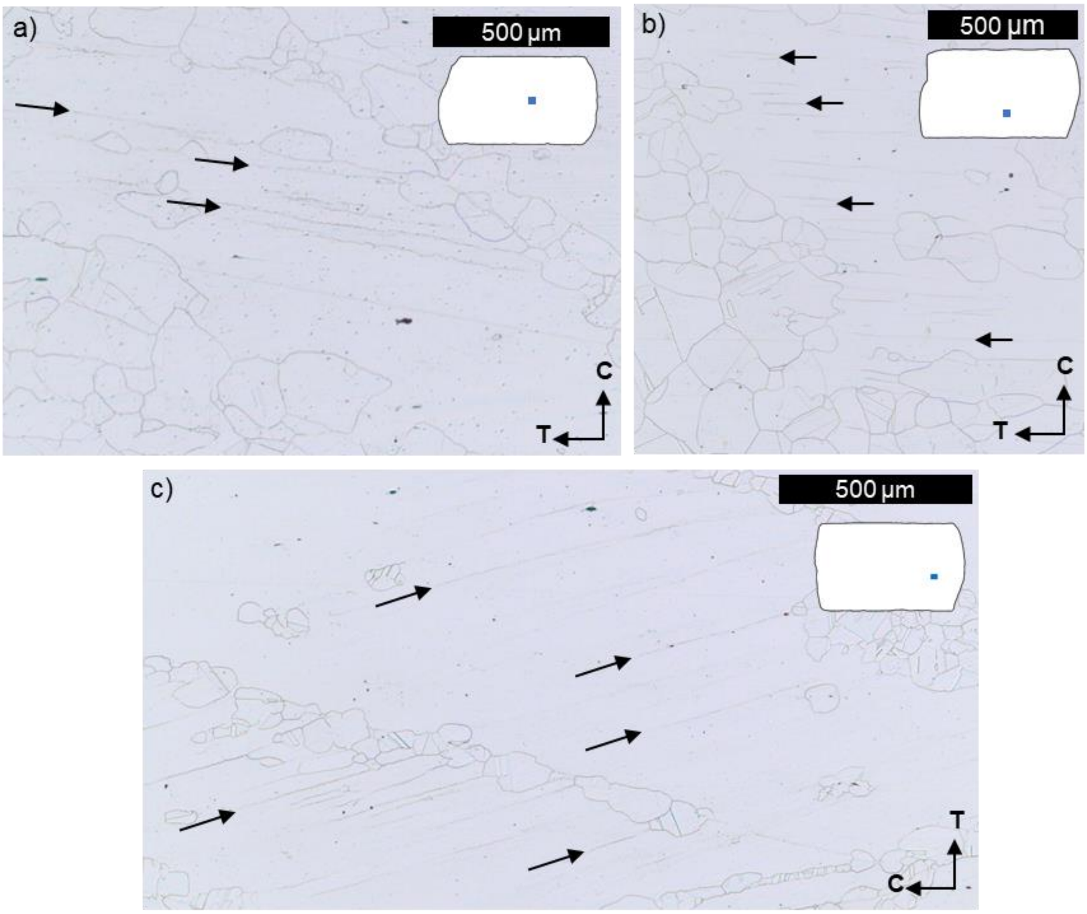

Figure 4.25 : Microstructure details of deformation bands observed in 316L samples: radial samples forged on the a) hydraulic and b) screw presses, and c) axial sample forged on the hydraulic press.

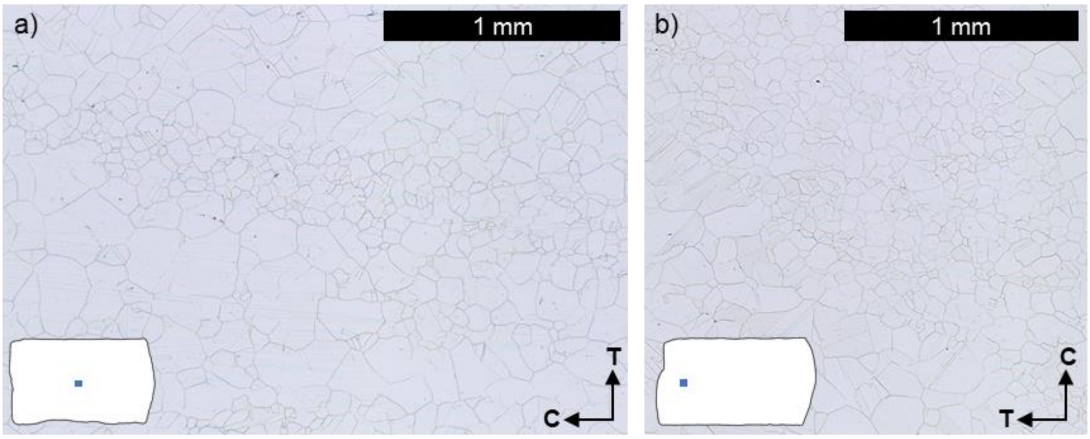

Figure 4.26 : Microstructure details of grain size heterogeneities observed in 316L samples forged on the screw press, a) axial, and b) radial samples.

The distribution of the equivalent grain diameter and the corresponding cumulative fractions measured on these selected micrographs are presented in Figures 4.27 and 4.28 for the samples forged by the screw and hydraulic presses, respectively. The measurements of the fraction of recrystallised grains and average equivalent grain diameters performed on these micrographs are summarised in Figure 4.29. Accordingly with the observation, the microstructure was partially recrystallised in the 316L (i.e., 39 and 34%) and 316Nb samples (i.e., 70 and 9%) forged by the hydraulic press, and fully recrystallised (i.e., ≈ 100%) in the samples forged by the screw press. For the samples forged by the hydraulic press, the average equivalent diameter of the recrystallised grains measured for the axial sample (58 μm) was smaller than that measured for the radial sample (78 μm), as shown in Figure 4.27 a). Conversely, the grain size distribution shown in Figure 4.28 for the samples forged by the screw press looked similar for both the axial and radial samples of each grade of material, but the measured equivalent grain diameters of the 316L samples were twice as large as those measured for the 316Nb samples (see Figure 4.29).

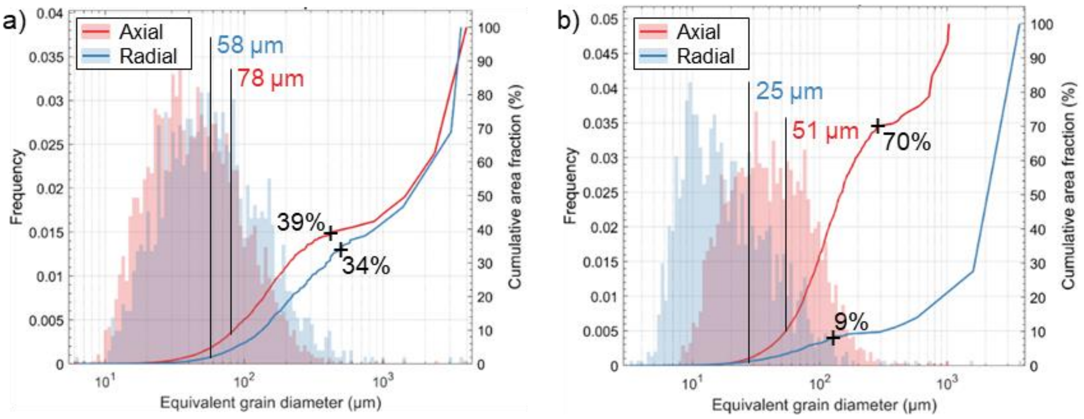

Figure 4.27 : Plots of the frequency of equivalent grain diameter and associated cumulative area fraction for the a) 316L, and b) 316Nb samples forged by the hydraulic press.

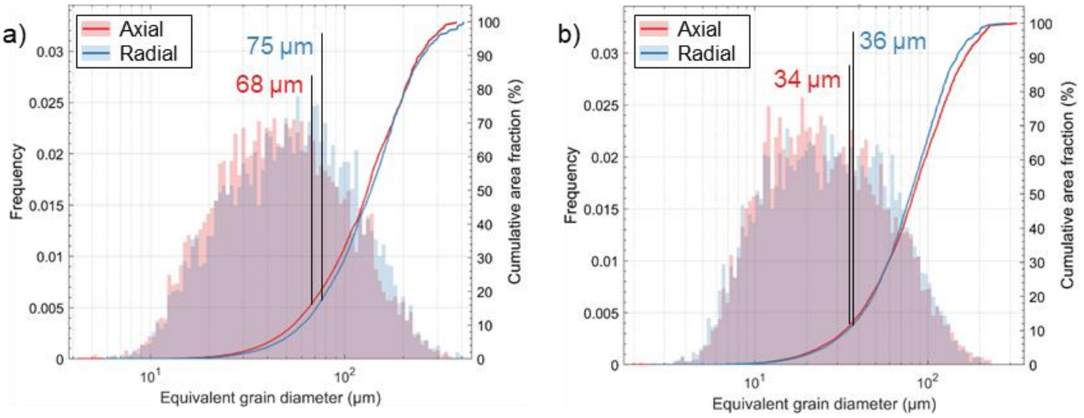

Figure 4.28 : Plots of the frequency of equivalent grain diameter and cumulative area fraction measured in the a) 316L, and b) 316Nb samples forged by the screw press.

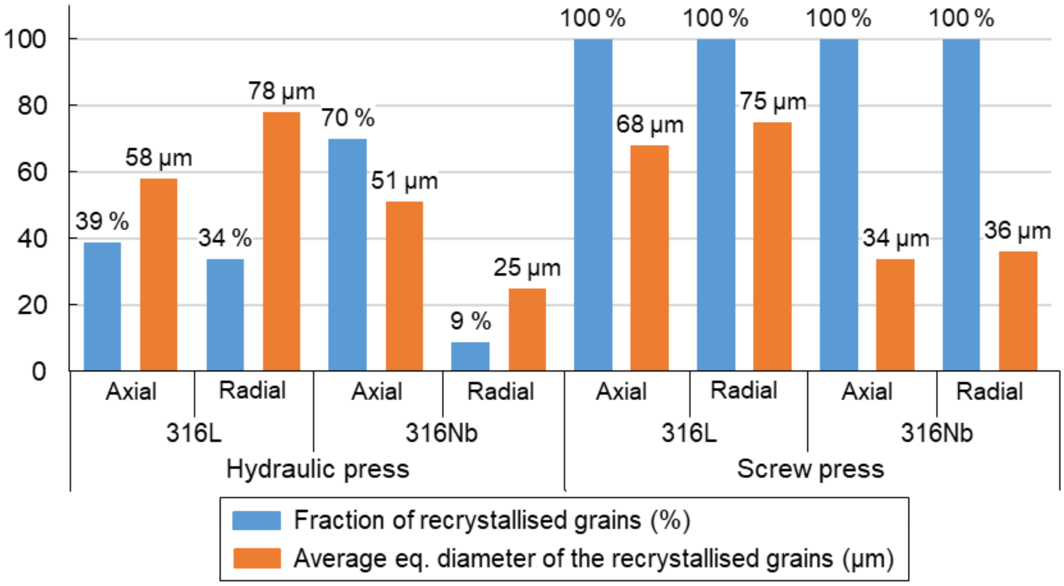

Figure 4.29 : Quantitative microstructure characteristics, including the fraction of recrystallised grains and the equivalent grain diameters, measured on the micrographs extracted from the Ø 60×60 mm samples after upsetting.

4.5 SUMMARY

In this Chapter, the evolution of the as-cast material during the ingot-to-billet conversion process was investigated using upsetting tests performed on Ø 60×60 mm samples taken out in two different orientations from 316L and 316Nb (0.7% Nb) ingots.

Use of FE models with as-cast material anisotropic flow behaviour integrated was validated on the basis of shape correlation. The quantitative analysis method developed for the measurements of the fraction of recrystallised grains and equivalent diameters of the recrystallised grains allowed to study the progress of recrystallisation throughout the experiments. Especially, the occurrence of recrystallisation and its heterogeneous nature was highlighted at the scale of the samples. Microstructure observations and correlation with FE results showed that few DRX occurred during the upsetting tests but that MDRX was probably the dominant grain refinement mechanism of the as-cast material under the investigated thermomechanical conditions. The addition of Nb in the 316Nb grade was shown to promote the recrystallisation and lead to a finer recrystallised microstructure. The sensibility of the evolution of microstructure to the test orientation remains however unclear due to the specific orientation of the elongated as-cast grains to the direction of the upsetting.

The representability of the results obtained at a small scale regarding the industrial ingot-to-billet conversion process (i.e., upsetting and cogging) performed on entire ingots has now to be assessed and validated through larger scale experiments.

Chapter 5 : FORGING TRIALS ON ENTIRE INGOTS

CONTENT

5.1 INTRODUCTION

This chapter summarises the results obtained for upsetting and cogging trials designed to simulate the initial stages of the industrial scale ingot-to-billet conversion, which were performed on ≈ Ø 185 mm VIM/VAR processed ingots made from types 316L and 316Nb austenitic stainless steels (see Section 3.2.2.2). The upsetting test was performed using a hydraulic press with 2 500 tonnes capacity, and the cogging trials using a screw press with 28.9 kJ capacity. The actual geometries of the forged ingots were measured and compared with those predicted by FE simulations, and the thermomechanical properties of the ingots throughout the trials are presented. Microstructural observations were made and quantitative measurements of the progress of recrystallisation were carried out on specimens extracted from longitudinal cross-sections of the ingots after the tests.

5.2 DEFORMATION BEHAVIOUR OF THE INGOTS

The 3D geometry of the 316Nb grade ingot after 40% upsetting, measured by optical GOM scanning, is presented in Figure 5.1, where the longitudinal and transversal gaps are the sections extracted for microstructure characterisations (see Figure 3.48). The shape of the ingot showed a different deformation behaviour between top, bottom and middle sections, which can be due to the presence of different starting microstructures throughout the ingot (e.g., the chill zone at the bottom where the remelting process initiated, see Figure 3.5). Areas prone to folding (highlighted by the circles in Figure 5.1) were observed at the surface of the ingot, corresponding to the transition between the chill zone and the middle of the ingot. The slight misalignment observed between the upper and lower surfaces of the ingot after upsetting suggests the occurrence of reasonable shearing during the upsetting trial, which can be attributed to the misalignment of the ingot with the lower die prior to the upsetting test, to the temperature and/or friction distribution, or to the microstructure heterogeneity. The predicted geometries obtained by the FE model for the 316Nb ingot after 40% upsetting, considering both isotropic and anisotropic material behaviours, are presented in Figure 5.2. Even though the FE model with anisotropic material model implemented does not account for local microstructure at the chill zone, the results presented in Figure 5.2 demonstrate that implementing material's anisotropic behavior predicted the diabolic shape of the ingot (see the arrows) after 40% upsetting, compared with the isotropic material model.

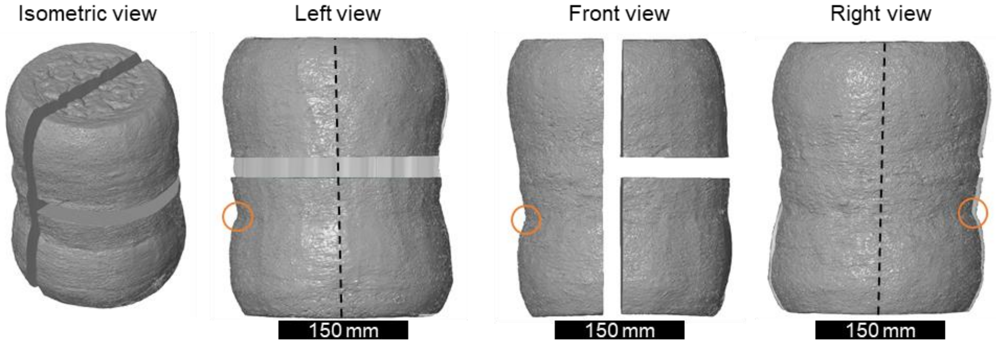

Figure 5.1 : Reconstructed 3D geometry of the 316Nb ingot after upsetting, obtained by GOM ATOS®, with the areas prone to folding highlighted by circles.

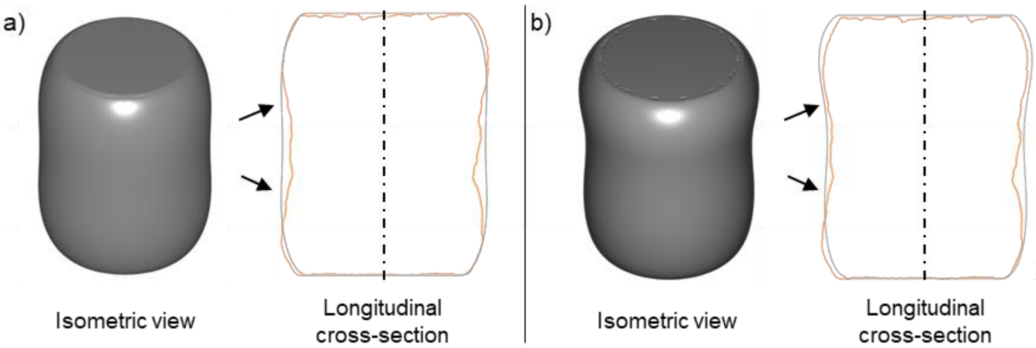

Figure 5.2 : The final geometry of the 316Nb ingot predicted by FE simulation after 40% upsetting; a) isotropic, and b) anisotropic material models implemented, and compared to the experimentally measured cross-section of the ingot (orange line). The arrows highlight the areas where main differences were observed.

The geometry of the ingots forged by cogging are presented in Figure 5.3, where indications are given to identify the "top" of the bars, according to the direction of remelting (i.e., head of the arrows). The bars forged with the bottom of the ingot held by the manipulator presented a peculiar feature, which was not as pronounced for the 316Nb ingot forged in the reversed direction (i.e., the area highlighted via a circle in Figure 5.3 in comparison with other cases in the same figure). This different behaviour can be due to local characteristics since the microstructure located at the end of the ingot was that of the chill zone, with the grains parallel to the axis of the ingot (see Figure 3.5). It can be seen from Figure 5.4 that the specific deformation behavior of the extremity of the cogged ingots was relatively well predicted by the FE model with anisotropic yield behavior implemented, and this model was therefore used to describe the thermomechanical properties of the ingots during cogging.

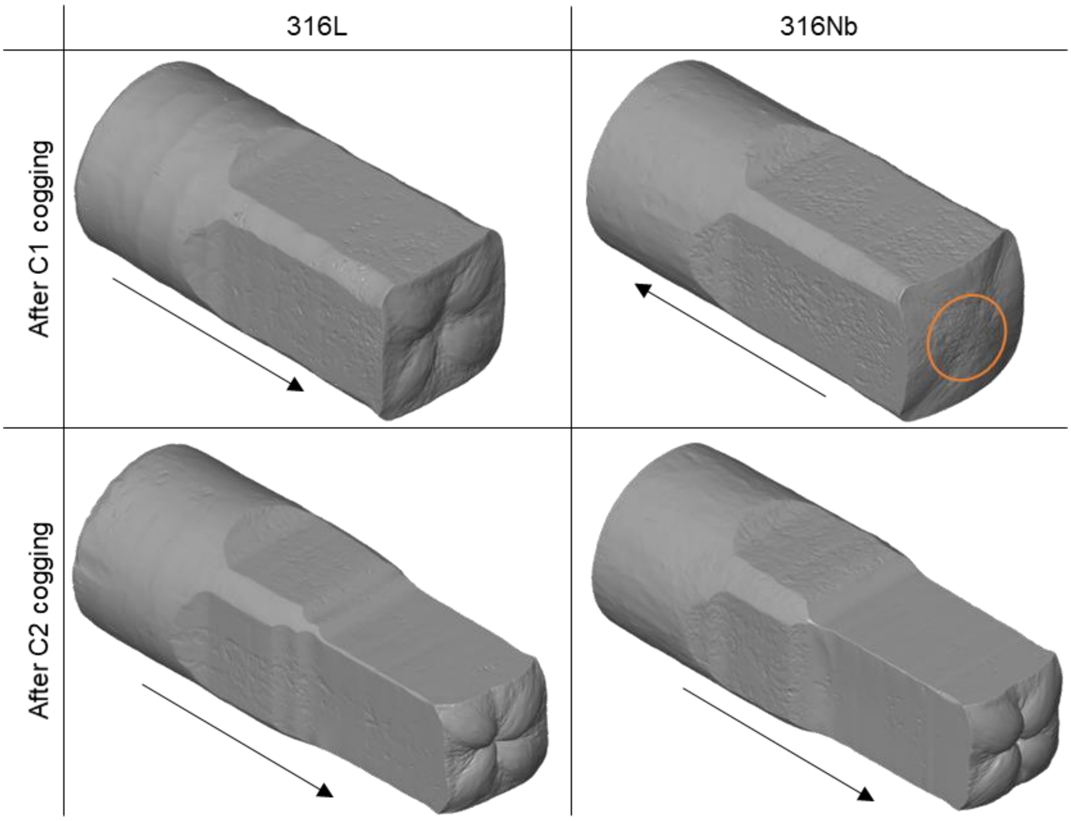

Figure 5.3 : 3D geometry of the 316L and 316Nb grade ingots after cogging, obtained by GOM ATOS®, showing a peculiar deformation behaviour of the extremity of the ingots, except for that forged in reverse orientation (highlighted by the orange circle). The direction of remelting is indicated by an arrow for each case. The round (i.e., non-deformed) end of the bar for each case was for holding by the manipulator.

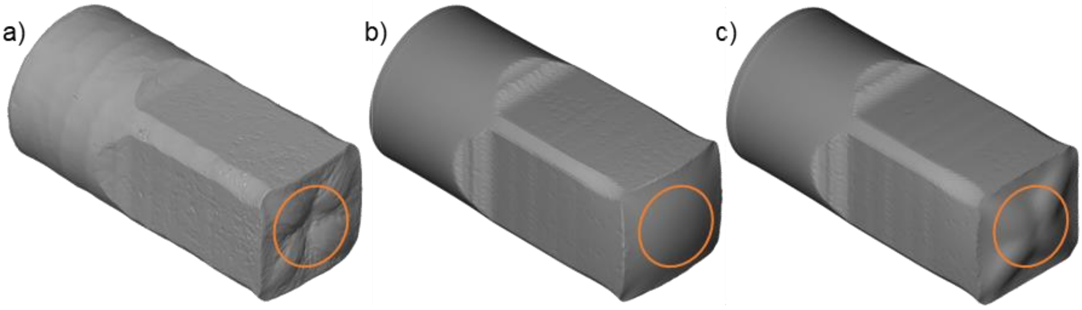

Figure 5.4 : Comparison between the experimentally measured 3D geometry and those predicted by FE simulations; a) the 3D scanned geometry, b) and c) FE predicted shapes of the 316Nb ingot after the cogging C1, obtained from isotropic and anisotropic material models, respectively.

5.3 THERMOMECHANICAL PROPERTIES

Plots of temperature distributions predicted by FE simulations at the beginning and at the end of upsetting and cogging operations are presented in Figures 5.5 and 5.6, respectively. In Figure 5.5 a), the zone with a temperature below 1200 °C prior to the upsetting had a thickness of ≈ 20 mm, as a consequence of the ≈ 60 seconds transfer of the ingot from the furnace to the press. The temperature in the central region of the ingot remained above 1245 °C at the end of the upsetting, and temperatures in the range of 1250 to 1275 °C were predicted at the core of the ingot (i.e., above the initial 1250 °C) which is a consequence of adiabatic heating generated during deformation. It can be seen from Figure 5.6 a) that a similar temperature profile was predicted for all ingots subjected to cogging. The low temperature zone at the proximity of the edges (i.e., T < 1200 °C) had a thickness of ≈ 10 mm, which is thinner than that predicted for the ingot prior to upsetting (i.e., ≈ 20 mm), as a refractory coating was applied on the surface of these ingots to minimise heat loss. Despite this, the FE predictions showed that a large volume of the ingots remained at elevated temperatures (i.e., above 1240 °C) before forging. Figure 5.6 b) shows a significant drop in temperature, below 1000 °C, occurred in the ingots during cogging as a consequence of a relatively long duration of these trials (i.e., from ≈ 7 to 9 minutes).

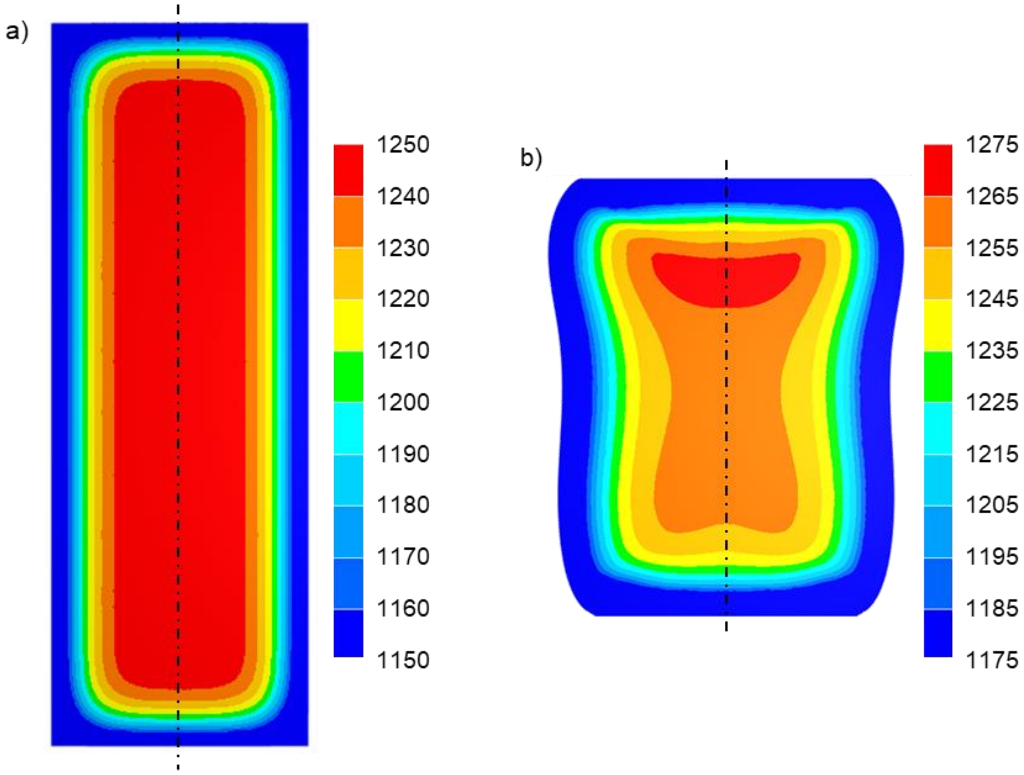

Figure 5.5 : Temperature (°C) distributions predicted by FE simulations at a) the beginning, and b) the end of the 40% upsetting. Note that the temperature scale used in b) is extended above 1250 °C to display the effects of adiabatic heating.

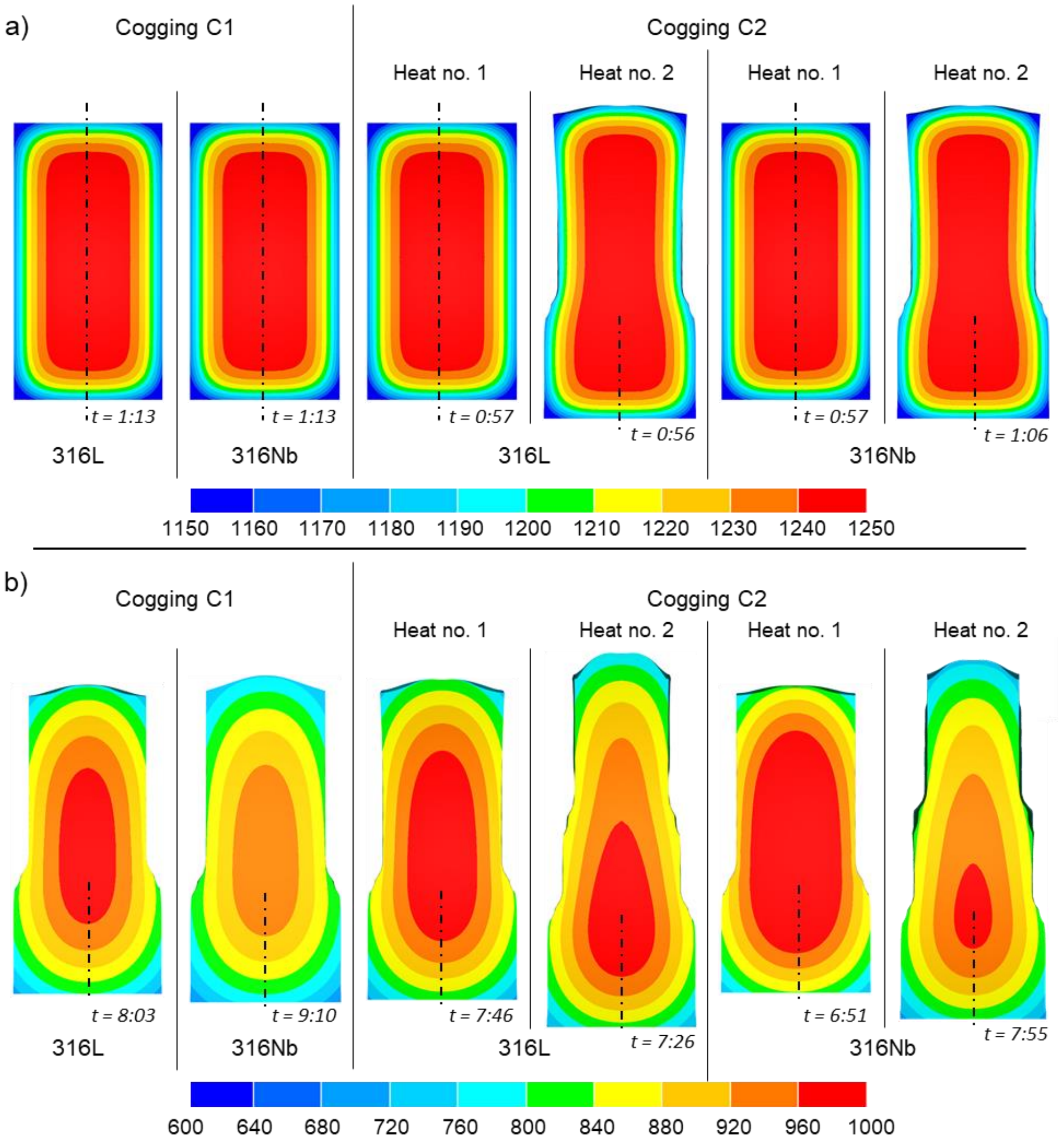

Figure 5.6 : Temperature (°C) distributions predicted by FE simulation along the longitudinal cross-section of the ingots; at the a) beginning, and b) end of coggings. The scale is set to highlight temperature gradients and differences between the ingots. Note that the duration of the transfer of the ingot from the furnace to the press, and of the cogging operations are indicated in each case in “mm:ss” format.

The cooling curves (i.e., the evolution of temperature during the air cooling stage) predicted by FE simulations in the ingots after the upsetting and coggings are displayed in Figures 5.7 and 5.8, respectively. The average cooling rate estimated from these curves, during the first five minutes of the post forging cooling stage, were ≈ 25 °C/min and ≈ 30 °C/min for the upset and cogged ingots, respectively. It must however be noted that, at the beginning of the cooling stage, the temperature was significantly higher in the ingot subjected to upsetting (i.e., ≈ 1200 °C, see Figure 5.7 a)) than the cogged ingots (i.e., below 1000 °C, see Figure 5.8).

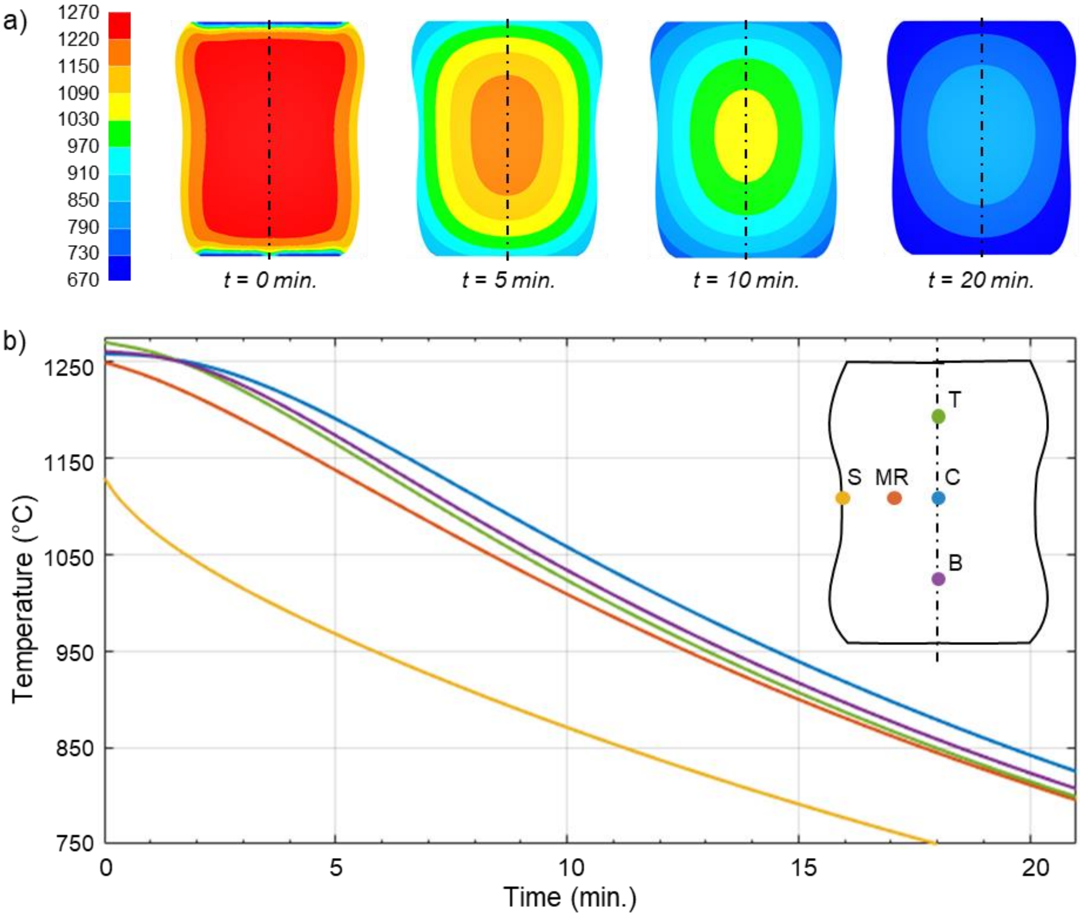

Figure 5.7 : Evolution of temperature predicted by FE simulation of the 316Nb ingot during the air cooling stage following the upsetting to 40% reduction in height; a) temperature distributions at different time, and b) cooling curves at different locations : top (T), middle (M), bottom (B), mid-radius (MR), and skin (S).

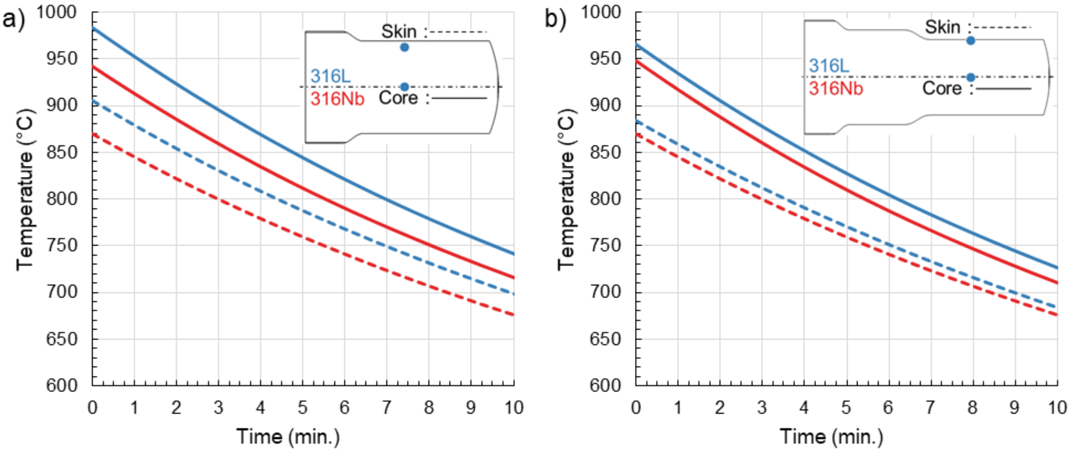

Figure 5.8 : Plots of the evolution of temperature predicted by FE simulation at the core and the edge of the 316L (blue curve) and 316Nb (red curve) ingots during the air cooling stage, at the end of cogging; a) C1, and b) C2.

Figure 5.9 shows the FE predicted distributions of equivalent strain and average strain rate at the end of the 40% upsetting performed on the 316Nb ingot. The predicted strain and average strain rate levels in the central region of that ingot were in the range 0.5 to 0.85 and 0.1 to 0.25 s^{-1}, respectively. However, heterogeneities of equivalent strain and average strain rate values can be observed in the dead zones, which were in contact with the dies, as well as at the top of the ingot. The higher equivalent strain and average strain rate values predicted at the top of the ingot corresponds to the high temperature zone observed previously in Figure 5.5 b), and these were ascribed to the anisotropic behaviour of the as-cast material.

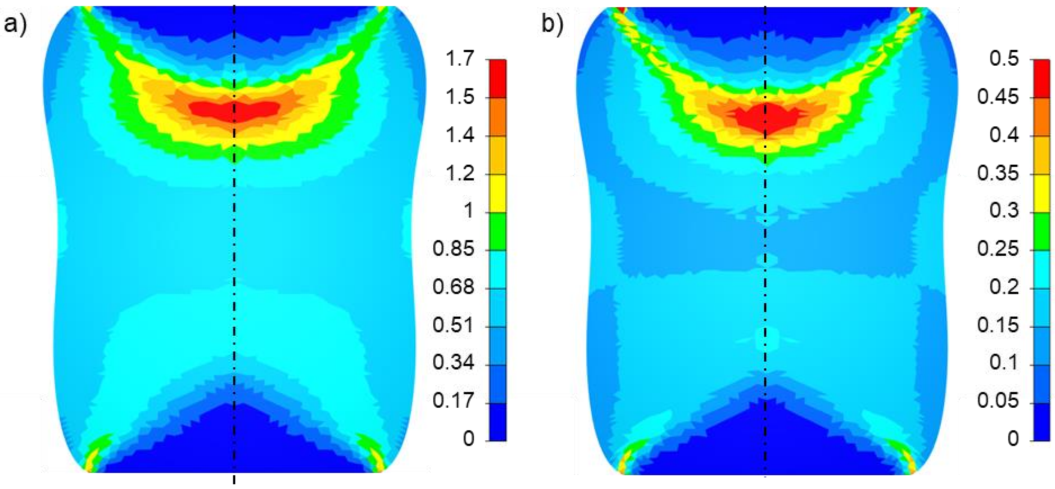

Figure 5.9 : a) Equivalent strain, and b) average strain rate (s^{-1}) distributions predicted by the FE simulation at the end of upsetting to 40% reduction in height of the 316Nb ingot.

The FE predicted distributions of equivalent strain at the end of cogging are presented in Figures 5.10 and 5.11 for the 316L and 316Nb grade ingots, respectively. Note that the strain distributions of the ingots after the C2 cogging display cumulative strain values, from the very first stroke applied on the ingots. In both cases, higher strain values were predicted at the extremity of the bars, and were ascribed to (i) edge effects due to the absence of material beyond the extremity of the bar, and (ii) to the anisotropic material behaviour, in the same manner as described previously for the ingot after upsetting. Localised higher strain values were observed along the edges of the cogged ingots and are highlighted by the arrows in Figures 5.10 and 5.11. In those figures, the surprisingly low amount of strain predicted at the core of the ingots by the FE model is considered as an artefact due to the integration of the anisotropic material model. It can be seen from Figure 5.12, which displays the strain distributions at the end of the first three strokes of the C1 cogging performed on the 316L ingot, that these high strain areas corresponds to the position of the edge of the anvils at the end of the strokes. The distance between these higher strain zones corresponds therefore to the feeding distance, according to the cogging stroke schedule of the pass.

Strain values in the range of 0.4 to 1, and 1.2 to 2.4, were predicted in the remaining cross-section of the ingots cogged to C1 and C2 schedules, respectively. Lower strain values of 0.4 to 0.6 were however predicted at the core of the 316Nb ingot after C1 cogging schedule (see Figure 5.11 a)). The strain distributions profile obtained at the end of the C1 cogging schedule (see Figures 5.10 a) and 5.11 a)) also differ at the extremities of the 316L and 316Nb ingots, as a consequence of the reversed orientation of the 316Nb ingot during cogging (i.e., top to bottom as opposed to bottom to top from the grips).

As explained in Section 3.3, the increments computed during the material deformation were not recorded to limit the amount of data stored during the computation of the FE model, and the strain rate distributions predicted by the FE model where therefore not recorded either. However, local values of strain rate applied during the 12th impact of the dies on the 316L ingot during the C1 cogging schedule were estimated as the ratio between the variation of strain during the stroke, and the duration of the deformation. Figure 5.13 a) and b) display the distribution of equivalent strain before and after the 12th impact of the dies, and Figure 5.13 c) provides a detailed overview of the extremity of the bar (see the rectangle in Figure 5.13 b)) with strain rate values evaluated in several positions across the longitudinal section of the ingot. It can be seen from Figure 5.13 c) that the highest strain rate values were located where the strain increased during the stroke, i.e., along the skin of the ingot and at the vertical edge of the anvil, with decreasing values from the skin to the core of the ingot. As observed previously in Figure 5.12 a) and c), it can also be seen that almost no deformation was provided by the stroke on the extremity of the ingot, and low strain rate values were therefore estimated in these areas. The analysis of the data recorded by the press during cogging (see Figure 3.34) have shown that the macroscopic strain rate was in the range 1 to 2 s^{-1}, which is far below the estimation displayed in Figure 5.13 c). However, it can be concluded from these results that the localised areas with higher strain levels observed along the skin of the ingot were induced by the cogging stroke schedule, and that these areas were deformed at higher strain rates (i.e., from 5 to 15 s^{-1}), as a consequence of the rapid deformation of the section of the ingot which was not forged during the previous hit.

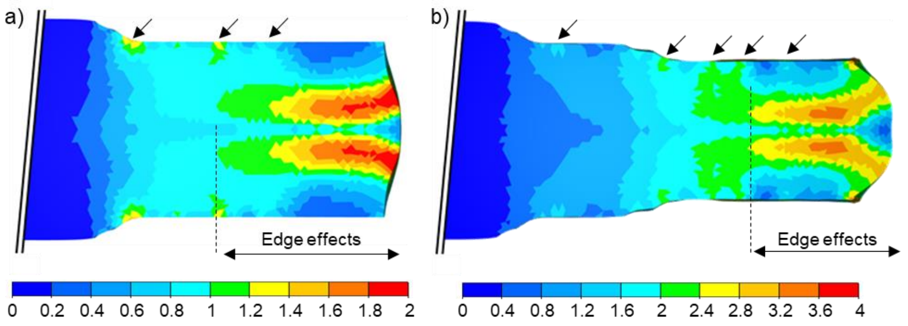

Figure 5.10 : Distributions of equivalent strain predicted by FE simulations for the 316L ingots after cogging to a) C1, and b) C2 schedules. Note that for each ingot, the un-deformed zone, held by the manipulator's grips was cropped for clearer display purpose.

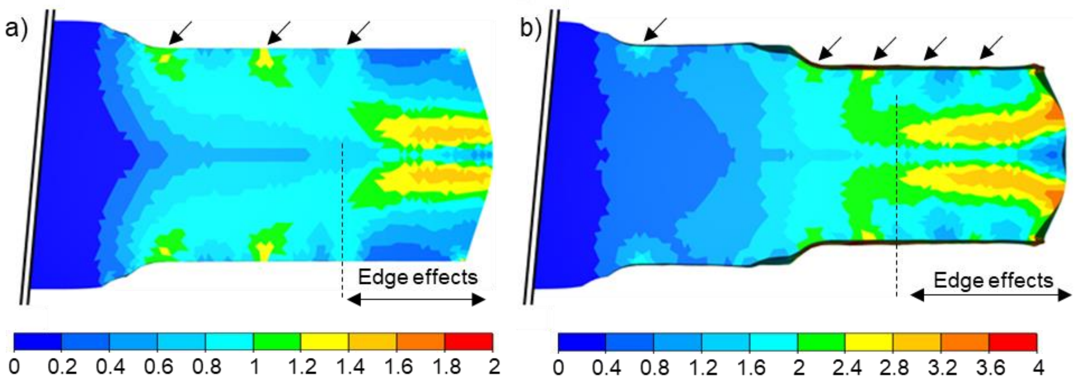

Figure 5.11 : Distributions of equivalent strain predicted by FE simulations for the 316Nb ingots after cogging to a) C1, and b) C2 schedules. Note that for each ingot, the un-deformed zone, held by the manipulator's grips was cropped for clearer display purpose. The arrows highlight higher local strain areas along the edges of the ingots.

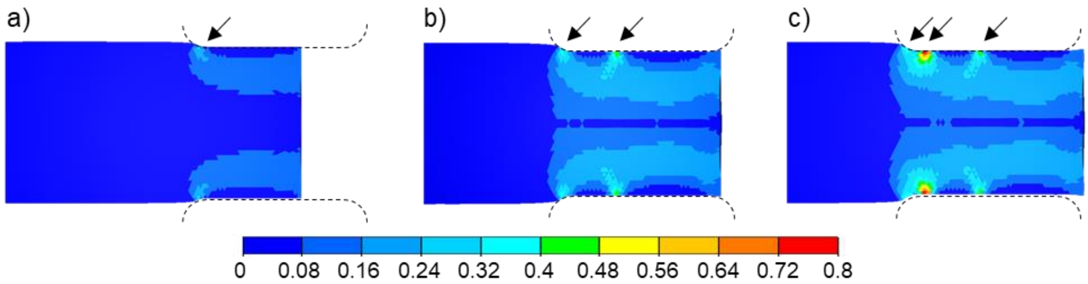

Figure 5.12 : Distributions of equivalent strain predicted by FE simulations at the end of the a) 1st, b) 2nd and c) 3rd strokes of the C1 cogging schedule performed on the 316L ingot. The positions of the anvils at the end of the strokes are indicated with dashed lines, and the arrows highlight the areas with higher local strain values.

Plots of temperature vs. strain behaviour predicted at different locations of the cogged ingots (i.e., close to the skin, mid-radius, and core), at the end of each pass of the C1 and C2 cogging schedules, are presented in Figures 5.14 and 5.15, respectively. The results were extracted from the FE results in the areas where specimens were taken for further microstructure characterisations. It can be seen from Figure 5.14 that the temperature vs. strain evolution obtained during C1 was similar to that of the first cogging stage of the C2 ("C1/C2") schedule, which was identical to C1. As seen previously in Figure 5.10, the strain level reached at the core of the 316Nb ingot after the C1 cogging (i.e., ≈ 0.5) was slightly lower than those reached for the other ingots (i.e., ≈ 0.6 to 0.75) as this ingot was forged in reverse orientation. In the same manner as that for the C1 cogging, Figure 5.15 shows that similar temperature vs. strain evolution were obtained during the final cogging stage of the C2 ("C2/C2") cogging schedule. These results assess the reproducibility of the cogging trials performed on the ingots, and the slight variability between each other was ascribed to the different (i) time schedule of the tests (i.e., the duration of the transfers from the furnace to the press, and between the successive strokes and passes); (ii) pass schedule; and (iii) energy used at each stroke (see Section 0). These results allow to consider that a similar evolution of temperature and strain occurred during cogging for all the four cogged ingots (i.e., made of 316L and 316Nb grades, and cogged via C1 and C2 forging routes); and therefore the specimens were dedicated to microstructure characterisation.

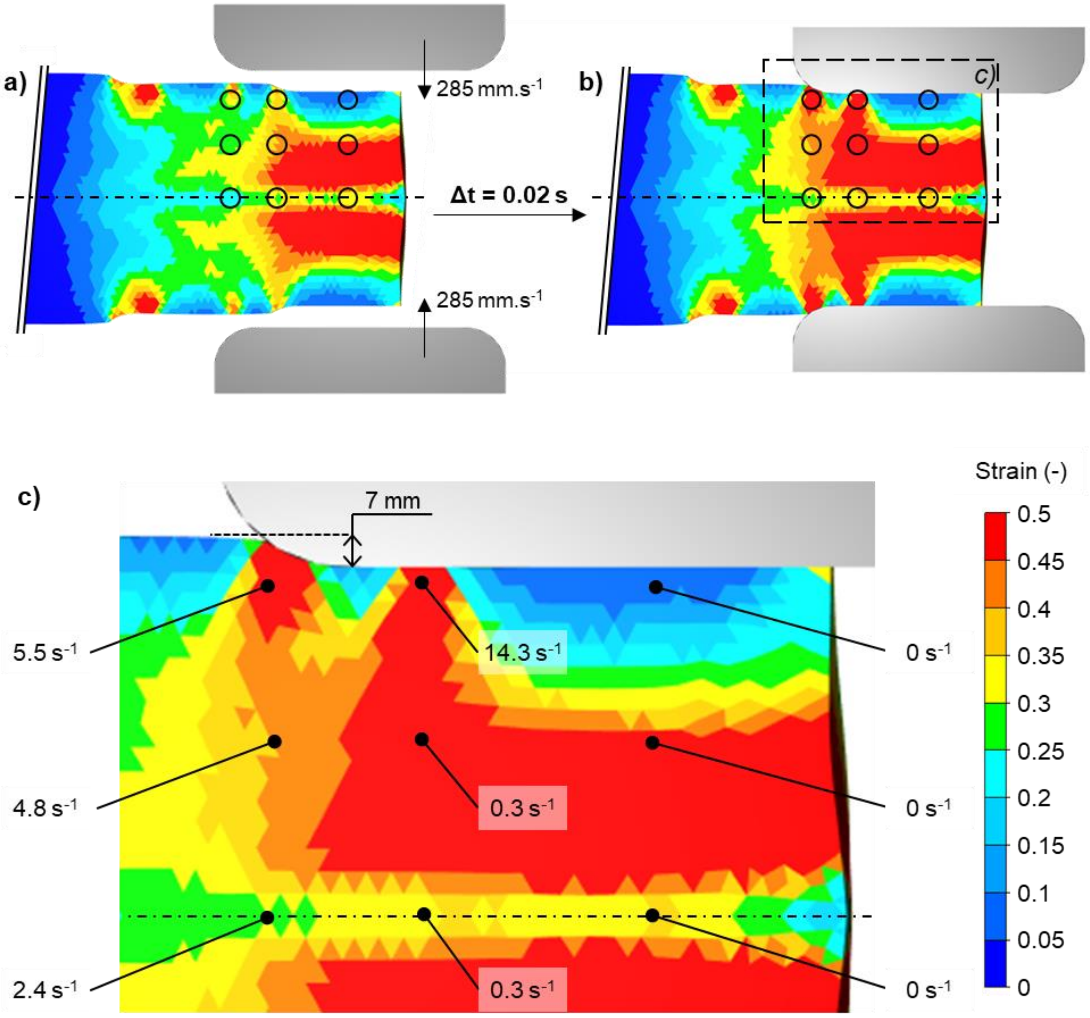

Figure 5.13 : Distributions of equivalent strain predicted by FE simulations for the 316L ingot forged to C1 schedule; a) before, and b) after the 12th stroke, and c) the details of the extremity of the bar with estimated strain rates values overlaid.

The upsetting and C2 cogging experiments performed on the 316Nb ingots are compared to each other in Figure 5.16, which displays the evolution of strain and temperature at different locations of the ingots during the tests, including the final air cooling stage. The data were extracted at mid-radius of the ingots during the upsetting and cogging tests. In the cogged ingots, the data were extracted in the section of the ingot which was cogged during both C1 and C2 cogging stages. As depicted in Figure 5.16, higher levels of strain were reached during the C1 cogging than that of the upsetting, and notable difference in terms of temperature evolution during and after the tests can be observed. The strain increased rapidly during the upsetting test and reached its final level at a temperature of ≈ 1250 °C; and the temperature then gradually decreased during the air cooling stage (see the blue curve in Figure 5.16). In contrast, the strain in the cogged ingot increased slowly, while the temperature decreased simultaneously, with the final strokes being achieved at temperatures below 1000 °C (see the orange curve in Figure 5.16). The evolution of temperature within the upset and cogged ingots was strongly impacted by (i) the successive contacts of the dies with the cogged ingot, promoting the thermal loss in the ingot; (ii) the occurrence of adiabatic heating in the early stage of the upsetting ingot, allowing the temperature to remain elevated for a longer duration; and (iii) the different geometries of both ingots, since the elongated shape of the cogged ingot promote the heat loss in comparison to the compact geometry of the cogged ingot. Also note that the occurrence of a few adiabatic heating throughout cogging had a negligible impact of the overall temperature evolution.

As can be seen from Figure 5.16, at the position of the ingots where the data were extracted from, the temperature of 1000 °C was reached about 11.5 and 8 minutes after the furnace unloading of the upset and cogged ingots, respectively.

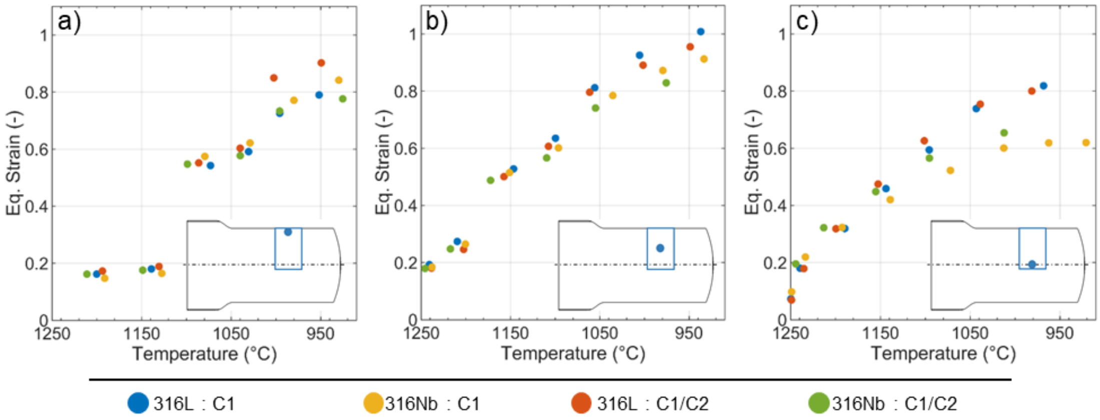

Figure 5.14 : Plots of temperature vs. strain values predicted by FE simulation at the end of each pass of the C1 cogging. Results extracted from areas a) close to the skin, b) at mid-radius, and c) at the core of the ingot. Legends "C1/C2" denotes the first cogging stage of the C2 schedule, which were identical to C1.

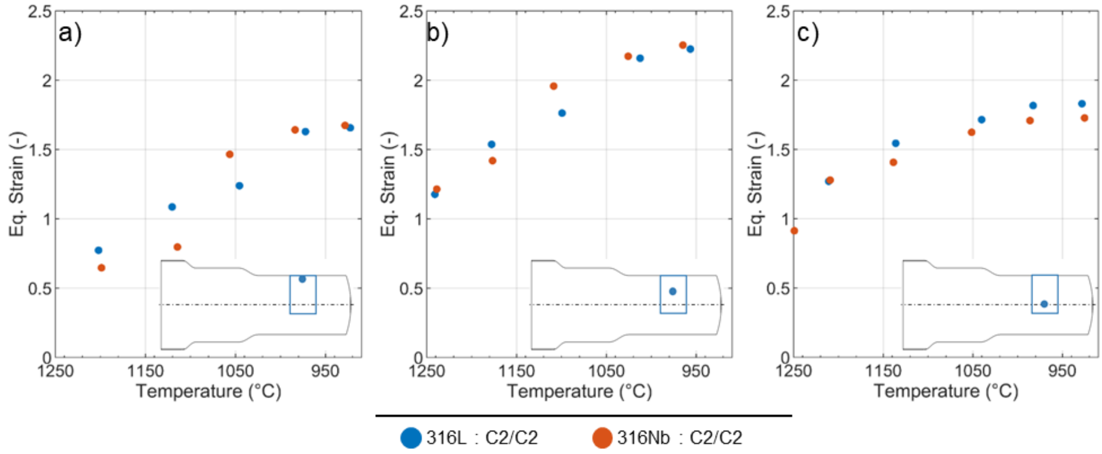

Figure 5.15 : Plots of temperature vs. strain values predicted by FE simulation at the end of each pass of the C2 schedule. Results extracted from areas a) close to the skin, b) at mid-radius and c) at the core of the ingot.

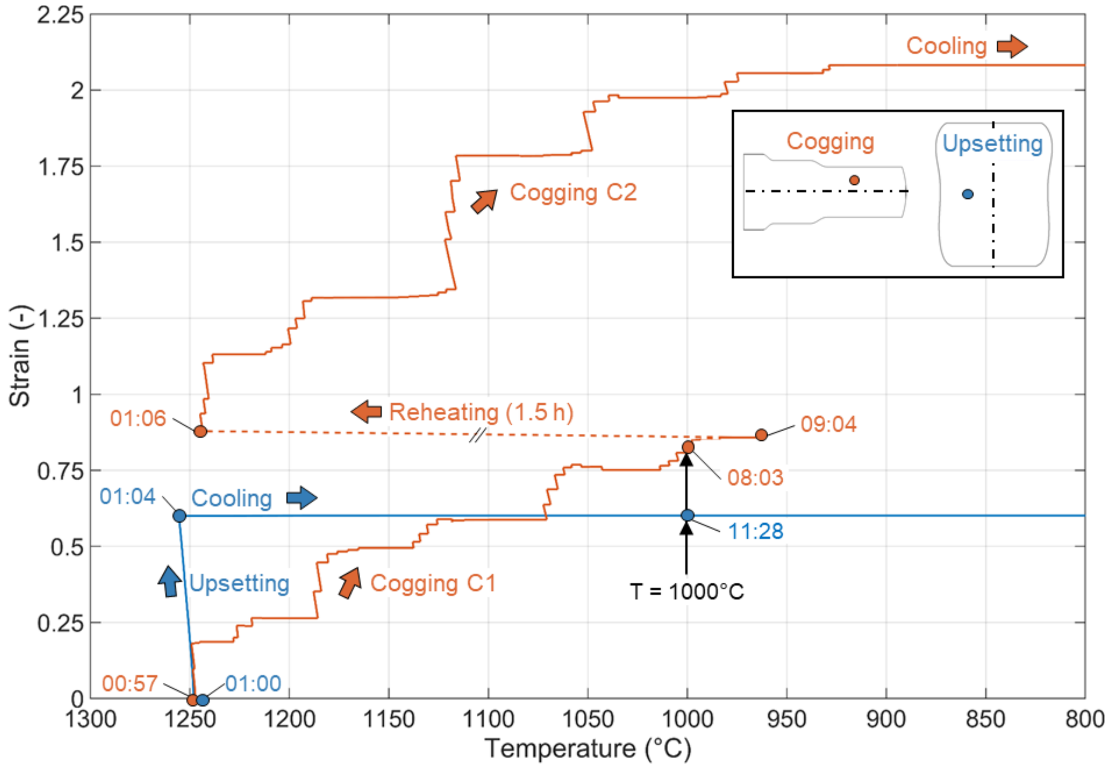

Figure 5.16 : Plots of the evolution of strain and temperature in selected area of the 316Nb ingots during the upsetting (blue), and C2 (orange) cogging schedule. Note that the durations from the furnace unloading are indicated using "mm:ss" format.

The FE results and comparison presented in this section for the thermomechanical properties of both grades of ingot during upsetting or cogging can be summarised as follow:

- The FE model with the anisotropic model implemented was more suitable than that with isotropic model for the prediction of the deformed shape of the ingots after the upsetting and cogging trials.
- The upsetting to 40% reduction in height of the 316Nb ingot was performed at elevated temperatures (i.e., above 1240 °C), to strain levels in the range 0.5 to 0.85, at strain rates of 0.1 to 0.2 s^{-1}. A localised area at the top of the ingot, along its axis, experienced higher strain values, in the range of 0.85 to 1.7, at a strain rate up to 0.5 s^{-1}. After the upsetting, the temperature of the ingot decreased at a rate of ≈ 20 °C/min, and the central region of the ingot remained above 1000 °C for about 10 minutes after the end of the upsetting test.
- The cogged ingots underwent strains ranging from 0.8 to 1 during the first cogging route (i.e., C1), and from 1.5 to 2.25 during the second cogging route (i.e., C2). The temperature at the core of the ingots was below 1000 °C at the end of the cogging C1 and C2. A comparable evolution of temperature and strain were observed during both cogging stages C1 and C2, in the areas of the cogged ingots which are dedicated to further characterisation of microstructure. Localised higher strain values were observed along the skin of the cogged ingots as a result of the cogging stroke schedule; and these zones experienced elevated strain rate, reaching up to 15 s^{-1}.
- Thermomechanical properties in the ingots during upsetting and cogging tests differ from each other in terms of the evolution of strain and temperature throughout the tests. The strain was applied in a few seconds during the upsetting test, at elevated temperatures prior to the slow air-cooling stage; whereas the temperature slowly decreased, simultaneously to the increase of strain applied during the cogging tests, which lasted for ≈ 5 to 9 minutes.

5.4 MICROSTRUCTURE EVOLUTION IN THE AS-CAST MATERIAL

Following the methodology presented in Section 0, longitudinal and transverse cross-sections of the upset and cogged ingots were extracted, ground, polished and etched to reveal their macrostructure. Micrographs were also collected from specimens taken in the longitudinal cross-sections of the ingots, prepared and etched for local observations and quantitative analysis of the microstructure.

The overall macrostructure of the 316Nb ingot after 40% upsetting by the 2 500 tonnes hydraulic press is presented in Figure 5.17, showing that the as-cast microstructure was recrystallised across the whole cross-sections of the ingot, with however a few non-recrystallised grains observed in some areas. For instance, the progress of recrystallisation was limited in the dead-zones of the ingot, highlighted by the white line in Figure 5.17 a), at the top and bottom of the ingot, where the FE simulations predicted lower temperatures (see Figure 5.5), strain and strain rate levels (see Figure 5.9) during the deformation. Large non-recrystallised grains were also observed at the core of the ingot (see Figure 5.17 c)), along its skin (see Figure 5.17 d)), and in the chill-zone (see Figure 5.17 e)). Microstructural details of some of these non-recrystallised grains observed along the skin and along the axis of the ingot are shown in Figures 5.18 and 5.19, respectively. Note that the colour levels of these micrographs was adjusted for the sake of visibility of microstructural details (i.e., the grain boundaries and the non-recrystallised grains). The shape of the non-recrystallised grains observed along the skin of the ingot after the upsetting remained elongated, with their long axis at ≈ 60° to the axis of the ingot, similar to the as-cast grains observed in the ingot prior to upsetting (see Section 3.2.1). Such grains were observed up to a distance of ≈ 40 mm below the skin of the ingot, where the temperature was predicted to be below 1200 °C at the end of the upsetting (see Figure 5.5). As a consequence of the electro-etching, the non-recrystallised grains appeared darker than the surrounding recrystallised grains. This characteristics of the observed microstructure allowed therefore to identify a few smaller non-recrystallised grains (i.e., having a similar size as the surrounding recrystallised grains; see the circles in Figure 5.20) in different locations of the ingot after upsetting. Apart from these locations where a few non-recrystallised grains were observed, the microstructure observed along the longitudinal cross-section of the ingot was fully recrystallised (see Figure 5.21). According to the FE simulations (see Section 3.3), these fully recrystallised areas underwent strain of 0.5 to 1.7 and strain rate from 0.1 to 0.5 s^{-1} at temperatures above 1200 °C; and the temperature decreased with a cooling rate of 20 °C/min after the upsetting.

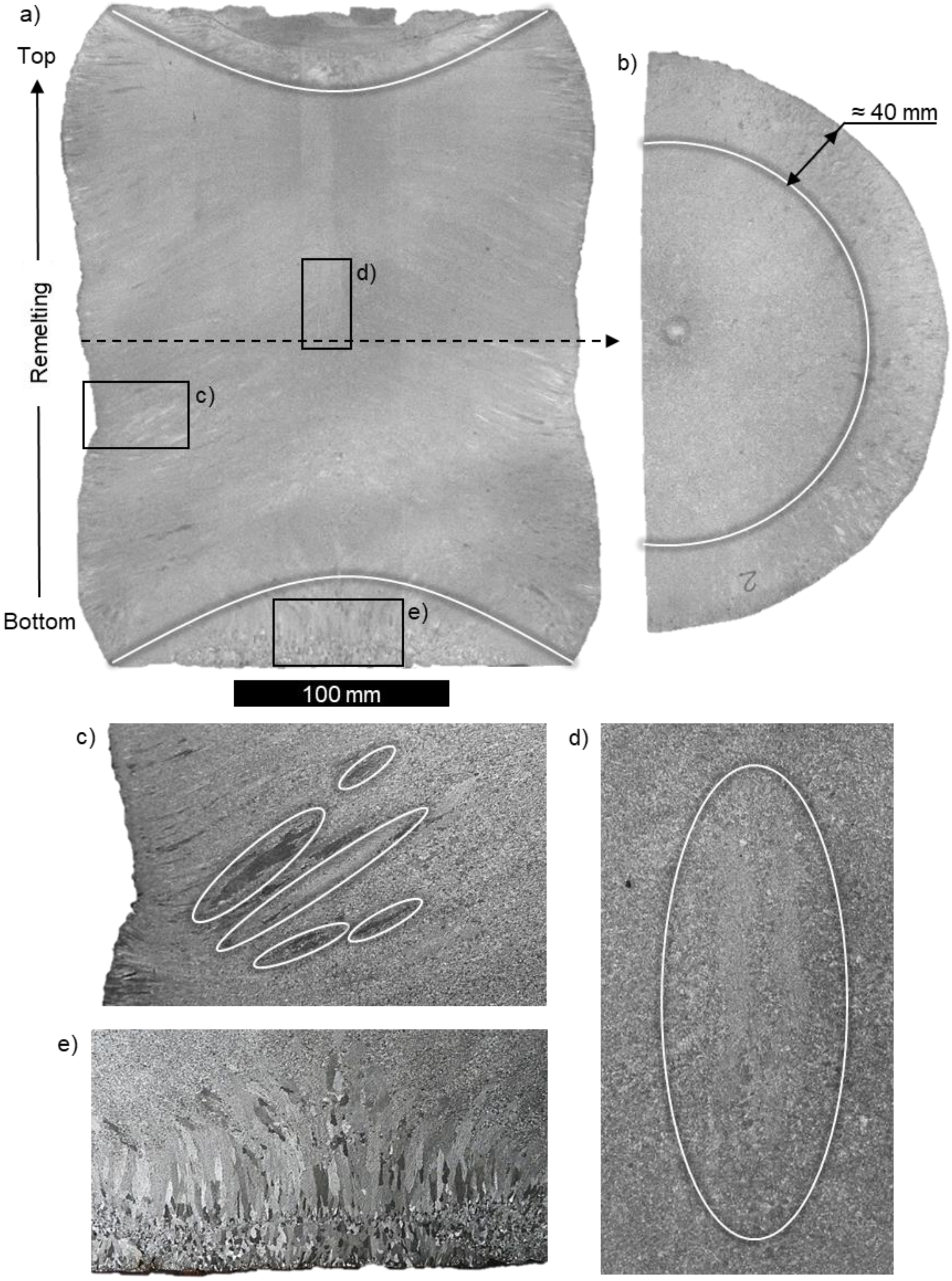

Figure 5.17 : Overall macrostructure of the 316Nb ingot after 40% upsetting; a) longitudinal and b) transverse cross-sections. Non-recrystallised grains highlighted in the dashed circles at the c) skin, and d) core of the ingot; e) displays the microstructure of the chill zone, which remains visible despite the occurrence of partial recrystallisation.

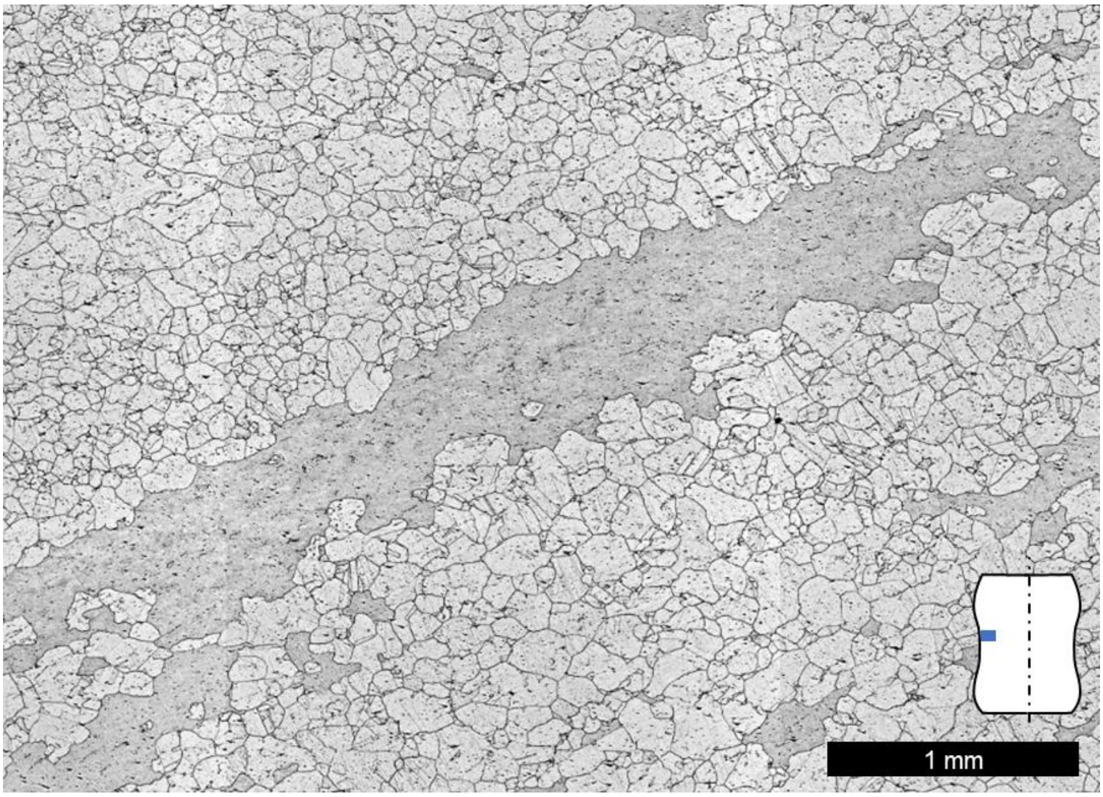

Figure 5.18 : Microstructural details of a large non-recrystallised grain observed in a recrystallised area, along the skin of the 316Nb ingot after upsetting to 40% reduction in height.

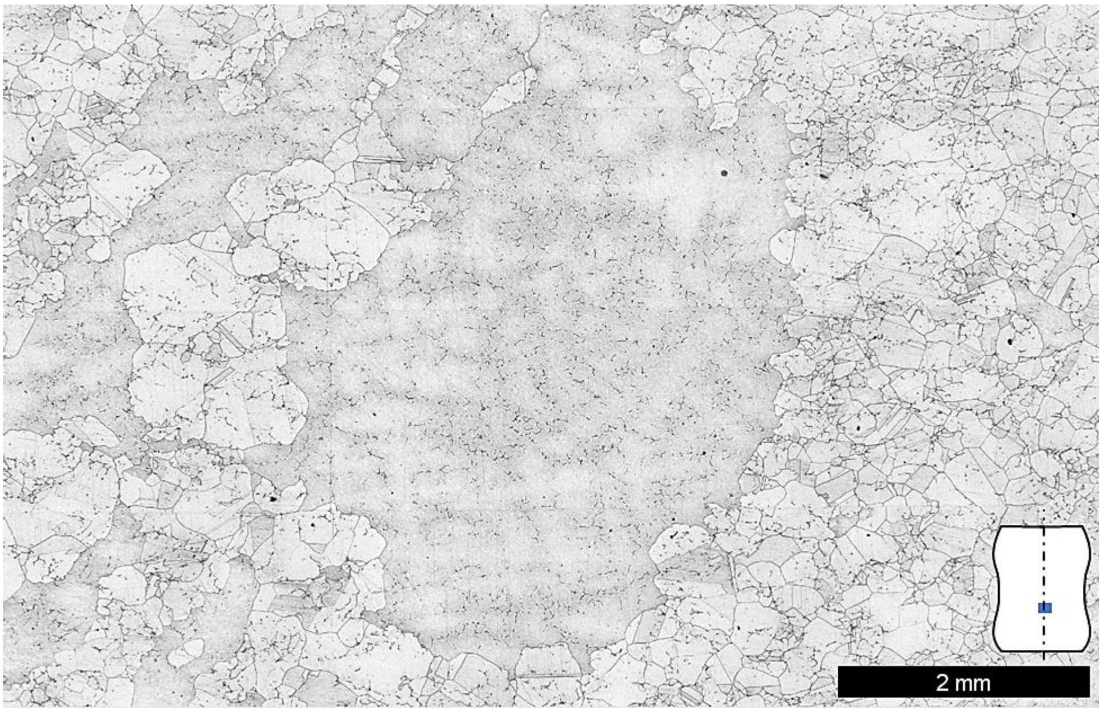

Figure 5.19 : Microstructural details of a large non-recrystallised grain observed in a recrystallised area, in the chill zone of the 316Nb ingot after upsetting to 40% reduction in height.

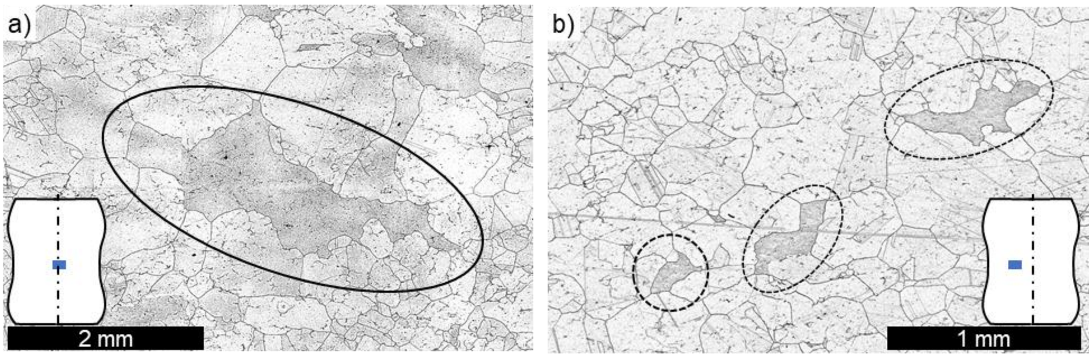

Figure 5.20 : Microstructural detail of darker non-recrystallised grains (see the circles) observed in recrystallised areas of the 316Nb ingot after upsetting to 40% reduction in height; a) mid-radius, and b) core of the ingot.

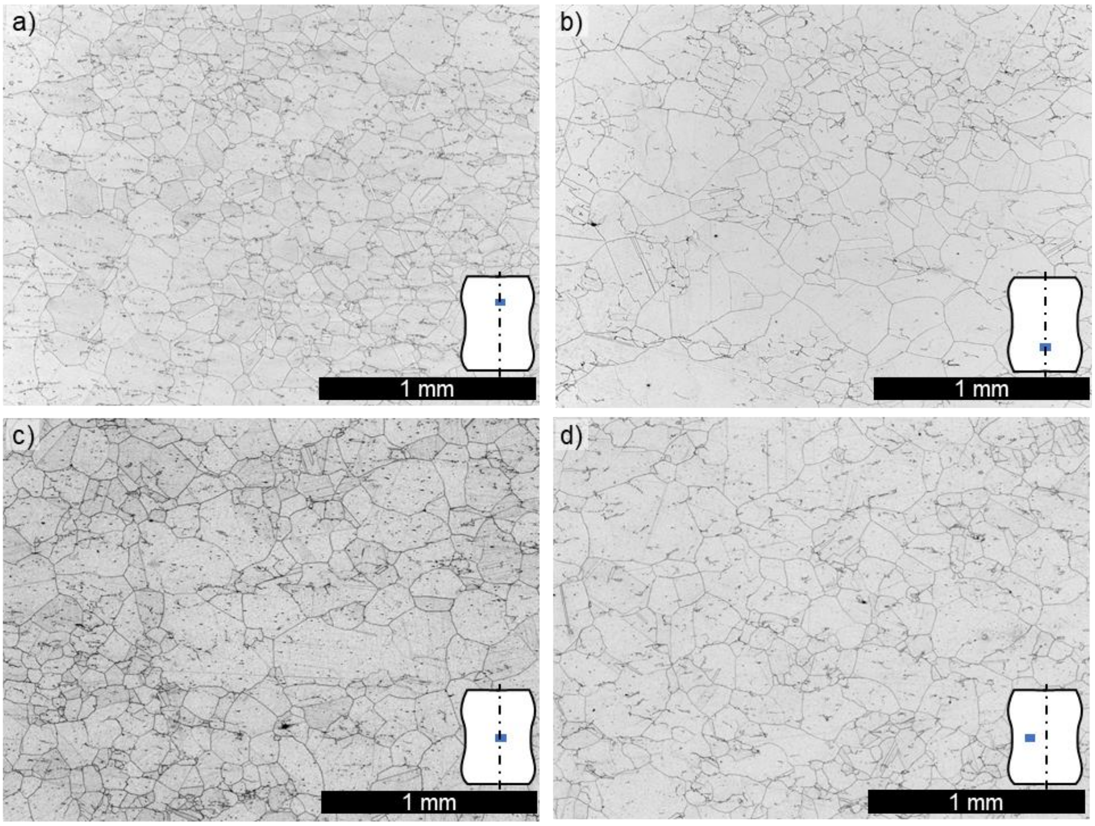

Figure 5.21 : Microstructural details at different locations of the 316Nb ingot after the upsetting. The micrographs were obtained by stitching 3×3 smaller micrographs together.

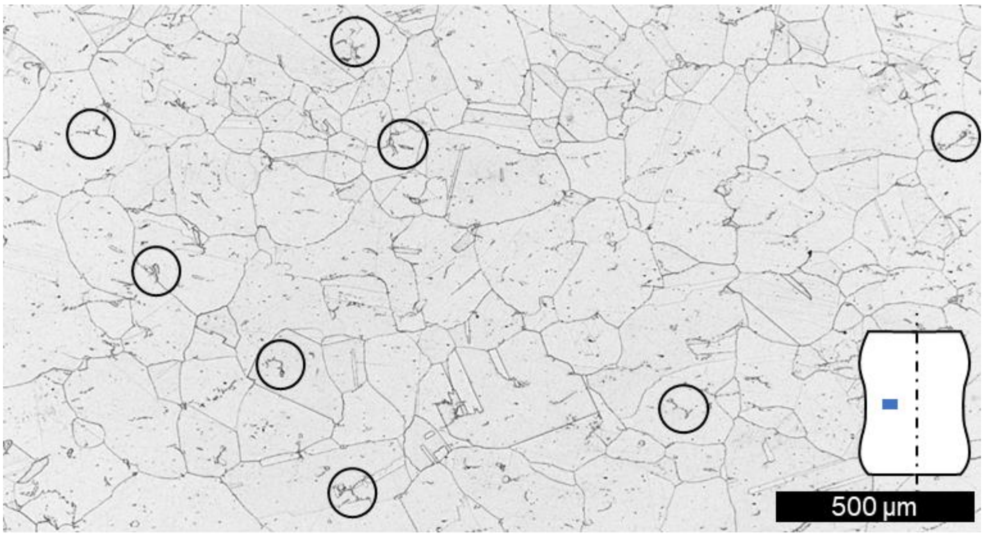

Figure 5.22 : Optical microscopy appearance of the 316Nb ingot after upsetting to 40% with a noticeable amount of undissolved secondary phases; a few of which are highlighted by the circles.

Grain size analyses were performed at different locations of the 316Nb ingot after upsetting to 40% in height. Results obtained for areas located along the axis of the ingot, in the half upper and lower parts of the ingot, are shown in Figure 5.23; and the corresponding plots of the frequency of equivalent grain diameter and cumulative area fraction are presented in Figure 5.24. The initial microstructure of these areas was different from each other since the bottom area was located in the chill zone, where the remelting process was initiated, and where the grains were aligned with the direction of remelting and progressively converged together to the axis of the ingot (see Figure 3.5). The results obtained for areas located at mid-height of the ingot, along its radius, are presented in the same manner in Figures 5.25 and 5.26. Note that the micrograph presented in Figure 5.25 a) was taken slightly away from the axis of the ingot, so that the microstructure of both areas were composed of grains oriented at ≈ 60° prior the upsetting.

As can be seen from Figures 5.24 and 5.26, similar average grain sizes of 74 to 81 µm were measured at the top (see Figure 5.23 a)), middle (see Figure 5.25 a)) and mid-radius (see Figure 5.25 b)) areas of the ingot. The microstructures were relatively homogeneous in these areas, with standard deviations of grain sizes in the range of 70 to 75 µm. It can therefore be noted that the excessive levels of strain and strain rate reached in the top area (i.e., ≈ 1.5 and ≈ 0.5 s^{-1}, respectively; see Figure 5.9), in comparison to the predictions for the other areas (i.e., ≈ 0.6 and ≈ 0.15 s^{-1}, respectively; see Figure 5.9), had no effect on the progress of recrystallisation, on the homogeneity of the microstructure or on the size of the recrystallised grains. In the chill-zone area the microstructure appeared less homogeneous than in the other areas, and a few larger grains were observed in Figure 5.23 b). In this area, the average grain size was of ≈ 89 µm (see Figure 5.23 b)), and the standard deviation of grain sizes of ≈ 110 µm. In this area, the FE simulations predicted similar strain, strain rate and temperature levels than in the middle area, where the microstructure was observed to be more homogeneous and composed of smaller grains; suggesting that the grain size, and the homogeneity of the microstructure, was affected by the different geometrical and crystallographic orientation of the grains.

Heterogeneities in grain size were identified based on the results presented in Figure 5.27 and Figure 5.28 for a 11×24 mm^2 area observed at the mid-radius of the ingot, after the upsetting process. Figure 5.27 illustrates the presence of bands composed of smaller or larger grains, with the same orientation as the as-cast grains (see Figure 3.5), and that of the non-recrystallised grain observed along the skin of the ingot (see Figure 5.18). This suggest a correlation between the width of the as-cast grains, and the progress of recrystallisation of the as-cast microstructure. Although the microstructure was fully recrystallised, these results demonstrate that traces of the parent as-cast microstructure remain presents in the ingot, in the form of bands composed of grains with various sizes. In this region, the average grain size was 69 µm, and the standard deviation of grain sizes was 58 µm (see Figure 5.28). The measured size of the grains was smaller in this area than in those observed at higher magnification (see Figures 5.23 and 5.25), but remain in the same order of magnitude.

Microstructure analyses were performed along the longitudinal cross-section of the 316Nb ingot after upsetting to 40% reduction in height, and the results were correlated with the FE results to identify the conditions for the recrystallisation of the as-cast microstructure. The main results of these analyses are summarised as follow:

- Fully recrystallised areas were observed along the longitudinal cross-section of the ingot; in the areas where the temperature was predicted above 1200 °C prior to the upsetting test, and the material was deformed at a strain rate of 0.2 s-1 to 0.5 s-1, to strain levels over 0.7. In this area, the temperature remained for ≈ 8 minutes above 1000 °C.
- The recrystallised grains were found to have an average size of ≈ 80 µm, and bands of grains with heterogeneous sizes were also observed, which can be described as “ghosts” of the parent microstructure.
- A few non-recrystallised grains were observed along the skin of the ingot, up to 40 mm below its surface, where the temperature was predicted to be below 1225 °C prior to the upsetting, and dropped below 1000 °C about 8 minutes after the upsetting was completed. A few partially recrystallised grains were also found in different areas of the ingot, and large non-recrystallised grains were observed along its axis.
- The recrystallised grains of the chill-zone were slightly larger than those observed in the other areas of the ingot, with notable heterogeneities of the grain size, suggesting the sensibility of microstructure recrystallisation to the geometric and crystallographic orientation of the grains towards that of the direction of compression.

- Strain and strain rate localisation was predicted by FE simulation at the top of the ingot, without noticeable impact observed on the progress of the recrystallisation or the size of the recrystallised grains.
- A noticeable presence of secondary phases remained present in the ingot after the homogenisation heat treatment and following upsetting to 40%.

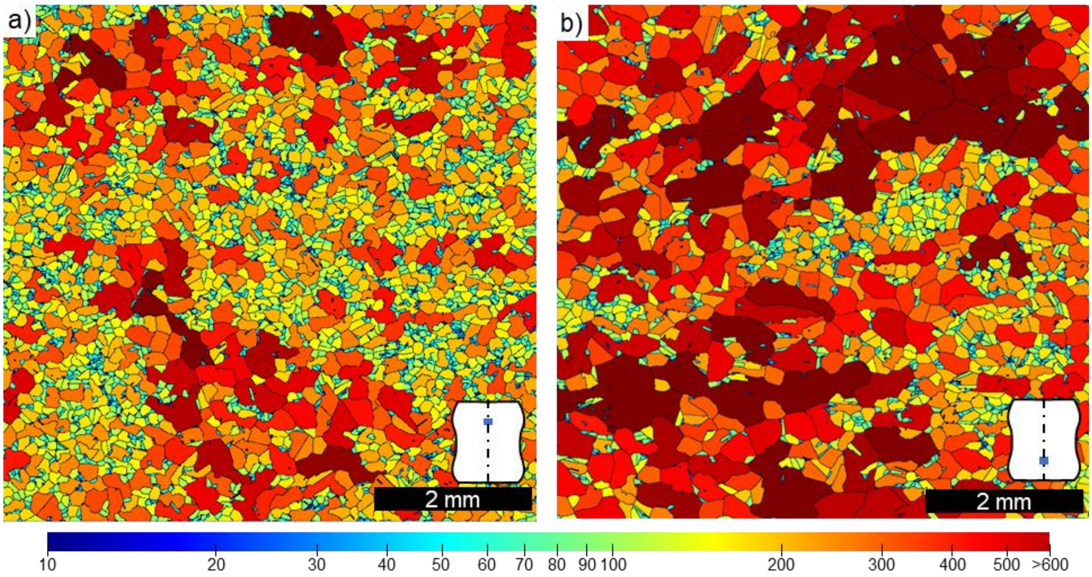

Figure 5.23 : Microstructures of the 316Nb ingot after upsetting to 40%, with the grains coloured according to their equivalent diameter (µm); a) top, and b) bottom. The micrographs were obtained by stitching 4×3 smaller micrographs together.

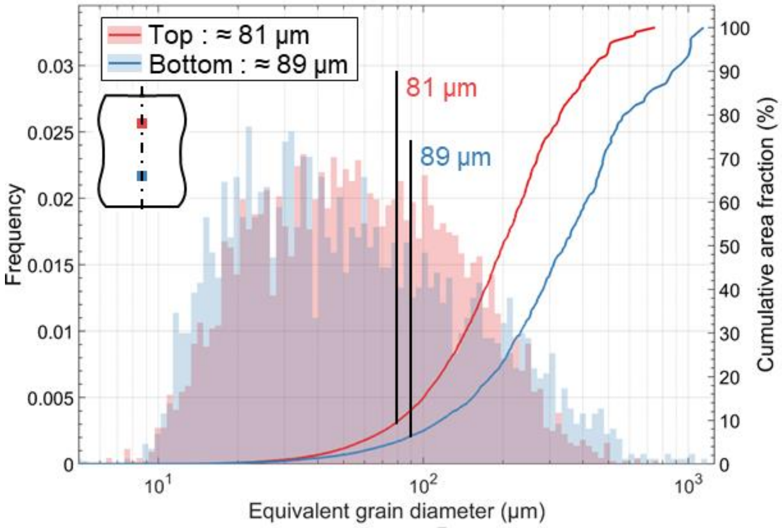

Figure 5.24 : Plots of the frequency of equivalent grain diameter and cumulative area fraction at top and bottom locations of the 316Nb ingot after upsetting. Measurements performed using the micrographs presented in Figure 5.23.

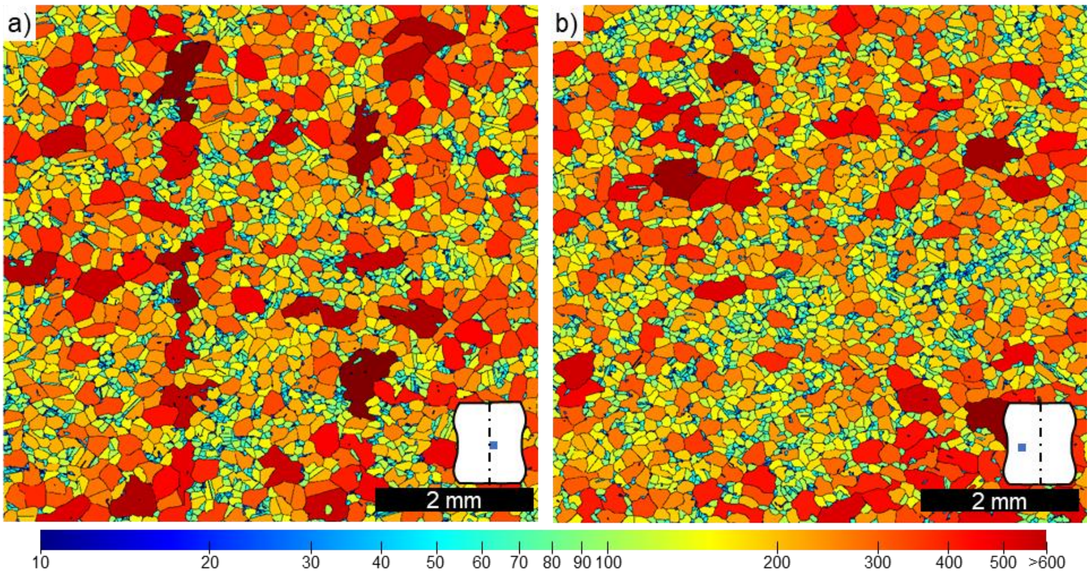

Figure 5.25 : Microstructures of the 316Nb ingot after upsetting to 40%, with the grains coloured according to their equivalent diameter (μm); a) core, and b) mid-radius. The micrographs were obtained by stitching 4×3 smaller micrographs together.

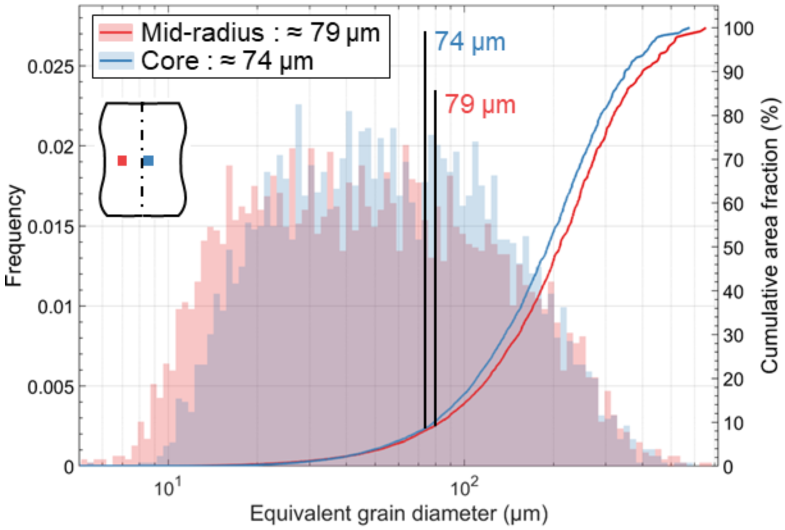

Figure 5.26 : Plots of the frequency of equivalent grain diameter and cumulative area fraction at the core and mid-radius of the 316Nb ingot after upsetting. Measurements performed on the micrographs presented in Figure 5.25.

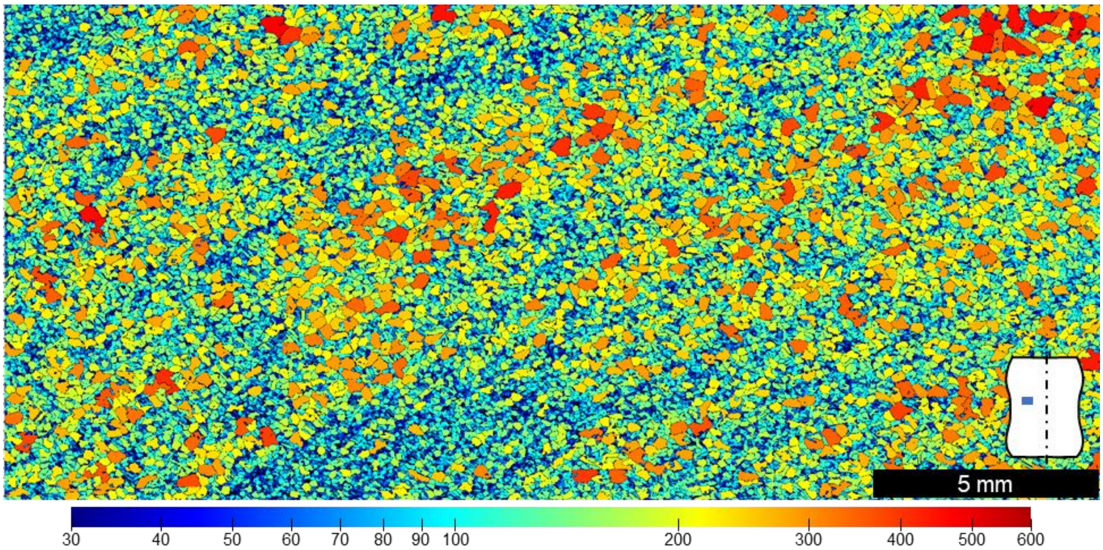

Figure 5.27 : Reconstructed microstructure of the 316Nb ingot after upsetting to 40% reduction in height with the grains coloured according to their equivalent grain diameter (µm). The micrograph used for the analysis was obtained by stitching 7×11 smaller micrographs together, covering a 11×24 mm^2 area.

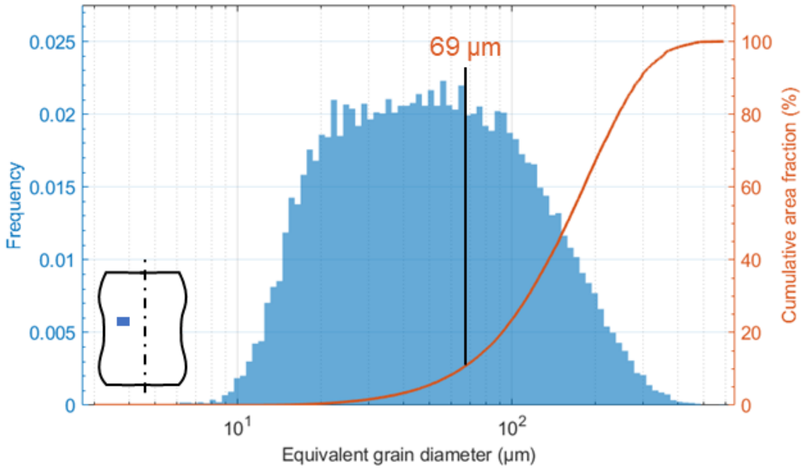

Figure 5.28 : Plots of the frequency of equivalent grain diameter and cumulative area fraction measured at mid-radius of the 316Nb ingot after upsetting. Measurements performed on the micrographs presented in Figure 5.27.

Macrostructures of 316L and 316Nb ingots after the C1 cogging are presented in Figure 5.29. It can be seen that the coarse and elongated starting solidification microstructure remained predominant after cogging in both longitudinal and transverse cross-sections of the ingots, the grains were strongly deformed in shape (see Figure 5.30), and no clear occurrence of recrystallisation was observed at this scale. As explained in Section 0, the 316Nb ingot was forged in the reverse orientation, and the chill zone of this ingot is therefore located at the extremity of the forged section (see the location of the chill zone in Figure 5.29, which are bounded by the yellow lines).

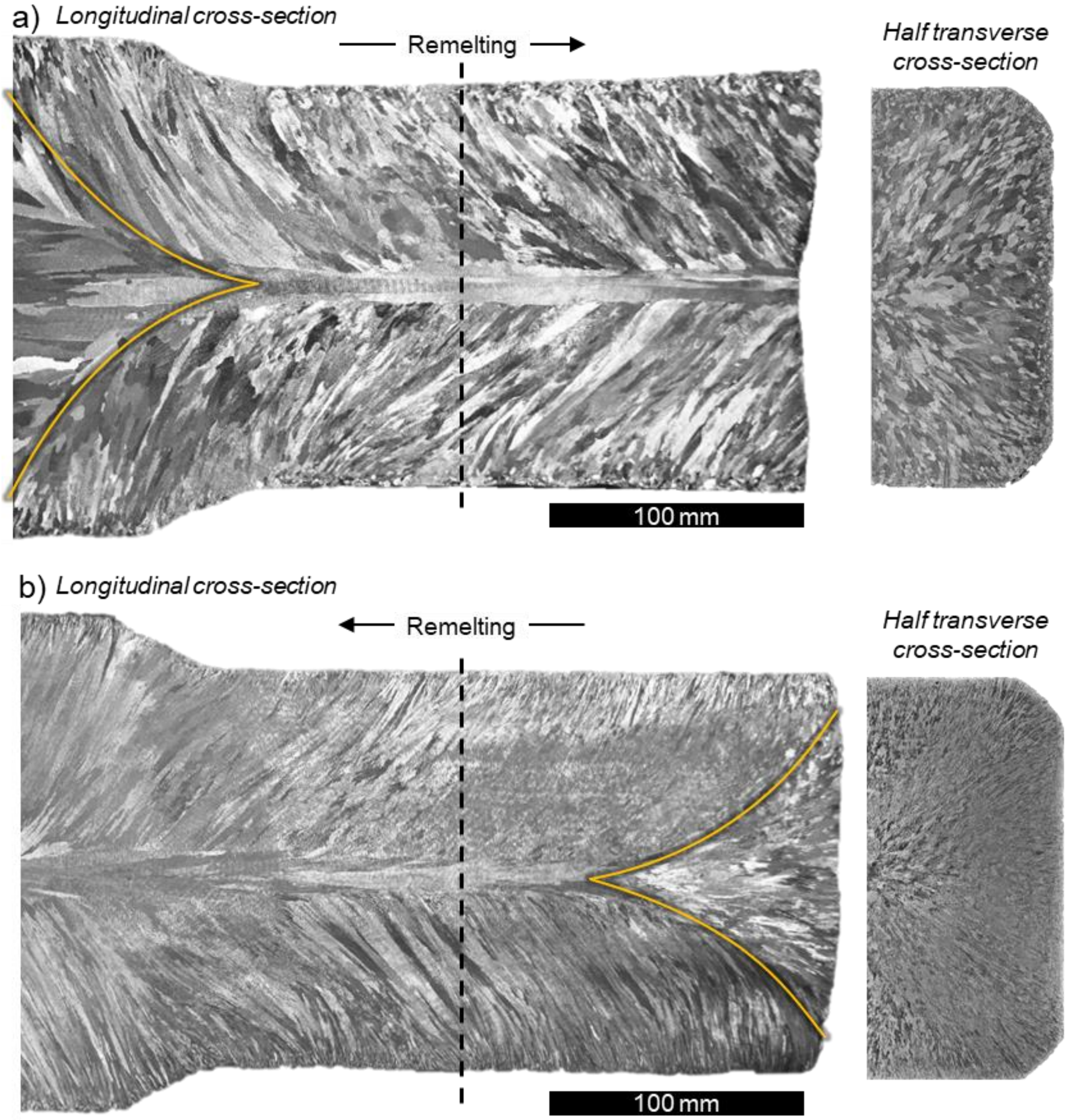

Figure 5.29 : Overall macrostructure of the ingots after the C1 cogging; a) 316L, and b) 316Nb grade. Observations performed along longitudinal and mid-height transverse cross-sections. The yellow lines bounds the chill zone in both longitudinal cross-sections.

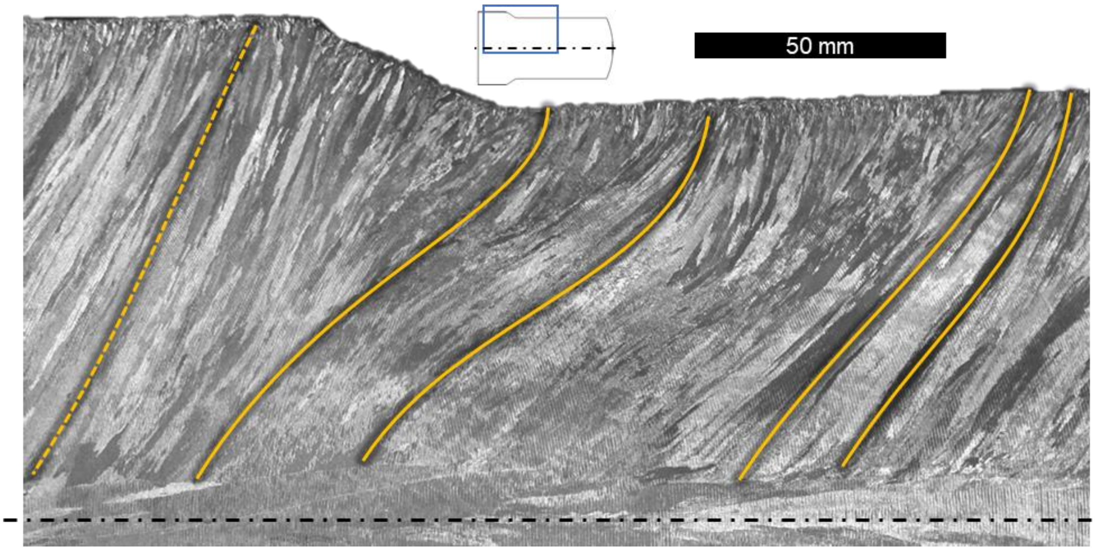

Figure 5.30 : Macrostructure appearance of the 316Nb ingot after the C1 cogging, with the strong deformation in shape of the grains highlighted by the lines in the cogged section. The dashed line indicates the orientation of major axis of the long grains in the zone which was held by the manipulator and was not cogged.

Occurrence of recrystallisation was however revealed for both grades by OM observations performed at higher magnifications. The recrystallised grains are highlighted in Figure 5.31 over the longitudinal cross-sections of 316L and 316Nb specimens taken out from the ingots.

In the 316L ingot, the areas underwent recrystallisation (i.e., recrystallised grains) were predominantly located at the boundaries of parent microstructure (see Figure 5.31 a)). Microstructural details of the large recrystallised zone observed along the skin of this ingot (see the yellow shape in Figure 5.31 a)) is provided in Figure 5.32, showing that a parent grain was almost fully recrystallised. This was the single partially-recrystallised grain observed along the skin of the 316L specimen, and the phenomenon is ascribed to the effect of the elevated strain and strain rate levels induced by the impact of the edge of the anvil at this position.

In the 316Nb ingot, the area underwent recrystallisation (see Figure 5.31 b)) showed that recrystallisation occurred at the boundaries of parent microstructure, and significantly extended in some grains (see Figure 5.33). Figure 5.34 illustrates preferential recrystallisation at some parent grain boundaries observed for both grades of material, where “Rx” and “NRx” indications highlight the parent grain boundaries with and without recrystallised grains, respectively.

Deformation bands were observed in microstructure of both ingots, up to a few centimetres below their skin. In the 316L ingot, only a few amount of deformation bands were found, up to ≈ 30 mm to its skin (see the arrows in Figures 5.32 and 5.35 a)). A greater amount of deformation bands were observed up to ≈ 45 mm below the skin of the ingot made of 316Nb (see the arrows in Figures 5.33 and 5.35 b)). The observations performed in both specimens highlighted that the deformation bands had similar orientations in adjacent grains, and in different areas of the specimens; an example of which is shown for the 316Nb grade in Figures 5.33 and 5.35 b). Small recrystallised grains were also observed along the deformation bands in the 316Nb ingot (see the circles in Figure 5.36).

A few amount of undissolved secondary phases was found in the ingot made of 316L (see the arrows in Figure 5.37 a)), and noticeable amount of undissolved secondary phases were observed in both recrystallised and non-recrystallised grains of the 316Nb ingot (see the arrows in Figure 5.37 b)), without obvious relationship with the higher progress of recrystallisation observed in this ingot (see Figure 5.31). In both ingots, a few recrystallised grains were observed at the interface with the parent grains (see the circles in Figure 5.37). A few serrated parent grain boundaries were also observed in the 316L specimen (see Figure 5.38), but not in the 316Nb ingot.

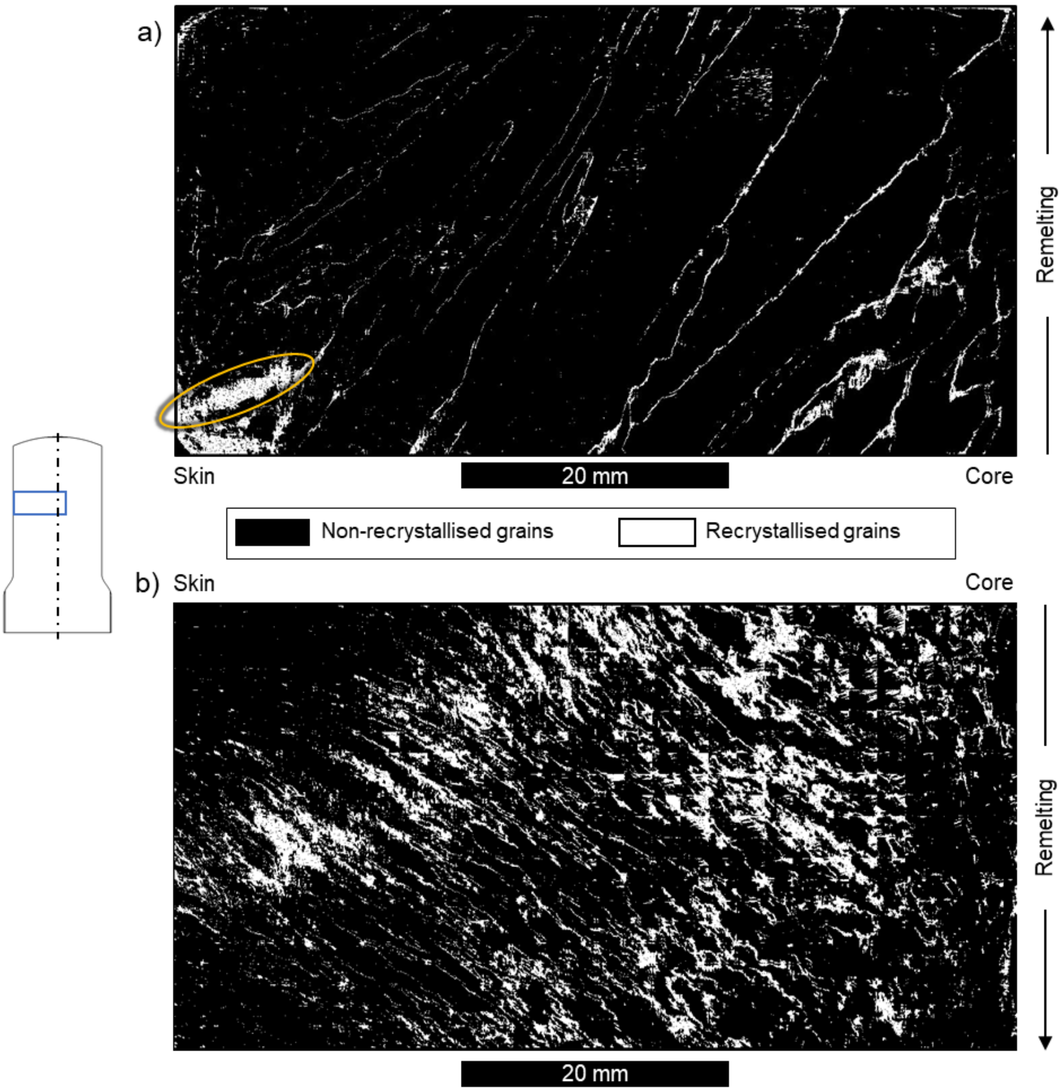

Figure 5.31 : Occurrence of recrystallisation highlighted over the surface of the specimens extracted from the longitudinal cross-sections of the ingots, after the C1 cogging schedule; a) 316L, and b) 316Nb. The circle in a) highlights a recrystallised zone along the skin of the 316L ingot.

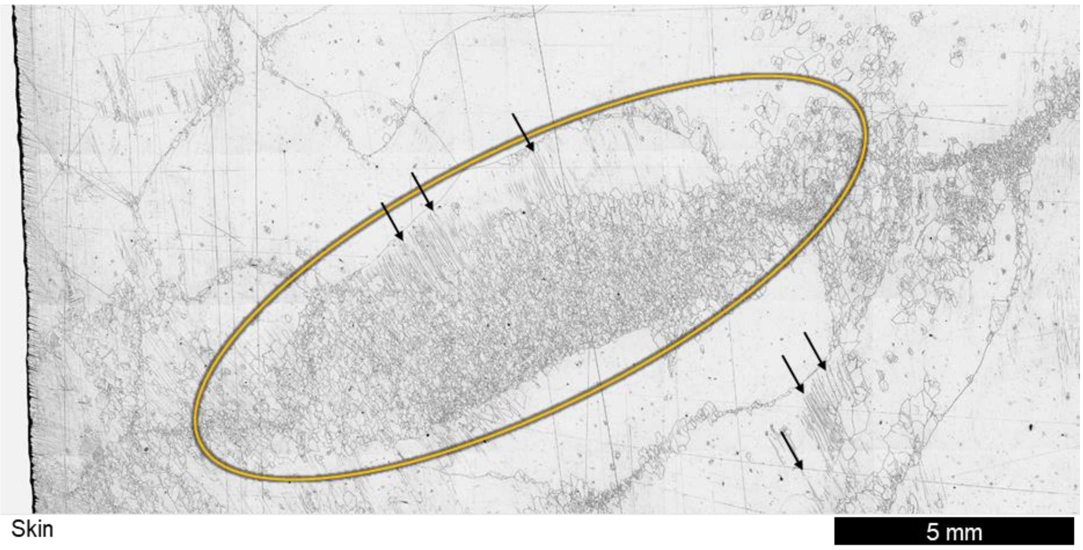

Figure 5.32 : Microstructural details of a partially recrystallised grain, highlighted by the yellow oval shape, observed along the skin of the 316L ingot after the C1 cogging. The presence of deformation bands are highlighted by the arrows.

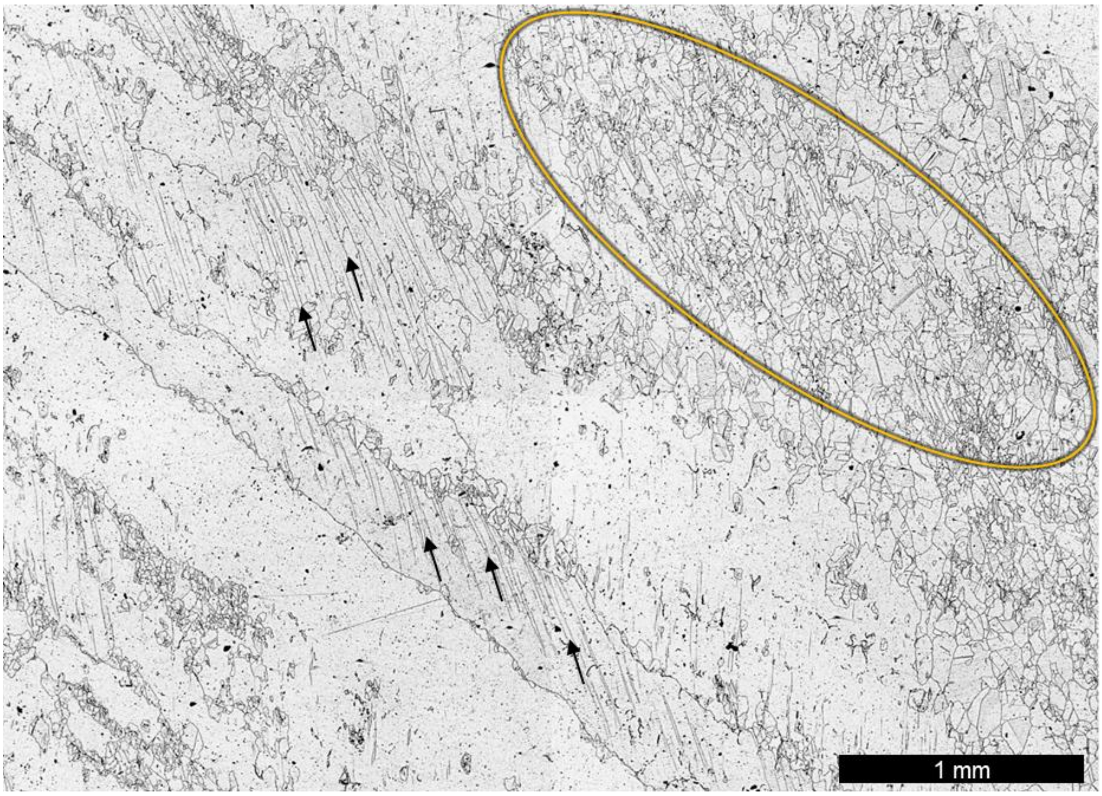

Figure 5.33 : Microstructural details of a partially recrystallised area, with a fully recrystallised parent grain highlighted by the yellow oval shape, observed in the 316Nb ingot after the C1 cogging. The presence of deformation bands are highlighted by the arrows.

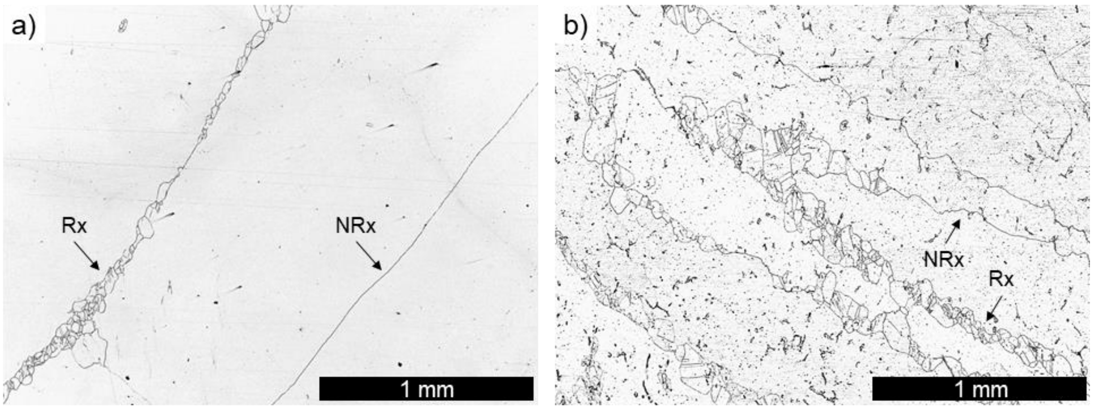

Figure 5.34 : Microstructural details of preferential recrystallisation along the boundaries of parent microstructure after the C1 cogging; a) 316L and b) 316Nb. “Rx” and “NRx” indicate the parent grain boundaries with or without recrystallised grains, respectively.

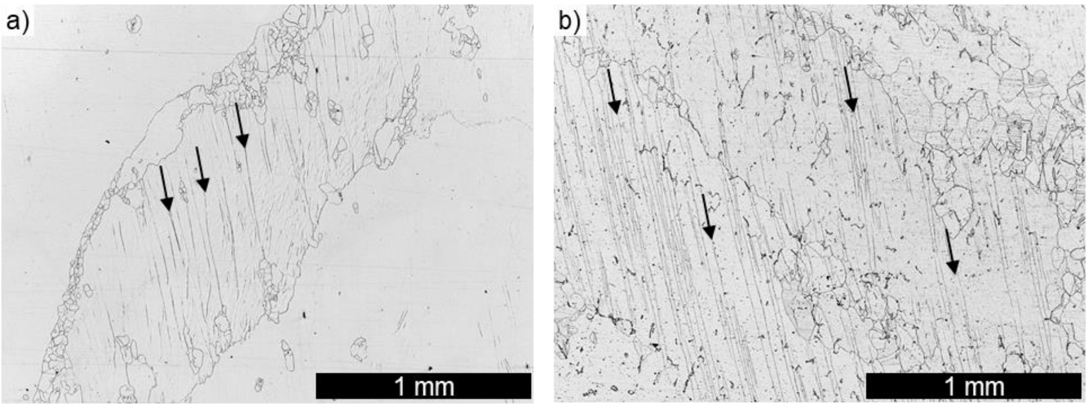

Figure 5.35 : Microstructural details of the a) 316L and b) 316Nb specimens taken from the ingots after the C1 cogging, showing deformation bands within non-recrystallised grains (arrows).

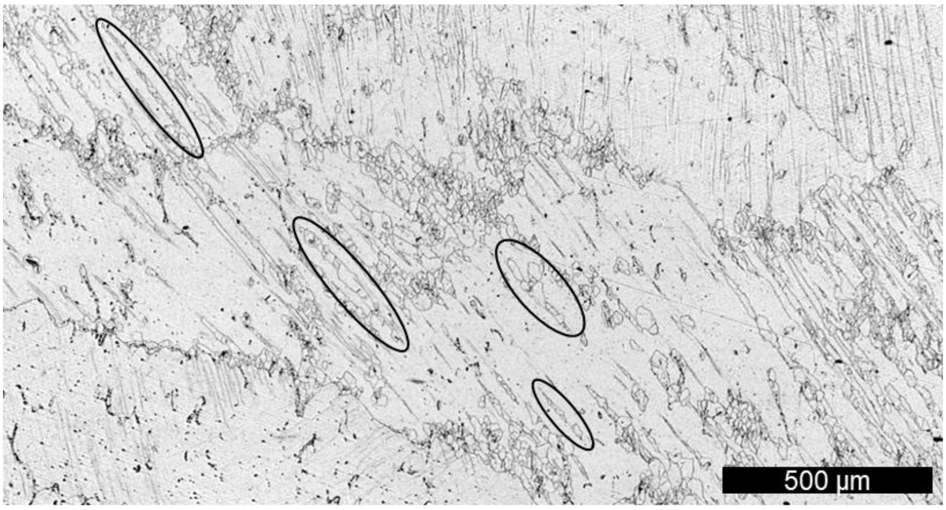

Figure 5.36 : Microstructural details of the 316Nb ingot after the C1 cogging, with some recrystallised grains located along the deformation bands highlighted by the ovals.

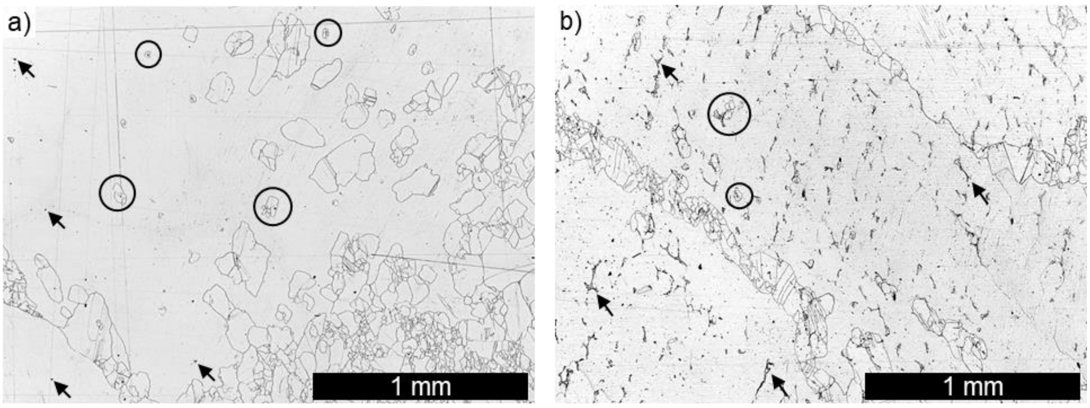

Figure 5.37 : Microstructural details of the ingots after the C1 cogging with secondary phases (arrows), and nucleation of recrystallised grains at the interface with the secondary phases (circles) highlighted; a) 316L, and b) 316Nb

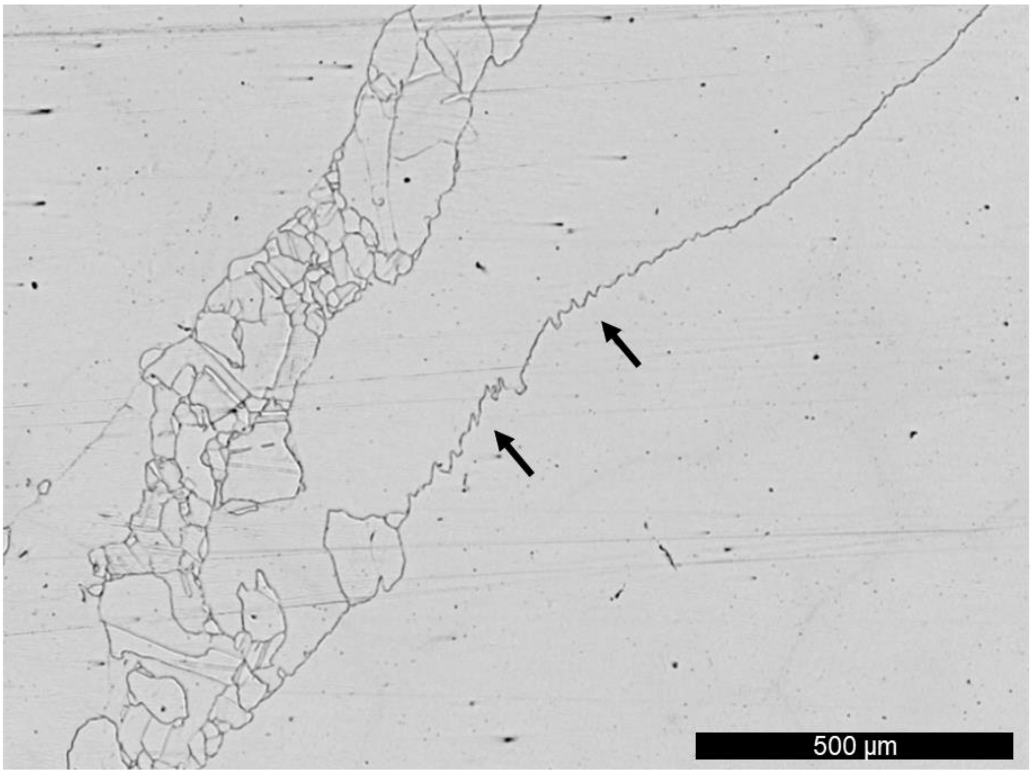

Figure 5.38 : Microstructural details of the 316L specimens taken from the ingots after the C1 cogging, showing serrated parent grain boundaries (arrows).

Observations performed on the 316Nb ingots showed that very different microstructures were obtained after upsetting and C1 cogging trials. The microstructure was fully recrystallised in the ingot after the upsetting, whereas only negligible recrystallisation was observed in the ingot after the C1 cogging, in which the recrystallised grains were predominantly located at the boundaries of the parent grains, and a noticeable presence of deformation bands was found along the skin of the ingot. The main differences between these experiments were: (i) the orientation between the axis of the ingots and the deformation direction; (ii) the strain rate at which the deformation was applied; and (iii) the evolution of strain and temperature during the trials.

This last hypothesis was investigated by the analysis of microstructure in the ingots cogged with the C2 forging route, during which the ingots were reheated to a temperature of 1250 °C for 1.5 hour immediately after the C1 cogging, and were then subjected to a final cogging operation on half of their length. As depicted in Figure 3.27, this final cogging process resulted in a section reduction ratio of $k_s \approx 50\%$. The macrostructures obtained for the 316L and 316Nb grade ingots after the C2 cogging are shown in Figure 5.39. At first glance, the microstructure appeared to be fully recrystallised for both grades in the deformed area of the ingots, with however smaller grains in the 316Nb ingot than in the 316L. In the 316L ingot, there is a noticeable sharp delimitation in the progression of recrystallisation at the transition limit of the chill zone, indicated by the curved line in Figure 5.39 a). This transition was not observed in the 316Nb ingot (see Figure 5.39 b)) since the chill zone of this ingot was held by the jaws of the manipulator, and was not displayed in the photograph. Coarser grains were also observed along the axis of the 316Nb ingot, highlighted by the circles in Figure 5.39 b), similar to the non-recrystallised grains observed along the axis of the 316Nb ingot after the upsetting (see Figure 5.17 d)).

To begin with, the investigations were focused on the section of these ingots that were cogged to $k_s \approx 23\%$ prior to the reheating, and were not subjected to the second cogging operation. This allowed for an examination of the effect of reheating on the deformed microstructure obtained after the C1 cogging. Microstructural observations performed along the radius of both ingots, in these regions cogged to $k_s \approx 23\%$, are presented in Figures 5.40 and 5.41 for 316L and 316Nb grades, respectively. Note that different magnifications were used in each case to display representative microstructures. Fully recrystallised microstructures consisting of equiaxed grains with relatively similar grain sizes were observed along the radius of the 316L ingot. The microstructure was also fully recrystallised in the 316Nb ingot (see Figure 5.41), with however different morphologies of the recrystallised grains along the radius of the ingot. The grains were equiaxed along the skin of the ingot (see Figure 5.41 a)), but were non-equiaxed at mid-radius (see Figure 5.41 b)) and at the core (see Figure 5.41 c)) of that ingot. The grains were also smaller along the skin of the ingot than at its mid-radius, which were also smaller than those observed along the axis of that ingot. A comparative analysis of the grain size was performed for both grades at the mid-radius of the ingots, using the micrographs presented in Figure 5.42. The grains were coloured according to their equivalent diameter; the micrographs were obtained by stitching 10×7 smaller micrographs together, and represents 8×8 mm^2 areas. The corresponding plots of the frequency of equivalent grain diameter and cumulative area fraction are presented in Figure 5.43. These results showed that the grains were significantly larger in the case of the 316L than for the 316Nb, with average grain size of 225 μm and 78 μm, respectively.

These results showed that for both grades of material, the microstructures obtained after cogging to $k_s \approx 23\%$, which was composed of few recrystallised grains located at some parent grain boundaries (see Figures 5.29 and 5.31), became fully recrystallised after the 1.5 hour reheating at 1250 °C. In comparison to the ingot which underwent the upsetting, these results demonstrate that the relatively low and decreasing temperatures at which the ingots underwent the deformation during the C1 cogging was a limiting factor to the progress of the recrystallisation during the test. The size of recrystallised grains was of ≈ 80 µm in both 316Nb ingots after the upsetting and cogging C1 tests.

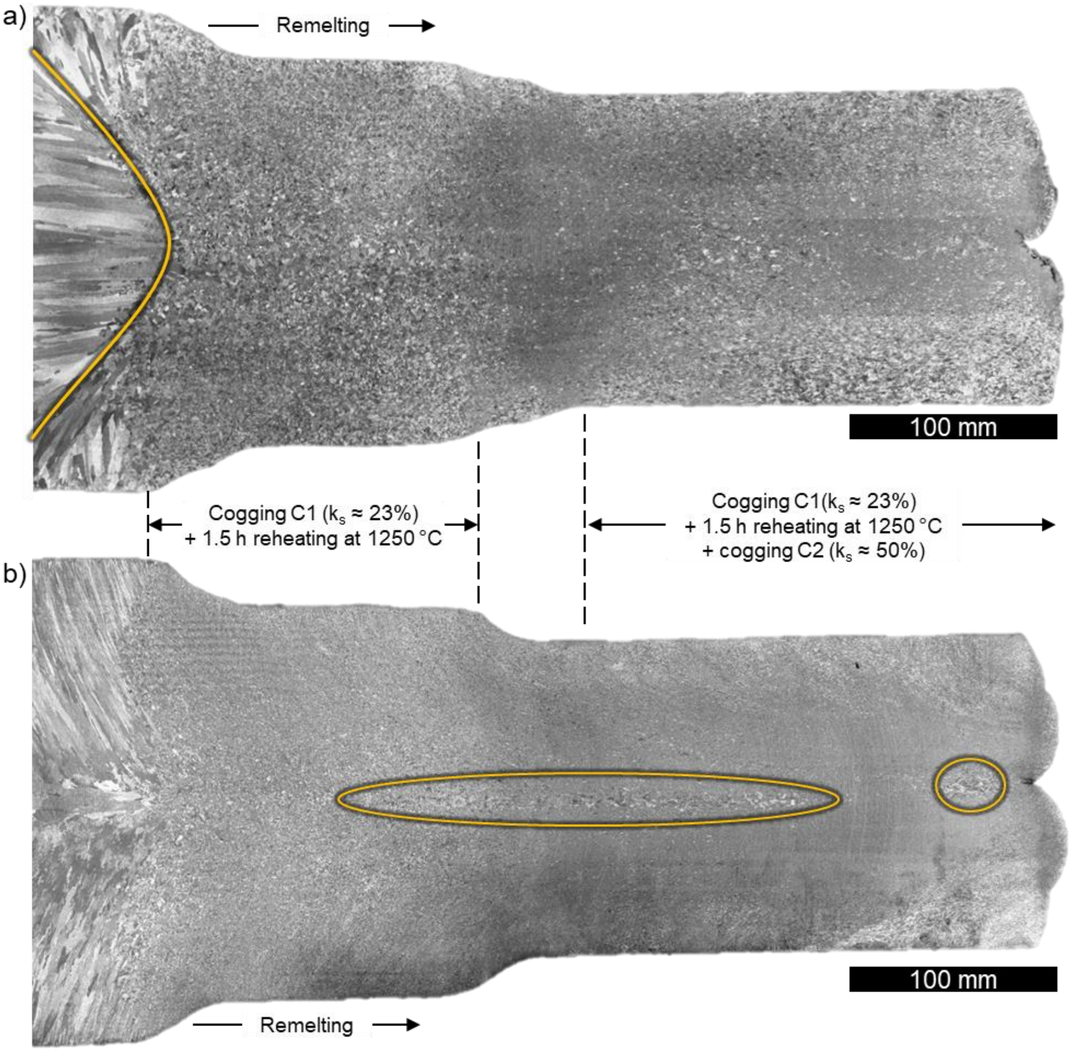

Figure 5.39 : Overall macrostructure of the ingots after the C2 cogging; a) 316L, and b) 316Nb. Observations performed along the longitudinal cross-sections of the ingots. The yellow curve in a) highlights the chill zone of the 316L ingot, and the coarser grains remaining at the core of the 316Nb ingot are encircled in b).

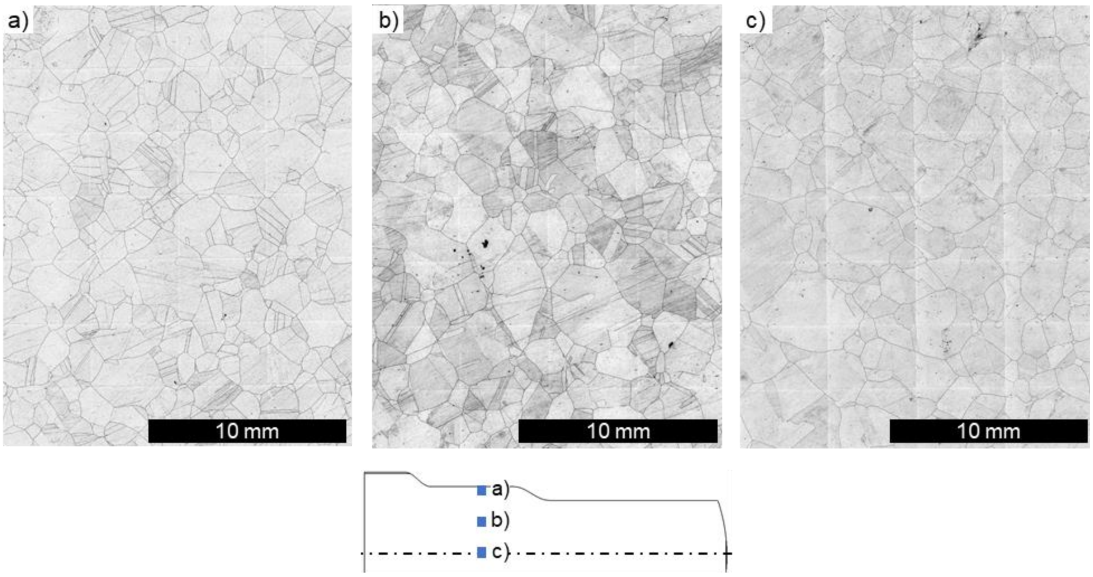

Figure 5.40 : Microstructural details of the cogged and reheated sections ($k_s = 23\%$) of the 316L ingot after the C2 cogging; a) skin, b) mid-radius and c) core. The micrographs were obtained by stitching 4×7 smaller micrographs together.

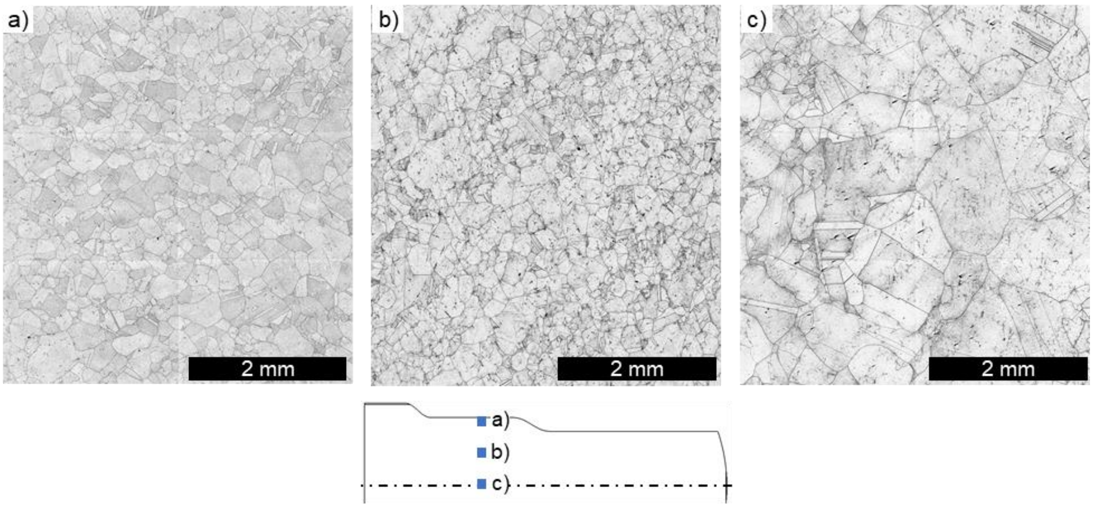

Figure 5.41 : Microstructural details of the cogged and reheated sections ($k_s = 23\%$) of the 316Nb ingot after the C2 cogging, showing recrystallised microstructures; a) skin, b) mid-radius, and c) core. The micrographs were obtained by stitching 3×2 smaller micrographs together.

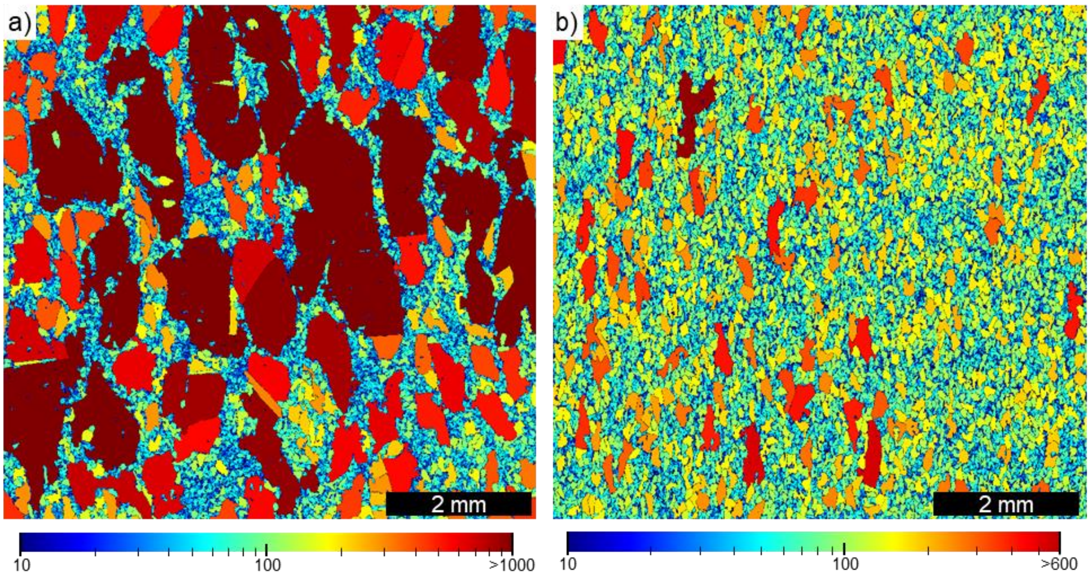

Figure 5.42 : Microstructures in the cogged ($k_s \approx 23\%$) and reheated section of the ingots after C2, with the grains coloured according to their equivalent diameter (µm); a) 316L, and b) 316Nb. Note that a different colour scale is used in each case. The micrographs were obtained by stitching 10×7 smaller micrographs together.

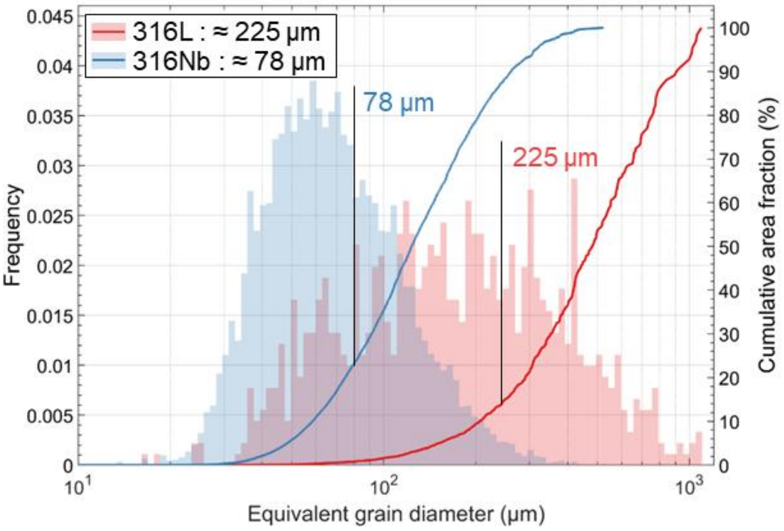

Figure 5.43 : Plots of grain size in the 316L and 316Nb ingots after the C2 cogging. Measurement performed on micrographs taken at mid-radius of the cogged ($k_s \approx 23\%$) and reheated regions of both ingots.

Following these results, the microstructure of both ingots is determined to be fully recrystallised after the 1.5 hour reheating at 1250 °C, and therefore at the beginning of the C2 cogging, performed on half the length of the ingots. The recrystallised grains that formed during the reheating are referred to as the “primary recrystallised grains” hereafter in order to distinguish them from the dynamically recrystallised grains that formed during the C2 cogging. Microstructures observed in the sections of the ingots cogged to $k_s \approx 50\%$ are presented in Figures 5.44 and 5.45 for the 316L and 316Nb grades, respectively. A global overview of the areas of the specimens witch underwent recrystallisation are also provided in each case. The fraction of recrystallised grains measured for these specimens are presented in Figure 5.46 in the form of heat maps, with the measurements performed on ≈ 2.5×3.5 mm^2 areas (i.e., at the scale of the individual micrographs collected over the surface of the specimens).

The progress of recrystallisation was relatively homogeneous in the 316L specimen, with necklace type microstructure composed of ≈ 45 % recrystallised grain (see Figures 5.44 and 5.46 a)). Areas with limited (see Figure 5.44 b)) or pronounced (see Figure 5.44 c)) fraction of recrystallisation were however observed along the skin of this ingot. As a consequence of the incomplete progress of the necklace type recrystallisation (i.e., ≈ 45 %), and coarse size of the starting grains (i.e., ≈ 225 µm), local grain size heterogeneities were observed in the specimen (see Figure 5.44 d) and e)).

Three zones with different progression of recrystallisation were observed along the radial direction of the 316Nb ingot after the C2 cogging (see Figures 5.45 a) and 5.46 b)). The 20 mm thick zone "I", located along the skin of the ingot, was heterogeneously recrystallised; with a "V" shaped area highlighted by the line in Figure 5.46 b), and containing ≈ 30 % of recrystallised grains, whereas the remaining areas of this zone had ≈ 30 to 60 % of recrystallised grains (see Figure 5.45 b) and Figure 5.45 c)). The microstructure was almost fully recrystallised in zone "II", at the mid-radius region of the ingot (i.e., from radius ≈ 1 to 4 cm) with ≈ 70 to 90 % of recrystallised grains (see Figure 5.45 d) and Figure 5.46 b)). In comparison to the 316L specimen, it can be seen from Figure 5.45 d) that the local heterogeneities observed in the 316Nb specimen were less pronounced in the homogeneously recrystallised zone "II" (i.e., at mid-radius) of the ingot; as a consequence of the advanced progress of recrystallisation (i.e., ≈ 70 %) and smaller initial grain size (i.e., ≈ 78 µm; see Figure 5.43). Finally, a few recrystallised grains (i.e., < 20 %) were observed in zone "III", located at the core of the ingot, where the as-cast grains had their long axis parallel to that of the ingot (see Figure 3.5). In this zone, the microstructure exhibits grain size heterogeneities, with notable fragmentation of the large as-cast grains into relatively smaller grains (see the circle in Figure 5.39 b)). As can be seen from Figure 5.45 a) and Figure 5.45 e), the fragmented grains had diameters larger than 1 mm, which is significantly larger than that of the primary recrystallised grains (i.e., ≈ 78 µm; see Figure 5.43); and demonstrate the limited progress of the static recrystallisation in this region of the 316Nb ingot. Despite the fact the thermomechanical history of both 316L and 316Nb ingots was similar throughout the C2 cogging (see Figures 5.14 and 5.15), the presence of fragmented grains was not observed in the 316L ingot.

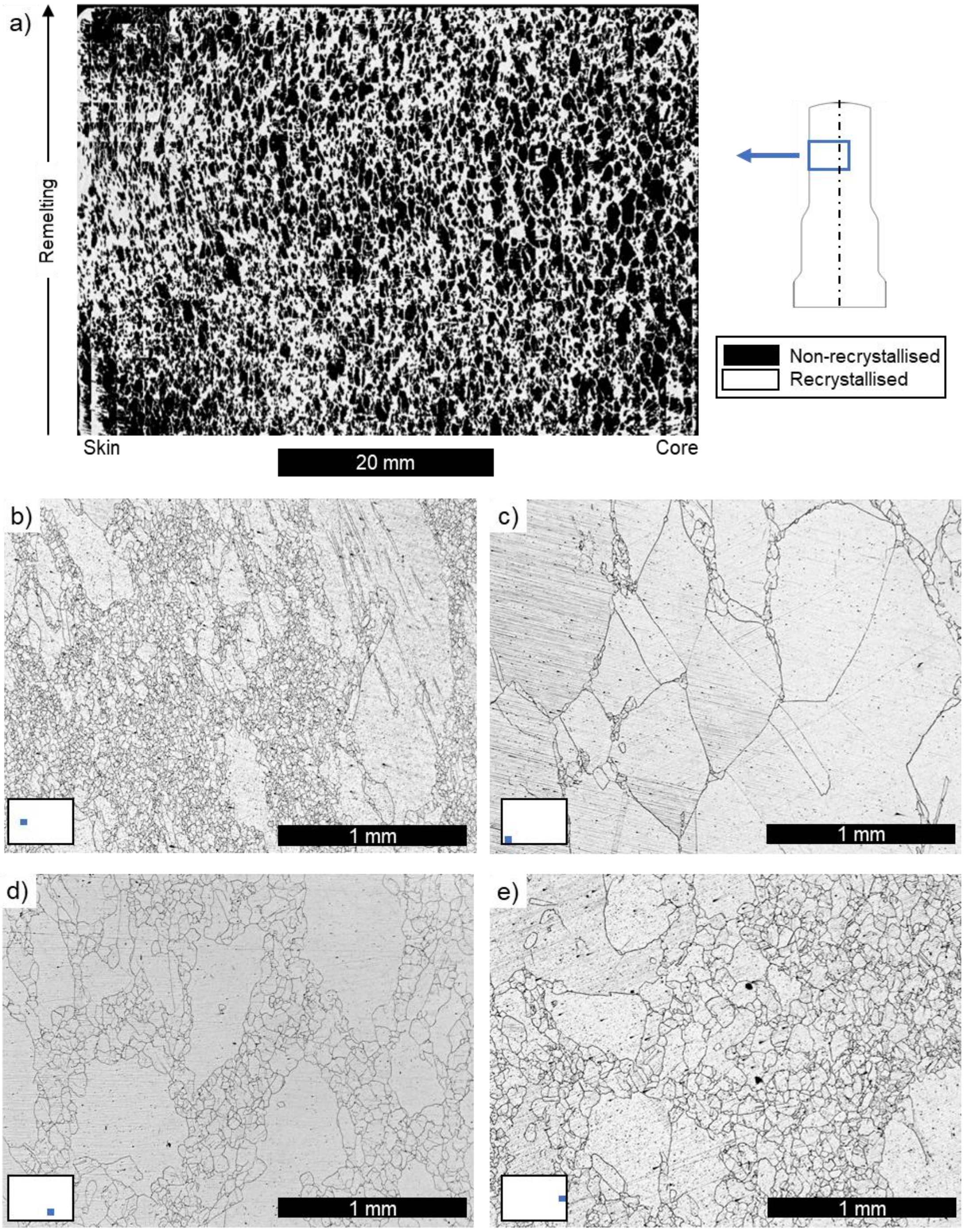

Figure 5.44 : Microstructure of the 316L specimen, taken from the longitudinal cross-section of the 316L ingot after the C2 cogging, in the section which was forged after the reheating; a) the occurrence of recrystallisation highlighted along the longitudinal cross-section of the ingot, and b), c), d) and e) microstructural details in the selected areas.

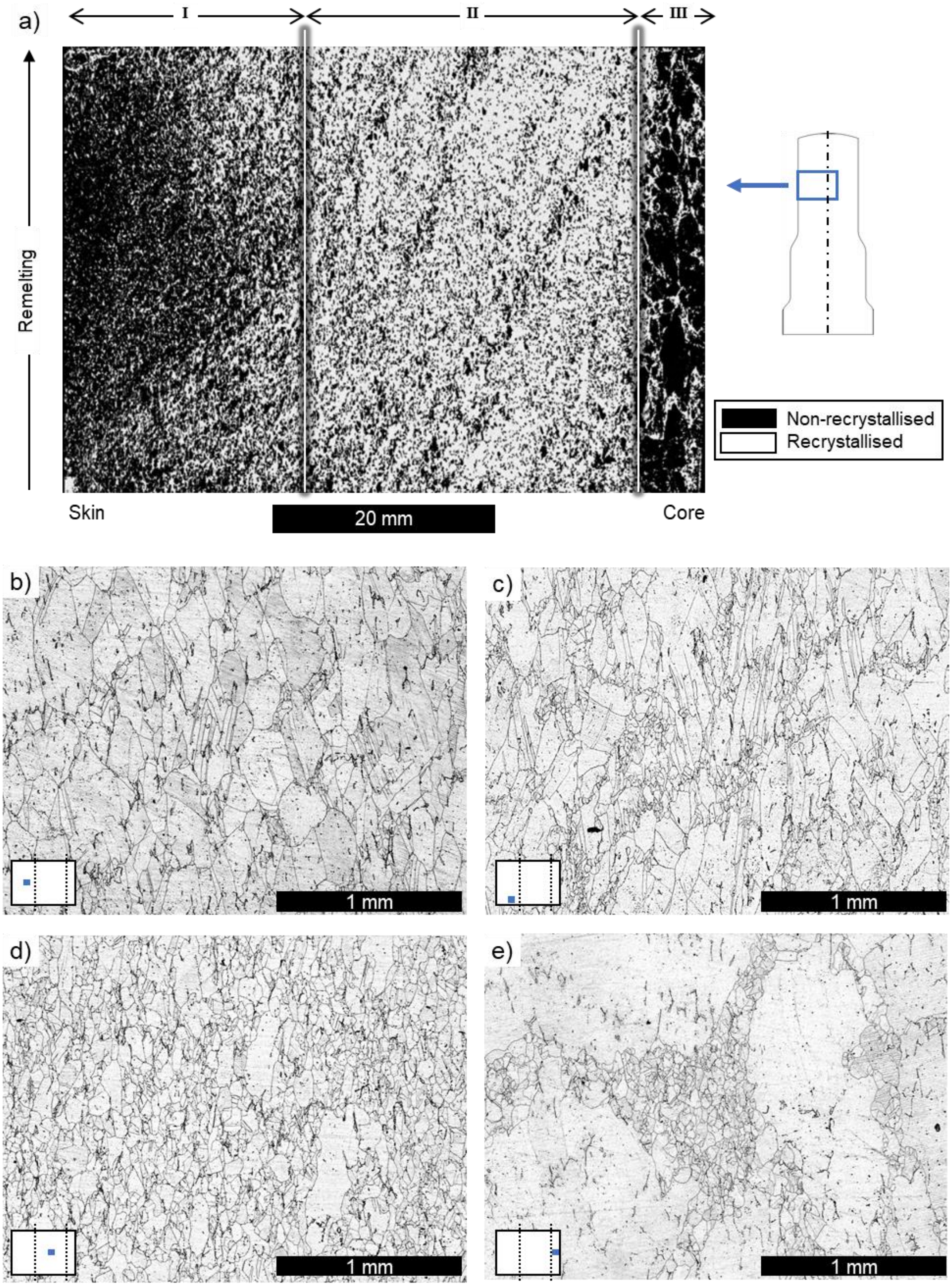

Figure 5.45 : Microstructure of the 316Nb specimen, taken from the longitudinal cross-section of the 316Nb ingot after the C2 cogging, in the section which was forged after the reheating; a) the occurrence of recrystallisation highlighted along the longitudinal cross-section of the ingot, and b), c), d) and e) microstructural details in the selected areas.

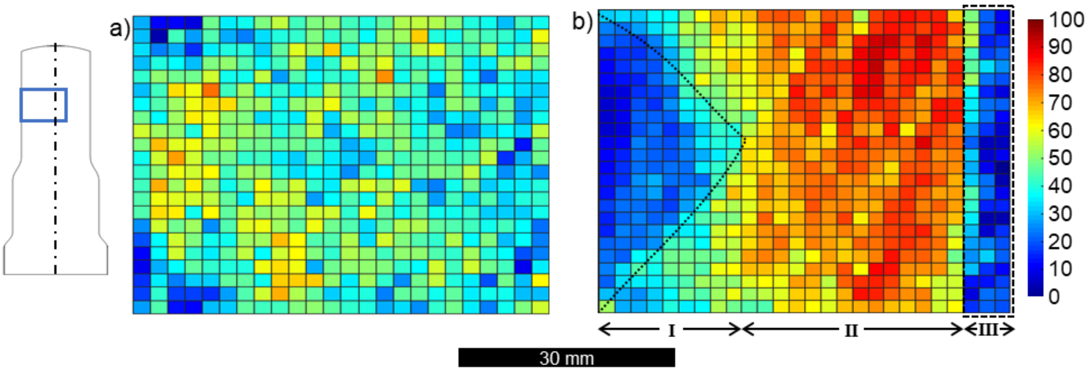

Figure 5.46 : Heat map of the fraction of recrystallised grains (%) measured in the specimens taken from the ingots after the C2 cogging, in the sections which were forged after the reheating; a) 316L and b) 316Nb. Each tile represents a ≈ 2.5×3.5 mm^2 area, corresponding to a single micrograph.

Figure 5.47 displays microstructures obtained for both grades after the C2 cogging, in the region cogged to k_s ≈ 50% after the reheating, with the grains coloured according to their equivalent diameters. The corresponding plots of the frequency of equivalent grain diameter and cumulative area fraction are presented in Figure 5.48. It can be seen from Figure 5.47 that the non-recrystallised grains (i.e., the remaining primary recrystallised grains) had an elongated shape, with their long axis oriented perpendicular to the direction of cogging (i.e., parallel to the axis of the ingot). Even though the fraction of recrystallised grains was 35% and 92% in the 316L and 316Nb grades, respectively, the average diameter of the recrystallised grains was relatively similar in both cases, at ≈ 35 µm. This grain size is significantly smaller than that of the primary recrystallised grains obtained after the reheating (i.e., of 225 and 78 µm in 316L and 316Nb grades, respectively; see Figure 5.43), and also smaller than that of the grains observed in the 316Nb ingot after the upsetting (i.e., ≈ 80 µm). Those grain size were consequently larger to those obtained in the fully recrystallised 60×60 mm samples deformed using the screw press (i.e., ≈ 70 µm and ≈ 35 µm in 316L and 316Nb grades, respectively, see Figures 4.27 and 4.28). The temperature of the small scale sample dropped down from 1250 °C to 1000 °C in ≈ 55 seconds following upsetting, whereas the ingots were reheated at 1250 °C for 90 minutes following C1 cogging schedule. Hence, the difference in size of recrystallised grains can be explained by the different duration at which the deformed and partially-recrystallised material remained at elevated temperature following the deformation stages. The larger size of recrystallised grains measured in the 316Nb ingot following upsetting (i.e., ≈ 70 µm) compared to that measured in the small scale samples made of the same grade following 30% upsettings (i.e., ≈ 35 µm) can be explained by the very different evolution of temperature between each case owing to the higher thermal inertia of the ingot compared to the small scale samples : the temperature dropped from 1250 °C to 1000 °C in 55 seconds and 10 minutes following the upsettings performed on the small scale samples and ingot, respectively. The slower cooling experienced in the 316Nb ingot following upsetting may hence have promoted grain growth, thus leading to the larger grain size obtained in the upset ingot. The grain size obtained following the upsetting (i.e., ≈ 70 µm) was slightly smaller than that obtained in the 316Nb ingot following C1+R (i.e., ≈ 80 µm), which was reheated at 1250 °C during 90 minutes. This slight difference in grain size achieved in both cases, compared to the different durations at which the material remained at elevated temperatures suggests a decrease in the kinetic of grain growth with time following recrystallisation (i.e., SRX followed by grain growth in the cogged ingot, and DDRX + MDRX followed by grain growth in the upset ingot). Although obtaining small grain sizes is not as critical as achieving the complete recrystallisation of the as-cast structure at this stage of the ingot-to-billet conversion process, those observations highlights the constraints associated with the different cooling rates experienced by the material during the experiments performed at different scales, owing to the different thermal inertia of the small scale samples and ingots.

Microstructural details observed along the skin of the ingots are provided in Figures 5.49 and 5.50. It can be seen from Figure 5.49 that the progress of recrystallisation was heterogeneous along the skin of the 316L ingot after the C2 cogging, in the section cogged to k_s ≈ 50%. Indeed, primary recrystallised grains with a few new recrystallised grains at some of their boundaries were observed in the area shown in Figure 5.49 a), whereas an almost fully recrystallised microstructure was observed at a distance of ≈ 20 mm from the first area (see Figure 5.49 b)). Some of the non-recrystallised grains located along the skin of that ingot were composed of a large amount of deformation bands, highlighted by the arrows in Figure 5.50. Similar observations were obtained for the 316Nb grade ingot cogged to k_s ≈ 50%. These results suggest that the heterogeneous strain levels predicted by FE simulations along the skin of the ingot (see Section 5.3), as a consequence of the cogging stroke schedule, induced the heterogeneous evolution of microstructure throughout the C2 cogging schedule.

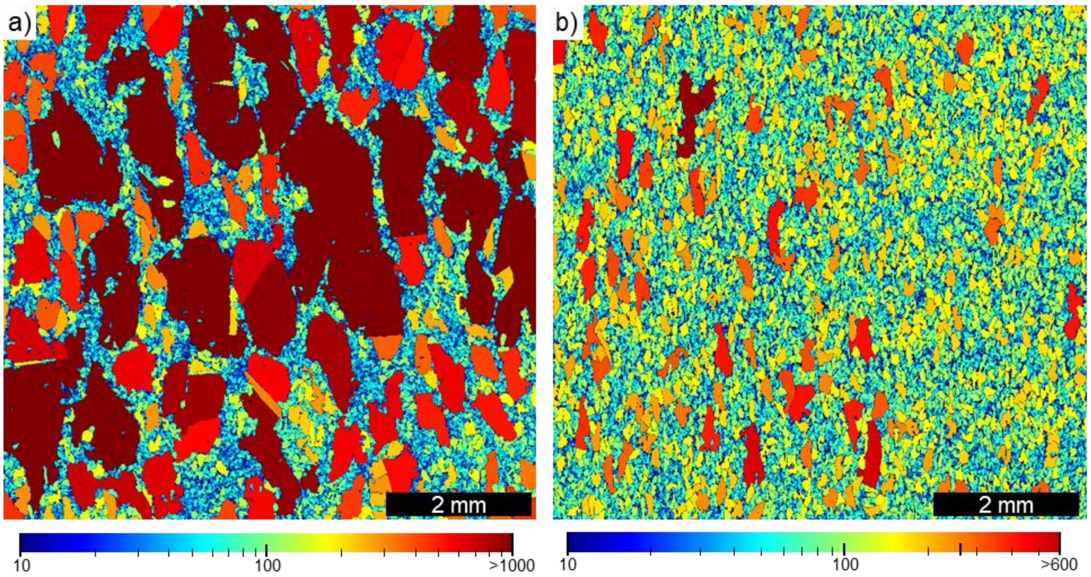

Figure 5.47 : Partially recrystallised microstructures of the ingots after C2, in the region cogged to $k_s \approx 50\%$, with the grains coloured according to their equivalent diameter (μm); a) 316L, and b) 316Nb. Note that a different colour scale is used in each case. The micrographs were obtained by stitching 4×3 smaller micrographs together.

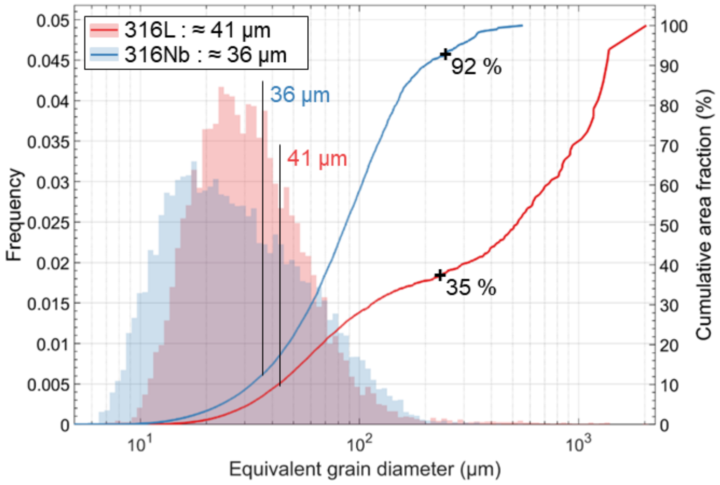

Figure 5.48 : Plots of grain size in the 316L and 316Nb ingots after the C2 cogging, at mid-radius of the section cogged to ks ≈ 50%. Note that the estimated fraction of recrystallised grains is indicated for each case.

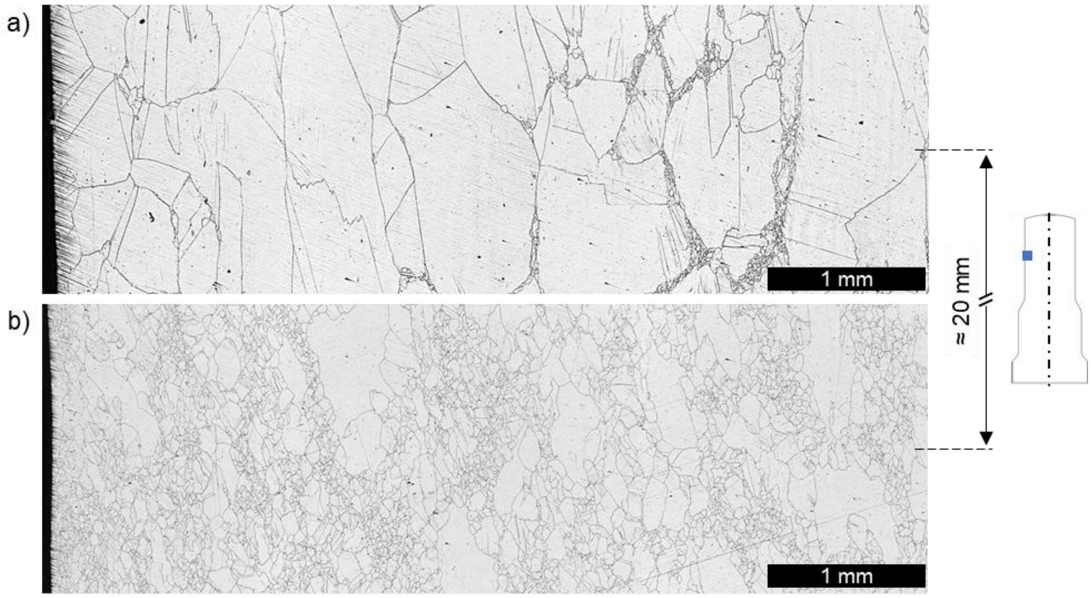

Figure 5.49 : Micrographs showing the heterogeneous microstructures observed along the skin of the 316L ingot after the C2 cogging, in the section cogged to $k_s \approx 50\%$. The micrographs a) and b) were distant by ≈ 20 mm.

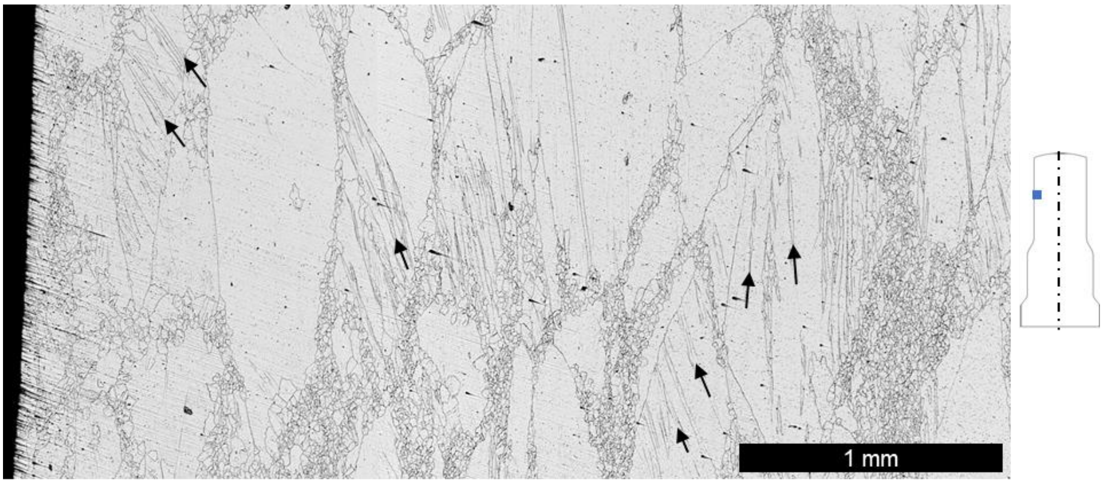

Figure 5.50 : Deformation bands observed along the skin of the 316L ingot after the C2 cogging, in the section cogged to $k_s \approx 50\%$. Some of the observed deformation bands are highlighted by the arrows.

To address this hypothesis, the results obtained from the analysis of the specimens' microstructure (i.e., the occurrence of recrystallisation, the fraction of recrystallised grains and their average diameter) are displayed together with the corresponding distribution of equivalent strain predicted by FE simulations, in Figures 5.51 and 5.52 for 316L and 316Nb grades, respectively.

For the 316L specimen, the areas highlighted by the white line were located along the skin of the ingot and had a relatively low fraction of recrystallised grains (i.e., $< \approx 30\%$, see Figure 5.51 b)), and therefore a relatively large grain size (i.e., $> \approx 40$ µm, see Figure 5.51 c)). These two areas correspond to the zones where strain values were predicted to be below 1.2 by FE simulations (see Figure 5.51 d)). The area where the edge of the anvil impacted the ingot is indicated by the arrow in Figure 5.51 d), and corresponds to an area containing grains with a diameter below 35 µm (see Figure 5.51 c)). The shape of that area containing smaller grains match relatively well with that of the high strain zone predicted by FE simulations just under the area where the edge of the anvil impacted the ingot (see Figure 5.12 c)). Similar trends were observed from the analysis of the micrographs and FE simulations obtained for the 316Nb grade, which results are provided in Figure 5.52. The "V" shaped area highlighted with the white line in Figure 5.52 a) bounds a region with a limited progress of recrystallisation (i.e., $< 20\%$), for which lower strain levels were predicted by FE simulations (i.e., < 1.5; see Figure 5.52 d)). The arrows in Figure 5.52 d) indicates the location where the edge of the anvil impacted the ingot during the cogging trials, which also match with the areas where the smaller recrystallised grains were observed (i.e. < 30 µm, see Figure 5.52 c)). Since similar strain levels in the range 1.8 to 2.1 were predicted by FE simulations in the mid-radius and central regions of the ingot (see Figure 5.52 d)), it was expected that a similar progress of recrystallisation would be observed in these regions. However, fractions of recrystallised grains of $\approx 70\%$ and $< 20\%$ were measured in the mid-radius and central regions of the ingot, respectively (see Figure 5.52 b)).

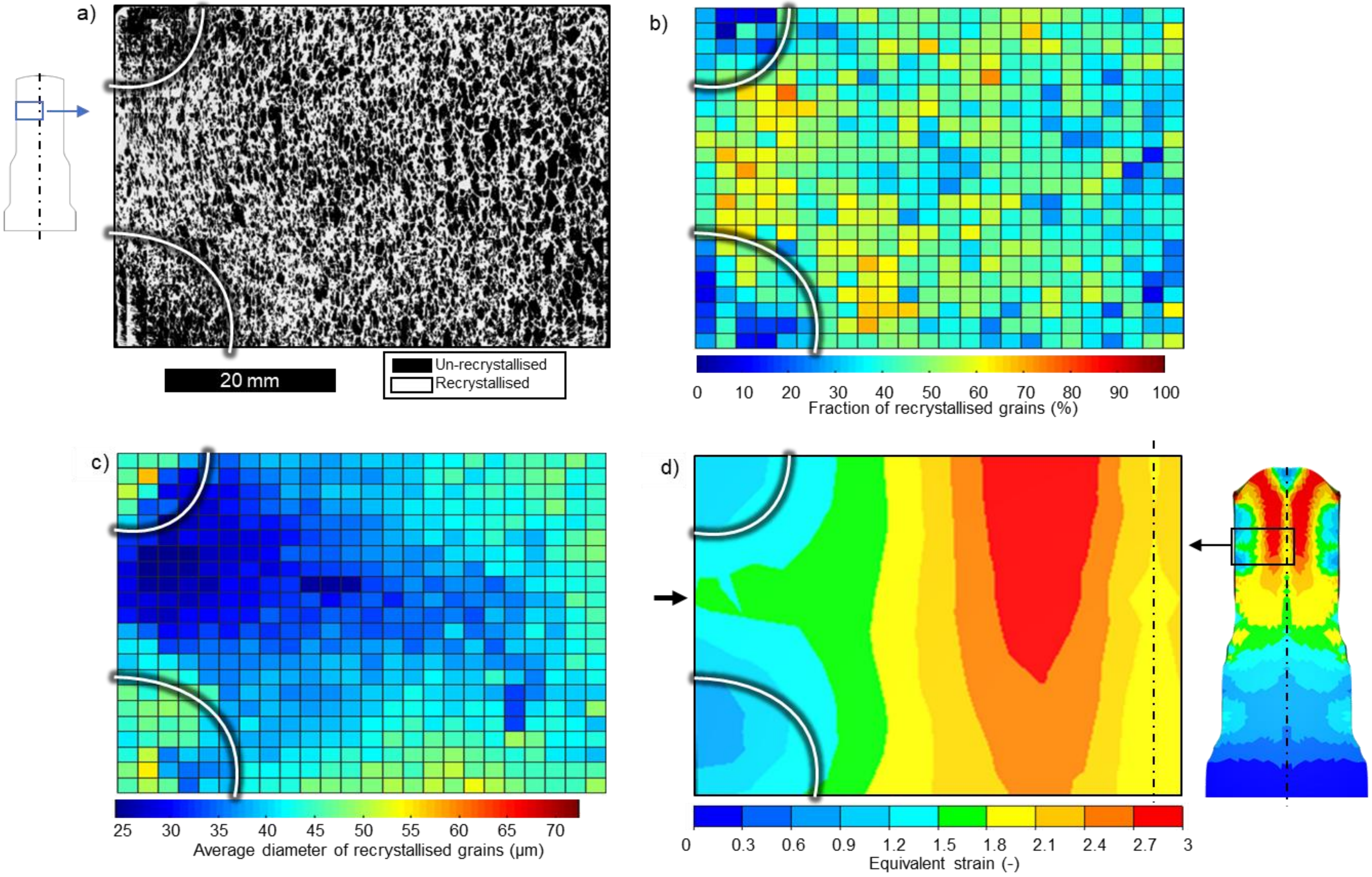

Figure 5.51 : Summary of the results obtained from the 316L specimen after the C2 cogging, in the section reduced to ks ≈ 50%; a) occurrence of recrystallisation highlighted along the surface of the specimen, b) heat maps of the fraction of recrystallised grains, c) their average diameter, and d) distribution of equivalent strain predicted by FE simulations.

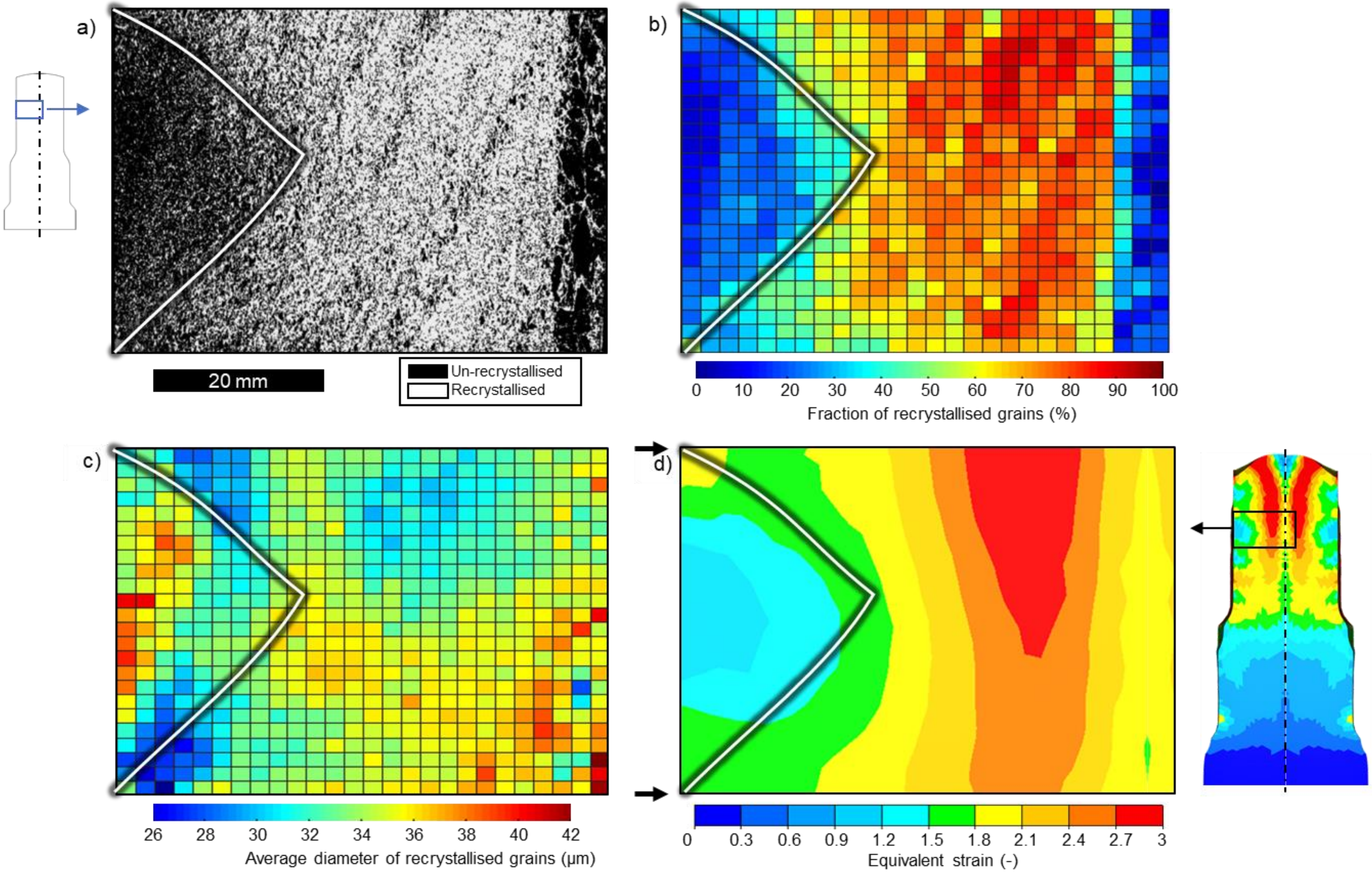

Figure 5.52 : Summary of the results obtained from the 316Nb specimen after the C2 cogging, in the section reduced to $k_s \approx 50\%$; a) occurrence of recrystallisation highlighted along the surface of the specimen, b) heat maps of the fraction of recrystallised grains, c) their average diameter, and d) distribution of equivalent strain predicted by FE simulations.

5.5 SUMMARY

In this chapter, the evolution of the as-cast microstructure of Ø185 mm VIM/VAR processed ingots made of 316L and 316Nb materials were investigated using upsetting and cogging trials, replicating the initial stages of industrial ingot-to-billet conversion processes.

The evolution of temperature, strain, and strain rate during the trials were predicted by means of FE simulations performed with anisotropic material model implemented, which demonstrated the good capability of the anisotropic model calibrated from the small-scale experiment at predicting the deformed geometry of the larger ingots. Despite of the variabilities induced by the cogging experiments (e.g., duration, cogging schedule, etc.), the experiments allowed to replicate a comparable evolution of thermomechanical history for the different ingots which underwent the cogging trials. Upsetting and cogging processes were found to respectively provide distinct evolution of strain and temperature throughout the tests.

Microstructure evolution was investigated by means of macroscopic observations of the etched longitudinal cross-sections of the ingots, OM observations, and quantitative analyses of the micrographs collected along the surface of specimens taken out from the ingots. The as-cast microstructure was fully recrystallised after the upsetting test performed on the 316Nb ingot, as well as after reheating the ingots which underwent cogging to $k_s \approx 23\%$. Primary recrystallised microstructures of the 316Nb ingot, following upsetting and cogging, had grains of ≈ 80 µm, whereas that of the 316L ingot was ≈ 225 µm. Despite the different size (i.e., width) of the as-cast grains in 316L and 316Nb grade ingots, the size of the recrystallised grains was similar for both grades after the second cogging stage (i.e., C2), at ≈ 35 µm. However, different fraction of recrystallised grains were measured in both cases (i.e., 35% and 92% in 316L and 316Nb ingots, respectively).

Chapter 6 : DISCUSSIONS

CONTENT

6.1 INTRODUCTION

This PhD thesis investigates the evolution of as-cast microstructures of 316L and 316Nb grades of austenitic stainless steel during the early stages of ingot-to-billet conversion process, with a focus on difference between microstructure evolution (i.e., recrystallisation behaviours) at laboratory-scale and industrial-scale processing conditions. By replicating conditions closer to those encountered in industrial settings, this work provides a more realistic approach to understanding of as-cast material behaviours compared to conventional laboratory-scale experiments. A comprehensive set of experiments were conducted on both small-scale samples and large-scale ingots, complemented with microstructure characterisations at various stages (i.e., partially and fully recrystallised microstructures). In addition, FE simulations were employed to predict local thermomechanical data (e.g., strain, strain rate and temperature), offering insights into the conditions experienced by the material throughout the experiments. The collected results were presented in Chapters 4 and 5 for the small-scale and industrial ingot-scale studies, respectively.

This Discussion chapter delves deeper into the deformation and recrystallisation behaviours of the as-cast microstructures during open-die forging (i.e., cogging and upsetting processes). The findings from this PhD thesis are contextualised by drawing connections between small- and ingot-scale experiments, as well as by comparing the collected results to existing studies published in literature. The comparison between the 316L and 316Nb grades further enables an evaluation of the influence of Nb on microstructural evolution at this stage of the ingot-to-billet conversion process. The methodology developed in this work is discussed in comparison to those typically employed in previous studies, and its benefit to future studies aiming at the improvement and optimisation of larger scale ingot-to-billet conversion process.

6.2 DEFORMATION BEHAVIOURS OF THE AS-CAST MICROSTRUCTURES

Heterogeneous deformation of the as-cast microstructures was manifested, at both macro- and micro-scales, through their impacts on surface characteristics of the small-scale samples following upsetting, and on the microstructure observed as a result of the experiments. The "orange peel" appearance observed on the surface of the small-scale samples following hot upsetting (see Chapter 4) lies in the different deformation behaviour of the neighbouring grains, resulting from their different crystallographic orientations. This was not observed for the large-scale ingots due to the thick oxide layer formed on their surfaces. These phenomena highlight the heterogeneous deformation behaviour of the as-cast microstructure. It is made visible by eye from the coarse size of the as-cast microstructure, and is commonly reported in the literature for as-cast materials (Mataya et al., 2003a) (Semiatin et al., 2004). It is stated in (Roebuck et al., 2006) that uniform deformation can be achieved in samples having at least 100 grains in their transverse cross-section. This requirement was satisfied for the Ø 60×60 mm small-scale samples subjected to 30% upsetting (i.e., containing from 6 500 to 45 000 grains, see Table 3.4), as well as in many studies focused on the recrystallisation of as-cast behaviour. However, in the study of (Yeom et al., 2007), the samples had a diameter of 10 mm, while the average grain diameter was 2 mm. Consequently, the samples had ≈ 25 grains in their transverse cross-section, which is far below the number of grains recommended in (Roebuck et al., 2006).

Laboratory-scale compression tests conducted by (Sahithya et al., 2019) on as-cast nickel-based superalloy involved samples with dimensions of Ø 8×12 mm, Ø 10×15 mm, and Ø 12×18 mm. Even though the average initial grain diameter was not disclosed by the authors, it was estimated at ≈ 700 µm based on OM provided in the study. Hence, the samples had about 130, 200 and 300 grains in their transverse cross-section, respectively. Unfortunately, the study did not include a comparison of results obtained under the same thermomechanical conditions for different sample dimensions; it is likely that the different sample dimensions were selected by the author to account for load limitations of their testing equipment, depending on the test condition (e.g., low temperature and/or high strain-rate). Nevertheless, such comparison would have allowed to assess the sensibility of the material flow behaviour to the number of grains across its transverse cross-section.

The heterogeneous deformation behaviour of the as-cast material was also highlighted by heterogeneous microstructure evolution, with localised formation of deformation bands and heterogeneous progress of recrystallisation. For instance, recrystallised and non-recrystallised areas were observed in areas where homogeneous thermomechanical properties were predicted by FE simulation, which demonstrates therefore the limitations of conventional FE models for accurate prediction of local thermomechanical properties. In the 316Nb grade, heterogeneous deformation was also made possible through flow localisation at the interface with the undissolved secondary phases, which promotes localised nucleation of recrystallisation along with these features, such as previously observed by (Mataya et al., 2003a) (Qin et al., 2017b).

The role of the heterogeneous deformation of the microstructure in the heterogeneous progress of recrystallisation was also suspected by (Weaver and Semiatin, 2007) for as-cast nickel-base superalloy. With the help of a CPFEM model, (Turner and Semiatin, 2011) were able to quantify the deformation heterogeneities formed during the hot upsetting of a coarse-grain nickel-base superalloy, and to highlight that heterogeneous levels of deformation were reached within the individual grains, as well as between the neighbouring grains. This causes the formation of areas with highly anisotropic distributions of the crystallographic orientation, which were found by (Quey et al., 2021) to exhibit high density of recrystallisation nuclei. The heterogeneous deformation behaviour of the as-cast microstructure promotes therefore the localised nucleation of recrystallisation. It must be noted that localised and heterogeneous progress of recrystallisation may, in turn, induce additional flow localisation and heterogeneous strain distribution across partially recrystallised microstructure.

The large as-cast columnar grains led to heterogeneous deformation at different scales, i.e., manifested at macro-scale in the form of irregular deformation of the samples and at micro-scale in the form of heterogeneous deformation within individual grains. In addition to the heterogeneous deformation underwent by the as-cast material due to the coarse grain size, the testing processes also introduced additional level of deformation heterogeneities, at macro-scale. During cogging process, local deformation gradients is applied to the ingot by anvils (e.g., see Figure 5.10). Owing to friction with the dies, the small-scale samples did not underwent homogeneous deformation, and barrelling led to the development of strain and strain rate gradients in the samples (e.g., see Figures 4.12 and 4.13). Consequently, the as-cast columnar grains individually experience different levels of strain under varying strain rates along their axes, due to their considerably large sizes, and the heterogeneous plastic deformation (i.e., strain localisation) in the as-cast microstructure led to non-uniform recrystallisation such that more recrystallisation occurred at highly strained area (i.e., due to higher driving force supplied by local strain energy), hence limiting the accuracy of correlations with the FE predicted thermomechanical data.

Although both heterogeneous deformation and recrystallisation behaviours are expected characteristics of as-cast materials, appropriate testing may be designed to help distinguish between the heterogeneous behaviours caused by the as-cast microstructure from those induced by the testing process. Most laboratory-scale experiments are performed on small cylindrical samples, but using double truncated cone (DTC) samples has now become a common practice for investigation of recrystallisation in wrought (Pérez et al., 2018) and as-cast materials (Semiatin et al., 2004). Compared to cylindrical sample geometry, using DTC samples has a valuable advantage of reducing the overall number of experiments required to cover the same range of thermomechanical testing conditions, at the expense of increased complexity in the interpretation of results due to the larger strain and strain-rate gradients experienced by the material along the cross-sections of the samples.

Anisotropic deformation behaviour of the as-cast material was systematically observed after thermomechanical processing, through direct observation and measurements of the deformed geometries of the small-scale samples, and predicted with FE simulations for all ingots after upsetting and cogging. The results shown clear effect of as-cast microstructure on the anisotropic deformation of the cylindrical samples (see Figure 4.1). This was further verified by the FE simulations where deformation heterogeneity was observed when using anisotropic materials properties in the form of Hill-48 (Hill and Orowan, 1948) parameters vs. uniform deformation when using isotropic material properties. Such behaviour is commonly reported in the literature (Semiatin et al., 2004) (Park et al., 2005), and is ascribed to the specific crystallographic texture resulting from the directional solidification of the molten material into columnar grains (Fischer et al., 2021). However, the anisotropic characteristics of as-cast materials are rarely considered in the existing studies.

A transition from anisotropic to isotropic material behaviour is expected at the end of the ingot-to-billet conversion process, since the initial as-cast microstructure is completely transformed to recrystallised and refined equiaxed grains. This also eliminates the preferential crystallographic texture associated with the as-cast microstructure due to directional growth. Although fully-recrystallised microstructures were obtained at the early stage of the ingot-to-billet conversion process, it remain unknown whether the anisotropic deformation behaviour of the material disappeared effectively. This could have been evaluated through EBSD texture analyses, or by conducting a series of compression tests on samples taken from recrystallised areas. It must be noted that the anisotropic material model was used all along the thermomechanical processes modelled by FE simulation, regardless of the progress of recrystallisation.

The results obtained from the experiments conducted at different scales showed that the anisotropic flow behaviour of the as-cast material had a significant impact on the deformed geometry of the samples and ingots, as well as on the resulting strain and strain-rate distributions. The FE simulations with implemented anisotropic material model (Hill-48) provided good predictions of the deformed geometries of the as-cast material, and allowed for more accurate estimation of thermomechanical properties when compared to an isotropic material model. The FE model did not consider the dependency of the material behaviour on microstructural evolution taking place during thermomechanical processing, including phenomena such as localised strain hardening and recrystallisation. The anisotropic flow behaviour of the as-cast material was implemented in the FE model using the Hill yield criterion (Hill and Orowan, 1948); and the value of the Hill parameters were calibrated by a debatable “trial and error” optimisation method based on the comparison of real and FE predicted geometries of the small-scale samples after upsetting (see Section 3.3).

The anisotropic material model calibrated from the geometries of the small-scale samples (see Figure 4.3) allowed for accurate prediction of the deformed geometry of the large ingots (e.g., see Figure 5.4) following upsetting and cogging, which confirm the validity of the Hill parameters and anisotropic material model used in this work. Assuming DRX primarily originate at the boundaries of parent as-cast microstructure, further validation of the model lies in the correspondence of the deformed marking grids implemented in the FE model to track the location of virtual grain boundaries, and the location of the recrystallised bands observed in the partially-recrystallised small-scale samples (i.e., those forged by the hydraulic press, see Chapter 4). A similar "trial and error" optimisation method was used by (Terhaar et al., 2012) for the calibration of anisotropic Barlat's yield parameters in the FE model of upsetting tests performed on intermediate-scale sample (i.e., Ø55.6×100 mm) taken from an Inconel 718® ingot, with a similar coarse, columnar as-cast microstructure. These demonstrate that analyses of the deformed geometry of large-scale samples containing a large number of columnar grains can be used for the determination of as-cast material anisotropic properties, the development of more accurate FE models, and therefore improve the accuracy of FE models for improvement and optimisation of the ingot-to-billet conversion process. Owing to the large number of grains comprised across the cross-section of the small-scale samples, the small-scale samples underwent relatively homogeneous deformation at macro-scale, hence allowing to calibrate the anisotropic material model based on shape correlation. In (Semiatin et al., 2004), the laboratory-scale samples subjected to isothermal testing developed strong irregularities in shape (see Figure 2.25), which would have impeded the calibration of the anisotropic material model such as performed in this PhD thesis using the significantly larger small-scale samples.

In this PhD thesis, the "trial and error" optimisation method was found to be the most suitable method to evaluate the anisotropic properties of the as-cast materials. Alternative methods with higher rigour and elegance however exists for the determination of anisotropic material properties. In sheet metal forming, the anisotropic material models are usually determined by performing a selected set of tensile, shear and compression tests on samples with representative microstructure, and the anisotropic parameters are derived from the resulting stress-strain curves (Liu et al., 2023). Unless considering the whole large-scale ingot, no sample with representative microstructure could be extracted from an ingot due to the rotational symmetry of its microstructure (i.e., of the morphologic and crystallographic textures). Also, the use of specific and high load capacities equipments are required for performing such tests on a bulk RVE of the as-cast microstructure containing enough grains to ensure a representative deformation behaviour. These limitations can however be overcome by performing the tests virtually using a CPFEM model on a RVE of a columnar microstructure aggregate, which was employed by (Fischer et al., 2021) to demonstrate the preponderant effect of the crystallographic texture of as-cast columnar microstructures over its morphologic texture. (Liu et al., 2023) also developed a CPFEM model to account for the evolving texture and induced anisotropic plasticity evolution in FE models of sheet metal forming. Those modelling approaches could be adapted to evaluate more accurately the anisotropic behaviour of columnar as-cast material. As used by (Turner and Semiatin, 2011), such CPFEM model can also be employed for additional investigations, such as for the evaluation of local deformation heterogeneities developed among the microstructure during thermomechanical processing. Even though advanced modelling techniques had been employed to evaluate the anisotropic behaviour of the as-cast material, it is noteworthy that intermediate- or large-scale experimentations would have been required for validating the anisotropic behaviour model; and intermediate or larger scale investigation consequently remain of interest.

6.3 EVOLUTION OF AS-CAST MICROSTRUCTURE DURING HOT PROCESSING

The progress of recrystallisation in the as-cast 316L and 316Nb grades occurred via several mechanisms. Limited DDRX occurred at lower temperatures (i.e., during the upsetting of the small-scale samples forged by hydraulic press, see Figure 4.16), and during C1 cogging schedules, see Figure 5.31). As previously observed for as-cast austenitic stainless steels by (Qin et al., 2017b) and (Wang et al., 2021a), DDRX was characterised by grain boundaries bulging. The adiabatic temperature raise experienced by the small-scale samples forged by a screw press resulted in full recrystallisation of both 316L and 316Nb grades via MDRX, which was enabled by the deformation and the adiabatic heat generated during the high strain rate deformation.

On the other hand, although the as-cast grains underwent significant deformation throughout C1 cogging schedules (see Figure 5.30), both grades exhibited low fraction of recrystallised grains. As seen in Figure 5.16, C1 cogging schedule comprised of small strain increments (i.e., ≤ 0.2) under high strain rates (i.e., up to 15 s^{-1}) with a continuous decrease in the ingot's temperature via cooling (i.e., below 1000 °C at the core of the ingots, at the end of C1), which thermomechanical history roughly match with those reported in (Mataya et al., 2003a) and (Han et al., 2015) to result in limited progress of DRX. Compared to the small-scale sampled forged by screw press, the ingots underwent cooling between each cogging passes (see Figure 5.16), thereby limiting the beneficial effects of adiabatic heating in promoting MDRX during cogging. Recrystallisation of the as-cast material subjected to cogging was only observed after applying a 90 minutes reheating at 1250 °C following C1 cogging schedule (i.e., C1+R), which is SRX. (Mataya et al., 2003a) observed that full recrystallisation of as-cast 316L subjected to hot upsetting could be achieved after applying at least 0.5 strain at 1150 °C under 1 s^{-1}, followed by 60 minutes heat treatment at the same temperature. Those conditions roughly matches the conditions applied for both grades during C1 cogging schedules and the subsequent reheating.

During the following C2 cogging schedule, the already recrystallised portion of the microstructure (i.e., just after C1+R) experienced further DDRX, with necklaces of recrystallised grains formed at the boundaries of the parent grains. The fraction of recrystallised grains were ≈ 50% and ≈ 70% for 316L and 316Nb grades, respectively, which are significantly higher than those observed after only C1 cogging schedule. (El Wahabi et al., 2005) demonstrated the strong sensibility of DDRX kinetic to the initial grain size owing to reduced mean free path for dislocation motion in fine grained microstructures, hence promoting higher rate of dislocation accumulation in the substructure. (Weaver and Semiatin, 2007) found that the DDRX kinetic of columnar as-cast Waspaloy material was slow compared to wrought material. The higher fraction of recrystallised grains obtained following C2 cogging schedule, compared to C1, can hence be attributed to the different initial material condition between each case (i.e., as-cast prior to C1 cogging schedule, and wrought prior to C2 cogging schedule).

Although homogeneously recrystallised microstructures were obtained following C1+R, remarkable heterogeneities in the progress of recrystallisation were observed along the edge of the ingots following C2 cogging schedules. This was a direct consequence of the incremental characteristic of the cogging process, which resulted in macroscopic gradient of strain and strain rate along the length of the ingots (see Figure 5.13). Such characteristics of the cogging process were already known since previous research aimed at designing optimal cogging schedules with homogeneous thermomechanical processing conditions (Dandre et al., 2000a). Their effects on the actual progress of recrystallisation during the early stage of the ingot-to-billet conversion process were used when designing experiments for this study. However, as a result of limited progress of DDRX during C1 cogging schedules, homogeneous recrystallisation of the as-cast microstructure was achieved following the subsequent reheating (i.e., following C1+R, see Figure 5.39). Full recrystallisation of the as-cast material was also achieved in the 316Nb ingot subjected to 40% upsetting at 1250 °C. During upsetting, the 316Nb ingot experienced a monotonic deformation to a strain of 0.5 to 1.7, at strain rates from 0.1 to 0.5 s^{-1} and temperatures over 1200 °C during the upsetting, which was followed by a slow air cooling stage (i.e. ≈ -25 °C/minute). Compared to C1 cogging schedule, such high temperature and low strain rate deformation conditions are more favourable to DDRX. As seen in Table 2.6, no laboratory-scale experiments were performed on austenitic stainless steels for temperatures in the range 1200 to 1250 °C, hence limiting the comparisons with existing literature.

Although microstructures of both grades were fully recrystallised following C1+R, as well as following the upsetting performed on the 316Nb ingot, it remain unclear whether remnants of the original as-cast crystallographic texture persisted at this stage of the ingot-to-billet conversion process. This could be effectively assessed by performing an EBSD texture analysis, which would provide detailed insights into the crystallographic orientation distribution obtained at this stage and thus reveal any residual effects of the as-cast texture, such as anisotropic material flow behaviour. In (Yu et al., 2024), the texture of DDRX grains was found to be random, whereas that of CDRX grains was similar to that of the deformed, non-recrystallised columnar grains. According to previous discussions, the difference in the evolution of microstructure observed between each experiment was attributed to the different thermomechanical conditions experienced by the material during processing, and no sensitivity of the progress of recrystallisation to the microstructure morphologic texture could be observed.

Such sensitivity was observed for columnar as-cast grains in (Semiatin et al., 2004) and (Semiatin et al., 2007) for compression tests on samples oriented at 0°, 45° and 90° to the long axes of the grains, as well as by (Wang et al., 2021a) for 0°, 30°, 60° and 90° orientations. In (Semiatin et al., 2007), the higher rate of recrystallisation was obtained for the samples with the columnar grains oriented at 45° to the compression axis. In as-cast Ni–Co–W superalloy, (Yu et al., 2024) observed that DDRX was significantly promoted by 90° orientation between the long axis of the grains and the direction of compression compared to a 0° orientation. The absence of orientation dependant progress of recrystallisation could also be explained by the specific orientation of the grains in the as-cast ingot. The material was subjected to deformation at 0° and 90° orientations to the axis of the ingot, and the as-cast grains were oriented at ≈ 60° to the ingot's axis. Consequently, the grains were effectively oriented at ≈ 30° or ≈ 60° to the compression axis during the deformation stages, which orientations were shown by (Wang et al., 2021a) to result in similar progress of recrystallisation.

Crystallographic features identified from OM observations as straight and dark boundaries were found in the small-scale samples (e.g., see Figure 4.25) as well as between the edges and the mid-radius regions of the 316L and 316Nb ingots following C1 and C2 cogging schedules (e.g., see Figure 5.35). These were areas with drastically different thermomechanical conditions, such as a relatively low temperature at the end of cogging (i.e., < 1000 °C) and high strain rates (i.e., up to 15 s^{-1}). Those features were arbitrary termed as "deformation bands", although their exact crystallographic orientation and misorientation require further EBSD analyses. These features were mostly observed at the vicinity of the parent grain boundaries, and parallel to one another within the same grain, and sometimes oriented parallel to each other in adjacent grains. Recrystallised grains were sometimes observed along or between them, and development of deformation bands hence promoted the progress of DDRX (Wang et al., 2024).

Although the characteristics of the observed grains underwent DRX comply mostly with DDRX characteristics (i.e., necklaces of recrystallised grains formed at parent grain boundaries and at the vicinity of delta-ferrite), those deformation bands highlights the development of dislocation substructures within the parent grains, which could be related with the initiation of CDRX. The exact processing stage at which the deformation bands formed in the as-cast material during cogging remains however unknown, and deformation bands and the associated substructure may only develop during the last cogging passes, when the temperature was the lowest. In contrast, no deformation bands were observed in the 316Nb ingot following upsetting. This can be explained by the fact that the material was almost fully recrystallised following the upsetting, impeding the ability to observe the deformation bands. Also, the edge region of the ingot subjected to upsetting remained at elevated temperature (i.e. > 1100 °C) throughout the upsetting stage, and underwent relatively low levels of strains (i.e., < 0.7) and strain rates (i.e., < 0.2 s^{-1}). In the high strain area located along the axis of this ingot, the upsetting resulted in levels of strain and strain rate of ≈ 1.5 and 0.5 s^{-1}, respectively, and the temperature remained over 1250 °C. Those thermomechanical conditions are prone to DDRX and grain growth rather than deformation bands formation and CDRX.

According to (Humphreys and Hatherly, 1995), the development of deformation bands is promoted by coarse grains size, and low deformation temperatures. Deformation bands which formed perpendicular to the deformation direction were observed by (Wang et al., 2021a) in as-cast 7% Mo super austenitic stainless steel featuring coarse, columnar microstructure oriented at 30° and 60° to the compression direction at 900 °C and 10 s^{-1}. With the help of EBSD analyses, these bands were identified as HAGBs which developed from the rotation of LAGBs. Such a behaviour was not observed for the same microstructure orientated at similar angles to the compression direction at higher temperatures of 1000 °C to 1200 °C, which suggest that this behaviour is characteristic of low temperature deformations conditions. Following hot compression tests performed on wrought 316LN (0.09% Nb), (Li and Liu, 2019) also observed the development of dislocation substructures (see the large amount of green LAGBs in Figure 6.1), and directly formed HAGBs (see the yellow shape in Figure 6.1 a)). Similar observations of directly formed HAGBs (see the white rectangle in Figure 6.2 a)) were made by (J. Li et al., 2023) in an as-cast and homogenised Co-free nickel-based superalloy deformed at 1200 °C, 1 s^{-1}. In those studies, the development of dislocation substructures and directly formed HAGBs were associated with CDRX. Although CDRX predominantly develops in high SFE materials (Humphreys and Hatherly, 1995) (Huang and Logé, 2016) and is not expected to take place in 316L and 316Nb grades (i.e., due to low SFE), simultaneous occurrence of DDRX and CDRX were widely reported in the literature for austenitic stainless steels under warm to hot temperature deformation conditions (Yanushkevich et al., 2015) (Li and Liu, 2019) (Wang et al., 2021a). It is explained by (Zhao et al., 2024) that dislocations are difficult to cross-slip and climb in 316L grade, leading to weak degree of DRV, and therefore allow for the development of CDRX in such low SFE materials. For low to medium SFE materials, it is also explained by (Dudova et al., 2010) that CDRX is favoured at low temperature deformation as a consequence of reduced mobility of grain boundaries, hence impeding the onset of DDRX.

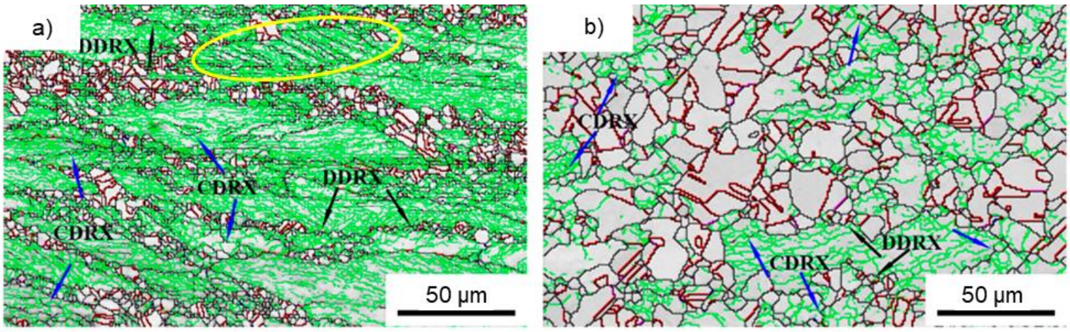

Figure 6.1 : EBSD grain boundary maps of wrought 316LN (0.09% Nb) compressed samples at a) 1000 °C, 1 s^{-1}, and b) 1100 °C, 0.1 s^{-1}. (2 to 15° green, Σ3 red, Σ9 purple, Σ11 yellow, Σ27 aqua, and other boundaries black). Adapted from (Li and Liu, 2019).

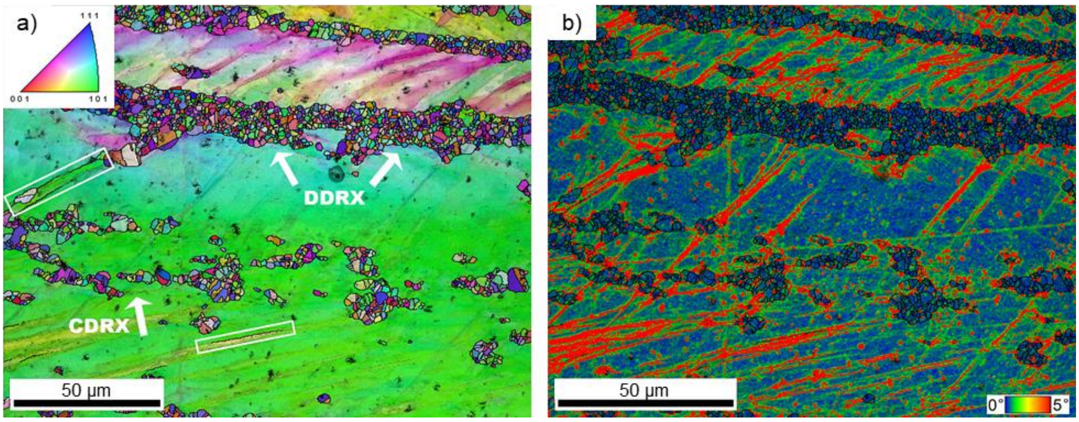

Figure 6.2 : EBSD maps of the explored alloy deformed at 1200 °C, 1 s^{-1} to a strain of 0.8; a) IPF map highlighting occurrence of both CDRX and DDRX mechanisms, with directly formed HAGBs in the white frame; and b) overlaid KAM and GBs maps showing that the dense deformation bands were constituted by dense LAGBs, corresponding to the higher KAM values. Adapted from (J. Li et al., 2023).

Non-recrystallised grains were observed within recrystallised regions of small-scale samples and ingots following thermomechanical processing (e.g., cogging and upsetting). These grains remained present among the recrystallised structure regardless of their initial orientations or positions in the as-cast microstructure. Some coarse and elongated parent grains were also fragmented into smaller segments during partial recrystallisation. The presence of non-recrystallised grains (i.e., incomplete recrystallisation) cannot be attributed to temperature variations, as they have experienced similar thermal histories to their recrystallised neighbours. Instead, lower deformation levels experienced by these grains are likely responsible, as insufficient strain does not provide enough driving force for an onset of recrystallisation. This is not uncommon and has for instances been reported in Nb-containing austenitic stainless steels (Silva et al., 2012), Udimet720 superalloy (Forbes Jones and Jackman, 1999), and 654SMO super-austenitic stainless steel (Liao et al., 2023). Such grains are often characterised by geometrically necessary dislocations and microbands (Gao and Huang, 2003) or low-angle grain boundaries, as observed by (Qin et al., 2017b).

Specific crystallographic orientations (i.e., texture) may also hinder recrystallisation and hence explain the presence of unrecrystallised grains. Grains with hard orientations relative to the applied stress direction deform less, with neighbouring grains accommodating more strains. C1 and C2 cogging schedules included $\pm 90°$ rotations of the ingots between each pass, and additional passes performed at $\pm 45°$ could have limited the amount of such hard-oriented grains. EBSD analyses of a few non-recrystallised grains located at the edge of the 316Nb ingot, following upsetting, could have allowed the identification of those grain orientations hindering recrystallisation as a consequence of common hard orientation relative to the upsetting direction. Limited strain accumulation, coupled with low misorientation gradients, can also prevent recrystallisation and inhibit these grains from being consumed by growing recrystallised grains, as shown in (Wu et al., 2022) on as-cast Mg alloys.

Deformation gradients along the long axis of as-cast grains, introduced by the cogging process, further promoted heterogeneities in the progress of recrystallisation. Deformation bands, which subdivide grains into regions with varying crystallographic orientations, often serve as sites for recrystallisation (Wang et al., 2024). Once recrystallisation begins, either at grain boundaries or along deformation bands, strain may localise in the softer recrystallised grains, further delaying recrystallisation in the remaining non-recrystallised fragments. Non-recrystallised grains observed during early stages of ingot processing (i.e., cogging or upsetting) lead to the formation of bimodal grain size distributions (see Figure 5.20). This partitioning of strain between recrystallised and non-recrystallised regions, as shown by (Keller et al., 2022) using CPFEM modelling, results in coarse grains accommodating more deformation. While this may eventually trigger recrystallisation during or following subsequent deformation stages, such strain partitioning may also reduce the process efficiency at resulting in homogenously refined microstructure. Also, a reduction in the number of processing stages during optimised conversion process could leave non-recrystallised grains in the final component. Investigations of the phenomenon using laboratory-scale experiments involves small samples with limited grain counts (see Table 2.6), which may not fully capture its effective impact at industrial-scale, such as revealed in this PhD thesis through larger scale investigations. Further research at larger scale remain however needed fully characterise the evolution behaviour of these non-recrystallised grains during further upsetting or cogging stages, and to address the non-recrystallisation phenomenon.

In line with existing knowledge (Mataya et al., 2003a) (Semiatin et al., 2004) (Mandal et al., 2012), recrystallisation in as-cast materials was observed to be highly heterogeneous, resulting from the combined effects of a reduced number of potential nucleation sites and the heterogeneous deformation inherent to the as-cast microstructure. These effects arise primarily from the coarse grain size of the material, while the deformation heterogeneity is further influenced by the thermomechanical processing conditions applied during testing. Intermediate- and large-scale samples, however, contain a substantially higher number of grains, thereby providing improved statistical representitivity and observability of the evolution of as-cast microstructures. Compared to laboratory-scale studies, where the limited number of grains constrains the reliability of microstructural observations, larger scale investigations offer deeper and more representative insights into the microstructure evolution and recrystallisation mechanisms occurring under industrial processing conditions.

6.4 INFLUENCE OF NB COMPOSITION

The trials performed in this work were replicated for both 316L and 316Nb grades, with the latter containing 0.7% Nb. The objective was to investigate the effect of Nb addition on microstructure evolution throughout the ingot-to-billet conversion process, and this section aims at reviewing and discussing the results obtained for both grades, including different microstructures observed in the as-cast materials, as well as the different microstructure evolutions observed during thermomechanical processing.

Both grades exhibited different grain size following the homogenisation heat treatment, with grain thicknesses of ≈ 0.8 and ≈ 0.4 mm for 316L and 316Nb, respectively (see Section 3.2.1). According to the ingot supplier, Aubert & Duval, the remelting conditions were consistent across all ingots for both grades, indicating that the variation in initial grain size was not due to remelting conditions, but rather attributed to the addition of Nb in the 316Nb grade. Increasing the Nb content in Nb-free compositions of austenitic (Padilha et al., 2005) and ferritic (Shan et al., 2011) stainless steels was shown to decrease both the liquidus and solidus temperatures, and enlarge the solidification interval. As a consequence of Nb addition, solid and liquid phases coexists over a broader temperature range (i.e., ≈ 1405-1450 °C at 0.7%Nb, compared to ≈ 1430-1460 °C without Nb addition according to (Padilha et al., 2005)), which enhances segregation of elements with low diffusion rates in the solid phase. This segregation effect can restrict grain boundary movement, subsequently slowing grain growth during solidification. Additionally, in a ferritic stainless steel, (Hou and Cheng, 2019) found that a 0.2% Nb addition reduced the slope of the growth-kinetic curve, indicating a lower growth velocity at comparable undercooling conditions. Microstructure observations revealed that the 0.2% Nb addition resulted in a finer grain size compared to the nominal grade composition (i.e., without Nb). By analogy, it is likely that the 0.7% Nb addition in the 316Nb ingot similarly reduced the growth rate during solidification, hence allowing for more nucleation events to take place during solidification. Consequently, this promoted a finer grain structure in the 316Nb ingot compared to that of 316L.

An alternative hypothesis for the finer grain structure observed in 316Nb ingots is the potential formation of Nb-rich precipitates (e.g., NbC, Nb(C,N), etc.) during early stages of solidification, which could provide additional sites for nucleation. However, phase stability diagrams computed for 316Nb alloys with 0.7% Nb by (Jolly et al., 2016) and (Perron et al., 2014) indicated that Nb-rich precipitates form only near the end of solidification. This suggests that Nb-rich precipitates would not be present early enough in the solidification process to act as nucleation sites in this case, and that Nb-rich precipitates do not contribute to the grain refinement observed in the 316Nb grade.

Another distinction between both 316L and 316Nb grades is the behaviour of secondary phases following casting and heat treatment. While both grades contained secondary phases immediately after casting, these phases completely dissolved in the 316L grade during homogenisation heat treatment. In contrast, undissolved secondary phases remained present in the 316Nb grade even after homogenisation and subsequent thermomechanical processing. This difference can be attributed to the presence of Nb, a ferrite-stabilising element known to form Nb-enriched secondary phases typically formed at the end of solidification in austenitic stainless steels (Mehmet Türker and Levon Josef Çapan, 2017) (Zhang and Yang, 2018) (Xie et al., 2022).

Except for the small-scale samples forged by hydraulic press, higher fraction of recrystallised grains were measured in partially recrystallised regions of small-scale samples (see Section 4.4) and ingots (see Section 5.4) of 316Nb, compared to those of 316L. Interestingly, the FE simulations predicted that during C1 cogging schedule, the temperature was higher in the 316L ingot than that in 316Nb (see Figure 5.6), which could have promoted higher fraction of recrystallised grains in the 316L ingot. At first sight, these results suggest that the Nb addition promoted the nucleation of recrystallised grains, which is contrary to the trends reported in the literature. As seen in Section 2.6.2.3, Nb addition to austenitic stainless steel grades is known to increase the SFE of the alloy and promote the occurrence of DRV over DRX, and hinder the grain boundaries motion by solute drag effect and Zener pinning. Hence, Nb is expected to delay the ignition of DDRX and restrict the growth of recrystallised grains (i.e., refine the recrystallised grain size). These statements were supported and demonstrated by numerous studies focused on the effect of Nb addition on recrystallisation kinetics in austenitic stainless steels. These apparently contradictory results from this work can however be explained by the different initial material conditions obtained for both grades after casting and homogenisation, with reduced initial grain size and presence of secondary phases in the 316Nb ingots. Prior to deformation stages, the 316Nb grade exhibited a ≈ 50% finer grain size compared to 316L, resulting in a higher density of grain boundaries. Since grain boundaries served as preferential sites for nucleation of recrystallisation, it can reasonably be stated that Nb addition indirectly promoted the nucleation of DDRX in 316Nb. Such an effect of the initial grain size on the initiation of DRX was observed by (El Wahabi et al., 2005) in wrought 304 austenitic stainless steels.

Similar interpretations can be made for the different levels of recrystallisation obtained in both grades following C2, with fractions of recrystallised grains of 35% and 92% for 316L and 316Nb grades, respectively. Prior to C2, grain sizes were of ≈ 225 µm and ≈ 78 µm in 316L and 316Nb ingots respectively. Based on a simulation where the microstructure was represented by periodical and identical tetrakaidecahedra, (El Wahabi et al., 2005) estimated the volume density of various types of nucleation site (i.e., vertex, edge and faces of the grains) in a microstructure with homogeneous grain size distribution. With grain sizes of 225 µm and 78 µm (i.e., such as those in 316L and 316Nb ingots prior to C2, respectively), it can be estimated that the 316Nb ingot had 96%, 86% and 65% more vertex, edges and faces, respectively, than those of 316L. Nucleation of recrystallised grains was also observed to take place in the interfaces with the undissolved secondary phases in the 316Nb grade, which could have led to a similar indirect effect of Nb addition in the 316Nb grade. The undissolved secondary phases are known to act as barriers to dislocation motion, hence providing additional sites for the nucleation of recrystallised grains (Mataya et al., 2003a). Presence of undissolved secondary phases in the as-cast 316Nb grade have therefore promoted the nucleation of recrystallised grains in this grade compared to the 316L.

The composition of the secondary phases found in the 316Nb grade were not quantified but is known to be enriched in Nb (Mehmet Türker and Levon Josef Çapan, 2017) (Zhang and Yang, 2018) (Xie et al., 2022). The presence of Nb-containing secondary phases in the material implies that the Nb content within the austenite matrix is lower than the nominal Nb composition of the alloy. For example, in 316Nb with 0.7% Nb, (Cliche et al., 2021) observed that after a 3 hour solution heat treatment at 1200 °C, the average Nb content in the austenite was only around 0.3%. This depletion of Nb in the austenitic matrix prior to thermomechanical processing could be expected to reduce the solute drag effect, which in turn accelerated the onset of recrystallisation by diminishing the delay that would typically takes place with higher Nb content. However, the ability of solute Nb atoms at reducing the grain boundary mobility remains pronounced even at very low Nb concentrations. For instance, in a 304L austenitic stainless steel, (Smagghe, 2017) observed a significant effect of a 0.15% Nb addition on the mobility of grain boundaries during MDRX and grain growth. Similar trends were found in Nb micro-alloyed steel with Nb amounts below 0.05% (Zhang et al., 2008) (Cao et al., 2015). According to (Humphreys and Hatherly, 1995), the presence of Nb-rich secondary phases dispersed within the microstructure of the 316Nb grade may have promoted the development of deformation bands in this grade. In turn, the deformation bands were shown to provide additional sites for nucleation of recrystallised grains, hence partially explaining the higher fraction of recrystallised grains observed in the 316Nb ingot following C1 cogging schedule, compared to that made of 316L.

As can be seen from Figure 6.3, Nb addition also had a significant impact on reducing the size of recrystallised grain. In fully recrystallised regions, the average grain size in the small-scale samples forged by a screw press (see Section 4.4) was ≈ 70 µm and ≈ 35 µm for 316L and 316Nb, respectively, and ≈ 225 µm and ≈ 78 µm following C1+R (see Section 5.4), respectively. These results clearly indicate that Nb addition considerably refines the size of recrystallised grains and are consistent with the role of Nb in inhibiting grain growth via solute drag and pinning effects (see Section 2.6.2.3). In the absence of quantitative chemical analyses, the role of each of these mechanisms cannot be determined. The finer grain structure of the 316Nb ingots compared to those of 316L is also known to favour smaller recrystallised grain size (El Wahabi et al., 2005).

It is also noteworthy to state that the size of recrystallised grains in 316Nb ingots after upsetting (i.e., ≈ 69 µm) and cogging C1+R (i.e., ≈ 78 µm) were significantly smaller than those reported in the literature for wrought 316Nb with similar composition. For instance, (Cliche et al., 2021) observed grain sizes ranging from 180 µm to 250 µm, while (Hermant et al., 2019) reported grain sizes of 130 µm and 250 µm following 1 hour solution treatment at 1100 °C and 1200 °C, respectively. Although the 316Nb grade contained 0.7% Nb, this suggests that the recrystallised grains may exhibit significant growth following thermomechanical processing. Also, this highlights that a significantly finer microstructure could be achieved at the very early stage of the ingot-to-billet conversion process, hence allowing for advantageous homogeneity of the material behaviour during further processing stage. Although similar experiments were conducted for both 316L and 316Nb grades, and that significant effect of Nb addition was highlighted, it appeared that the Nb addition led to different characteristics in the initial microstructures. Hence, limited quantitative comparison of the actual effect of the Nb addition to the 316Nb grade could be achieved.

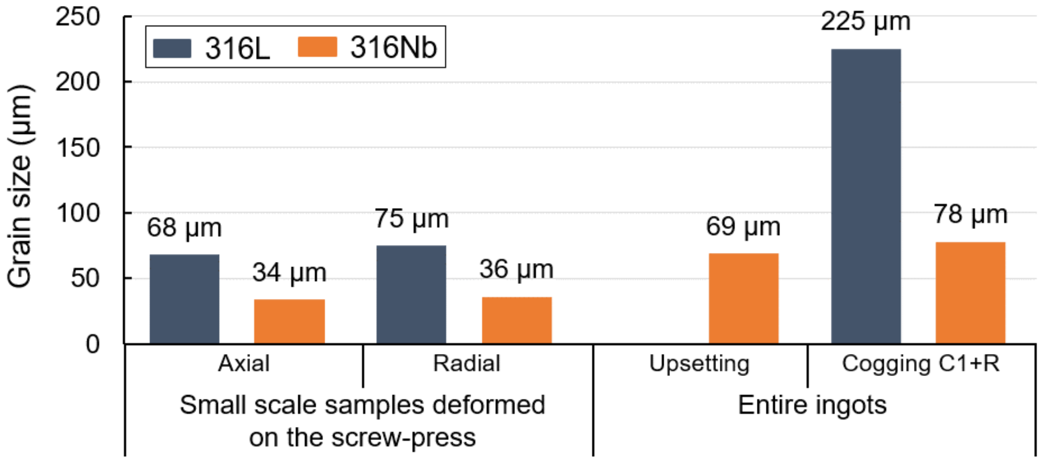

Figure 6.3 : Comparison of grain sizes measured in fully recrystallised regions of small-scale samples and entire ingots after thermomechanical processing of 316L and 316Nb grades.

6.5 METHODOLOGIES TAKEN TO INVESTIGATE AS-CAST MATERIAL BEHAVIOURS

The methodology employed to investigate the evolution of recrystallisation in the as-cast microstructures during the early stages of the ingot-to-billet conversion process is schematically illustrated in Figure 3.1. This approach was specifically designed to assess the benefits of conducting experimental studies at an intermediate scale (i.e., between laboratory- and industrial-scales) for the optimisation of industrial ingot-to-billet conversion routes. Numerous studies were performed to allow for a better understanding of as-cast materials behaviour throughout thermomechanical processing, as well as for the optimisation of the ingot-to-billet conversion process itself, and both type of "material characterisation and modelling" and "process optimisation" focused studies provide valuable knowledge for the optimisation of the ingot-to-billet conversion process. This PhD thesis explored a novel approach focused on macroscopic characterisations of material and process interactions for the optimisation of ingot-to-billet manufacturing routes compared to the other studies, and the outcome are discussed in the following.

Several limits were reached while trying to produce the stress-strain curves from the small-scale samples deformed to 30% of reduction in height through upsetting experiments using hydraulic and screw presses. While accurate records of load-position data were expected with sufficient instrumentation of both hydraulic and screw presses (see Section 3.2.2.1), the conversion of load-displacement records to stress-strain curves was challenging, due to the anisotropic deformation (i.e., non-cylindrical) of the small-scale samples, which did not allow a clear measurement of the characteristic radius (i.e., R_M and R_T) required by the existing method to account for the effects of friction. The upsetting trials were performed in non-isotherm conditions at a starting temperature of 1250°C, leading to an increase in stress with strain due to the simultaneous cooling experienced by the samples. Hence, limited interpretation and analyses could be performed from the partial set of stress-strain data established with the small-scale samples.

Although the purpose of the small-scale samples (30% upsetting) was not to develop any constitutive flow or recrystallisation behaviour models for the grades investigated and, although they provided a better representitivity of the material's behaviour compared to laboratory-scale investigations, it clearly appeared that the challenges faced for extracting the stress-strain data, and their lack of accuracy, remain a strong limiting factor in using such an experiments for modelling the flow and recrystallisation behaviour of columnar as-cast material. However, most models for as-cast material flow and recrystallisation behaviours are derived from the analysis of load-position data collected from laboratory-scale experiments owing to the need for collecting accurate data over a broad range of thermomechanical conditions. Obtaining the stress-strain curves from experimental load-position records is a common practice for the characterisation and modelling of as-cast materials and does not appear as an issue in the literature. In most studies, the method used for converting the load-position records into stress-strain data assume axisymmetric deformation and may involve the use of corrective barrelling factors to account for friction effects, which are typically determined from the geometry of the deformed samples (see Section 3.2.2.1).

(Mataya et al., 2003a) and (Mataya et al., 2003b) performed compression tests on as-cast samples with columnar microstructures, where the tests were performed with the long axes of the grains oriented parallel to the compression direction. In these studies, a specific sample geometry and lubrication techniques were used to supress the barrelling of the samples, hence avoiding the need for correcting the stress-strain curves for friction effects. (Semiatin et al., 2004) observed the anisotropic deformation behaviour of as-cast samples with columnar microstructures oriented parallel and perpendicular to the compression direction. The stress-strain data, which revealed the dependence of the material flow behaviour to the orientation of the microstructure, were however derived from the experimental records assuming uniform material deformation, and no correction for friction was performed. (Han et al., 2013) and (Han et al., 2015) successfully determined the hyperbolic-sine Arrhenius type constitutive equation of as-cast FCC materials with equiaxed microstructures with average grain size of ≈ 200 µm. No specific challenges were reported for the determination of the stress-strain data from the experimental records. It can reasonably be assumed that the samples underwent isotropic deformation owing to the equiaxed geometry of the as-cast grains, hence differing from the observation made on the small-scale samples subjected to 30% upsetting.

(Wang et al., 2021b) investigated the effect of the orientation of the columnar as-cast microstructure to the compression direction (i.e., 0°, 30°, 60° and 90°). The stress-strain curves obtained for the different orientation condition were not compared to each other in the study, but were reproduced and superimposed in a graph shown in Figure 2.28, highlighting different deformation behaviours of the as-cast material in each orientation condition. However, no explicit mention of anisotropic deformation of the samples nor elliptical barrelling was reported by the authors, and the methodology followed to determine the stress-strain curves from the load-displacement records was not fully explained. In (Han et al., 2015) and (Wang et al., 2021b), the end faces of the samples were polished, and a graphite lubricant was used on tantalum foils placed between the samples and the anvils to reduce the effects of friction. These efforts to significantly reduce friction effects on material deformation behaviour eliminate the need to measure the characteristic diameters of deformed samples. This also explains why the issue of diameter measurement in the case of anisotropic deformation is rarely addressed in the literature.

As reviewed in Section 2.7, JMAK based recrystallisation models are developed either from (i) the determination of flow softening effect induced by the initiation of recrystallisation during compression tests (Han et al., 2015) (Zhang et al., 2016), or (ii) correlation of FE predictions of the thermomechanical properties experienced by the material and actual measurements of the resulting microstructure (Semiatin et al., 2004) (Mataya et al., 2003a). Beyond the limits of the FE models in accurate prediction of the fraction of recrystallised grains using JMAK models, i.e., owing to the heterogeneous deformation and recrystallisation behaviour of columnar as-cast microstructures, both methods have limitation in effectively predicting recrystallisation behaviours in the as-cast materials. The accuracy of the former method rely on the stress-strain curves, which is debatable according to the earlier discussions in this Section; and the latter method contains combined errors resulting from (i) the FE estimated thermomechanical path which does not account for the heterogeneous deformation behaviour of the as-cast materials, and (ii) the measurement of the fraction of recrystallised grains which does not account for its heterogeneous distribution across the microstructure. These limitations agree with those reported in the literature for the effectiveness of using JMAK models for simulating ingot-to-billet conversion.

(Bylya et al., 2017) showed that the accuracy of JMAK models are compromised with increasing complexity of the thermomechanical process, in agreement with (Bandar et al., 2007) who also highlighted that JMAK models are not appropriate to model recrystallisation in columnar as-cast microstructures. Consequently, the use of JMAK recrystallisation models may result in inaccurate prediction of the progress of recrystallisation, with the risk of over-evaluating the actual fraction of recrystallised grains. Although it remains unclear whether JMAK models could carefully be used for modelling recrystallisation of as-cast materials, their suspected lack of accuracy would require further quantification. For instance, both methods reported for the development of JMAK models can be compared by using the same set of experimental data. Despite these limitations, the development of JMAK recrystallisation models remain of interest in literature.

Similarly to JMAK recrystallisation models, the development of processing maps is based on the analysis of constitutive models derived from experimental stress-strain curves. Although they provide a global overview of safe and efficient processing conditions and are usually complemented with microstructure observations (Han et al., 2013), the aforementioned challenges in developing accurate constitutive flow models for as-cast materials may introduce errors in further use of the processing maps. In addition to JMAK models, which provide phenomenological prediction of recrystallisation, CA models coupled with CPFEM models allow, at the cost of extensive computational and storage resources, to capture complex interactions between thermomechanical response of a material and its microstructural evolution, as well as to predict nucleation and progress of recrystallisation in materials undergoing heterogeneous deformation (Li et al., 2015) (Li et al., 2016). Hence, such models provide valuable capabilities to perform virtual experiments, which could be used for the investigation of the behaviour of as-cast materials and for the comparison between different processing scenarios.

The microstructures resulting from the small-scale testing (i.e., 30% upsetting) and those from the upsetting and cogging of the entire ingots (i.e., larger scales) were characterised at macroscopic-scale, with large longitudinal and transverse cross-sections subjected to etching, as well as at microscopic-scale, with semi-automated quantitative analysis of OM collected across large surface areas (i.e., up to $\approx 4\times6$ cm^2). Macroscopic-scale characterisations via macro-etching provided valuable information on the as-cast microstructure, such as the distribution of grain morphology across the cross-sections of the ingots. These characterisations also provided insight into the microstructure resulting from the upsetting and cogging performed on the entire ingots and allowed to reveal the presence of non-recrystallised grains within recrystallised areas. Such large-scale characterisation of the ingot's microstructure is a common practice, as it allows to appropriately select the locations where the testing samples need to be extracted. Depending on the specific requirements of the study, the sample can hence be taken from regions containing either equiaxed or columnar grains, with specific morphologic orientation for the latter (Ramuhalli et al., 2009) (Mataya et al., 2003a) (X. Li et al., 2023) (Park et al., 2005).

(Semiatin et al., 2004) performed unusual EBSD characterisation of the as-cast material at a relatively large-scale, with a scanned area of 24×8.5 mm^2 with step size of ≈ 0.5 mm. This study also included a macro etched transverse cross-section of a compressed sample with an area of 15.5×6 mm^2, from which EBSD maps of ≈ 0.55×0.25 mm^2 area were acquired with a step size of ≈ 5 µm. Among the few studies found having performed industrial-scale forging trials, macroscopic-scale characterisation of the resulting microstructure allowed (Dandre et al., 2000b) to observe the persistence of coarse grains in the area of the ingot where low deformation levels were predicted by FE simulation. This was however not performed in the study of (Wang et al., 2016a). Instead, the accuracy of the implemented microstructure prediction model was evaluated using OM observations collected from a few locations within the cogged ingot. In light of the heterogeneous progress of recrystallisation observed in the entire ingots following cogging (e.g., see Figure 5.31), such a limited number of sampling limits the evaluation of the effectiveness of the recrystallisation models in the prediction of recrystallisation in the ingot.

(Cheng et al., 2024) investigated the influence of rolling schedules on the internal quality of a 75×75 mm^2 37CrMo4 steel ingot following continuous casting and compared the resulting microstructures from the macro etched transverse cross-sections of the ingots. In addition to macroscopic characterisations via macro-etching, large-scale OM characterisations allowed for quantitative evaluation of the fraction and size of recrystallised grains (e.g., see Figure 5.46). A key advantage of the method was to reconstruct an overall microstructure with the progress of recrystallisation highlighted at a representative scale of the process and microstructure (e.g., see Figure 5.45), hence allowing to capture the heterogeneous nature of the progress of recrystallisation in the as-cast material. As an example, Figure 5.49 depicts two very different microstructural appearances in areas distanced by 20 mm, which is not significant compared to the size of the ingot (i.e., ≈ Ø 185 mm). This method however revealed numerous drawbacks. The manual definition of grain segmentation parameters and grain size threshold values for the measurements of the fraction of recrystallised grains was prone to subjective user interpretations. As recrystallised grains were significantly smaller than the as-cast grains (e.g., see Figure 5.47), their identification based on a threshold grain area value was a relevant and suitable strategy for the present analysis, even though a few small number of non-recrystallised grains issued from the segmentation of larger parent grains were incorrectly identified as recrystallised grains. Finally, the large characterisation method for quantitative analyses of recrystallisation progress could been further developed to allow similar large-scale quantitative measurements of the amounts of δ-ferrite and σ-phase in the samples. Both phases could for instance being revealed in different colour using colour etching techniques (e.g., electrolytic etching using 40% aqueous sodium hydroxide, Beraha II etchant, etc.).

Twins, deformation bands, incomplete grain boundaries, and grinding scratches similarly introduce uncertainties in the in the image processing and consequently grain segmentations. It is noteworthy to highlight that processing micrographs and measurements of grain size and fraction of recrystallised grains rely on high quality micro/macro-graphs which depend on proper surface preparation (i.e., polishing), etching homogeneity, observation conditions (i.e., specimen levelling, focus, illumination, etc.), and camera settings (brightness, contrast, etc.). Hence, the need for such large-scale material characterisation leaves room for the development of dedicated and appropriate sample preparation equipment. Although unique results were obtained by implementing an in-house developed large-scale characterisation method, obtaining such results remain time-consuming and require extensive preparation and post-processing work. It also require the acquisition and storage of large number of high-resolution micrographs, which are huge amount of data.

In (Yeom et al., 2007), the capability of a set of recrystallisation and grain growth models in accurately predicting the size and fraction of recrystallised grains was evaluated by comparing FE predictions with local measurements performed on Ø 10×15 mm samples subjected to side-pressing. Owing to the large initial grain size of 2 mm compared to the dimensions of the samples, it can reasonably be assumed that heterogeneous deformation and recrystallisation took place in the samples during thermomechanical processing. Hence, performing quantitative analysis of the size and fraction of recrystallised grains across the entire cross-section of the samples would have allowed the authors to provide a more representative correlation of experimental and FE predicted microstructures. Also, those microstructure evolution models were implemented by the authors in the FE simulation of the industrial cogging process of Ø 400 mm ingot. Although no 1:1 scale corresponding experiment was performed by the authors, the large-scale microstructure characterisation method would have allowed for representative comparison of experimental and predicted results. Previous results and discussions demonstrated the relevance of the as-developed method used for semi-automated quantitative analysis over a large number of micrographs; and allowed for gaining significant knowledge from the large-scale experiments performed on as-cast materials. Although the large-scale experiments and associated methods used for the analysis of resulting microstructure allowed for collecting qualitative and quantitative data on the progress of recrystallisation, additional crystallographic textures or local compositions analyses via EBSD and SEM would have helped for further understanding on the evolution of as-cast microstructure during the ingot-to-billet conversion process. Among others, such analyses could have been helpful to:

- Evaluate and track the evolution of austenite and second phase composition in the 316Nb grade.
- Identify and characterise the potential Nb-rich particles dispersed among the microstructure of 316Nb grade, hence distinguishing solute drag and Zener pinning effects (e.g., see (Hermant et al., 2019)).
- Identify the exact crystallographic nature of the deformation bands and explore into more detail the non-recrystallisation behaviour of some as-cast grains (e.g., see (Jorge-Badiola et al., 2005)).
- Assess whether the specific texture of the as-cast material has disappear following the recrystallisations achieved throughout the different trials (e.g., see (Yu et al., 2024)).
- Accurately identify and distinguish DDRX, CDRX and MDRX recrystallisation mechanisms (e.g., see (Qin et al., 2017b) (Wang et al., 2021a)).

The upsetting and cogging experiments conducted in this thesis were performed at a much larger scale than those usually involved in studies devoted to characterisation of evolution and recrystallisation of as-cast microstructures during the ingot-to-billet conversion process. These allowed to replicate the industrial processes and corresponding thermomechanical conditions. The experiments highlighted challenges in ensuring appropriate control of the thermomechanical testing conditions. As an example, the upsetting performed on the small-scale samples began from 8 to 20 seconds following furnace unloading, which led to significantly different temperature distribution in the samples at the beginning of their upsetting (see Figure 4.10). Conversely, accurate control of thermomechanical testing conditions can be achieved through laboratory-scale experiments, which allow for collecting high quality data to be used for model developments. Cogging experiments were also performed with different time schedules owing to the time required for manual estimation of the energy to set on the screw press for each hit, which resulted in different temperature distribution during cogging (see Figure 5.6).

The experiments performed on the entire ingots required specific developments so that cogging could be performed using the screw press, and the upsetting had to be performed in industrial environment. Also, the screw press used for the cogging experiments does not allow to cover a broad range of ram speeds (i.e., strain rate) experienced during industrial cogging processes. The experiments were designed to focus on the early stage of the conversion process, so that the effects of the processing conditions on recrystallisation could be compared easily. Many different experiments were performed in this PhD thesis, but none of them was replicated to evaluate the repeatability of the material behaviour. As an example, the results obtained for the small-scale radial 316Nb sample subjected to 30% upsetting using a hydraulic press were subject to interrogations (see Section 4.4).

The upsetting trials performed on the small-scale samples in the axial and radial directions aimed at resembling the material behaviour during larger scale upsetting and cogging experiments, respectively. However, different temperature evolution took place between the small and large-scale experiments, and the results obtained at small-scale cannot really represent the larger scale ingot processing conditions. The progress of recrystallisation was observed to be at different levels depending on the press type used for the upsetting, but the samples deformed using the screw press underwent higher strain rate which induced adiabatic heating leading to a significant progress of MDRX. Hence, limited evaluation of the effect of the strain rate on the progress of recrystallisation could be determined. With laboratory-scale samples, the microstructure resulting from thermomechanical processing can be effectively preserved by quenching the samples in water immediately after the deformation stage. This prevents the occurrence of recovery and MDRX, which could otherwise affect the accuracy of subsequent microstructural characterisation. This also allow to clearly distinguish DDRX from MDRX, which latter occurs without an incubation delay.

For this purpose, (Semiatin et al., 2004) used a dedicated quenching ring positioned below the heating induction coil, allowing quenching to be achieved within one second after deformation. Similarly, in the studies reported by (Han et al., 2015) and (Wang et al., 2021a), the samples were quenched “immediately” after deformation. The efforts to ensure rapid quenching highlight the critical importance of this practice, which is made feasible by the small volume of laboratory-scale samples that can be quickly cooled in a large volume of cold water. Hence, despite the significantly larger amount of heat to be extracted from the small-scale samples subjected to 30% upsetting compared to laboratory-scale samples, the effect of the press-type (i.e., strain rate) on the progress of DDRX could have been determined from the small-scale upsetting tests if the samples had been quenched immediately after the end of the deformation stage. By doing so, the actual time required for the core of the samples (i.e., the region that experienced the most favourable conditions for MDRX) to cool down to a non-recrystallisation temperature could be assessed by FE simulation. This cooling time could then be compared between the different cases, providing insight into how quenching efficiency and strain rate influenced the resulting microstructure.

6.6 IMPLICATIONS FOR INDUSTRIAL-SCALE INGOT-TO-BILLET CONVERSION PROCESSES

As can be seen in Figure 3.4, a 2.3 tonnes bottom-poured 316Nb ingot was cut along longitudinal and transverse cross-sections to get an overview of the microstructure in larger scale ingots. The grains had a columnar morphology and were oriented at ≈ 80° to the axis of the ingot in its longitudinal cross-section, hence differing to the VIM/VAR processed ingots in this PhD thesis (i.e., ≈ 60°, see Figure 3.5). In the transverse cross-section, the grains were oriented perpendicular to the skin of the ingot, forming a specific pattern along the diagonals of the transverse cross-section, with discontinuities in the morphologic orientation of the grains. In addition, the characterisation performed along the longitudinal cross-section of the ingot revealed the presence of "V" shaped shrinkage porosities at the core, due to the bottom-pouring nature of the ingot production. Consequently, the conversion process of that ingot must result in (i) a completely refined and equiaxed microstructure, and (ii) effectively closed and bonded void porosities. This PhD thesis contributed to improve the knowledge on the as-cast material deformation and recrystallisation behaviour during industrial ingot-to-billet conversion processes. However, for the reasons listed below further research are still to be done to fully articulate these results to industrial scale forging.

- The difference in the size and morphology of the as-cast microstructure between the VIM/VAR processed ingots and that produced through bottom pouring lead to different deformation and recrystallisation behaviours at larger scales.
- The larger scale ingot exhibits higher thermal inertia compared to the intermediate-scale ingots, and the time-schedule for the manufacturing route also differs for both cases, hence affecting the evolution of the as-cast microstructure. This aspect was a limiting factor while trying to compare the upsetting tests performed on the small-scale samples compared to those performed on the intermediate-size ingots.
- A direct application of the section reduction ratios conducted during the upsetting and cogging experiments performed on the intermediate-scale ingots result in unrealistic load capacities at larger scale.

Hence, a methodology for the design of the ingot-to-billet conversion process of such an ingot, considering both recrystallisation and void closure constraints, is proposed and discussed hereafter in light of the findings from the literature and from this PhD thesis.

To begin with, the topic of void porosities closure is an interesting topic to be assessed together with that of the recrystallisation of as-cast materials for several reasons: (i) void porosities are found in as-cast ingot subjected to further hot-working stages aiming at the recrystallisation of the as-cast structure, and (ii) investigations on closure and bonding of void porosities often involves intermediate-scale experiments aiming at replicating the industrial scale conditions. Hence, it is of main scientific and industrial interest. The closure of void porosities was a subject of several studies in the recent years, whose investigation methods included characterisations of the void geometry whereby experiments and simulations performed at different scales. The geometry of the void porosities observed in the 2.3 tonnes ingot are different from those investigated in the literature, which either consider the void porosity as spheres, cylinders (Christiansen et al., 2014) or ellipsoids (Feng et al., 2016). They are also different from those investigated in (Lee et al., 2011) and (Pondaven et al., 2021), where the experimental and simulation studies were based on real void geometries obtained from an as-cast material by X-ray tomography.

The capability of manufacturing routes in ensuring effective closure of void porosities is evaluated through the computation of the stress triaxiality (Saby et al., 2013) (Harris et al., 2017), which can be easily computed with FE simulations of the ingot-to-billet conversion process. According to (Feng et al., 2016), upsetting is only effective in closing the void porosities located around the central regions of the ingot, whereas cogging is effective in closing the void porosities located along the ingot longitudinal axis. Different die geometry (i.e., large flat anvils, V-shaped anvils, etc.) can also be used to favour the closure of the porosities (Kukuryk, 2023). The need for effective closure of the central void porosities adds another level of constrains to the design of the conversion process, and the ability to design appropriate manufacturing route which ensures effective closure of shrinkage porosities consequently require accurate prediction of the thermomechanical history experienced by the material throughout the manufacturing route. Consequently, the development of accurate models for the material flow behaviour is required. The presence of void porosities in the 2.3 tonnes ingot, with a different geometry to those studied in the literature, also provides the opportunity at conducting additional research on this topic. The void porosities investigated in literature have relatively simple geometries, which can be reproduced in FE models in the form of simple spherical or ellipsoidal voids. However, no study was found to evaluate the closure of "V-shaped" porosities such as those observed in the 2.3 tonnes ingot. Hence, the actual knowledge on void porosity closure would benefit from further X-ray tomography characterisation of the "V-shaped" void porosities observed at the centre of the ingot, as well as from thermomechanical experiments (i.e., upsetting and/or cogging) performed on intermediate-scale samples extracted from the central region of the ingot, with void porosities in their inner volume.

An overall view of the microstructure in the 2.3 tonnes ingot produced through bottom pouring was obtained from a macro-etched transverse and longitudinal cross-sections taken from the central region of the ingot. However, further qualitative and quantitative characterisations of the as-cast material (i.e., distribution of grain size and morphology, amount and composition of secondary phases, geometry of the void porosities, etc.) are required.

Secondary phases were found in the as-cast ingots (i.e., both 316Nb and 316L grades), but almost completely dissolved in the 316L following the homogenisation heat treatment. In contrast, secondary phases remained in the 316Nb ingots, and their presence provided additional sites for nucleation of recrystallisation. Although partial or complete dissolution of secondary phases may be achieved by homogenisation heat treatments, owing to the need of developing manufacturing routes with improved sustainability, the duration of the homogenisation heat treatment must remain realistic and ensure efficient use of available energy resources. For instance, (Perron et al., 2014) evaluated for a 316Nb grade with ≈ 25 % δ-ferrite following casting, that an unrealistic

≈ 76 days homogenisation heat treatment at 1150 °C would be required to reach the thermodynamic equilibrium of δ-ferrite (i.e., 3 %). According to (Mataya et al., 2003a) and (Rezayat et al., 2016), the introduction of lattice defects during thermomechanical processing facilitate the spheroidisation and dissolution of δ-ferrite via pipe diffusion. Hence, the dissolution of secondary phases may be achieved by a combination of initial homogenisation heat treatments and further thermomechanical processing stages, which would require further investigations.

As secondary phases promoted recrystallisation in the 316Nb grade, their dissolution may in turn affect the kinetic of recrystallisation. This imply a need for proper characterisation of the kinetic of dissolution of the secondary phases present in the as-cast 2.3 tonnes ingot. As secondary phases have significant effects on the recrystallisation behaviour of the alloy, the determination of the homogenisation heat treatment parameters (i.e., temperature and duration) is required prior to further investigation on the material flow and recrystallisation behaviours. To ensure their reliability and applicability, the material dedicated to those investigations must be subjected to the same homogenisation heat treatment as that of the 2.3 tonnes ingot experiences during the industrial manufacturing route. As seen in Table 2.6, many studies on investigating recrystallisation in as-cast materials were performed on non-homogenised as-cast materials.

As discussed earlier, as-cast materials with coarse and columnar grains are prone to anisotropic deformation. Despite uncertainties, FE models can predict macroscopic deformation behaviour of as-cast materials with appropriate constitutive material model integrated. Meanwhile, their applications to 1:1 scale manufacturing process and benchmarking different manufacturing scenarios, remain a challenge.

In contrast to the microstructure of the VIM/VAR processed ingots, the microstructure of the bottom-poured ingot was not axisymmetric (i.e., not distributed around the longitudinal axis of the ingot) and therefore RVEs of the columnar microstructure can be extracted from the ingot in the form of cylindrical samples in the axial, radial, and orthoradial orientations of the ingot. Owing to the aforementioned limitations of usual laboratory-scale compression tests, no innovative methodology could be proposed for the determination of materials constitutive behaviours.

As observed in this PhD thesis, complete recrystallisation of the as-cast microstructure can be achieved through various thermomechanical processing histories, and the different recrystallisation mechanisms identified from the experiments matched with those investigated in the literature with the help of laboratory-scale experiments. Also, the progress of recrystallisation in the as-cast materials exhibited material- and process-induced heterogeneities, which were captured with the help of a semi-automated quantitative microstructure characterisation method. The results from this PhD thesis demonstrated that laboratory-scale experiments provide sufficient insight into determining the thermomechanical conditions for the onset of the different mechanisms responsible for the recrystallisation of the as-cast microstructure. Consequently, laboratory-scale experiments remain relevant for the investigation of the recrystallisation in the 2.3 tonnes ingot.

The experiments needed to develop the material's anisotropic and flow behaviours are also suggested to be used for the characterisation of microstructure evolution and recrystallisation. Such small-scale samples allow for OM and SEM/EBSD analyses and to collect useful data to aid understanding of the recrystallisation mechanisms. At reduced additional costs and efforts, the data recorded through these experiments could allow the development of JMAK models for SRX, DRX and MDRX, as well as the development of processing maps. Although the relevance of processing maps are controversial (Ghosh, 2000) (Ghosh, 2002), they allow the determination of safe and efficient processing conditions, enabling different manufacturing scenarios to be benchmarked by FE simulation.

6.7 SUMMARY

As-cast types 316L and 316Nb materials were subjected to heterogeneous deformations and subsequent heat treatment, and the recrystallisation behaviours were investigated. This of interest primarily due to their coarse as-cast grains morphologies, which can lead to anisotropic deformation and uneven strain distributions during the ingot-to-billet conversion process. Anisotropic deformation was observed in the as-cat materials consistently, resulting from the crystallographic texture of the columnar as-cast microstructure. The anisotropic behaviour was successfully implemented in FE process models for both small- and large-scales ingots, with the latter being used for validating the anisotropic material flow behaviours model. The FE simulations with the incorporated materials anisotropic flow behaviour provided accurate predictions of the deformed geometries, though the calibration of anisotropic parameters relied on a "trial and error" approach. More advanced modelling techniques, such as CPFEM, could improve the accuracy of deformation behaviour predictions and enhance the optimisation of industrial ingot-to-billet conversion processes. Both 316L and 316Nb grades exhibited recrystallisation mechanisms in line with existing literature. However, full understanding of specific features of interest such as the role of deformation bands or the persistence of non-recrystallised grains observed in the large-scale experiments require further analyses, which is beyond the scope of this PhD thesis and are proposed in Chapter 8.

Comparison between 316L and 316Nb grades highlighted the role of Nb on the recrystallisation behaviours. The addition of Nb in the 316Nb grade led to a finer as-cast grain structure compared to the 316L grade due to a broader solidification interval, which restricted grain growth during solidification through segregation of elements with low diffusion rates in the solid phase. Another key difference was the persistence of secondary phases in 316Nb after homogenisation, whereas they fully dissolved in 316L. Despite previous suggestions in literature expecting that Nb additions should hinder recrystallisation by increasing stacking fault energy and impeding grain boundary motion, the results from these investigations showed higher fractions of recrystallised grains in the 316Nb ingots compared to those measured for 316L. This can be due to the initial finer grain structure and the presence of secondary phases in the 316Nb grade, both providing additional nucleation sites for recrystallisation.

While laboratory-scale experiments remain the most suitable mean for detailed investigations on the as-cast materials (e.g., flow behaviour, recrystallisation, etc.), which are essential for the design and optimisation of an effective manufacturing route, large-scale experiments allow for preserving key ingot features (e.g., columnar grain morphology, large grain count, etc.) and revealing specific behaviours of the as-cast material which cannot be captured from smaller experimental scales (e.g., impact of anisotropic deformation behaviour, heterogeneous progress of recrystallisation, presence of non-recrystallised grains, etc.). These characteristics of the as-cast material are however of critical interest to guarantee the complete and homogeneous recrystallisation of the as-cast microstructure at the end of the ingot-to-billet conversion process, hence ensuring the compliance of the manufactured components to the required quality standards. Owing to the differences in the microstructure size and morphology distributions in as-cast ingots, and also the increasing thermal inertia with increasing length-scales, transferring the results from smaller scales to larger scales (i.e., and vice versa) remain challenging.

Chapter 7 : CONCLUSIONS

This PhD thesis investigated deformation and microstructure evolution (e.g., recrystallisation) behaviours of as-cast 316L and 316Nb austenitic stainless steels during the ingot-to-billet conversion process, focusing on intermediate scales aiming to bridge the gap between laboratory- and industrial-scales studies. Particular attention was given to understanding the behaviours of coarse and columnar as-cast microstructure under different thermomechanical conditions representative of industrial processing, during the early stages of the ingot-to-billet conversion processes. Through the integration of FE modelling and tailored characterisation techniques, this study significantly advanced current knowledge and know-hows on microstructural evolution in austenitic stainless steels ingots. The investigations revealed the complementary inputs from intermediate-scale experiments compared to laboratory-scale research, offering an effective approach to support more efficient, cost-effective, and quality-driven ingot-to-billet conversion processes.

The conclusions and main findings of this PhD are summarised as the following:

1. **Anisotropic deformation of the as-cast materials:** Due to a strong crystallographic texture induced by directional grain growth during solidification (i.e., formation of large columnar grains), the as-cast material exhibited significant anisotropic deformation during thermomechanical processing. This anisotropic deformation behaviour is essential to be considered in FE models to predict (i) the deformed geometry of the ingots accurately, and (ii) the macroscopic thermomechanical history undergone by the material. This was achieved using the orthotropic Hill-48 yield criterion, which was successfully incorporated into FE models. The investigated smaller-scale samples allowed the calibration of the model, and the larger scale experiments demonstrated its validity. Although a "trial-and-error" approach was used for the determination of Hill-48 coefficients and the model calibration, demonstrating the integration of the anisotropic deformation behaviour in FE models implies that more advanced calibration methods could be used for further enhancement and more elegant integration of the anisotropic models into FE predictions of large scales ingot-to-billet conversion.

2. **Heterogeneous deformation of as-cast materials:** Owing to their coarse and columnar morphology, the grains underwent heterogeneous deformation (i.e., material-induced). This was reinforced by strain and strain-rate gradients (i.e., process-induced) which developed in the material during thermomechanical processing. This effect is even more pronounced during cogging due to the incremental characteristic of the process itself. Although the heterogeneities in deformation levels underwent by the material could not be directly quantified, they were predicted by FE simulations, and their effects on the resulting microstructure were observed in the form of heterogeneous nucleation and

progress of recrystallisation and the persistence of non-recrystallised grains (i.e., survived due to lack of deformation).

3. **Recrystallisation mechanisms in the as-cast materials:** Both 316L and 316Nb grades exhibited usual recrystallisation mechanisms reported in literature, including DRX, MDRX and SRX as functions of the processing conditions. Complete recrystallisation of the as-cast microstructure was achieved at the early stage of the ingot-to-billet conversion process, for both investigated scales (i.e., intermediate and large). With advantageous adiabatic heating generated during upsetting (i.e., 30% in height) in the samples tested using a screw press, the microstructure underwent DRX followed by MDRX up to complete recrystallisation. In contrast, incomplete DRX and MDRX were obtained in the small-scale samples deformed using a hydraulic press, owing to the absence of adiabatic heating generated during the upsetting. The 316Nb ingot subjected to 40% upsetting in height underwent DRX followed by MDRX up to complete recrystallisation. Little DRX was achieved in the 316L and 316Nb ingots subjected to cogging up to 23% section reduction, and fully recrystallised microstructures were obtained via SRX throughout the following reheating.

4. **Role of Nb content:** These investigations were conducted on both 316L and 316Nb grades of austenitic stainless steel, and the results revealed significant differences between the behaviours of both grades. The addition of Nb in the 316Nb grade promoted a microstructure with finer as-cast grains. Also, the Nb-rich secondary phases formed in the 316Nb grade during solidification survived following the homogenisation heat treatment, whereas the secondary phases in the 316L grade were fully dissolved. With finer as-cast grains and dispersed secondary phases, in contrary to common assumptions in the literature, the 316Nb grade was characterised with a higher volume fraction of nucleation sites compared to the 316L. The 316Nb ingots consequently exhibited higher fractions of recrystallised grains under the same thermomechanical conditions. Also, the effect of Nb at reducing grain boundary mobility contributed to higher levels of recrystallised microstructures with smaller grain sizes compared to the 316L grade.

5. **Experimental methodologies:** An innovative experimental methodology was developed for the investigation of the as-cast material behaviours at larger scales compared to the most common laboratory-scale studies published in literature. Although laboratory-scale investigations provide highly controlled instruments with possibilities to record most of the thermomechanical testing conditions for the development of material models, they are not fully representative of the larger scale behaviours of as-cast materials due to the limited number of grain comprised across the cross-section of the samples. In contrast, larger samples or entire ingots provide a larger grain population, which ensure better statistical representitivity of the deformation and recrystallisation behaviours underwent

by coarse, as-cast microstructures at industrial processing scales. In addition, larger scale experiments were shown to provide more representative processing conditions to those encountered during industrial-scale processing and therefore can be more representative of the as-cast material behaviours. Larger scale studies also allow to validate models and hypotheses developed using laboratory-scale data and corroborated FE optimisation studies, which yet remain in the scope of industrial know-how and are rarely enclosed into scientific papers. Due to limited control over the thermomechanical conditions applied to the ingots at larger scales, those experiments could not be used for extracting high-quality data required for the development of material models. Consequently, this PhD thesis highlights the unique insight gained into the behaviours of as-cast materials during the ingot-to-billet conversion process through larger scale investigations. These insight complement laboratory-scale studies and contribute to the effective design and optimisation of ingot-to-billet manufacturing routes.

6. **Characterisation techniques:** As a results of localised effects of processing on microstructure evolution, large-scale samples had to be collected from the material subjected to thermomechanical processing. Hence, adequate characterisation techniques had to be developed to successfully characterise the extracted samples. Although the usual "macro-etching" technique allows for drawing qualitative relationship between the thermomechanical history and the progress of recrystallisation, the as-developed semi-automated analysis method of OM collected across large surface areas demonstrated strong capabilities at quantitatively capturing the microstructural evolution in the materials. Nevertheless, those large-scale characterisation techniques do not replace the usual smaller-scale investigations methods (e.g., SEM, EBSD, etc.), which allow for in-depth characterisation of the material structure, but provide additional tools to obtain valuable and sufficient information from larger scale experiments.

7. **Articulation of results through scales:** Transferring the results from smaller scales to larger scales (i.e., and vice versa) remain challenging owing to the scale-induced differences in terms of as-cast microstructure, thermal inertia of the ingots and processing schedules. Although modelling techniques allow for upscaling the results obtained at laboratory-scale, this PhD thesis outlined the partial representability of the material behaviours investigated at smaller scales to reasonably replicate the larger scale behaviours of the ingots subjected to industrial processing. The large-scale experimental and characterisation techniques developed in this PhD thesis hence extends the existing methods for the development and optimisation of the ingot-to-billet conversion process.

Chapter 8 : FUTURE WORKS

Optimisation of manufacturing routes is essential to ensure the time- and cost-efficiency of manufacturing processes while enhancing their sustainability through energy savings. However, such improvements must not compromise the quality standards required for the final components. Based on the findings of this PhD thesis, and in light of recent developments in the literature, it is evident that further investigations are needed to strengthen the robustness of the ingot-to-billet conversion process, particularly in efficiently achieving fully and homogeneously recrystallised microstructures. The following topics are proposed as key areas for future research.

8.1 CONTROL OF THE INITIAL MATERIAL CONDITION

Better insight and understanding of the initial material condition are critical for the design of robust ingot-to-billet manufacturing routes. In particular, the presence and distribution of secondary phases in as-cast materials can significantly affect recrystallisation kinetics, deformation behaviour, and even the corrosion resistance of the final components. Because secondary phases play a critical role in recrystallisation behaviour and deformation homogeneity, and to ensure that the initial condition of the material used in further experiments closely replicates that of industrially processed ingots, thus improving both the reliability and applicability of the investigations, the following investigations are suggested to be conducted in the early stage of further studies:

- **Quantitative assessment of secondary phases**: Compare the amounts and distribution of secondary phases measured in the as-cast ingot (e.g., via quantitative OM or SEM/EDS analyses) with equilibrium predictions from Schaeffler or Delong diagrams, or from computational thermodynamic methods (e.g., (Jolly et al., 2016)).
- **Investigation of secondary phase dissolution kinetics**: Experimentally determine the dissolution kinetics of secondary phases during homogenisation and thermomechanical processing. This could follow the methodology of (Rezayat et al., 2016). Consideration should also be given to potential precipitation during cooling or intermediate reheating stages.
- **Design of homogenisation heat treatments**: Optimise homogenisation parameters (i.e., temperature and duration) to ensure maximal dissolution of detrimental secondary phases while considering industrial constraints such as treatment duration and energy costs. The remaining secondary phase content should be evaluated against theoretical predictions to assess their expected evolution during subsequent thermomechanical processing.

- **Sensitivity to composition and solidification conditions**: the presence and stability of secondary phases are highly sensitive to both the chemical composition of the alloy and the solidification conditions. Therefore, the findings from the aforementioned investigations must be contextualised across a range of compositional and processing variables which also must be determined.

8.2 A NEED FOR ADVANCED MODELLING CAPABILITIES

To ensure quality, cost-effectiveness, and sustainability of manufacturing processes—and given the deeper insights that modelling provides compared to physical trials—the development of advanced modelling capabilities remains critical for optimising the ingot-to-billet manufacturing route.

8.2.1 Quantifying the limitations of JMAK models

This thesis and other studies (e.g., (Bandar et al., 2007) (Bylya et al., 2017)) have identified major limitations in applying JMAK models to as-cast materials. Despite these limitations, further development of such models remains of interest. To improve their reliability, their suspected lack of accuracy must be quantitatively assessed.

A comparative study can be conducted using a shared experimental dataset, such as results from replicated isothermal compression tests. Two types of JMAK models can then be developed:

1. Based on flow softening induced by recrystallisation during deformation (e.g., (Han et al., 2015)),
2. Based on correlating FE-predicted thermomechanical properties with experimentally observed microstructures (e.g., (Semiatin et al., 2004)).

The in-house large-scale quantitative characterisation method developed during this PhD work could then be used to assess model accuracy across full cross-sections. These models should also be validated at larger experimental scales.

8.2.2 Development of advanced deformation and recrystallisation models

Among the numerous modelling methods available for predicting deformation and recrystallisation behaviour of metallic materials, and despite the need for extensive computational and storage resources of such models, the approach used by (Li et al., 2016) and (Majta et al., 2016), consisting in using fully-coupled FE, CPFEM and 3D CA models provides promising progress in modelling deformation and recrystallisation of as-cast materials. Examples of what could be achieved with such model are listed below:

- More accurately describe the anisotropic deformation behaviour of columnar as-cast microstructures. For instance, this could be used for determining the Hill parameters to be used in FE models.
- Investigate the heterogeneous deformation behaviour of as-cast microstructures, and how more efficient manufacturing route could be developed to improve the homogeneity of deformation, hence allowing for more homogeneously refined microstructures.
- Investigate the non-recrystallisation behaviour of as-cast microstructures.
- Investigate the specific deformation and recrystallisation behaviour of as-cast microstructure with abrupt changes in grain morphology, such as observed along the transverse cross-section of the 2.3 tonnes ingot (i.e., see Figure 3.4 a)), or at the columnar-to-equiaxed transition of larger ingots.

8.2.3 Further use and integration of solidification models

Solidification models play a crucial role in bridging the gap between casting design and downstream thermomechanical processing. By enabling accurate predictions of grain size and morphology in the ingots, these models can significantly reduce the need for extensive experimental characterisation of the as-cast microstructure. They also offer valuable guidance for optimising the solidification conditions.

Models such as those developed by (Maduriya and Yadav, 2018) could be employed to design casting processes that produce smaller-scale ingots replicating the key features of industrial full-scale ingots (e.g., such as the 2.3 tonnes ingot shown in Figure 3.4). These features include cross-sectional geometry, columnar grain orientation and morphology, etc.. Producing such smaller-scale but representative ingots would enable more cost-effective experimentation and process optimisation. For instance, cogging experiments could be performed on such ingots using the experimental setup developed for the intermediate-scale forging trials on the Ø 190 mm ingots.

Using these representative ingots, researchers could investigate the influence of microstructural features (e.g., columnar grain length, orientation relative to deformation, etc.) on recrystallisation behaviour during cogging or upsetting operations. This would support the development of manufacturing schedules that more reliably promote complete and homogeneous recrystallisation across the billet, thereby enhancing product quality and reducing energy consumption. This can also be extended to accurate reproduction of central void porosities found in large ingots, and enabling investigation on their efficient closure during the ingot-to-billet manufacturing route.

In addition to the deformation and recrystallisation modelling capabilities suggested in Section 8.2.2, a fully integrated modelling approach including the design of ingot geometry and casting parameters, the ingot-to-billet conversion and following thermomechanical processing stages (e.g., open- and closed-die forging, etc.) could be achieved by chaining casting simulations to deformation and recrystallisation models, enabling a more robust and cost-effective design of manufacturing routes for engineering components.

8.3 A NEED FOR ADVANCED CHARACTERISATION EQUIPMENT

Laboratory-scale experiments provide limited capabilities at faithfully replicating the industrial-scale behaviour of as-cast ingots, and larger scale characterisation techniques cannot achieve the required levels of control and record of thermomechanical testing conditions required for the development of material behaviour models. Consequently, further research on as-cast material behaviour would benefit from the development of innovative testing equipments capable of testing the material behaviour using larger scale samples.

Such equipment should be able to provide isothermal capabilities and high loads capacities, with accurate records and control of the testing conditions. Characterisation of the equipment stiffness is also required to guarantee the accuracy of the recorded data. During thermomechanical experiments, reducing the friction between the samples and the testing dies also needs to be addressed to restrain the deformation heterogeneities, and supress the inaccuracies introduced by the lack of control and inaccurate records into the determined stress-strain curves.

With further improvements to cope with larger samples and temperatures ranging up to 1250 °C, the miniaturised open-die forging set-up developed by (Connolly et al., 2023) provides experimental capabilities which supplement those of usual laboratory-scale uniaxial compression tests.

8.4 EXTENSION TO OTHER MATERIALS AND PROCESSES

Although this PhD thesis focused on specific grades of austenitic stainless steels, the methodology developed for the investigation on the deformation and recrystallisation behaviour of the as-cast material can be used for further investigations on other type of material (e.g., Ni- or Ti-based superalloy) or processes (e.g., hot rolling, etc.).

REFERENCES

Abrams, H., Maniar, G.N., Nail, D.A., Solomon, H.D., 2018. MiCon 78: Optimization of processing, properties, and service performance through microstructural control 657.

AFRC FutureForge, 2024.

Aghajani Derazkola, H., Garcia, E., Murillo-Marrodán, A., Conde Fernandez, A., 2022. Review on modeling and simulation of dynamic recrystallization of martensitic stainless steels during bulk hot deformation. Journal of Materials Research and Technology 18, 2993–3025. https://doi.org/10.1016/j.jmrt.2022.03.179

Anitha Lakshmi, A., Srinivasa Rao, Ch., Gangadhar, J., Srinivasu, Ch., Singh, S.K., 2017. Review of Processing Maps and Development of Qualitative Processing Maps. Materials Today: Proceedings, 5th International Conference of Materials Processing and Characterization (ICMPC 2016) 4, 946–956. https://doi.org/10.1016/j.matpr.2017.01.106

Anoop, C.R., Singh, R.K., Kumar, R.R., Jayalakshmi, M., Narayana Murty, S.V.S., Thomas Tharian, K., 2020. Hot Deformation Studies and Optimization of Hot Working Parameters in Custom 465® Martensitic Precipitation Hardenable Stainless Steel. Matls. Perf. Charact. 9, 20190087. https://doi.org/10.1520/MPC20190087

ASM International (Ed.), 1990. ASM_Metalworking: Bulk Forming. ASM International, Materials Park, Ohio.

ASTM A240/A240M-22, 2022. Specification for Chromium and Chromium-Nickel Stainless Steel Plate, Sheet, and Strip for Pressure Vessels and for General Applications. ASTM International. https://doi.org/10.1520/A0240_A0240M-22

ASTM E 407, 1999. Standard Practice for Microetching Metals and Alloys. ASTM International. https://doi.org/10.1520/E0407-99

Avrami, M., 1941. Kinetics of Phase Change. III Granulation, Phase Change, and Microstructure. J. Chem. Phys. 9, 177–184. https://doi.org/10.1063/1.1750872

Bandar, A.R., Shankar, R., Cai, L., Wu, W.-T., 2007. Microstructure Modeling of the Superalloy Ingot Breakdown Process (Preprint) 12.

Barraclough, D.R., Sellars, C.M., 1979. Static recrystallization and restoration after hot deformation of Type 304 stainless steel. Metal Science 13, 257–268. https://doi.org/10.1179/msc.1979.13.3-4.257

Beijiang, Z., Guangpu, Z., Wenyun, Z., Shuo, H., Shifu, C., 2015. Investigation of high performance disc alloy GH4065 and associated processing techniques. ACTA METALLURGICA SINICA 8. https://doi.org/10.11900/0412.1961.2015.00368

Burke, J.E., Turnbull, D., 1952. Recrystallization and grain growth. Progress in Metal Physics 3, 220–292. https://doi.org/10.1016/0502-8205(52)90009-9

Bylya, O., Reshetov, A., Stefani, N., Rosochowska, M., Blackwell, P., 2017. Applicability of JMAK-type model for predicting microstructural evolution in nickel-based superalloys. Procedia Engineering, International Conference on the Technology of Plasticity, ICTP 2017, 17-22 September 2017, Cambridge, United Kingdom 207, 1105–1110. https://doi.org/10.1016/j.proeng.2017.10.1067

Cahn, J.W., 1962. The impurity-drag effect in grain boundary motion. Acta Metallurgica 10, 789–798. https://doi.org/10.1016/0001-6160(62)90092-5

Campbell, J., 2015. Complete Casting Handbook (Second Edition). Butterworth-Heinemann, Boston.

Cao, L., Yang, Z., Chen, Y., Wang, H., Zhao, X., 2015. Effects of Nitrogen Content and Austenitization Temperature on Precipitation in Niobium Micro-alloyed Steels. Journal of Iron and Steel

Research, International 22, 1164–1173. https://doi.org/10.1016/S1006-706X(15)30128-X

Chen, F., Qi, K., Cui, Z., Lai, X., 2014. Modeling the dynamic recrystallization in austenitic stainless steel using cellular automaton method. Computational Materials Science 83, 331–340. https://doi.org/10.1016/j.commatsci.2013.11.029

Chen, S.F., Li, D.Y., Zhang, S.H., Han, H.N., Lee, H.W., Lee, M.G., 2020. Modelling continuous dynamic recrystallization of aluminum alloys based on the polycrystal plasticity approach. International Journal of Plasticity 131, 102710. https://doi.org/10.1016/j.ijplas.2020.102710

Cheng, Z., Liu, H., Liu, Y., Ning, Z., Li, M., Yu, W., Cai, Q., 2024. Effects of Deformation Penetration and Recrystallization on the Internal Quality of Casting Ingot. steel research international 95, 2300422. https://doi.org/10.1002/srin.202300422

Cho, J.R., Park, C.Y., Yang, D.Y., 1992. Investigation of the Cogging Process by Three-Dimensional Thermo-Viscoplastic Finite Element Analysis. Proceedings of the Institution of Mechanical Engineers, Part B: Journal of Engineering Manufacture 206, 277–286. https://doi.org/10.1243/PIME_PROC_1992_206_084_02

Choi, S.K., Chun, M.S., Van Tyne, C.J., Moon, Y.H., 2006. Optimization of open die forging of round shapes using FEM analysis. Journal of Materials Processing Technology 172, 88–95. https://doi.org/10.1016/j.jmatprotec.2005.09.010

Christiansen, P., 2014. Modelling of defects in ingot forging: with the finite element flow formulation.

Christiansen, P., Hattel, J.H., Bay, N., Martins, P.A., 2014. Physical modeling and numerical simulation of V-die forging ingot with central void. Proceedings of the Institution of Mechanical Engineers, Part C: Journal of Mechanical Engineering Science 228, 2347–2356. https://doi.org/10.1177/0954406213517878

Chu, H.-Y., Shiue, R.-K., Cheng, S.-Y., 2024. The Effect of Homogenization Heat Treatment on 316L Stainless Steel Cast Billet. Materials 17, 232. https://doi.org/10.3390/ma17010232

Cliche, N., Ringeval, S., Petit, P., Bellus, J., Georges, E., Cortial, F., Heuzé, J.-L., Gourgues-Lorenzon, A.-F., Esin, V.A., 2021. Thermokinetic Modelling of High-Temperature Evolution of Primary Nb(C,N) in Austenite Applied to Recrystallization of 316Nb Austenitic Stainless Steel. Metals 11, 715. https://doi.org/10.3390/met11050715

Connolly, D., Sivaswamy, G., Rahimi, S., Vorontsov, V., 2023. Miniaturised experimental simulation of open-die forging. Journal of Materials Research and Technology 26, 3146–3161. https://doi.org/10.1016/j.jmrt.2023.08.073

Czerwinski, F., Cho, J.Y., Brodtka, A., Zielinska-Lipiec, A., Sunwoo, J.H., Szpunar, J.A., 1999. The edge-cracking of AISI 304 stainless steel during hot-rolling. Journal of Materials Science 34, 4727–4735. https://doi.org/10.1023/A:1004670602478

Dandre, C.A., Roberts, S.M., Evans, R.W., Reed, R.C., 2000a. Microstructural evolution of Inconel* 718 during ingot breakdown: process modelling and validation. Materials Science and Technology 16, 14–25. https://doi.org/10.1179/026708300773002627

Dandre, C.A., Roberts, S.M., Evans, R.W., Reed, R.C., 2000b. Microstructural evolution of Inconel 718 during ingot breakdown: process modelling and validation. Materials Science and Technology 16, 14–25. https://doi.org/10.1179/026708300773002627

Dandre, C.A., Roberts, S.M., Evans, R.W., Reed, R.C., 1999. A model describing microstructural evolution for Ni-base superalloy forgings during the cogging process. J. Phys. IV France 09, Pr9-33-Pr9-42. https://doi.org/10.1051/jp4:1999904

Dandre, C.A., Walsh, C.A., Evans, R.W., Reed, R.C., Roberts, S.M., 2000c. Microstructural evolution of nickel-base superalloy forgings during ingot-to-billet conversion: process modelling and validation. Superalloys 85–94.

Dantzig, J.A., Rappaz, M., 2016. Solidification. EPFL Press.

David, S.A., 1981. Ferrite Morphology and Variations in Ferrite Content in Austenitic Stainless Steel Welds. Welding Research Supplement.

De Jaeger, J., Solas, D., Fandeur, O., Schmitt, J.-H., Rey, C., 2015. 3D numerical modeling of dynamic recrystallization under hot working: Application to Inconel 718. Materials Science and Engineering: A 646, 33–44. https://doi.org/10.1016/j.msea.2015.08.038

Debayle, J., Pinoli, J.-C., 2006. General Adaptive Neighborhood Image Processing: Part II: Practical Application Examples. J Math Imaging Vis 25, 267–284. https://doi.org/10.1007/s10851-006-7452-7

DeNonno, O., Saville, A., Benzing, J., Klemm-Toole, J., Yu, Z., 2024. Solidification behavior and texture of 316L austenitic stainless steel by laser wire directed energy deposition. Materials Characterization 211, 113916. https://doi.org/10.1016/j.matchar.2024.113916

Doherty, R.D., Hughes, D.A., Humphreys, F.J., Jonas, J.J., Jensen, D.J., Kassner, M.E., King, W.E., McNelley, T.R., McQueen, H.J., Rollett, A.D., 1997. Current issues in recrystallization: a review. Materials Science and Engineering: A 238, 219–274. https://doi.org/10.1016/S0921-5093(97)00424-3

Dudova, N., Belyakov, A., Sakai, T., Kaibyshev, R., 2010. Dynamic recrystallization mechanisms operating in a Ni–20%Cr alloy under hot-to-warm working. Acta Materialia 58, 3624–3632. https://doi.org/10.1016/j.actamat.2010.02.032

DuPont, J.N., Farren, J.D., 2011. Influence of Heat Treatment Time and Temperature on the Microstructure and Corrosion Resistance of Cast Superaustenitic Stainless Steels. Corrosion 67, 055002–1. https://doi.org/10.5006/1.3586019

Ebrahimi, R., Najafizadeh, A., 2004. A new method for evaluation of friction in bulk metal forming. Journal of Materials Processing Technology 152, 136–143. https://doi.org/10.1016/j.jmatprotec.2004.03.029

El Wahabi, M., Gavard, L., Montheillet, F., Cabrera, J.M., Prado, J.M., 2005. Effect of initial grain size on dynamic recrystallization in high purity austenitic stainless steels. Acta Materialia 53, 4605–4612. https://doi.org/10.1016/j.actamat.2005.06.020

Eriksson, R., Jonsson, L., Jönsson, P.G., 2004. Effect of Entrance Nozzle Design on the Fluid Flow in an Ingot Mold during Filling. ISIJ International 44, 1358–1365. https://doi.org/10.2355/isijinternational.44.1358

Evans, R.W., Scharning, P.J., 2001. Axisymmetric compression test and hot working properties of alloys. Materials Science and Technology 17, 995–1004. https://doi.org/10.1179/026708301101510843

Fan, H., Jiang, H., Dong, J., Yao, Z., Zhang, M., 2019. An optimization method of upsetting process for homogenized, nickel-based superalloy Udimet 720Li ingot considering both cracking and recrystallization. Journal of Materials Processing Technology 269, 52–64. https://doi.org/10.1016/j.jmatprotec.2019.01.013

Feng, C., Cui, Z., Liu, M., Shang, X., Sui, D., Liu, J., 2016. Investigation on the void closure efficiency in cogging processes of the large ingot by using a 3D void evolution model. Journal of Materials Processing Technology 237, 371–385. https://doi.org/10.1016/j.jmatprotec.2016.06.030

Fernández, A.I., López, B., Rodriguez-Ibabe, J.M., 2002. Static recrystallization mechanisms in a coarse-grained Nb-microalloyed austenite. Metall Mater Trans A 33, 3089–3098. https://doi.org/10.1007/s11661-002-0293-0

Fischer, T., Hitzler, L., Werner, E., 2021. Morphological and Crystallographic Effects in the Laser Powder-Bed Fused Stainless Steel Microstructure. Crystals 11, 672. https://doi.org/10.3390/cryst11060672

Forbes Jones, R.M., Jackman, L.A., 1999. The structural evolution of superalloy ingots during hot working. JOM 51, 27–31. https://doi.org/10.1007/s11837-999-0007-9

Freund, L., Langlois, L., Bigot, R., Gyss, O., 2020. Study of the dynamic recrystallization of Inconel 625 alloys through cogging. Procedia Manufacturing, 18th International Conference on Metal Forming 2020 50, 658–662. https://doi.org/10.1016/j.promfg.2020.08.118

Gao, H., Huang, Y., 2003. Geometrically necessary dislocation and size-dependent plasticity. Scripta Materialia 48, 113–118. https://doi.org/10.1016/S1359-6462(02)00329-9

Gholamzadeh, A., Karimi Taheri, A., 2009. The prediction of hot flow behavior of Al-6%Mg alloy. Mechanics Research Communications 36, 252–259. https://doi.org/10.1016/j.mechrescom.2008.06.011

Ghosh, S., 2002. Interpretation of flow instability using dynamic material modeling. Metall Mater Trans A 33, 1569–1572. https://doi.org/10.1007/s11661-002-0081-x

Ghosh, S., 2000. Interpretation of microstructural evolution using dynamic materials modeling. Metall Mater Trans A 31, 2973–2974. https://doi.org/10.1007/BF02830342

Guo, Y.-N., Li, Y.-T., Tian, W.-Y., Qi, H.-P., Yan, H.-H., 2018. Combined Cellular Automaton Model for Dynamic Recrystallization Evolution of 42CrMo Cast Steel. Chinese Journal of Mechanical Engineering 31, 85. https://doi.org/10.1186/s10033-018-0284-8

Hallberg, H., 2011. Approaches to Modeling of Recrystallization. Metals 1, 16–48. https://doi.org/10.3390/met1010016

Han, Y., Liu, G., Zou, D., Liu, R., Qiao, G., 2013. Deformation behavior and microstructural evolution of as-cast 904L austenitic stainless steel during hot compression. Materials Science and Engineering: A 565, 342–350. https://doi.org/10.1016/j.msea.2012.12.043

Han, Y., Wu, H., Zhang, W., Zou, D., Liu, G., Qiao, G., 2015. Constitutive equation and dynamic recrystallization behavior of as-cast 254SMO super-austenitic stainless steel. Materials & Design 69, 230–240. https://doi.org/10.1016/j.matdes.2014.12.049

Harris, N., Shahriari, D., Jahazi, M., 2017. Development of a fast converging material specific void closure model during ingot forging. Journal of Manufacturing Processes 26, 131–141. https://doi.org/10.1016/j.jmapro.2017.02.021

Hermant, A., Suzon, E., Petit, P., Bellus, J., Georges, E., Cortial, F., Sennour, M., Gourgues-Lorenzon, A.-F., 2019. Hot Deformation and Recrystallization Mechanisms in a Coarse-Grained, Niobium Stabilized Austenitic Stainless Steel (316Nb). Metall and Mat Trans A 50, 1625–1642. https://doi.org/10.1007/s11661-018-05103-x

Hill, R., Orowan, E., 1948. A theory of the yielding and plastic flow of anisotropic metals. Proceedings of the Royal Society of London. Series A. Mathematical and Physical Sciences 193, 281–297. https://doi.org/10.1098/rspa.1948.0045

Hillert, M., Sundman, B., 1976. A treatment of the solute drag on moving grain boundaries and phase interfaces in binary alloys. Acta Metallurgica 24, 731–743. https://doi.org/10.1016/0001-6160(76)90108-5

Hou, Y., Cheng, G., 2019. Effects of Nucleus Density and Dendritic Growth Influenced by Ti and Nb on Solidification Structure of Fe-18 Pct Cr Ferritic Stainless Steel. Metall Mater Trans B 50, 1322–1333. https://doi.org/10.1007/s11663-019-01557-5

Huang, K., Logé, R.E., 2016. A review of dynamic recrystallization phenomena in metallic materials. Materials & Design 111, 548–574. https://doi.org/10.1016/j.matdes.2016.09.012

Humphreys, F.J., Hatherly, M., 1995. Recrystallization and related annealing phenomena, 1. ed., 2nd impr. ed. Pergamon Press, Oxford.

International Stainless Steel Forum, 2021. Stainless Steel in Figures.

Ion, S.E., Humphreys, F.J., White, S.H., 1982. Dynamic recrystallisation and the development of microstructure during the high temperature deformation of magnesium. Acta Metallurgica 30, 1909–1919. https://doi.org/10.1016/0001-6160(82)90031-1

Jia, L., Li, Y., Zhang, Y., 2017. A Characterization for the Deformation Behavior of As-Cast P91 Alloy Steel and Utilization in Hot Extrusion Process. Advances in Materials Science and Engineering 2017, 1–11. https://doi.org/10.1155/2017/6582739

Jin, M., Lu, B., Liu, X., Guo, H., Ji, H., Guo, B., 2013. Static Recrystallization Behavior of 316LN Austenitic Stainless Steel. Journal of Iron and Steel Research, International 20, 67–72. https://doi.org/10.1016/S1006-706X(13)60198-3

Johnson, W.A., Mehl, R., 1939. Reaction kinetics in processes of nucleation and growth. Trans. Metall. Soc. AIME 416–442.

Jolly, W., Toffolon-Masclet, C., Joubert, J.-M., Marini, B., Porcher, F., André, G., Cortial, F., Petit, Ph., Ringeval, S., 2016. In situ monitoring of isothermal phase transformation in two Nb stabilized austenitic stainless steels (316Nb) by neutron diffraction. Journal of Alloys and Compounds 688, 695–702. https://doi.org/10.1016/j.jallcom.2016.07.244

Jorge-Badiola, D., Iza-Mendia, A., Gutiérrez, I., 2005. Study by EBSD of the development of the substructure in a hot deformed 304 stainless steel. Materials Science and Engineering: A 394, 445–454. https://doi.org/10.1016/j.msea.2004.11.049

Katayama, S., Fujimoto, T., Matsunawa, A., 1985. Correlation among Solidification Process, Microstructure, Microsegregation and Solidification Cracking Susceptibility in Stainless Steel Weld Metals(Materials, Metallurgy & Weldability).

Kawaguchi, S., Tsukada, H., Suzuki, K., Sato, I., Onodera, S., 1986. Manufacturing of Large and Integral-Type Steel Forgings for Nuclear Steam Supply System Components, in: Nisbett, E., Melilli, A. (Eds.), Steel Forgings. ASTM International, p. 0. https://doi.org/10.1520/STP17370S

Kelkar, K.M., Patankar, S.V., Mitchell, A., Kanou, O., Fukada, N., 2007. Computational Modeling of the Vacuum Arc Remelting (VAR) Process Used for the Production of Ingots of Titanium Alloys. Proceedings of the International Symposium on Liquid Metal Processing and Casting 4.

Keller, C., Calvat, M., Flipon, B., Barbe, F., 2022. Experimental and numerical investigations of plastic strain mechanisms of AISI 316L alloys with bimodal grain size distribution. International Journal of Plasticity 153, 103246. https://doi.org/10.1016/j.ijplas.2022.103246

Kim, Y., Cho, J., Bae, W., 2011. Efficient forging process to improve the closing effect of the inner void on an ultra-large ingot. Journal of Materials Processing Technology 211, 1005–1013. https://doi.org/10.1016/j.jmatprotec.2011.01.001

Kolmogorov, A.N., 1937. On the statistical theory of crystallization of metals. Izv. Akad. Nauk SSSR, Ser. Mat. 3 355–359.

Kou, S., 2003. Welding metallurgy, 2nd ed. ed. Wiley-Interscience, Hoboken, N.J.

Kukuryk, M., 2023. Experimental and numerical study of the closure of voids with different size and various locations in the three-dimensional cogging process. Int J Mater Form 17, 3. https://doi.org/10.1007/s12289-023-01798-5

Kukuryk, M., 2020. Analysis of Deformation and Prediction of Cracks in the Cogging Process for Die Steel at Elevated Temperatures. Materials 13, 5589. https://doi.org/10.3390/ma13245589

Kukuryk, M., 2018. Numerical analysis of strains and stresses in the hot cogging process. Journal of Applied Mathematics and Computational Mechanics 17, 45–52. https://doi.org/10.17512/jamcm.2018.3.04

Kurz, W., D.J. Fisher, 1992. Fundamentals of solidification, 3rd ed.

Ledoux, X., Buy, F., Perron, A., Suzon, E., Farré, J., Marini, B., Guilbert, T., Wident, P., Texier, G., Vignal, V., Cortial, F., Petit, P., 2014. Kinetics of Sigma Phase Precipitation in Niobium-Stabilized Austenitic Stainless Steel and Effect on the Mechanical Properties. MSF 783–786, 848–853. https://doi.org/10.4028/www.scientific.net/MSF.783-786.848

Lee, Y.S., Lee, S.U., Van Tyne, C.J., Joo, B.D., Moon, Y.H., 2011. Internal void closure during the forging of large cast ingots using a simulation approach. Journal of Materials Processing Technology 211, 1136–1145. https://doi.org/10.1016/j.jmatprotec.2011.01.017

Li, H., Sun, X., Yang, H., 2016. A three-dimensional cellular automata-crystal plasticity finite element model for predicting the multiscale interaction among heterogeneous deformation, DRX microstructural evolution and mechanical responses in titanium alloys. International Journal of Plasticity 87, 154–180. https://doi.org/10.1016/j.ijplas.2016.09.008

Li, J., Liu, J., 2019. Strain Compensation Constitutive Model and Parameter Optimization for Nb-Contained 316LN. Metals 9, 212. https://doi.org/10.3390/met9020212

Li, J., Wu, Y., Zhang, H., Zhang, X., 2023. Study on the dynamic recrystallization mechanisms tailored by dislocation substructures of a coarse grained Co-free nickel-based superalloy. Materials Characterization 201, 112961. https://doi.org/10.1016/j.matchar.2023.112961

Li, X., Zhang, T., Jiang, H., Dong, J., 2023. Predicting the three-dimensional grain structure of superalloys during vacuum arc remelting process. Journal of Materials Research and Technology 25, 5938–5949. https://doi.org/10.1016/j.jmrt.2023.07.060

Li, Z., Xu, Q., Liu, B., 2015. Microstructure simulation on recrystallization of an as-cast nickel based single crystal superalloy. Computational Materials Science 107, 122–133. https://doi.org/10.1016/j.commatsci.2015.05.020

Liao, L., Zhao, Z., Zhang, W., Li, J., Chen, Y., Pan, L., 2023. Unveiling Hot Deformation Behavior and Dynamic Recrystallization Mechanism of 654SMO Super-Austenitic Stainless Steel. Metall Mater Trans A 54, 2554–2575. https://doi.org/10.1007/s11661-023-07019-7

Lippold, C.J., Kotecki, D.J., 2005. Welding Metallurgy and Weldability of Stainless Steels. Wiley-Interscience.

Liu, G., Han, Y., Shi, Z., Sun, J., Zou, D., Qiao, G., 2014. Hot deformation and optimization of process parameters of an as-cast 6Mo superaustenitic stainless steel: A study with processing map. Materials & Design 53, 662–672. https://doi.org/10.1016/j.matdes.2013.07.065

Liu, W., Huang, J., Pang, Y., Zhu, K., Li, S., Ma, J., 2023. Multi-scale modelling of evolving plastic anisotropy during Al-alloy sheet forming. International Journal of Mechanical Sciences 247, 108168. https://doi.org/10.1016/j.ijmecsci.2023.108168

López, B., Rodriguez-Ibabe, J.M., 2012. Recrystallisation and grain growth in hot working of steels, in: Microstructure Evolution in Metal Forming Processes. Elsevier, pp. 67–113. https://doi.org/10.1533/9780857096340.1.67

Lu, S., Hu, Q.-M., Johansson, B., Vitos, L., 2011. Stacking fault energies of Mn, Co and Nb alloyed austenitic stainless steels. Acta Materialia 59, 5728–5734. https://doi.org/10.1016/j.actamat.2011.05.049

Lücke, K., Stüwe, H.P., 1971. On the theory of impurity controlled grain boundary motion. Acta Metallurgica 19, 1087–1099. https://doi.org/10.1016/0001-6160(71)90041-1

Majta, J., Madej, Ł., Svyetlichnyy, D.S., Perzyński, K., Kwiecień, M., Muszka, K., 2016. Modeling of the inhomogeneity of grain refinement during combined metal forming process by finite element and cellular automata methods. Materials Science and Engineering: A 671, 204–213. https://doi.org/10.1016/j.msea.2016.06.052

Mandal, G.K., Stanford, N., Hodgson, P., Beynon, J.H., 2012. Effect of hot working on dynamic recrystallisation study of as-cast austenitic stainless steel. Materials Science and Engineering: A 556, 685–695. https://doi.org/10.1016/j.msea.2012.07.050

Manohar, P.A., Ferry, M., Chandra, T., 1998. Five Decades of the Zener Equation. ISIJ International 38, 913–924. https://doi.org/10.2355/isijinternational.38.913

Mataya, M.C., Nilsson, E.R., Brown, E.L., Krauss, G., 2003a. Hot working and recrystallization of as-cast 316L. Metall and Mat Trans A 34, 1683–1703. https://doi.org/10.1007/s11661-003-0313-8

Mataya, M.C., Nilsson, E.R., Brown, E.L., Krauss, G., 2003b. Hot working and recrystallization of as-cast 317L. Metall and Mat Trans A 34, 3021–3041. https://doi.org/10.1007/s11661-003-0201-2

Mataya, M.C., Perkins, C.A., Thompson, S.W., Matlock, D.K., 1996. Flow stress and microstructural evolution during hot working of alloy 22Cr-13Ni-5Mn-0.3N austenitic stainless steel. Metallurgical and Materials Transactions A 27, 1251–1266. https://doi.org/10.1007/BF02649862

Mehmet Türker, Levon Josef Çapan, 2017. Effect of inclusions on mechanical properties of Nb stabilized austenitic stainless steels (316Nb) with centrifugal and sand casting techniques 105. https://doi.org/10.1051/mattech/2017035

Miodownik, M.A., 2002. A review of microstructural computer models used to simulate grain growth and recrystallisation in aluminium alloys. Journal of Light Metals, Modelling of Light Metals 2, 125–135. https://doi.org/10.1016/S1471-5317(02)00039-1

Murugan, N., Parmar, R.S., 1997. Effect of Welding Conditions on Microstructure and Properties of Type 316L Stainless Steel Submerged Arc Cladding. Welding Research Supplement 11.

Orend, J., Hagemann, F., Klose, F.B., Maas, B., Palkowski, H., 2015. A new unified approach for modeling recrystallization during hot rolling of steel. Materials Science and Engineering: A 647, 191–200. https://doi.org/10.1016/j.msea.2015.08.085

Padilha, A.F., Machado, I.F., Plaut, R.L., 2005. Microstructures and mechanical properties of Fe–15% Cr–15% Ni austenitic stainless steels containing different levels of niobium additions submitted to various processing stages. Journal of Materials Processing Technology 170, 89–96. https://doi.org/10.1016/j.jmatprotec.2005.05.002

Park, J., Kim, Y., Jeong, H., Kwon, H., Kwon, Y., Kim, N., 2023. Cogging process design of M50 bearing steel for billet quality. Journal of Materials Research and Technology 26, 5576–5593. https://doi.org/10.1016/j.jmrt.2023.08.275

Park, N.-K., Yeom, J.-T., Kim, J.-H., Cui, X.-X., 2005. Characteristics of VIM/VAR-Processed Alloy 718 Ingot and the Evolution of Microstructure During Cogging, in: Superalloys 718, 625, 706 and Various Derivatives (2005). Presented at the Superalloys, TMS, pp. 253–260. https://doi.org/10.7449/2005/Superalloys_2005_253_260

Park, S.Y., Kim, W.J., 2016. Difference in the Hot Compressive Behavior and Processing Maps between the As-cast and Homogenized Al-Zn-Mg-Cu (7075) Alloys. Journal of Materials Science & Technology 32, 660–670. https://doi.org/10.1016/j.jmst.2016.04.006

Pérez, M., Dumont, C., Nodin, O., Nouveau, S., 2018. Impact of forging direction on the recrystallization behaviour of nickel base superalloy AD730 billet material at subsolvus temperatures. Materials Characterization 146, 169–181. https://doi.org/10.1016/j.matchar.2018.10.003

Perron, A., Toffolon-Masclet, C., Ledoux, X., Buy, F., Guilbert, T., Urvoy, S., Bosonnet, S., Marini, B., Cortial, F., Texier, G., Harder, C., Vignal, V., Petit, Ph., Farré, J., Suzon, E., 2014. Understanding sigma-phase precipitation in a stabilized austenitic stainless steel (316Nb) through complementary CALPHAD-based and experimental investigations. Acta Materialia 79, 16–29. https://doi.org/10.1016/j.actamat.2014.06.066

Poddar, D., Cizek, P., Beladi, H., Hodgson, P.D., 2015. Orientation Dependence of the Deformation Microstructure in a Fe-30Ni-Nb Model Austenitic Steel Subjected to Hot Uniaxial Compression. Metall Mater Trans A 46, 5933–5951. https://doi.org/10.1007/s11661-015-3182-z

Poliak, E.I., Jonas, J.J., 1996. A one-parameter approach to determining the critical conditions for the initiation of dynamic recrystallization. Acta Materialia 44, 127–136. https://doi.org/10.1016/1359-6454(95)00146-7

Pondaven, C., Langlois, L., Erzar, B., Bigot, R., 2021. Numerical and experimental simulation of shrinkage porosity closure during hot rolling of bars. ESAFORM 2021. https://doi.org/10.25518/esaform21.1896

Prasad, Y.V.R.K., 2003. Processing maps: A status report. J. of Materi Eng and Perform 12, 638–645. https://doi.org/10.1361/105994903322692420

Prasad, Y.V.R.K., Gegel, H.L., Doraivelu, S.M., Malas, J.C., Morgan, J.T., Lark, K.A., Barker, D.R., 1984. Modeling of dynamic material behavior in hot deformation: Forging of Ti-6242. Metallurgical Transactions A 15, 1883–1892. https://doi.org/10.1007/BF02664902

Prasad, Y.V.R.K., Seshacharyulu, T., 1998. Processing maps for hot working of titanium alloys. Materials Science and Engineering: A 243, 82–88. https://doi.org/10.1016/S0921-5093(97)00782-X

Qin, F., Li, Y., He, W., Zhao, X., Chen, H., 2017a. Effects of deformation microbands and twins on microstructure evolution of as-cast Mn18Cr18N austenitic stainless steel. Journal of Materials Research 32, 3864–3874. https://doi.org/10.1557/jmr.2017.389

Qin, F., Zhu, H., Wang, Z., Zhao, X., He, W., Chen, H., 2017b. Dislocation and twinning mechanisms for dynamic recrystallization of as-cast Mn18Cr18N steel. Materials Science and Engineering: A 684, 634–644. https://doi.org/10.1016/j.msea.2016.12.095

Quey, R., Fan, G.-H., Zhang, Y., Juul Jensen, D., 2021. Importance of deformation-induced local orientation distributions for nucleation of recrystallisation. Acta Materialia 210, 116808. https://doi.org/10.1016/j.actamat.2021.116808

Ramadan, M., Fourment, L., Digonnet, H., 2014. Fast resolution of incremental forming processes by the Multi-Mesh method. Application to cogging. Int J Mater Form 7, 207–219. https://doi.org/10.1007/s12289-012-1121-8

Ramadan, M., Khaled, M., Fourment, L., 2019. Speeding-up simulation of cogging process by multigrid method. Int J Mater Form 12, 45–55. https://doi.org/10.1007/s12289-018-1405-8

Ramuhalli, P., Good, M.S., Diaz, A.A., Anderson, M.T., Watson, B.E., Peters, T.J., Dixit, M., Bond, L.J., 2009. Ultrasonic Characterization of Cast Austenitic Stainless Steel Microstructure: Discrimination between Equiaxed- and Columnar-Grain Material ? An Interim Study (No. PNNL-18912, 967235). https://doi.org/10.2172/967235

Reardon, A.C. (Ed.), 2011. ASM_Metallurgy for the non-metallurgist, 2nd ed. ed. ASM International, Materials Park, Ohio.

Rezayat, M., Mirzadeh, H., Namdar, M., Parsa, M.H., 2016. Unraveling the Effect of Thermomechanical Treatment on the Dissolution of Delta Ferrite in Austenitic Stainless Steels. Metallurgical and Materials Transactions A 47, 641–648. https://doi.org/10.1007/s11661-015-3242-4

Roebuck, B., Lord, J.D., Brooks, M., Loveday, M.S., Sellars, C.M., Evans, R.W., 2006. Measurement of flow stress in hot axisymmetric compression tests. Materials at High Temperatures 23, 59–83. https://doi.org/10.1179/mht.2006.005

Rosenstock, D., Recker, D., Hirt, G., Steingießer, K.J., Rech, R., Gehrmann, B., Lamm, R., 2013. Application of a Fast Calculation Model for the Process Monitoring of Open Die Forging Processes. KEM 554–557, 248–263. https://doi.org/10.4028/www.scientific.net/KEM.554-557.248

Saby, M., Bernacki, M., Roux, E., Bouchard, P.-O., 2013. Three-dimensional analysis of real void closure at the meso-scale during hot metal forming processes. Computational Materials Science 77, 194–201. https://doi.org/10.1016/j.commatsci.2013.05.002

Sah, J.P., Richardson, G.J., Sellars, C.M., 1974. Grain-Size Effects during Dynamic Recrystallization of Nickel. Metal Science 8, 325–331. https://doi.org/10.1179/msc.1974.8.1.325

Sahithya, K., Balasundar, I., Pant, P., Raghu, T., Nandi, H.K., Singh, V., Ghosal, P., Ramakrishna, M., 2019. Deformation behaviour of an as-cast nickel base superalloy during primary hot working above and below the gamma prime solvus. Materials Science and Engineering: A 754, 521–534. https://doi.org/10.1016/j.msea.2019.03.083

Sakai, T., Belyakov, A., Kaibyshev, R., Miura, H., Jonas, J.J., 2014. Dynamic and post-dynamic recrystallization under hot, cold and severe plastic deformation conditions. Progress in Materials Science 60, 130–207. https://doi.org/10.1016/j.pmatsci.2013.09.002

Sakai, T., Belyakov, A., Miura, H., 2008. Ultrafine Grain Formation in Ferritic Stainless Steel during Severe Plastic Deformation. Metall Mater Trans A 39, 2206–2214. https://doi.org/10.1007/s11661-008-9556-8

Sakai, T., Jonas, J.J., 1984. Overview no. 35 Dynamic recrystallization: Mechanical and microstructural considerations. Acta Metallurgica 32, 189–209. https://doi.org/10.1016/0001-6160(84)90049-X

Sedriks, A.J., 1996. Corrosion of stainless steel, 2nd Edition, Wiley. ed. New York, USA.

Sellars, C.M., McTegart, W.J., 1966. On the mechanism of hot deformation. Acta Metallurgica 14, 1136–1138. https://doi.org/10.1016/0001-6160(66)90207-0

Semiatin, S.L., Weaver, D.S., Goetz, R.L., Thomas, J.P., Turner, T.J., 2007. Deformation and Recrystallization during Thermomechanical Processing of a Nickel-Base Superalloy Ingot Material. MSF 550, 129–140. https://doi.org/10.4028/www.scientific.net/MSF.550.129

Semiatin, S.L., Weaver, D.S., Kramb, R.C., Fagin, P.N., Glavicic, M.G., Goetz, R.L., Frey, N.D., Antony, M.M., 2004. Deformation and recrystallization behavior during hot working of a coarse-grain, nickel-base superalloy ingot material. Metall and Mat Trans A 35, 679–693. https://doi.org/10.1007/s11661-004-0379-y

Shackelford, J.F., 2015. Introduction to materials science for engineers, Eighth edition. ed. Pearson, Boston.

Shan, Y., Luo, X., Hu, X., Liu, S., 2011. Mechanisms of Solidification Structure Improvement of Ultra Pure 17 wt% Cr Ferritic Stainless Steel by Ti, Nb Addition. Journal of Materials Science & Technology 27, 352–358. https://doi.org/10.1016/S1005-0302(11)60073-X

Silva, E.S., Sousa, R.C., Jorge, A.M., Balancin, O., 2012. Hot deformation behavior of an Nb- and N-bearing austenitic stainless steel biomaterial. Materials Science and Engineering: A 543, 69–75. https://doi.org/10.1016/j.msea.2012.02.048

Sinclair, C.W., Hutchinson, C.R., Bréchet, Y., 2007. The Effect of Nb on the Recrystallization and Grain Growth of Ultra-High-Purity α-Fe: A Combinatorial Approach. Metall and Mat Trans A 38, 821–830. https://doi.org/10.1007/s11661-007-9106-9

Smagghe, G., 2017. Modélisation de la recristallisation lors du forgeage à chaud de l’acier 304L – une approche semi-topologique pour les modèles en champs moyens.

Smith, C.S., Zener, C., 1948. Introduction to Grains, Phases, and Interfaces - an Interpretation of Microstructure. Metall Mater Trans A 175, 15–51. https://doi.org/10.1007/s11661-010-0215-5

Sohrabi, M.J., Mirzadeh, H., Rafiei, M., 2018. Solidification behavior and Laves phase dissolution during homogenization heat treatment of Inconel 718 superalloy. Vacuum 154, 235–243. https://doi.org/10.1016/j.vacuum.2018.05.019

Spittle, J.A., 2006. Columnar to equiaxed grain transition in as solidified alloys. International Materials Reviews 51, 247–269. https://doi.org/10.1179/174328006X102493

Stamborska, M., Lapin, J., 2018. Effect of anisotropic microstructure on high-temperature compression deformation of CoCrFeNi based complex concentrated alloy. km 55, 369–378. https://doi.org/10.4149/km_2017_6_369

Suutala, N., 1983. Effect of solidification conditions on the solidification mode in austenitic stainless steels. MTA 14, 191–197. https://doi.org/10.1007/BF02651615

Svyetlichnyy, D., 2023. Frontal cellular automata for modelling microstructure evolution: Computational complexity analysis. Computational Materials Science 230, 112478. https://doi.org/10.1016/j.commatsci.2023.112478

Tamura, K., Tajima, J., 2004. Optimization of open-die forging process design to ensure homogeneous grain size refinement of cast structures by three-dimensional rigid-plastic finite element analysis. Proceedings of the Institution of Mechanical Engineers, Part C: Journal of Mechanical Engineering Science 218, 931–946. https://doi.org/10.1243/0954406041991305

Tempelman, E., Shercliff, H., van Eyben, B.N., 2014. Chapter 6 - Forging of Metals, in: Tempelman, E., Shercliff, H., van Eyben, B.N. (Eds.), Manufacturing and Design. Butterworth-Heinemann, Boston, pp. 85–103. https://doi.org/10.1016/B978-0-08-099922-7.00006-8

Terhaar, J., Poppenhäger, J., Bokelmann, D., Schafstall, H., Kelkar, K., 2012. Considering the solidification structure of VAR ingots in the numerical simulation of the cogging process. 7th International Symposium on Superalloy 718 and Derivatives 2010 1, 13. https://doi.org/10.1002/9781118495223.ch4

Tikhonova, M., Belyakov, A., Kaibyshev, R., 2013. Strain-induced grain evolution in an austenitic stainless steel under warm multiple forging. Materials Science and Engineering: A 564, 413–422. https://doi.org/10.1016/j.msea.2012.11.088

Tikhonova, M., Kaibyshev, R., Belyakov, A., 2018. Microstructure and Mechanical Properties of Austenitic Stainless Steels after Dynamic and Post-Dynamic Recrystallization Treatment. Advanced Engineering Materials 20, 1700960. https://doi.org/10.1002/adem.201700960

Turner, T.J., Semiatin, S.L., 2011. Modeling large-strain deformation behavior and neighborhood effects during hot working of a coarse-grain nickel-base superalloy. Modelling Simul. Mater. Sci. Eng. 19, 065010. https://doi.org/10.1088/0965-0393/19/6/065010

Villanueva, D.M.E., Junior, F.C.P., Plaut, R.L., Padilha, A.F., 2006. Comparative study on sigma phase precipitation of three types of stainless steels: austenitic, superferritic and duplex. Materials Science and Technology 22, 1098–1104. https://doi.org/10.1179/174328406X109230

Viswanathan, S., Diran Apelian, Raymond J. Donahue, Babu DasGupta, Michael Gywn, John L. Jorstad, Raymond W. Monroe, Mahi Sahoo, Thomas E. Prucha, Daniel Twarog, 2008. Casting, 10th editon. ed, ASM Handbook. ASM International, Materials Park, Ohio.

Vitos, L., Nilsson, J.-O., Johansson, B., 2006. Alloying effects on the stacking fault energy in austenitic stainless steels from first-principles theory. Acta Materialia 54, 3821–3826. https://doi.org/10.1016/j.actamat.2006.04.013

Wang, J., Fu, P., Liu, H., Li, D., Li, Y., 2012. Shrinkage porosity criteria and optimized design of a 100-ton 30Cr2Ni4MoV forging ingot. Materials & Design, New Rubber Materials, Test Methods and Processes 35, 446–456. https://doi.org/10.1016/j.matdes.2011.09.056

Wang, L., Chen, C., Li, Z., Wang, Z., Lv, B., Zhang, F., 2021a. Orientation-dependent dynamic recrystallization of super austenitic stainless steels. Journal of Materials Research and Technology 15, 6769–6785. https://doi.org/10.1016/j.jmrt.2021.11.110

Wang, L., Li, Z., Hu, X., Lv, B., Chen, C., Zhang, F., 2021b. Hot deformation behavior and 3D processing map of super austenitic stainless steel containing 7Mo–0.46N–0.02Ce: Effect of the solidification direction orientation of columnar crystal to loading direction. Journal of Materials Research and Technology 13, 618–634. https://doi.org/10.1016/j.jmrt.2021.05.006

Wang, Q., Liu, X., Feng, Y., Wang, D., Zhang, W., Gu, D., Chen, H., Sun, L., Mao, C., Wang, K., 2024. Study on the grain evolution of austenitic steel for nuclear power during hot working based on large area EBSD mapping. Journal of Materials Research and Technology 30, 2551–2562. https://doi.org/10.1016/j.jmrt.2024.04.028

Wang, S., Yang, B., Zhang, M., Wu, H., Peng, J., Gao, Y., 2016a. Numerical simulation and experimental verification of microstructure evolution in large forged pipe used for AP1000 nuclear power plants. Annals of Nuclear Energy 87, 176–185. https://doi.org/10.1016/j.anucene.2015.07.042

Wang, S., Yu, X., Yang, B., Zhang, M., Wu, H., 2016b. FEM Analysis and Experimental Verification of the Integral Forging Process for AP1000 Primary Coolant Pipe. Metall and Mat Trans A 47, 5114–5124. https://doi.org/10.1007/s11661-016-3696-z

Wang, Y., Wang, J., Dong, J., Li, A., Li, Z., Xie, G., Lou, L., 2018. Hot deformation characteristics and hot working window of as-cast large-tonnage GH3535 superalloy ingot. Journal of Materials Science & Technology 34, 2439–2446. https://doi.org/10.1016/j.jmst.2018.04.001

Weaver, D.S., Semiatin, S.L., 2007. Recrystallization and grain-growth behavior of a nickel-base superalloy during multi-hit deformation. Scripta Materialia 57, 1044–1047. https://doi.org/10.1016/j.scriptamat.2007.07.033

Weis, M.J., Mataya, M.C., Thompson, S.W., Matlock, D.K., 1989. The Hot Deformation Behavior of an As-Cast Alloy 718 Ingot, in: Superalloys 718 Metallurgy and Applications (1989). Presented at the Superalloys, TMS, pp. 135–154. https://doi.org/10.7449/1989/Superalloys_1989_135_154

Wenhui, Z., Shuhua, S., Deli, Z., Baozhong, W., Zhenhua, W., Wantang, F., 2011. Hot deformation behavior of a Nb-containing 316LN stainless steel. Materials & Design 32, 4173–4179. https://doi.org/10.1016/j.matdes.2011.04.043

Wolfgarten, M., Rosenstock, D., Rudolph, F., Hirt, G., 2019. New approach for the optimization of pass-schedules in open-die forging. Int J Mater Form 12, 973–983. https://doi.org/10.1007/s12289-019-01471-w

Wu, X., Jing, X., Xiao, H., Ouyang, S., Tang, A., Peng, P., Feng, B., Rashad, M., She, J., Chen, X., Zheng, K., Pan, F., 2022. Controlling grain size and texture in Mg–Zn–Mn alloys from the interaction of recrystallization and precipitation. Journal of Materials Research and Technology 21, 1395–1407. https://doi.org/10.1016/j.jmrt.2022.09.108

Xie, A., Chen, S., Wu, Y., Jiang, H., Rong, L., 2022. Homogenization temperature dependent microstructural evolution and mechanical properties in a Nb-stabilized cast austenitic stainless steel. Materials Characterization 194, 112384. https://doi.org/10.1016/j.matchar.2022.112384

Yang, X., He, A., Wu, C., Li, S., Zhang, H., Wang, X., 2015. Study of Static Recrystallization Behavior of a Nitrogen-Alloyed Ultralow Carbon Austenitic Stainless Steel by Experiment and Simulation. J. of Materi Eng and Perform 24, 4346–4357. https://doi.org/10.1007/s11665-015-1705-9

Yanushkevich, Z., Belyakov, A., Kaibyshev, R., 2015. Microstructural evolution of a 304-type austenitic stainless steel during rolling at temperatures of 773–1273K. Acta Materialia 82, 244–254. https://doi.org/10.1016/j.actamat.2014.09.023

Yeom, J.T., Lee, C.S., Kim, J.H., Park, N.-K., 2007. Finite-element analysis of microstructure evolution in the cogging of an Alloy 718 ingot. Materials Science and Engineering: A, Proceedings of the 12th International Conference on Rapidly Quenched & Metastable Materials 449–451, 722–726. https://doi.org/10.1016/j.msea.2006.02.415

Yu, H., Meng, Q., Ning, Y., Wang, Z., Huang, S., Zhang, W., 2024. Microstructure control and DRX characteristics of Ni–Co–W superalloys affected by changing deformation direction on [001] columnar grain. Journal of Materials Research and Technology 33, 785–795. https://doi.org/10.1016/j.jmrt.2024.09.110

Yu, Q.Y., Yao, Z.H., Dong, J.X., 2015. Deformation and recrystallization behavior of a coarse-grain, nickel-base superalloy Udimet720Li ingot material. Materials Characterization 107, 398–410. https://doi.org/10.1016/j.matchar.2015.07.035

Zener, C., Hollomon, J.H., 1944. Effect of Strain Rate Upon Plastic Flow of Steel. Journal of Applied Physics 15, 22–32. https://doi.org/10.1063/1.1707363

Zhang, H.Y., Zhang, S.H., Li, Z.X., Cheng, M., 2010. Hot die forging process optimization of superalloy IN718 turbine disc using processing map and finite element method. Proceedings of the Institution of Mechanical Engineers, Part B: Journal of Engineering Manufacture 224, 103–110. https://doi.org/10.1243/09544054JEM1571

Zhang, R., He, J., Xu, S., Zhang, F., Wang, X., 2023. The Optimized Homogenization Process of Cast 7Mo Super Austenitic Stainless Steel. Materials 16, 3438. https://doi.org/10.3390/ma16093438

Zhang, W., Zhang, J., Han, Y., Liu, R., Zou, D., Qiao, G., 2016. Metadynamic Recrystallization Behavior of As-cast 904L Superaustenitic Stainless Steel. J. Iron Steel Res. Int. 23, 151–159. https://doi.org/10.1016/S1006-706X(16)30027-9

Zhang, Y., Yang, J., 2018. Formation of Nb(C,N) Carbonitride in Cast Austenitic Heat-Resistant Steel during Directional Solidification under Different Withdraw Rates. Materials (Basel) 11. https://doi.org/10.3390/ma11122397

Zhang, Z., Liu, Y., Liang, X., She, Y., 2008. The effect of Nb on recrystallization behavior of a Nb micro-alloyed steel. Materials Science and Engineering: A 474, 254–260. https://doi.org/10.1016/j.msea.2007.04.041

Zhao, G., Tian, Y., Li, H., Ma, L., Li, Y., Li, J., 2024. Microstructure evolution and dynamic recrystallization mechanisms of 316L stainless steel during hot deformation. Archiv.Civ.Mech.Eng 24, 35. https://doi.org/10.1007/s43452-023-00844-y

Appendix A - Records of the forging experiments on intermediate industrial scale ingots

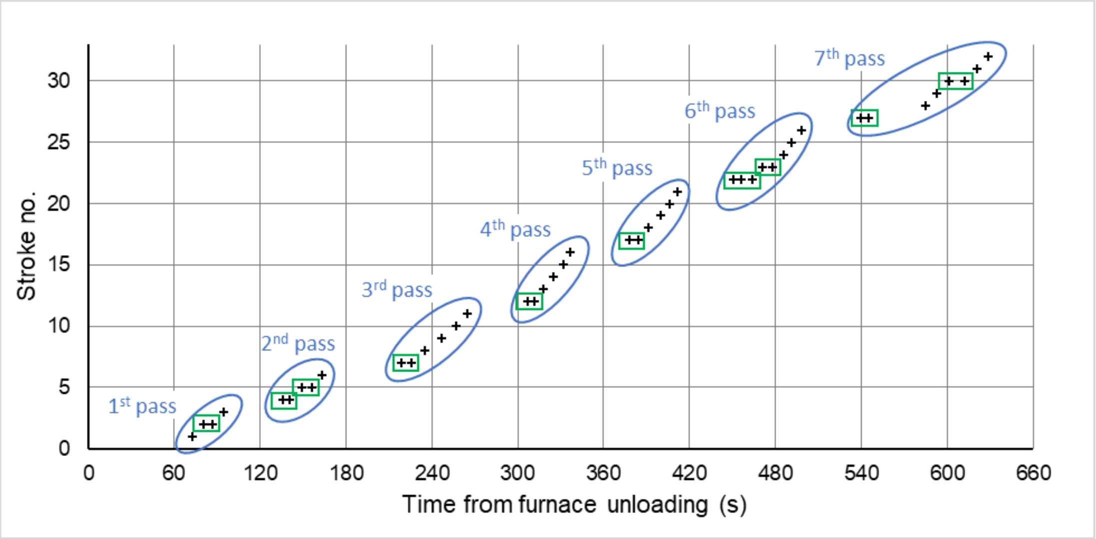

Figure A.1 : Experimental time records of the forging operations performed on the 316L ingot during the cogging C1; with the different passes highlighted by the blue circles, and the strokes achieved after several hits by the green rectangles.

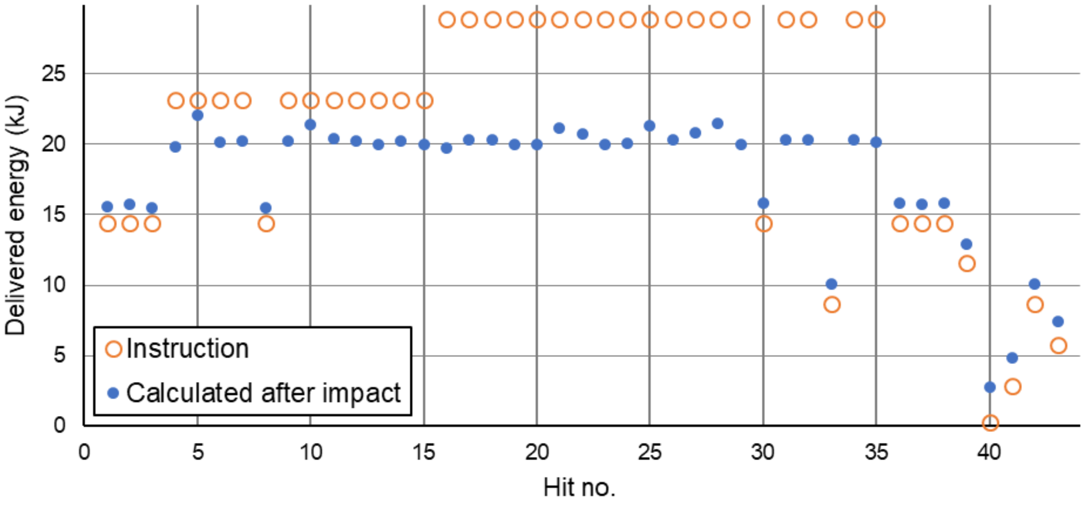

Figure A.2 : Plots of the energy instructions and post-forging calculations for the 316L ingot during the cogging C1. The calculated values were calculated using the speed records of the press, at the impact with the ingot.

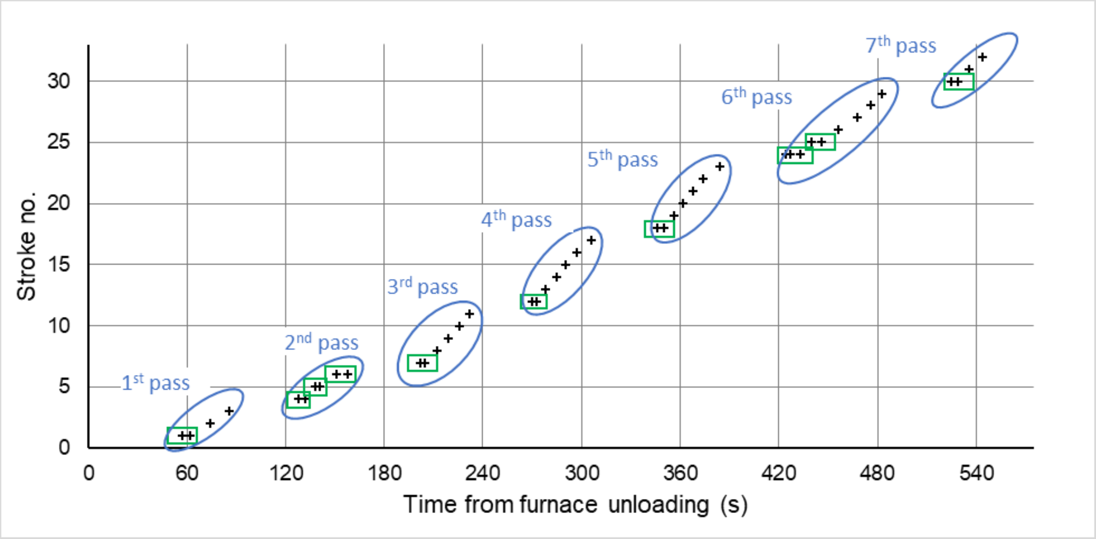

Figure A.3 : Experimental time records of the forging operations performed on the 316L ingot during the 1st cogging stage of the cogging C2; with the different passes highlighted by the blue circles, and the strokes achieved after several hits by the green rectangles.

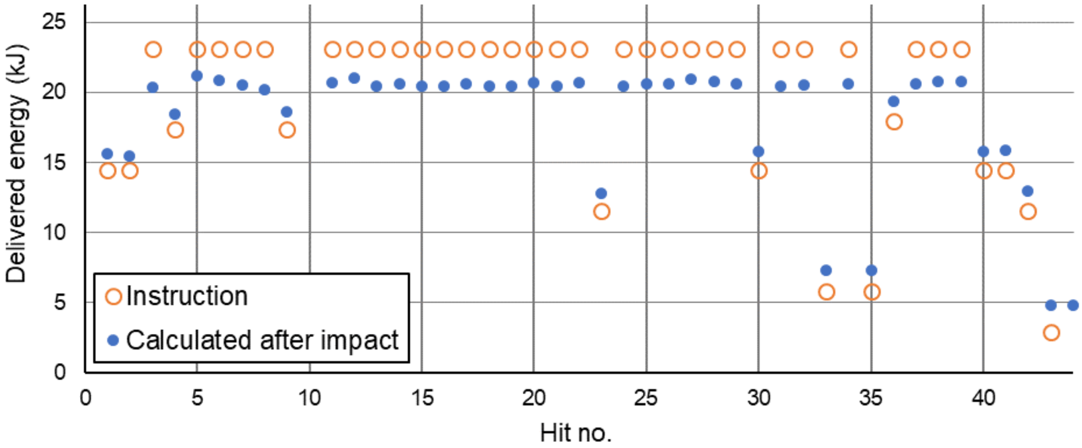

Figure A.4 : Plots of the energy instructions and post-forging calculations for the 316L ingot during the 1st cogging stage of the cogging C2. The calculated values were calculated using the speed records of the press, at the impact with the ingot.

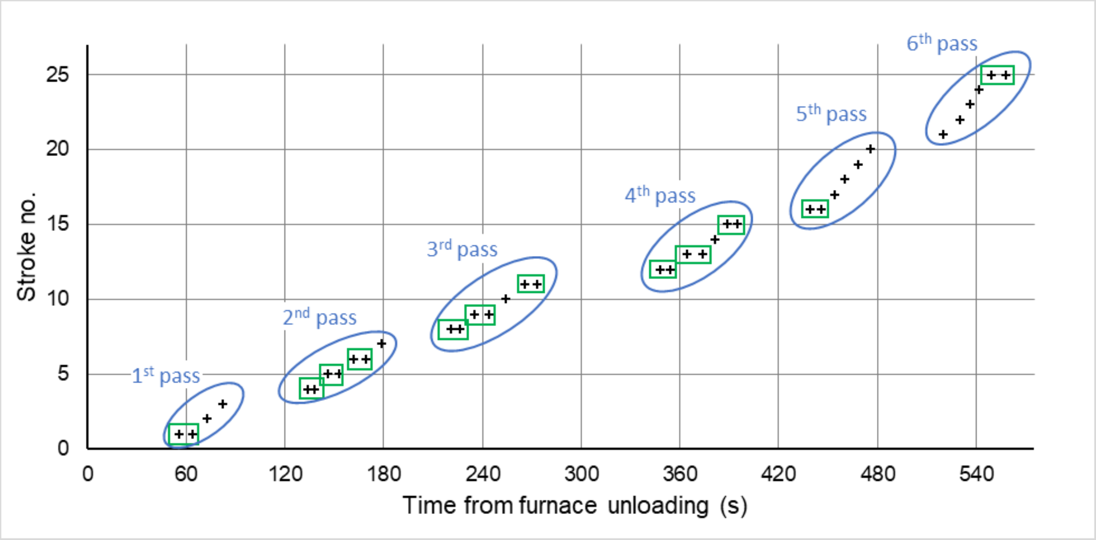

Figure A.5 : Experimental time records of the forging operations performed on the 316L ingot during the 2nd cogging stage of the cogging C2; with the different passes highlighted by the blue circles, and the strokes achieved after several hits by the green rectangles.

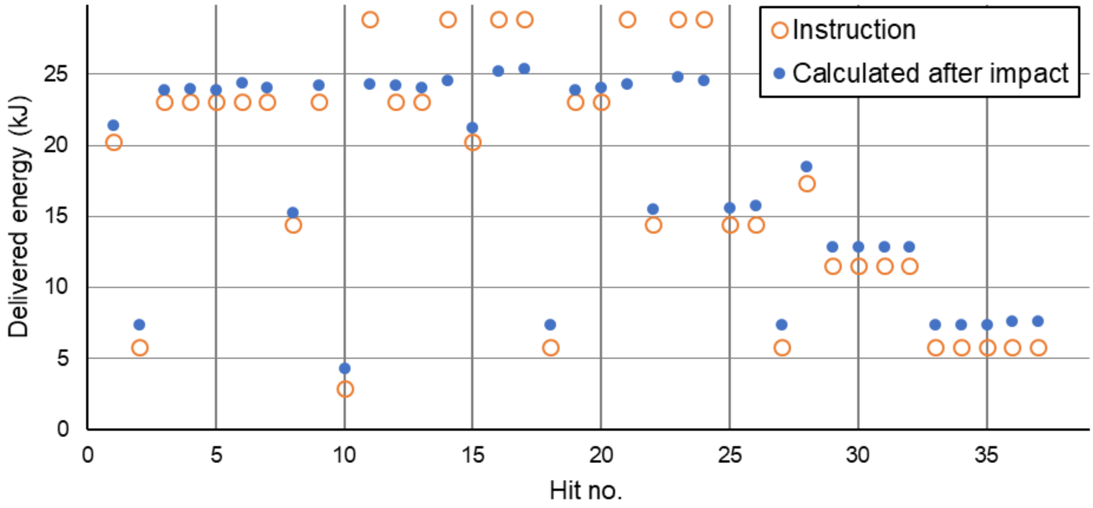

Figure A.6 : Plots of the energy instructions and post-forging calculations for the 316L ingot during the 2nd cogging stage of the cogging C2. The calculated values were calculated using the speed records of the press, at the impact with the ingot.

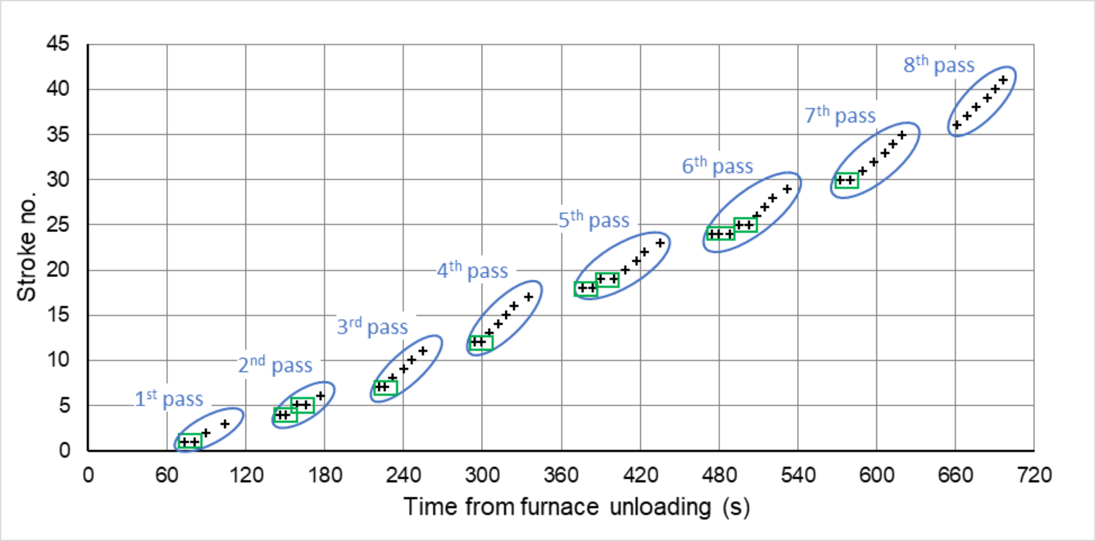

Figure A.7 : Experimental time records of the forging operations performed on the 316Nb ingot during the cogging C1; with the different passes highlighted by the blue circles, and the strokes achieved after several hits by the green rectangles.

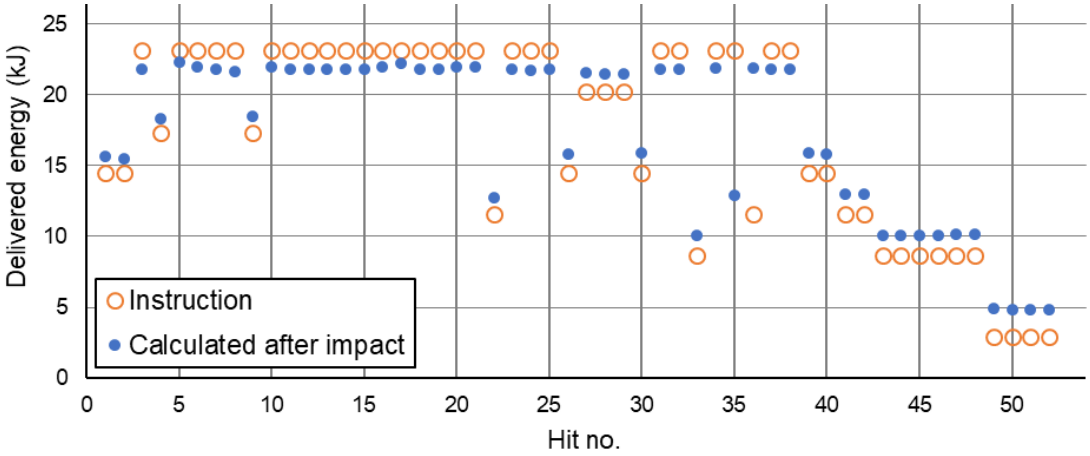

Figure A.8 : Plots of the energy instructions and post-forging calculations for the 316Nb ingot during the cogging C1. The calculated values were calculated using the speed records of the press, at the impact with the ingot.

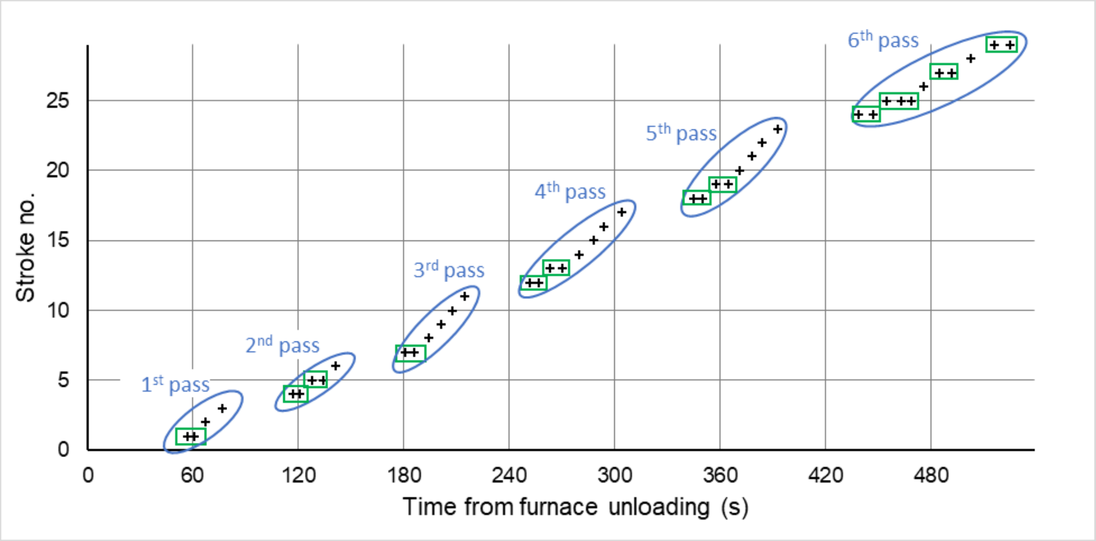

Figure A.9 : Experimental time records of the forging operations performed on the 316Nb ingot during the 1st cogging stage of the cogging C2; with the different passes highlighted by the blue circles, and the strokes achieved after several hits by the green rectangles.

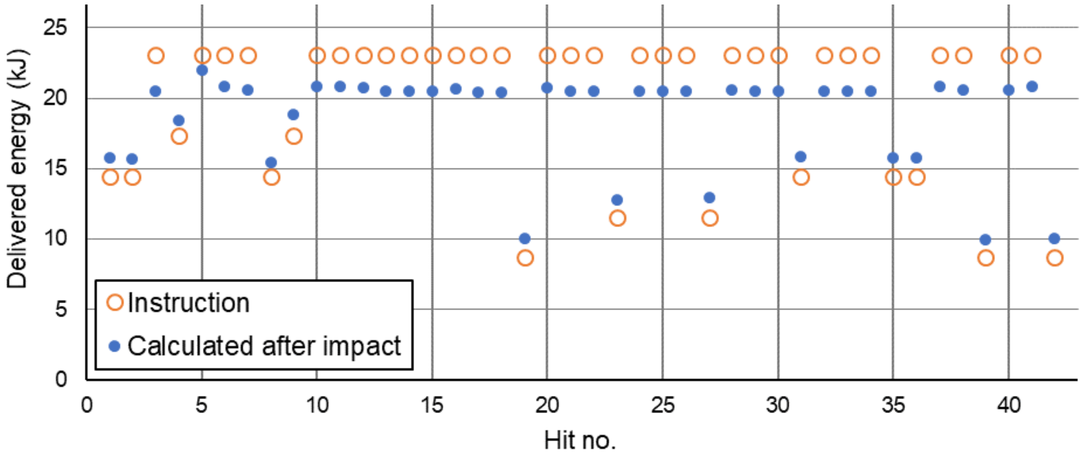

Figure A.10 : Plots of the energy instructions and post-forging calculations for the 316Nb ingot during the 1st cogging stage of the cogging C2. The calculated values were calculated using the speed records of the press, at the impact with the ingot.

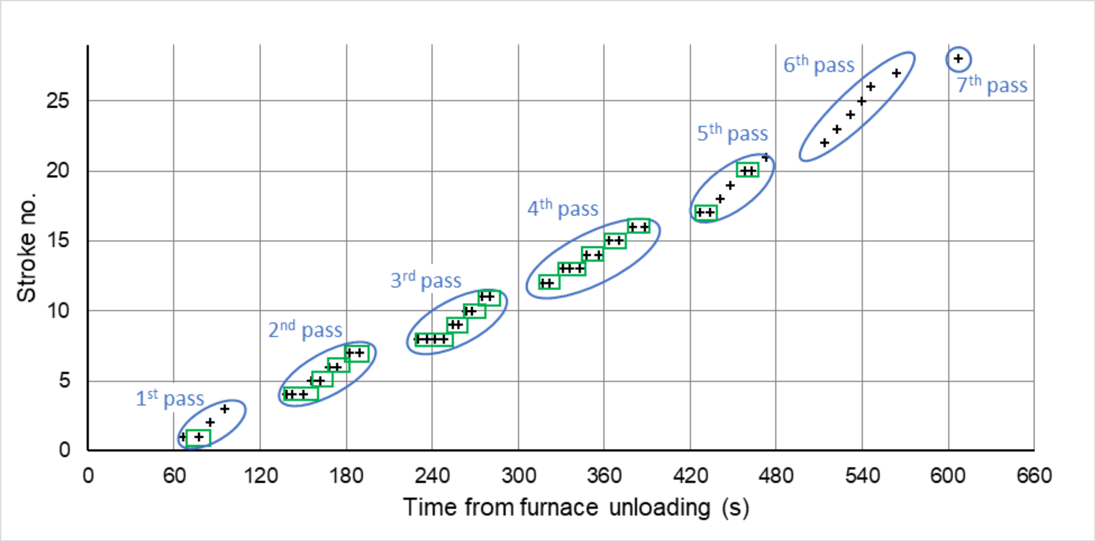

Figure A.11 : Experimental time records of the forging operations performed on the 316Nb ingot during the 2nd cogging stage of the cogging C2; with the different passes highlighted by the blue circles, and the strokes achieved after several hits by the green rectangles.

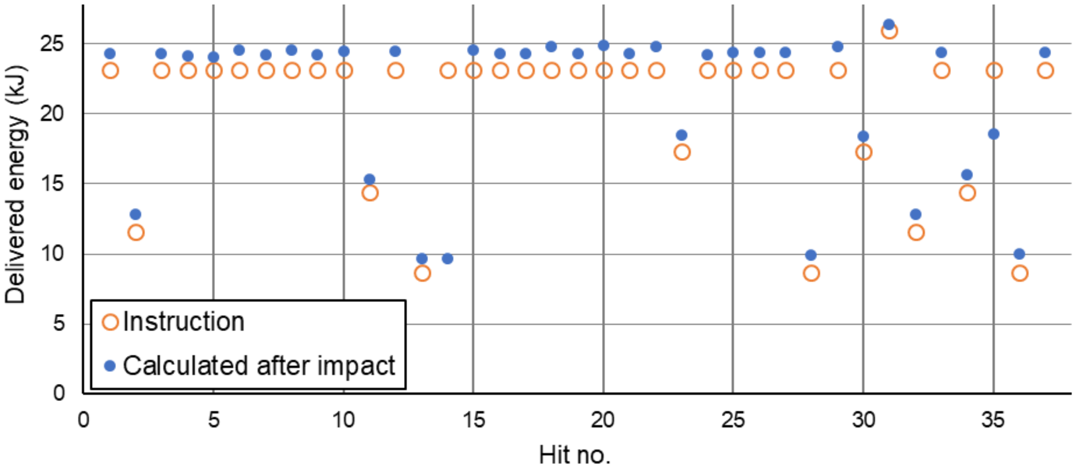

Figure A.12 : Plots of the energy instructions and post-forging calculations for the 316Nb ingot during the 2nd cogging stage of the cogging C2. The calculated values were calculated using the speed records of the press, at the impact with the ingot.

Appendix B - In-house image processing software developed for quantitative microstructure analyses

Appendix B gives more detail on the innovative image processing analysis software developed using the commercial software Matlab R2018a® for the quantitative analysis of resulting microstructures. Figure B.1 shows the algorithm used for the segmentation of grain boundaries, and screenshots of the graphical user interface of the developed software are shown in Figures B.2, B.3, and B.4.

```
function [WS_Img, WS_rgb, GB_Img, Grain_Img, WS_GB_Overlay, SegFctn,
Seg_ParamTable] = Segmentation(Img2Segment, SegParam_GF,
SegParam_StrlFctn, SegParam_StrlSize, SegParam_RegMrk)

%% Sequential image optimisation
    %- “Bottom” & “top” hat filtering
    se_pp = strel(SegParam_StrlFctn, SegParam_StrlSize);
    ImgTop = imtophat(Img2Segment, se_pp);
    ImgBot = imbothat(Img2Segment, se_pp);
    ppi_1 = imsubtract(imadd(ImgTop, Img2Segment), ImgBot);

    %- Gaussian filtering
    ppi_2 = imgaussfilt(ppi_1, SegParam_GF);

%% Mark “background objects”: grain boundaries
    bgm1 = imcomplement(ppi_2);

%% Mark “foreground objects”: grains
    se_fgm = strel(‘disk’, 1);
    fgm1 = imclose(bgm1, se_fgm);
    fgm2 = imerode(fgm1, se_fgm);
    fgm3 = imadd(imextendedmin(fgm1, SegParam_RegMrk), imextendedmin(fgm2,
    SegParam_RegMrk));

%% Definition of the segmentation function
    SegFctn = imimposemin(bgm1, fgm3);

%% Watershed transform of the segmentation function
    clear WS_img; clear Lrgb;
    WS_Img = watershed(SegFctn);

%% Create resulting images
    WS_rgb = label2rgb(WS_Img, ‘jet’, [0 0 0], ‘shuffle’);
    GB_Img = imdilate(WS_Img == 0, ones(1,1));
    Grain_Img = imcomplement(GB_Img);
    try
        WS_GB_Overlay  =  labeloverlay(Img2Segment,  GB_Img,  ‘Colormap’,
        ‘autumn’);
    catch
        [ImgHeight_pixel, ImgWidth_pixel, ~] = size(Img2Segment);
        WS_GB_Overlay = 255 * ones(ImgHeight_pixel, ImgWidth_pixel);
    End

End
```

Figure B.1 : Algorithm implemented in Matlab R2018a® for segmenting the grain boundaries from OM micrographs.

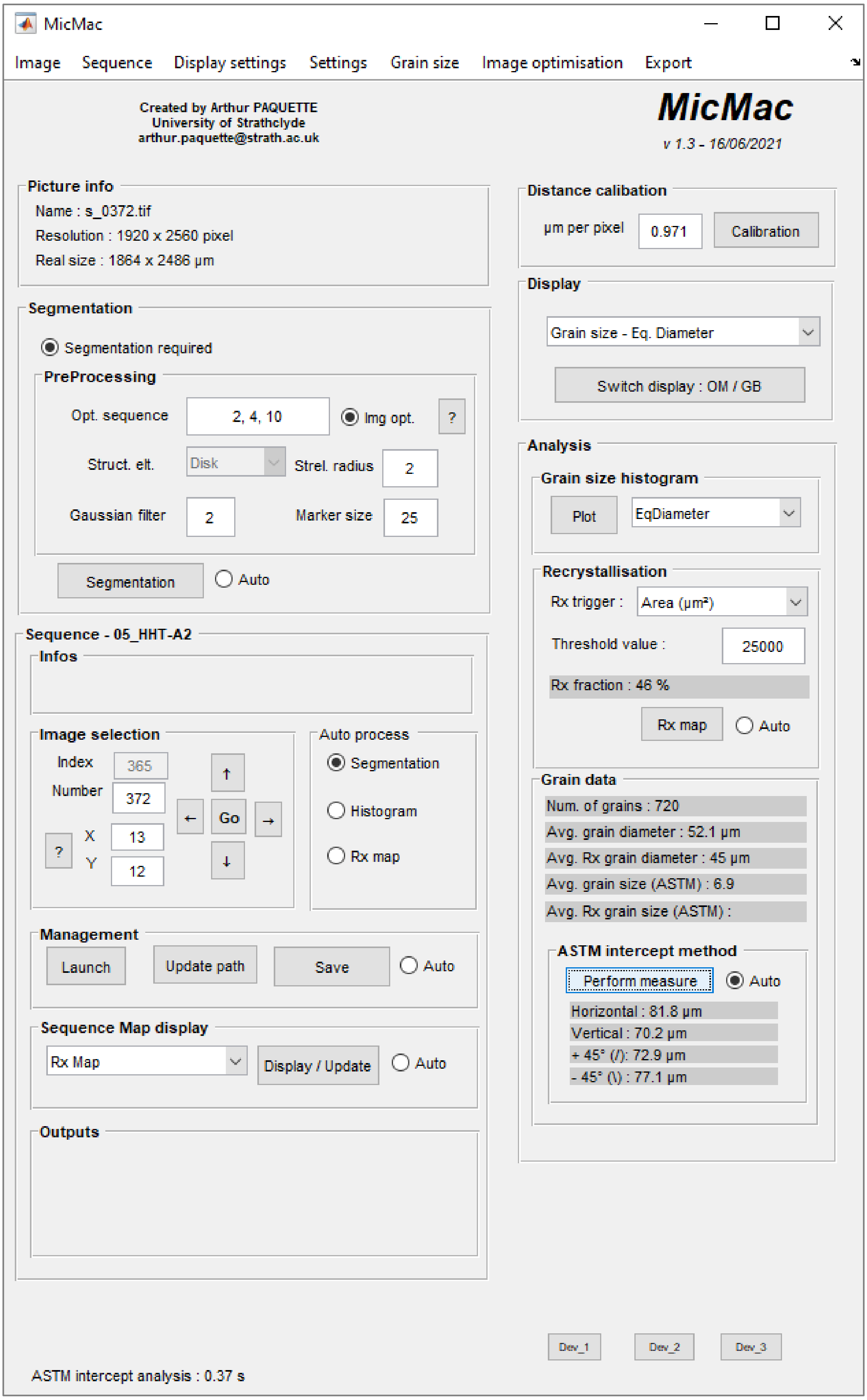

Created by Arthur PAQUETTE
University of Strathclyde
arthur.paquette@strath.ac.uk

MicMac
v 1.3 - 16/06/2021

Picture info
Name : s_0372.tif
Resolution : 1920 x 2560 pixel
Real size : 1864 x 2486 µm

Segmentation
● Segmentation required

PreProcessing
Opt. sequence: 2, 4, 10 ● Img opt.
Struct. elt.: Disk
Strel. radius: 2
Gaussian filter: 2
Marker size: 25
○ Auto

Sequence - 05_HHT-A2
Infos

Image selection
Index: 365
Number: 372
X: 13
Y: 12

Auto process
● Segmentation
○ Histogram
○ Rx map

Management
○ Auto

Sequence Map display
Rx Map
○ Auto

Outputs

Distance calibration
µm per pixel: 0.971

Display
Grain size - Eq. Diameter

Analysis

Grain size histogram
EqDiameter

Recrystallisation
Rx trigger : Area (µm²)
Threshold value : 25000
Rx fraction : 46 %
○ Auto

Grain data
Num. of grains : 720
Avg. grain diameter : 52.1 µm
Avg. Rx grain diameter : 45 µm
Avg. grain size (ASTM) : 6.9
Avg. Rx grain size (ASTM) :

ASTM intercept method
● Auto
Horizontal : 81.8 µm
Vertical : 70.2 µm
+ 45° (/): 72.9 µm
- 45° (\) : 77.1 µm

ASTM intercept analysis : 0.37 s

Figure B.2 : A screenshot of the graphical user interface of the in-house software developed for the quantitative analysis of resulting microstructures.

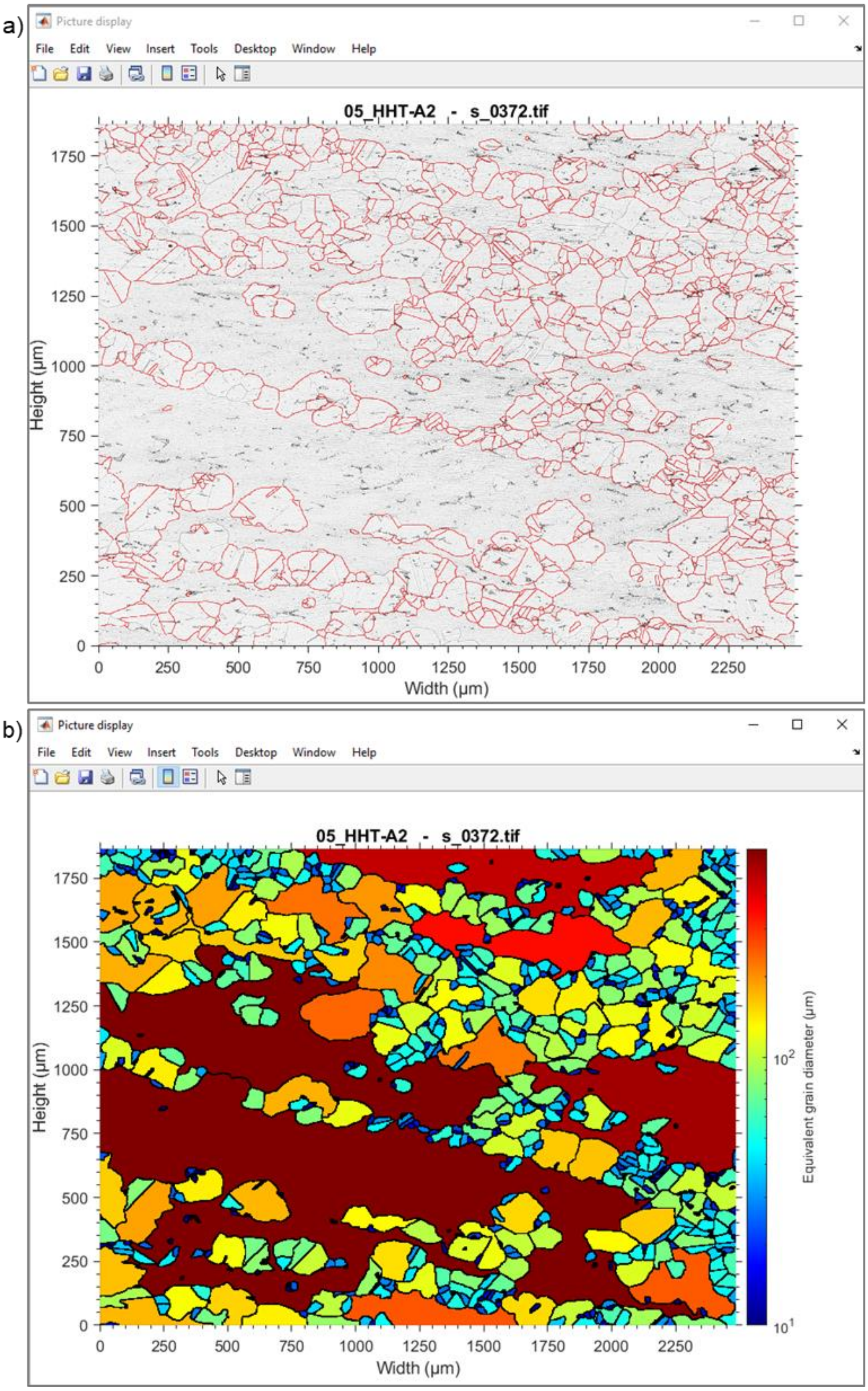

Figure B.3 : Screenshots of the windows used to display segmentation and results of quantitative analyses: a) an optical micrograph with the identified grain boundaries highlighted, and b) with the grains coloured according to their equivalent diameter (µm).

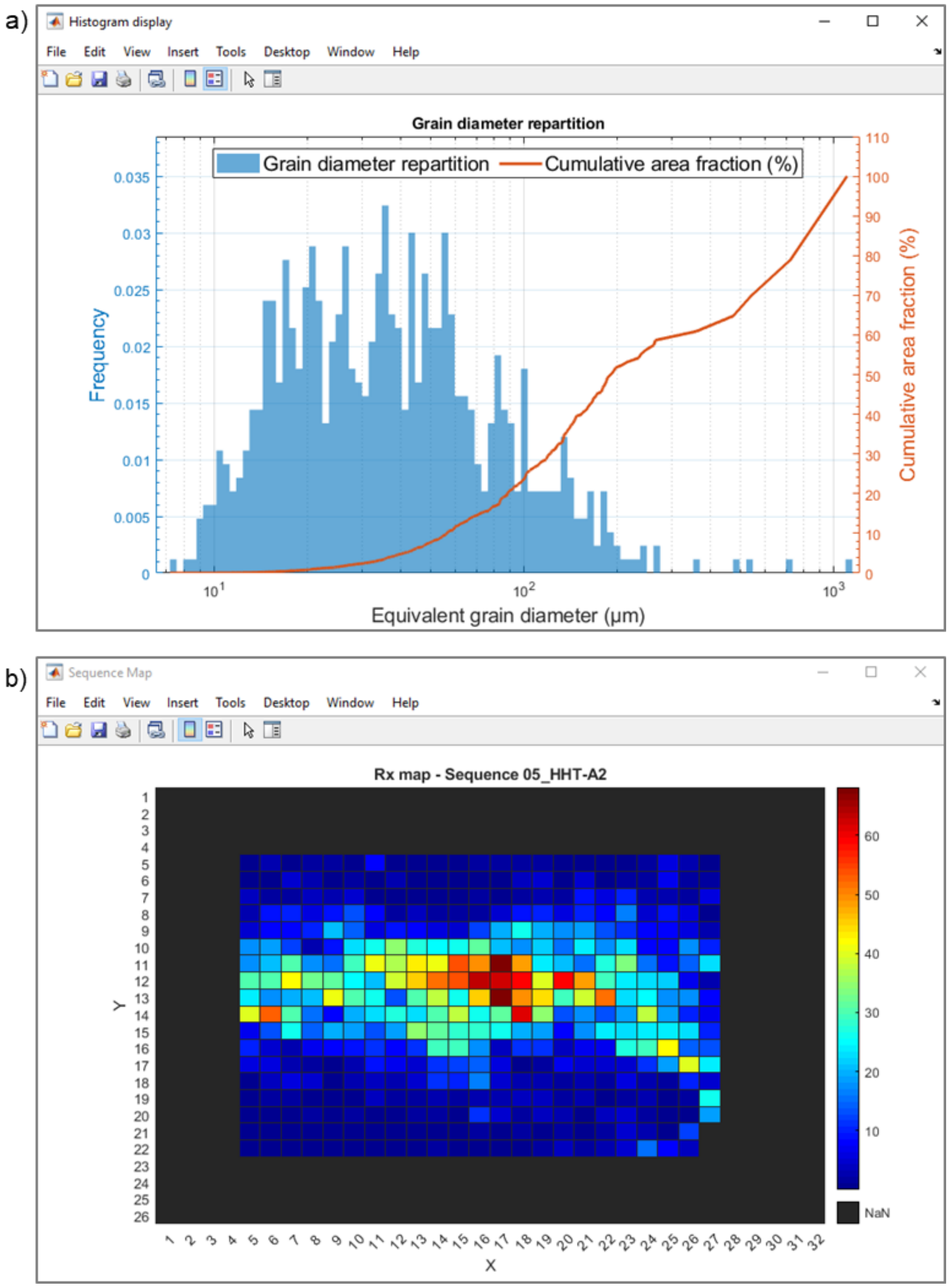

Figure B.4 : Screenshots of the windows used to display segmentation and results of quantitative analyses: a) plots of the frequency of equivalent grain diameter and associated cumulative area fraction, and b) heat maps of the fraction of recrystallised grains across the transverse cross-section of the sample.

Appendix C - Detailed geometry of the Ø 60×60 mm sample after upsetting

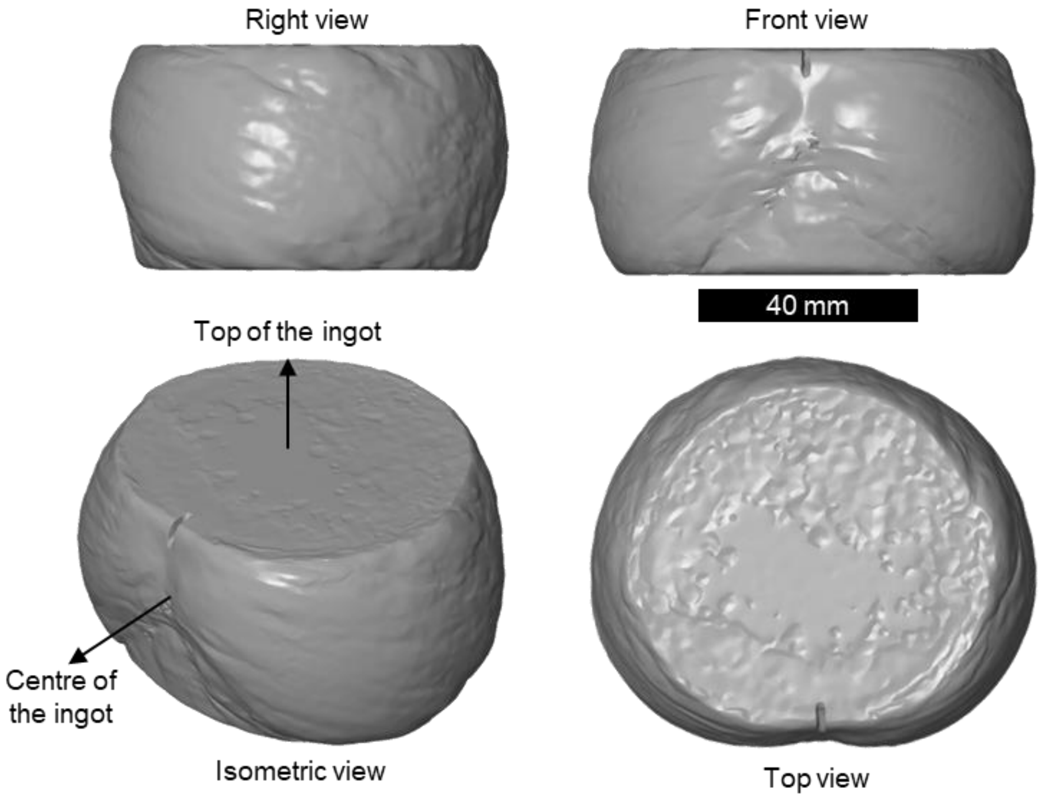

Figure C.1 : 3D model obtained by GOM ATOS® of the axial 316L sample after upsetting using the hydraulic press.

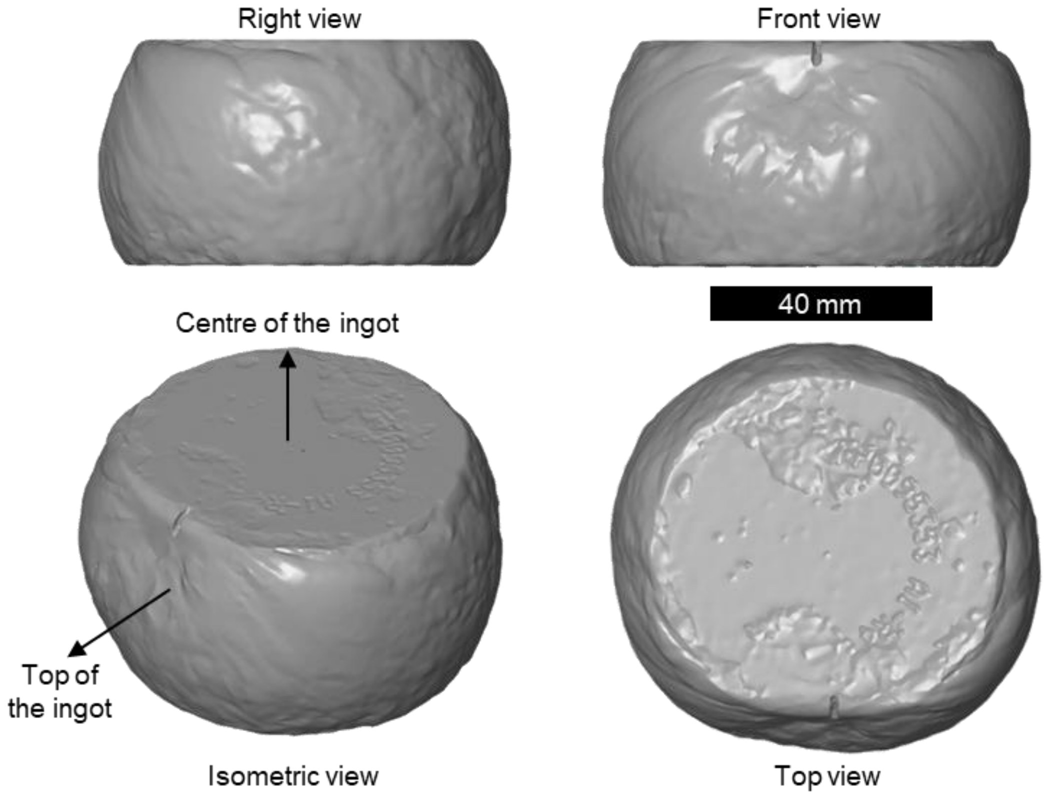

Figure C.2 : 3D model obtained by GOM ATOS® of the radial 316L sample after upsetting using the hydraulic press.

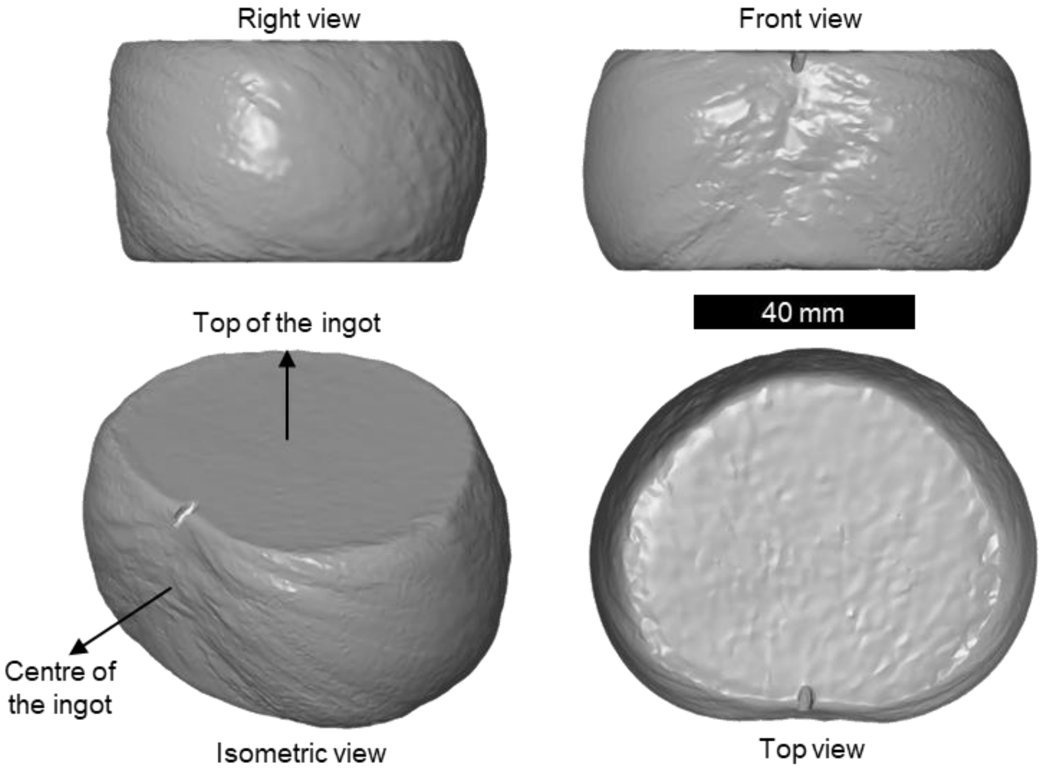

Figure C.3 : 3D model obtained by GOM ATOS® of the axial 316Nb sample after upsetting using the hydraulic press.

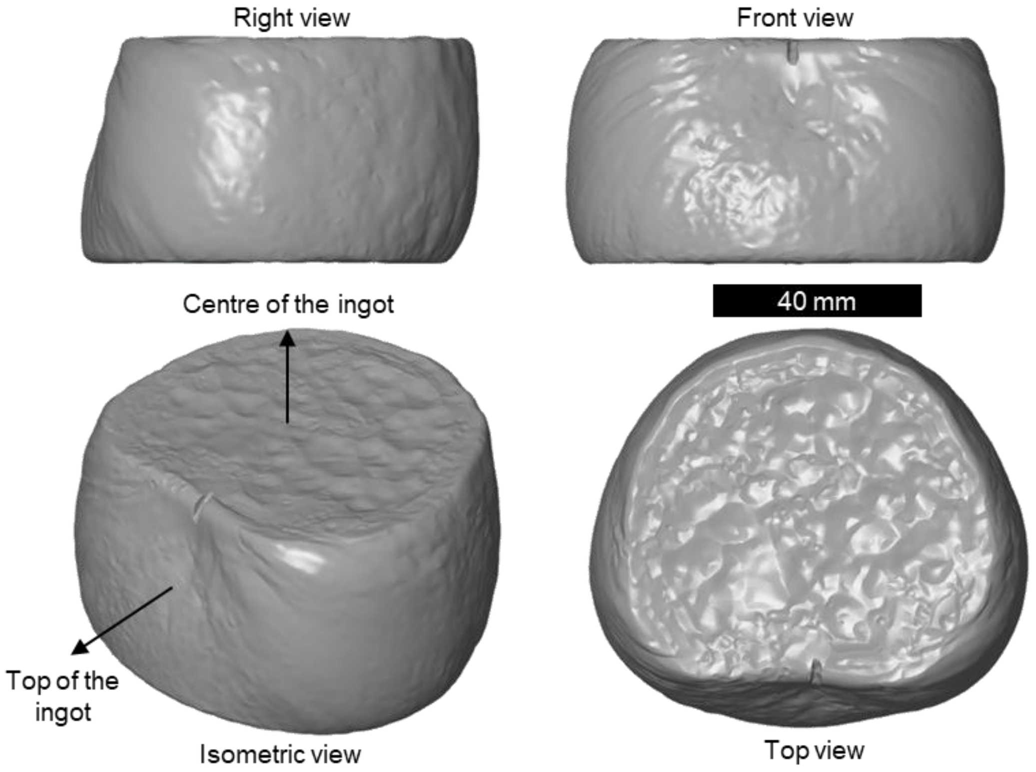

Figure C.4 : 3D model obtained by GOM ATOS® of the radial 316Nb sample after upsetting using the hydraulic press.

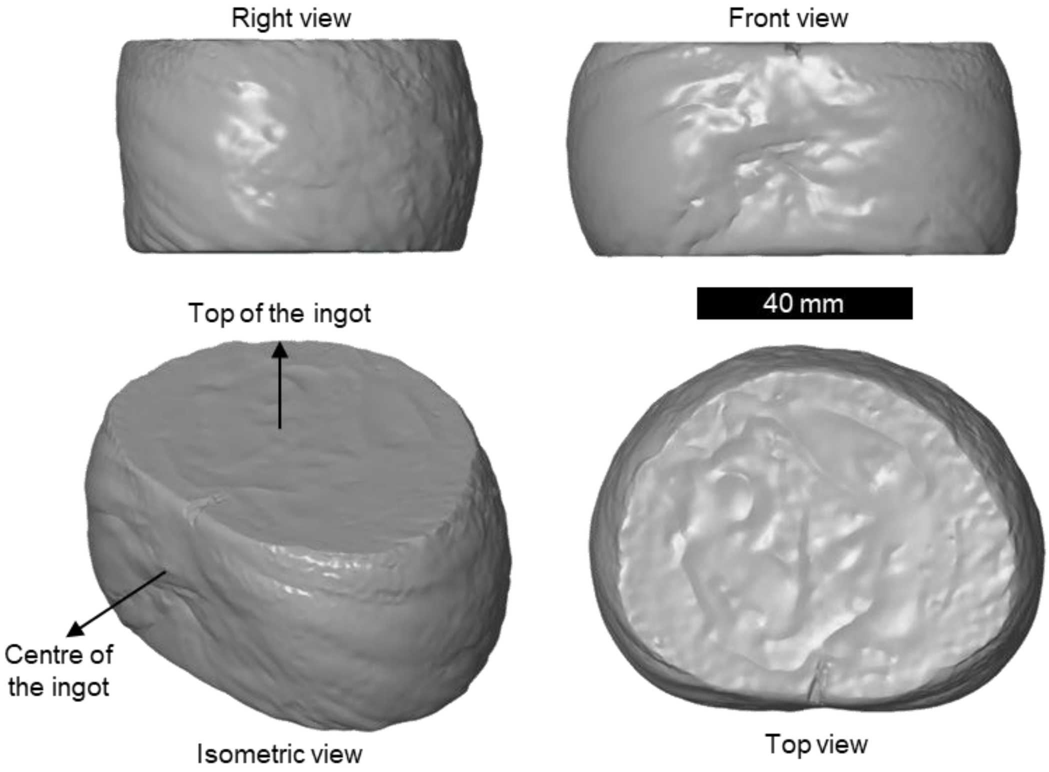

Figure C.5 : 3D model obtained by GOM ATOS® of the axial 316L sample after upsetting using the screw press.

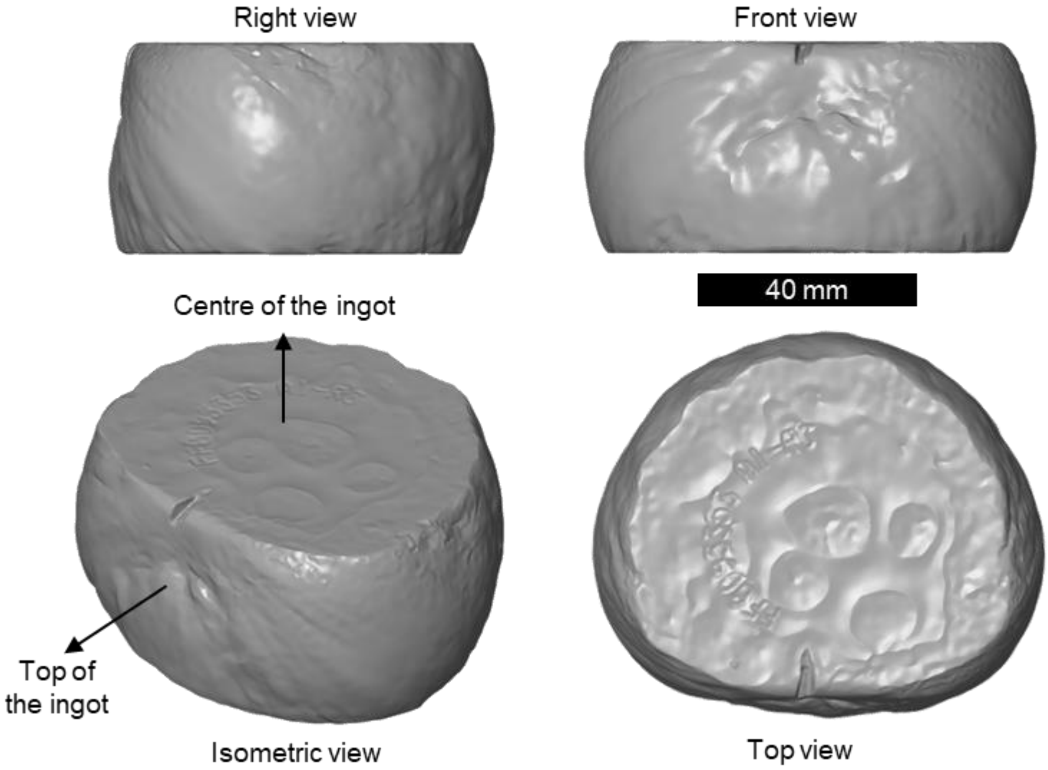

Figure C.6 : 3D model obtained by GOM ATOS® of the radial 316L sample after upsetting using the screw press.

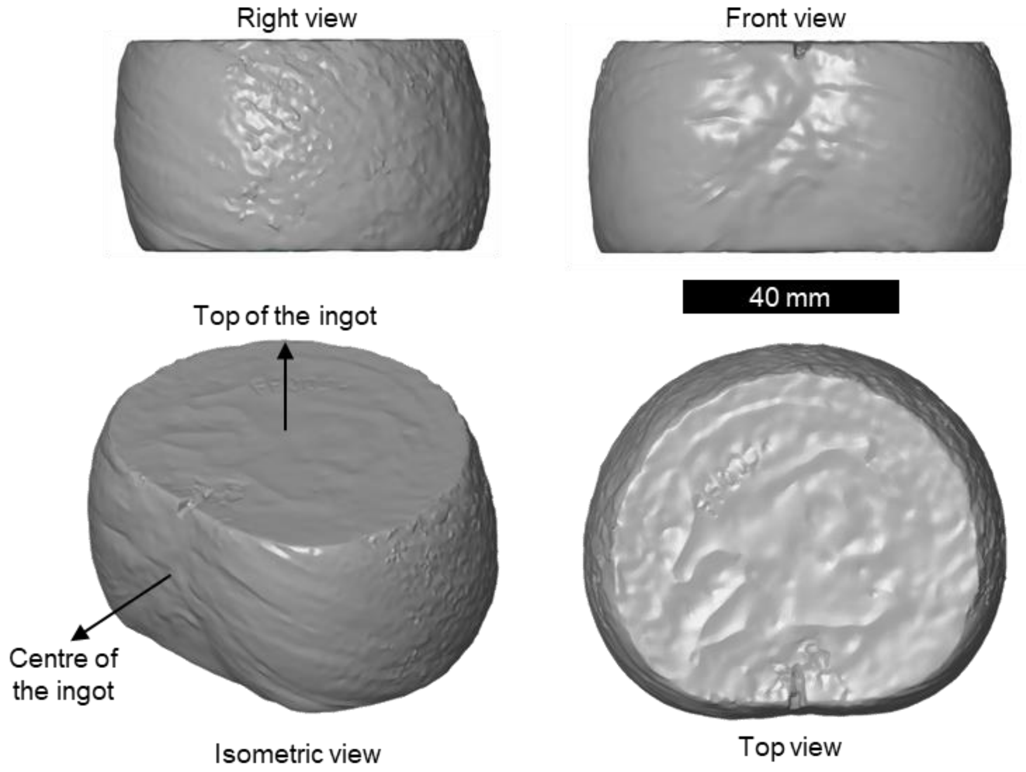

Figure C.7 : 3D model obtained by GOM ATOS® of the axial 316Nb sample after upsetting using the screw press.

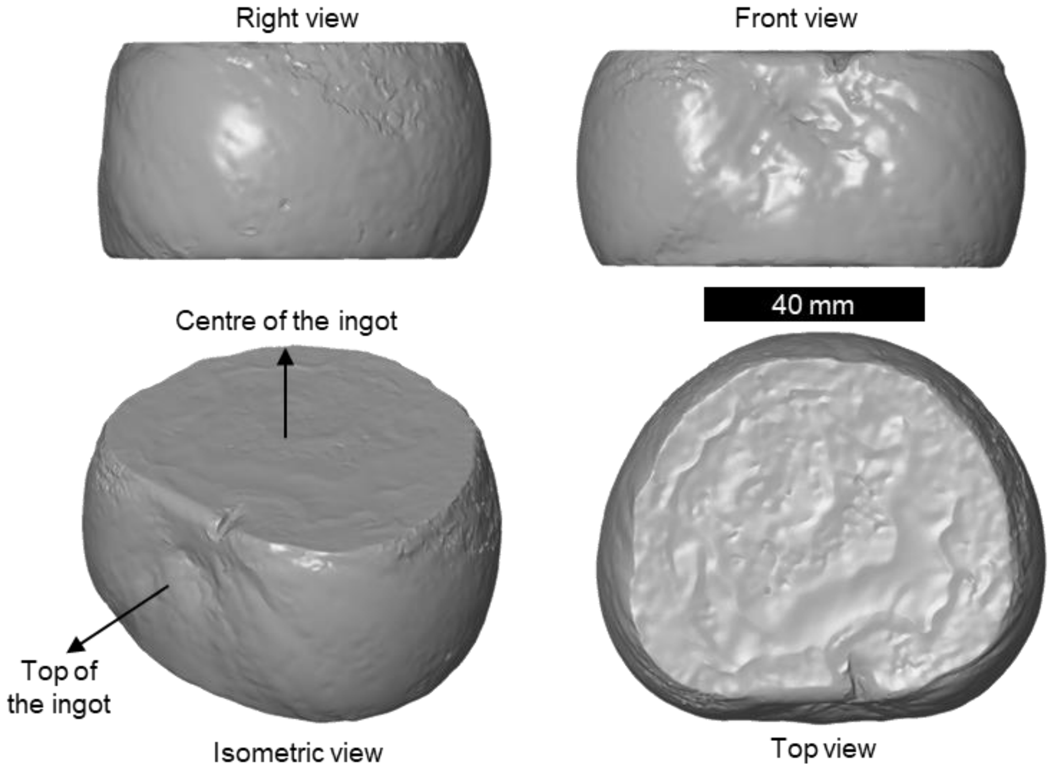

Figure C.8 : 3D model obtained by GOM ATOS® of the radial 316Nb sample after upsetting using the screw press.

Appendix D - Microstructure in the Ø 60×60 mm samples after upsetting

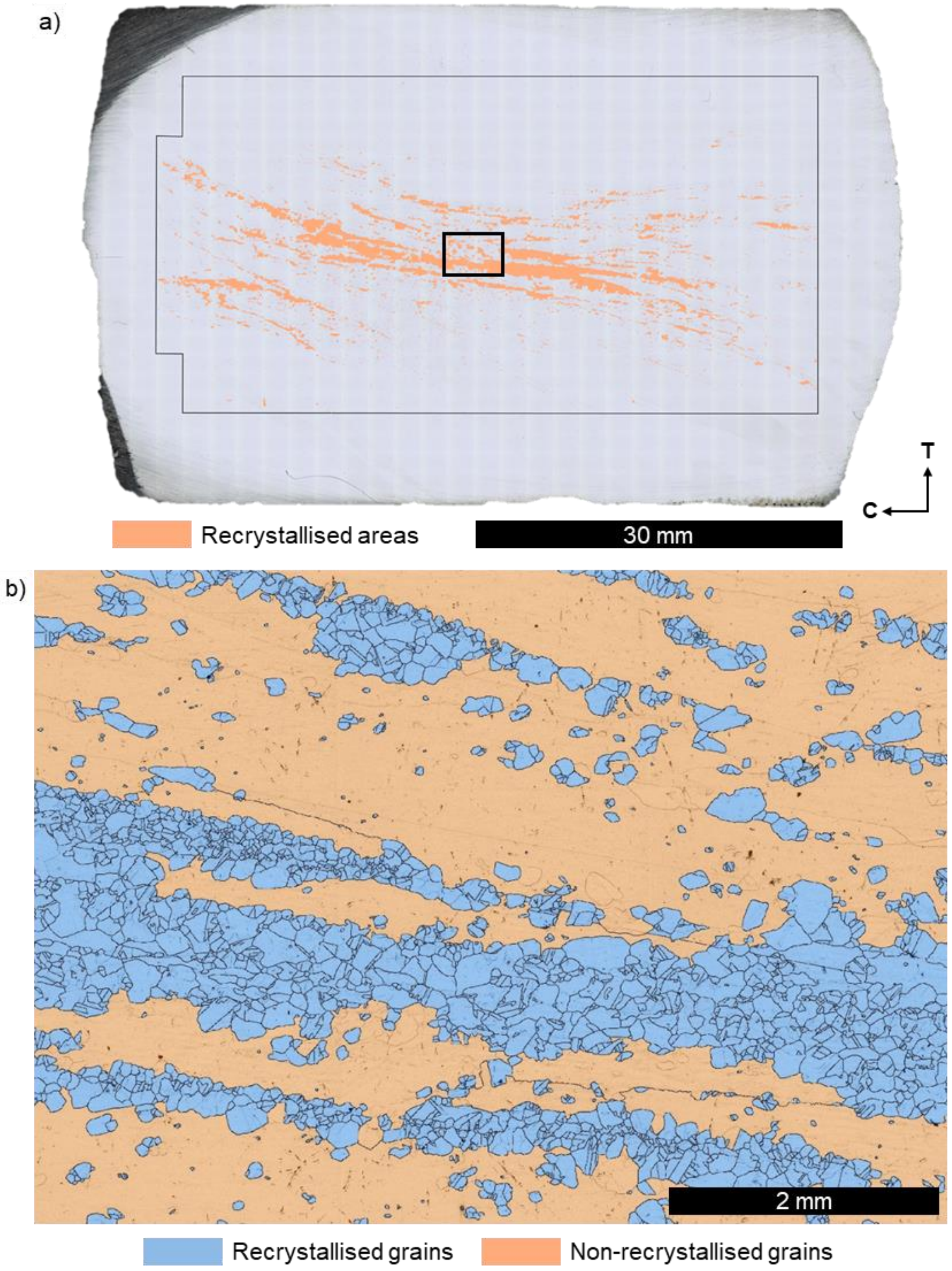

Figure D.1 : a) Reconstructed image of the longitudinal cross-section of the axial 316L sample after 30% upsetting at 1250 °C using the hydraulic press with the areas underwent recrystallisation superimposed, and b) microstructure detail in the high strain zone (i.e., see the solid rectangle in a)) with recrystallised (blue) and non-recrystallised (orange) grains highlighted.

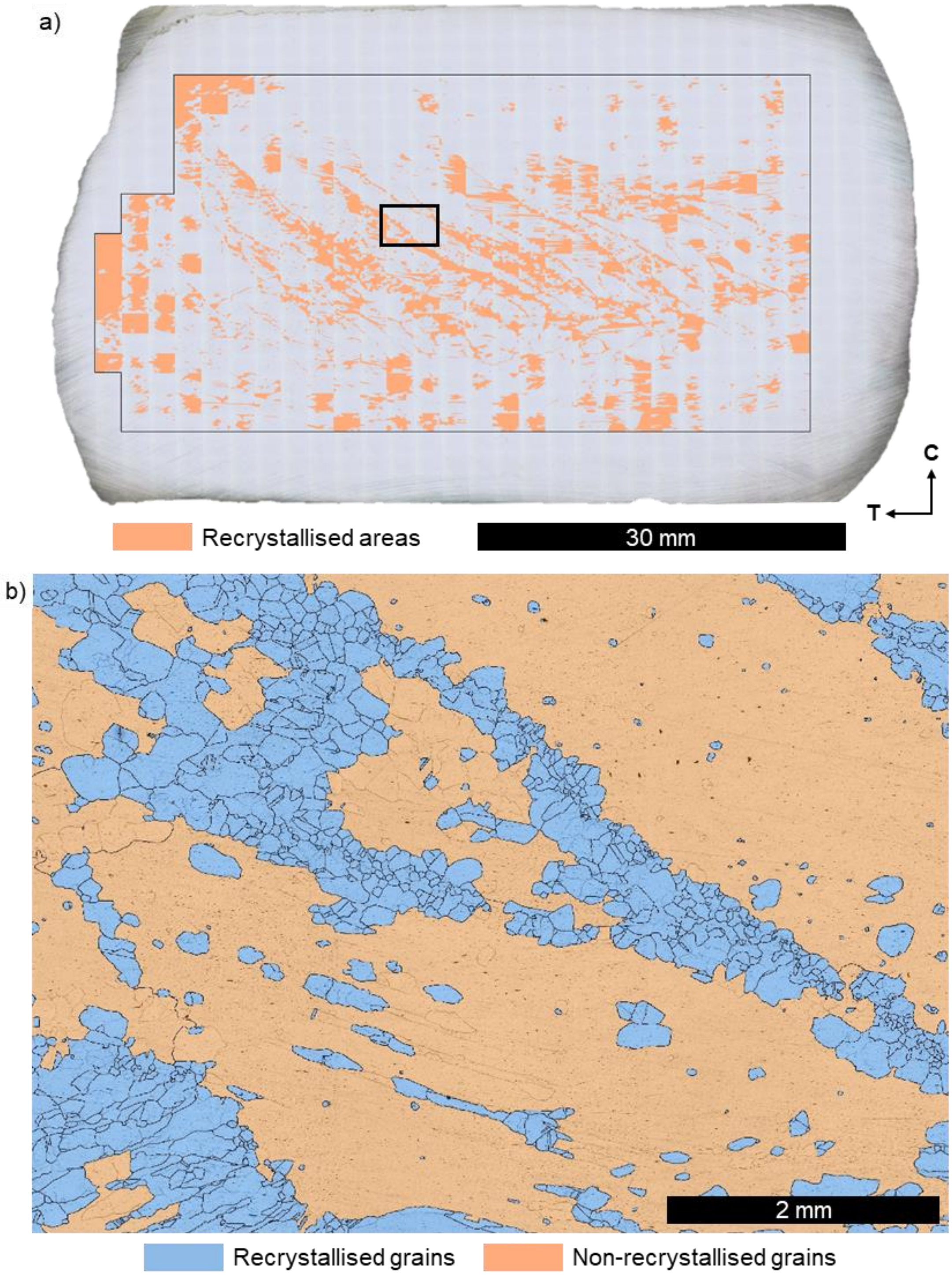

Figure D.2 : a) Reconstructed image of the longitudinal cross-section of the radial 316L sample after 30% upsetting at 1250 °C using the hydraulic press with the areas underwent recrystallisation superimposed, and b) microstructure detail in the high strain zone (i.e., see the solid rectangle in a)) with recrystallised (blue) and non-recrystallised (orange) grains highlighted.

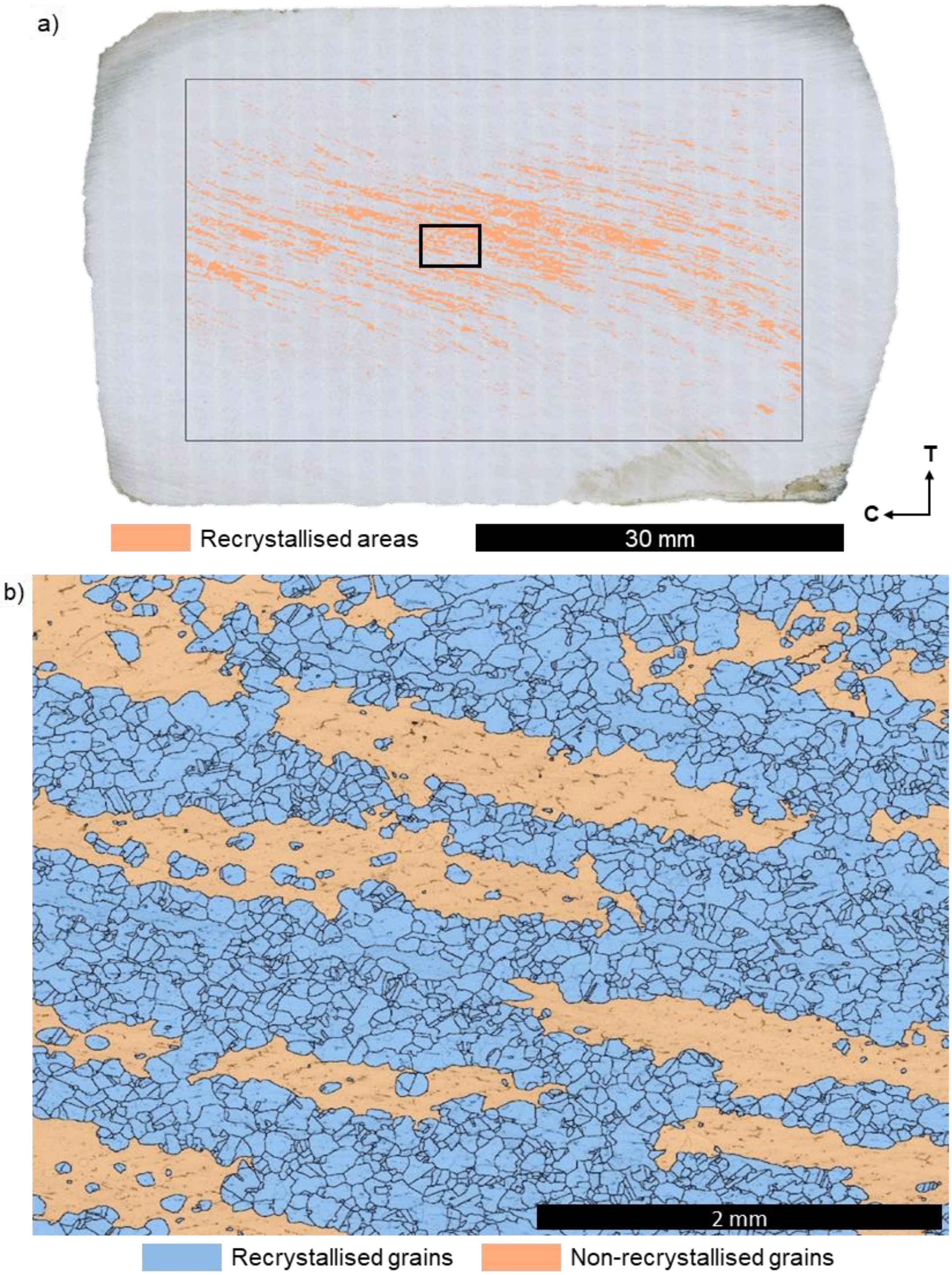

Figure D.3 : a) Reconstructed image of the longitudinal cross-section of the axial 316Nb sample after 30% upsetting at 1250 °C using the hydraulic press with the areas underwent recrystallisation superimposed, and b) microstructure detail in the high strain zone (i.e., see the solid rectangle in a)) with recrystallised (blue) and non-recrystallised (orange) grains highlighted.

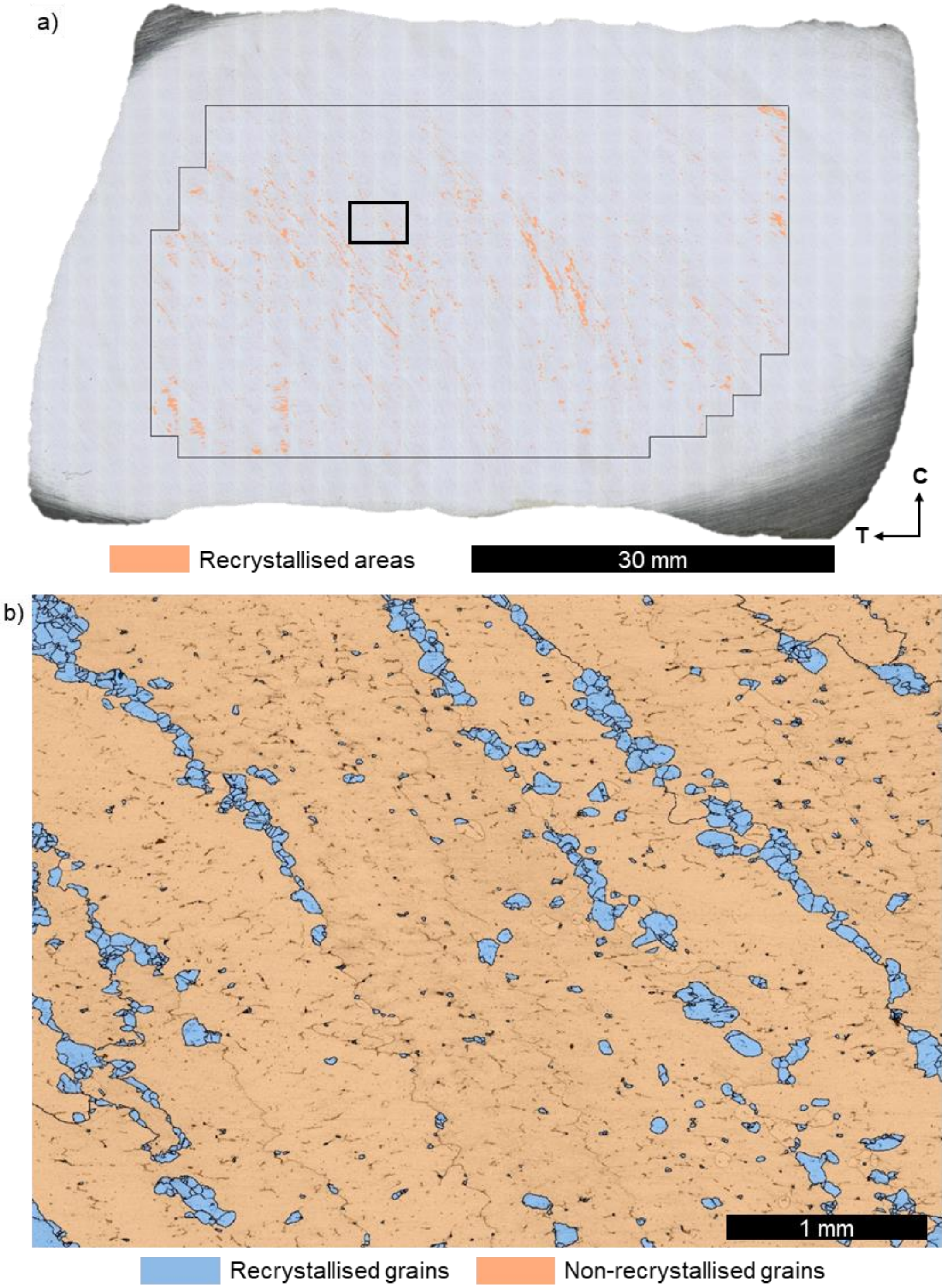

Figure D.4 : a) Reconstructed image of the longitudinal cross-section of the radial 316Nb sample after 30% upsetting at 1250 °C using the hydraulic press with the areas underwent recrystallisation superimposed, and b) microstructure detail in the high strain zone (i.e., see the solid rectangle in a)) with recrystallised (blue) and non-recrystallised (orange) grains highlighted.

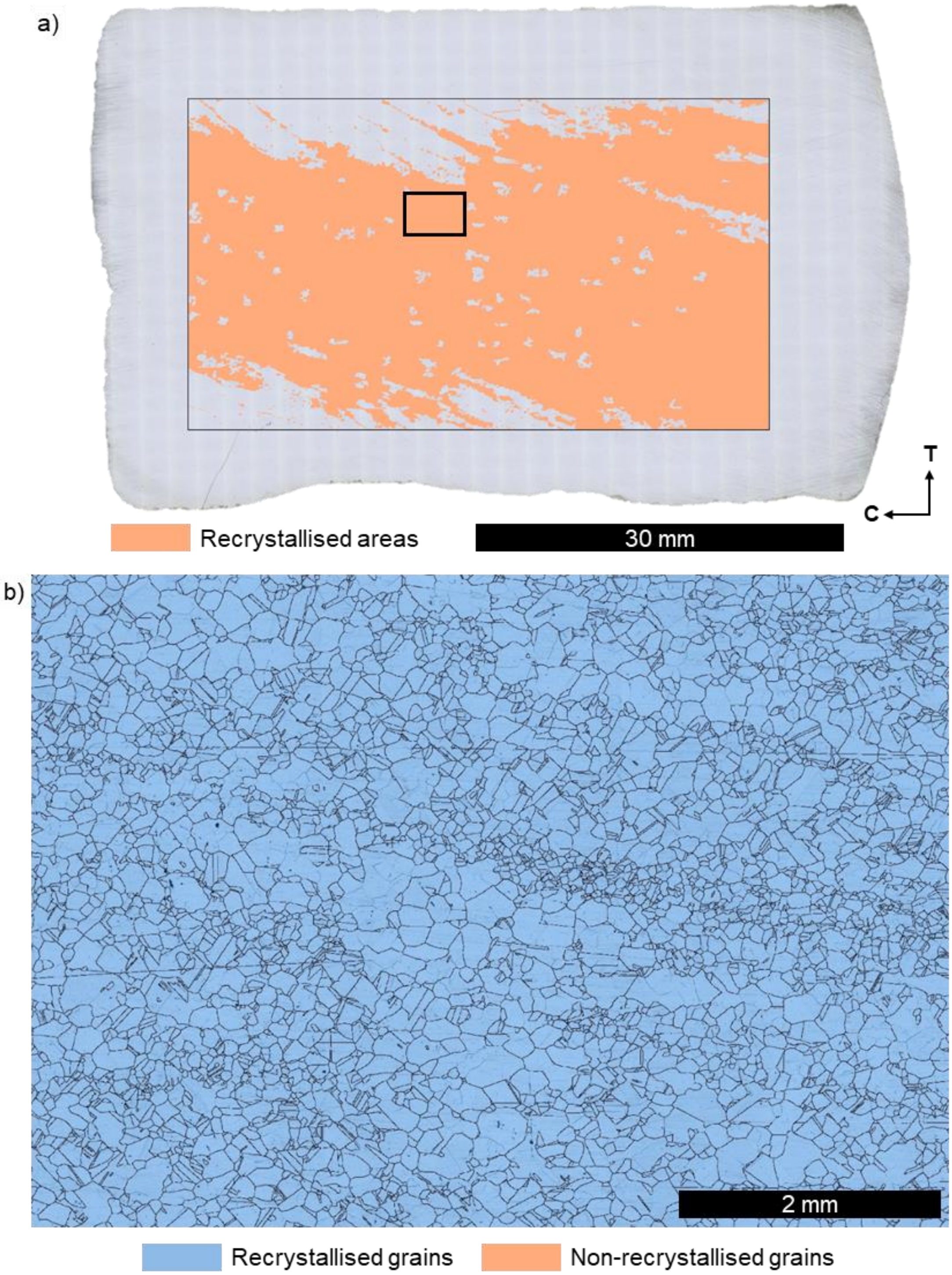

Figure D.5 : a) Reconstructed image of the longitudinal cross-section of the axial 316L sample after 30% upsetting at 1250 °C using the screw press with the areas underwent recrystallisation superimposed, and b) microstructure detail in the high strain zone (i.e., see the solid rectangle in a)) with recrystallised (blue) and non-recrystallised (orange) grains highlighted.

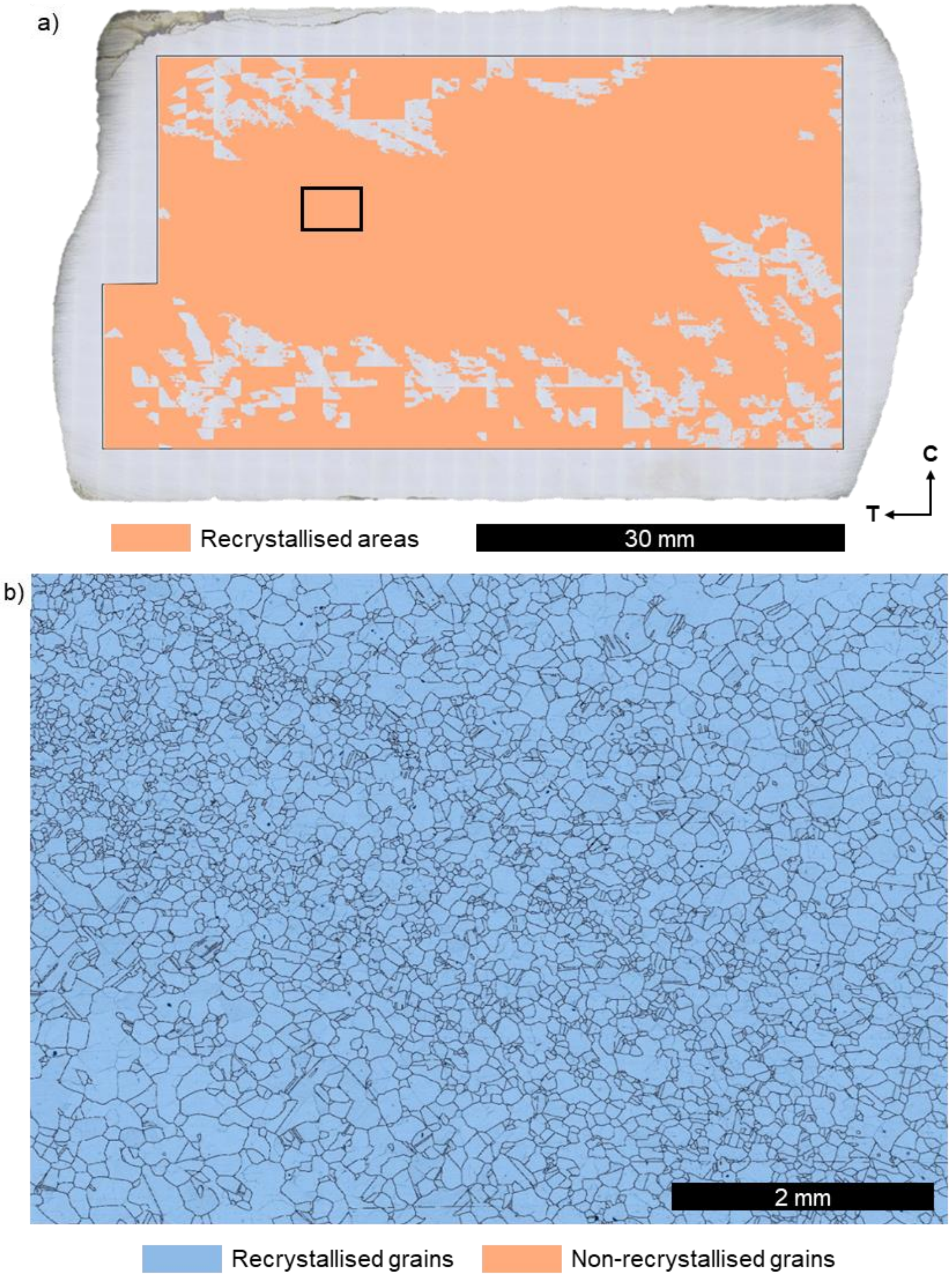

Figure D.6 : a) Reconstructed image of the longitudinal cross-section of the radial 316L sample after 30% upsetting at 1250 °C using the screw press with the areas underwent recrystallisation superimposed, and b) microstructure detail in the high strain zone (i.e., see the solid rectangle in a)) with recrystallised (blue) and non-recrystallised (orange) grains highlighted.

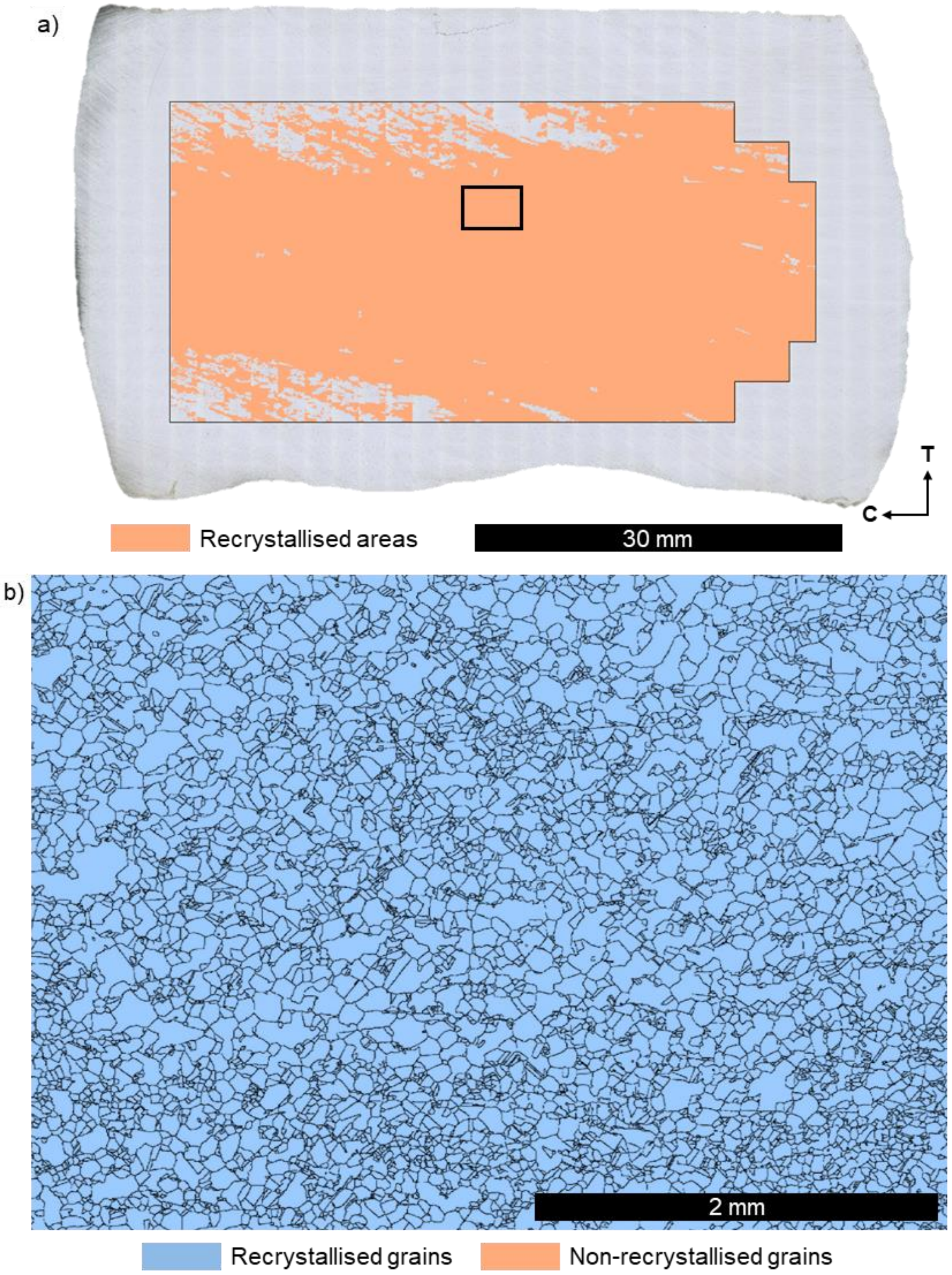

Figure D.7 : a) Reconstructed image of the longitudinal cross-section of the axial 316Nb sample after 30% upsetting at 1250 °C using the screw press with the areas underwent recrystallisation superimposed, and b) microstructure detail in the high strain zone (i.e., see the solid rectangle in a)) with recrystallised (blue) and non-recrystallised (orange) grains highlighted.

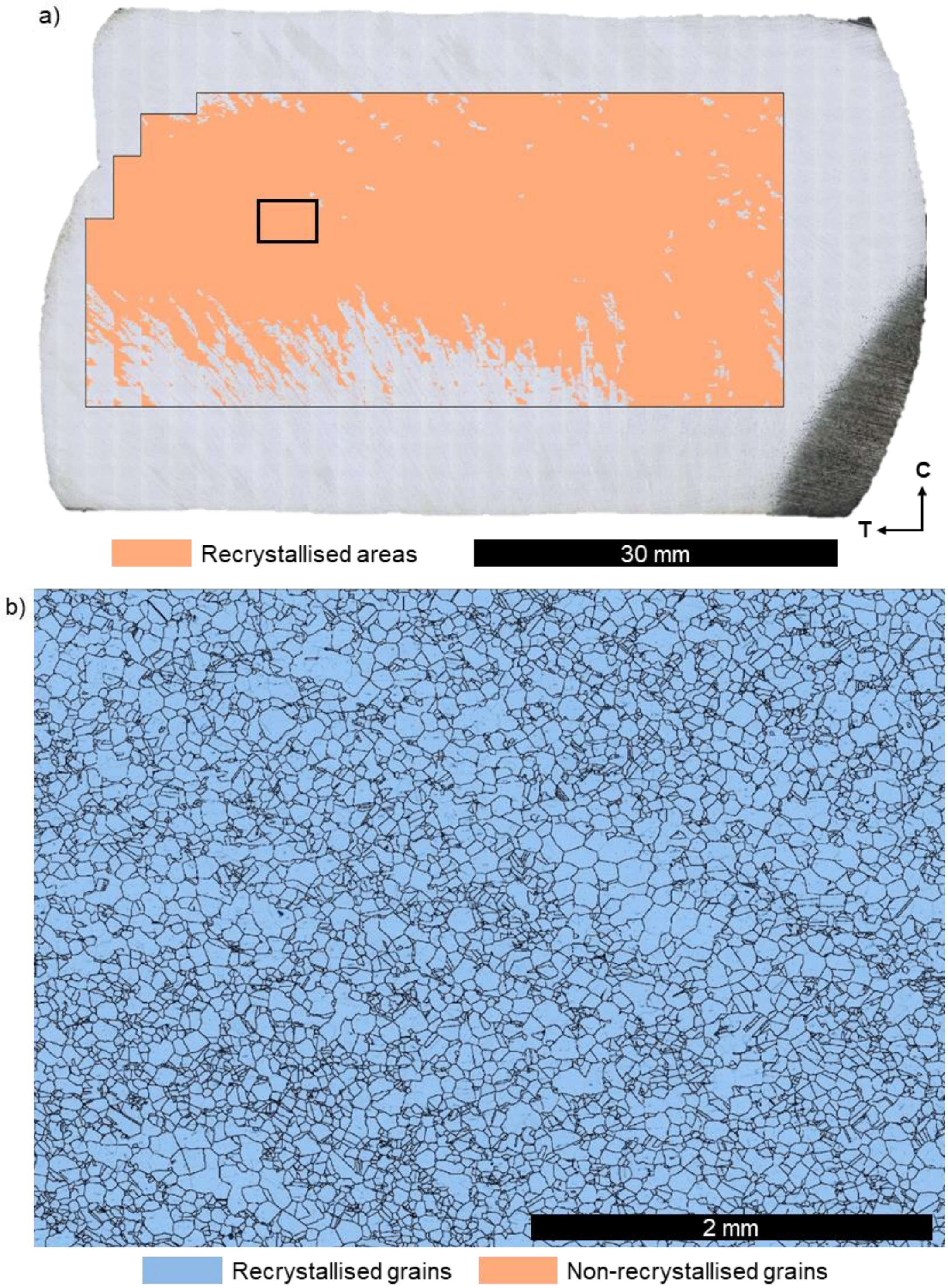

Figure D.8 : a) Reconstructed image of the longitudinal cross-section of the radial 316Nb sample after 30% upsetting at 1250 °C using the screw press with the areas underwent recrystallisation superimposed, and b) microstructure detail in the high strain zone (i.e., see the solid rectangle in a)) with recrystallised (blue) and non-recrystallised (orange) grains highlighted.